APPLICATIONS OF SINGLE-CELL RAMAN MICRO-SPECTROSCOPY TO THE STUDY OF CANCER METABOLISM



Tong Yu

St Peter's College

University of Oxford

A thesis submitted for the degree of

Doctor of Philosophy

Hilary 2023

Acknowledgements

I would like to express my heartfelt gratitude to all the participants for their support throughout my research journey.

First and foremost, I am grateful to my supervisors, Profs Wei E. Huang, Adrian L. Harris, and Ian P. Thompson, for their invaluable guidance and encouragement. Their expertise and knowledge have been indispensable in shaping the direction of this project. I would like to offer my special thanks to Prof Wei Huang for his patience and unwavering belief in me.

I would also like to extend my sincere thanks to Drs Christos E. Zois and Jiabao Xu for their assistance at every stage of the research project. I am especially grateful to the members of my group like Drs Catharine Fan, Fariza Ammam, Chun Kiat Ng, Helen Sheldon, Ellen De Heer, Marina Petrenko, Mira Kreuzer, and many more, for their assistance and stimulating discussions that helped me refine my ideas.

I am also grateful to my friends May Sin Ke, Yipei Wang, Yang Zhang, Shuai Ren, Wenyuan Zhang, and Wei Wei for their kind help and support, which made my study and life in Oxford a wonderful time.

I would also like to express my gratitude to the Departments of Engineering Science and Oncology, the Weatherall Institute of Molecular Medicine, and Prof Francesca Buffa's wet lab for providing me with the resources and facilities necessary to carry out my research.

Finally, I am deeply appreciative of my family for their unconditional love and support throughout my PhD study. Their understanding, sacrifices, encouragement have been a constant source of strength and motivation. Without their support, this achievement would not have been possible, and I am forever indebted to them for their love.

Declaration

I, Tong Yu, hereby declare that the work presented in this thesis was completed by me from October 2018 to September 2022 in the Department of Engineering Science and the Department of Oncology at the University of Oxford, under the supervision of Profs Wei E. Huang, Adrian L. Harris, and Ian P. Thompson.

Except for the collaboration described below, the work presented in this thesis has been done solely by me.

Chapter 2: The background on Raman spectroscopy is based on a published review paper, which I have co-authored with Dr Jiabao Xu.

Chapter 3: Western blot data for CA9 and HIF-1α protein expression induced by hypoxia in U87 and SUM159 were provided by Dr Christos E. Zois.

Chapter 6: This chapter is a published paper in *Cancers*, where I am a co-first author. The subject of the research was a collaborative project between Prof Wei E. Huang, Prof Venugopal Nair, Dr Archana Chandrabhan Jadhav, Dr Jiabao Xu, and me. Dr Jadhav was responsible for viral infections and cell activity assays, while I conducted Raman measurements of cell metabolism. The data and methods used in the study were provided by Archana and me, and the data visualisation and majority of writing were undertaken by Dr Xu and me.

List of Publications

Published papers:

1. Yu T, Jadhav A C, Xu J, et al. Metabolic Reprogramming in Colon Cancer Cells Persistently Infected with Newcastle Disease Virus[J]. Cancers, 2023, 15(3): 811.
2. Xu J, Yu T, Zois C E, et al. Unveiling Cancer Metabolism through Spontaneous and Coherent Raman Spectroscopy and Stable Isotope Probing[J]. Cancers, 2021, 13(7): 1718.
3. González-Cebrián A, Almenar-Pérez E, Xu J, Yu T, et al. Diagnosis of Myalgic Encephalomyelitis/Chronic Fatigue Syndrome with Partial Least Squares Discriminant Analysis: Relevance of Blood Extracellular Vesicles[J]. Frontiers in Medicine, 2022: 664.

Manuscripts under preparation:

1. Tong Yu, Christos E. Zois, Jiabao Xu, Ian P. Thompson, Adrian L. Harris and Wei E. Huang. “Regulation of intracellular HCO_3^- by Carbonic Anhydrase 9 and mitochondrial metabolism measured by Raman single cell spectroscopy”.
2. Tong Yu, Christos E. Zois, Jiabao Xu, Ian P. Thompson, Adrian L. Harris and Wei E. Huang. “Application of single-cell Raman micro-spectroscopy using ^{13}C–glucose to study glycogen metabolism in human glioblastoma cells”.

Abstract

Tumours are composed of cancer cells with various phenotypes and metabolic activities. Even though cells are from the same tumour with the same genotypes, they can manifest distinct phenotypic states in different locations. It is one of the key challenges to understand cancer metabolism and intratumorally heterogeneity using accurate, reliable, and non-destructive approaches. Single-cell Raman micro-spectroscopy (SCRM) is a label-free biochemical profiling technology that can reveal intrinsic chemical information of individual cells and give insight into metabolic profiles at the single cell and subcellular level. An informative approach to the application of Raman spectroscopy is to use stable isotope probing (Raman–SIP) to study single cell metabolism, heterogeneity, interactions in cancer cells.

Here, I applied SCRM and Raman–SIP to the study of bicarbonate, glycogen, and glutamine metabolism in the U87 and SUM159 cell lines and analysed metabolic reprogramming in Caco-2, which showed resistance to cancer therapy by an oncolytic virus – Newcastle disease virus.

Our findings indicate that the 1043-cm^{-1} band is a characteristic band of intracellular HCO_3^-. Carbonic anhydrase 9 and mitochondria are the two main factors regulating external/internal HCO_3^- amounts, respectively. The metabolism of bicarbonate is also upregulated by hypoxia and low glucose

concentration. Glycogen has three characteristic Raman peaks, and the assignments of the bands are related to its structure. ^{13}C labelling shows the dynamic turnover of glycogen and its distribution at the single-cell level. Glutamine is rapidly metabolised in the synthesis of endogenous cellular molecules and is heavily involved in the synthesis of proteins, lipids and nucleic acids, but the carbon in glutamine is not directly responsible for the synthesis of glycogen.

To conclude, Raman techniques are invaluable to analyse the metabolic response in cancers at single cell level. It provides thousands of data points for subcellular localisation, which could be exploited to develop metabolic targeting therapies and may become a key approach to future clinical developments of novel anticancer treatment.

Contents

List of Figures ..... **i**

List of Tables ..... **v**

List of Abbreviations ..... **vi**

Chapter 1 Introduction **1**

1.1 Project aims **2**

1.2 Structure of the thesis and key findings **3**

Chapter 2 Background **6**

2.1 Cancer metabolism **7**

2.1.1 Glycogen metabolism 9

2.1.2 Glutamine metabolism 15

2.1.3 Bicarbonate metabolism 19

2.2 Single-cell Raman micro-spectroscopy **21**

2.2.1 Principles of Raman spectroscopy 22

2.2.2 Principles of Raman–stable isotope probing (Raman–SIP) 24

2.2.3 Advantages of Raman–SIP in cancer study 26

2.2.4 Raman–SIP monitors intracellular metabolic activities 29

2.3 Outlook **35**

Chapter 3 Regulation of intracellular HCO_3^- by Carbonic Anhydrase 9 and mitochondrial metabolism measured by Raman single cell spectroscopy **37**

3.1 Introduction **41**

3.2 Experimental section 44

3.3 Results 49

3.3.1 Spatially resolved Raman mapping of cancer single cells 50

3.3.2 Identification of the intracellular bicarbonate Raman band 50

3.3.3 Role of CA9 51

3.3.4 Role of hypoxia 53

3.3.5 Effects of bicarbonate and U-104 on mitochondrial metabolism 57

3.3.6 Metformin effects on bicarbonate 58

3.3.7 Effects of metformin and CA9 knockdown on bicarbonate metabolism 62

3.3.8 Metformin effects on cytochrome c 65

3.3.9 Bicarbonate accumulation under different oxygen and glucose concentrations 67

3.4 Discussion 72

3.4.1 Bicarbonate band validation 72

3.4.2 Where does bicarbonate come from? 72

3.4.3 Mitochondria play a key role in bicarbonate metabolism and regulation 74

3.4.4 Bicarbonate accumulation and glycolytic activity may be correlated 75

3.4.5 Cytochrome c has intratumoural heterogeneity 77

3.4.6 Application of Raman analysis to bicarbonate metabolism 78

3.5 Supporting information 80

Chapter 4 Application of SCRM–SIP using ^{13}C-glucose to study glycogen metabolism in cancer cells 87

4.1 Introduction 88

4.2 Materials and methods 91

4.3 Results and discussion 94

4.3.1 Glycogen extraction and identification of Raman characteristic bands of glycogen 94

4.3.2 Glycogen semi-quantitative analysis and high-resolution Raman mapping of glycogen and DNA distribution 98

4.3.3 ^{13}C-glucose isotope probing 103

4.3.4 Glycogen metabolic profiles in ^{12}C and ^{13}C-glucose medium 106

4.3.5 Metabolic phenotyping of other bio-components with ^{13}C-glucose stable isotope probing 121

4.3.6 Acute breakdown of glycogen in short-term glucose-free incubations 129

4.4 Conclusions 134

Chapter 5 Phenotypic alterations in the metabolism of cancer cells labelled with ^{13}C-glutamine and deuterium isotope probing 136

5.1 Introduction 137

5.2 Materials and methods 140

5.3 Results and discussion 143

5.3.1 Validation of ^{13}C-glutamine labelling in cancer cells 143

5.3.2 Changes in Raman band shifts of cancer cells after ^{13}C-glutamine labelling 149

5.3.3 Intracellular metabolic activities revealed by SCRM–DIP and ^{13}C-isotope probing 155

5.4 Conclusions 162

Chapter 6 Metabolic reprogramming in colon cancer cells persistently infected by Newcastle disease virus 164

6.1 Introduction 168

6.2 Materials and methods 170

6.3 Results and discussion 174

6.3.1 Cell line screening for establishing an NDV–susceptible cancer cell system 174

6.3.2 Identification of persistently infected VR Caco-2 cells 177

6.3.3 Persistent VR Caco-2 can be identified by metabolic profiles at single-cell level 180

6.3.4 Raman profiles differentiate VR Caco-2 and Caco-2 cells 182

6.3.5 Raman–DIP reveals metabolic reprogramming via newly synthesised biomolecules 184

6.4 Conclusions 188

Chapter 7 Summary and perspectives 191

7.1 Work summaries 191

7.2 Limitations 196

7.3 Perspectives 198

References 201

Appendix 227

List of Figures

Figure 2.1 The pathway of glycogen, glutamine, and bicarbonate metabolism in cancer cell.....8

Figure 2.2 The structure of glycogen.....11

Figure 2.3 The glutamine metabolic footprint of notrogen and carbon in cancer 17

Figure 2.4 (A) Electromagnetic radiation interacting with a vibrating molecule. (B) Schematic energy diagrams of spontaneous Raman scattering and coherent Raman scattering (CRS). 24

Figure 2.5 Raman spectrum—a cell's fingerprint. 24

Figure 2.6 Raman–SIP strategies to study cellular metabolism.....29

Figure 3.1 Schematic of subcellular spatial Raman mapping of single cells based on poly-L-lysine modified Raman slides. 49

Figure 3.2 Bicarbonate production and mitochondria activity in response to MDA-MB-468 CA9 mutants under effect of an CA9 inhibitor in hypoxic condition 52

Figure 3.3 Bicarbonate expression of U87 & SUM159 with the effect of CA9 inhibitor in 10-mM DMEM culture. 55

Figure 3.4 Comparison of the inhibitory effect at different concentrations of metformin on bicarbonate.....60

Figure 3.5 Effect of metformin on bicarbonate production in MDA-MB-468 EV and shCA9.....64

Figure 3.6 Variations in bicarbonate production in cells under different concentrations of oxygen and glucose. 70

Figure 3S1 Comparison of poly-L-lysine-modified and untreated Raman slides and its applications on different cancer cell line. 80

Figure 3S2 Raman spectra of pure $NaHCO_3$ with a characteristic 1043-cm^{-1} peak. 81

Figure 3S3 Metabolism of bicarbonate in cytoplasm and mitochondria in cancer cells. 82

Figure 3S4 Validation of hypoxia-induced expression of hypoxia-inducible factor 1-alpha (HIF-1α) enzyme and CA9 protein. 83

Figure 3S5 Comparison of the inhibitory effect of metformin on bicarbonate under hypoxia in MDA-MB-468 EV. 84

Figure 3S6 Glycogen changes in response to U-104 inhibition. 85

Figure 4.1 Key pathways for glycogen metabolism process in cancer cells .. 89

Figure 4.2 Identification of glycogen characteristic Raman bands 94

Figure 4.3 Comparison of glycogen characteristic Raman bands with cellular background in Raman mapping within a single cell. 97

Figure 4.4 Single-cell Raman micro-spectroscopy detects intensity of glycogen in U87 WT and PYGL KD cells under normoxia, hypoxia and γ radiation treatment 99

Figure 4.5 Effect of different gradients of ^{13}C-glucose medium on cellular activity and comparison of ^{12}C and ^{13}C-labelled glycogen peak positions… 103

Figure 4.6 Raman profiles of ^{12}C and ^{13}C-glucose labelled U87 cells cultured in normoxia and hypoxia for 3, 6, 12, 24 and 48 hours. 106

Figure 4.7 Comparation of Raman mapping and statistical analysis of glycogen labelled by ^{12}C and ^{13}C-glucose. 110

Figure 4.8 Intracellular distribution of the three characteristic bands of large

glycogen granules at 48 hours timepoint.....115

Figure 4.9 Schematic diagram of the relationship between the Raman characterisitc band of glycogen and its structure 117

Figure 4.10 Band area comparisons of (A) ^{12}C glycogen and (B) ^{13}C glycogen in U87 cells cultured for 3, 6, 12, 24 and 48 hours under normoxia and hypoxia. 118

Figure 4.11 Comparason of Raman band shifts after different times of incubation with ^{12}C and ^{13}C-glucose.....125

Figure 4.12 SCRM mapping images of the main biochemicals after 24 hours-^{13}C labelling. 125

Figure 4.13 The tracing pathway of ^{13}C-glucose metabolic activity.....127

Figure 4.14 The averaged Raman spectra of U87 cell incubated in glucose-free media at different time points under normoxia. 129

Figure 4.15 Metabolic analysis of the rapid degradation of glycogen in the short term 133

Figure 5.1 Raman spectra of glutamine and ^{13}C-lablled glutamine.....143

Figure 5.2 The averaged Raman spectra of (A) U87 and (B) SUM159 cultured at different gradients of ^{13}C-glutamine for 24 hours. 145

Figure 5.3 Cell activity under different rates of ^{13}C-glutamine incubation. ...146

Figure 5.4 Raman fluorescence imaging of U87 cells stained with neutral red. 147

Figure 5.5 Band shifts of different biocomponents in cancer cells after labelling with ^{13}C-gulamine for 48 hours......155

Figure 5.6 SCRM of U87 and SUM159 for 24 hours in a culture medium with 35% D_2O and increasing gradients of ^{13}C-glutamine. 157

Figure 5.7 SCRM of U87 grown for 48 hours within 35% D_2O and high gradients of ^{13}C-glutamine. 159

Figure 5.8 Raman-SCRM band shifts of U87 cells under double labelling with deuterium and ^{13}C. 161

Figure 6.1 Time- and NDV dose-dependent cell viability assay in different human cancer cells. 175

Figure 6.2 Characterisation of VR Caco-2 and Caco-2 cells. 178

Figure 6.3 Distinct Raman profiles of Caco-2 and VR Caco-2 cells. 181

Figure 6.4 Quantification of biomolecules in Caco-2 and VR Caco-2 based on their SCRS 183

Figure 6.5 Raman-DIP of newly synthesised DNA, proteins and lipids 186

List of Tables

Table 1.1 Studies using Raman–SIP to probe metabolism in mammalian cells. 30

Table 6.1 Molecular vibrations and biological assignment of Raman wavenumbers of importance via LDA model. 187

List of Abbreviations

ABC	ATP-binding cassette
BT	Bicarbonate transporters
CA9	Carbonic anhydrase IX
CAIs	CA inhibitors
CAs	Carbonic anhydrases
CCD	Charge coupled device
CFSE	Carboxyfluorescein succinimidyl ester
Cit	Citrate
CO_2	Carbon dioxide
CRS	Coherent Raman scattering
Cyt c	Cytochrome c
D_2O	Heavy water
DIP	Deuterium isotope probe
DMEM	Dulbecco’s modified eagle's medium
DNA	Deoxyribonucleic acid
dpi	Day post infection
EDTA	Ethylenediaminetetraacetic acid
EV	Empty vector
$FADH_2$	Flavine adenine dinucleotide
FBS	Fetal bovine serum
FISH	Fluorescence in situ hybridisation
G1P	Glucose-1-phosphate
G6P	Glucose-6-phosphate
GBE	Glycogen branching enzyme
GC-MS	Gas chromatography-mass spectrometry

GFP	Green fluorescent protein
GLS/GLS2	Kidney/liver-type glutaminase
GLUD	Glutamate dehydrogenase
GLUT	Glucose transporter
GSH	Glutathione
H&E	Hematoxylin and eosin
H^+	Hydron
HCO_3^-	Bicarbonate
HIF-1	Hypoxia-inducible transcription factor 1
hpi	Hour post infection
HREs	Hypoxia-response elements
IR	Infrared spectroscopy
ISE	Ion-selective electrode
ISR	Integrated stress response
KOH	Potassium hydroxide
Lac	Lactate
LDA	Linear discriminant analysis
Mal	Malate
MCTs	Monocarboxylate transporters
MEM	Minimum essential medium eagle
MFI	Mean fluorescence intensity
MOI	Multiplicity of infection
mtDNA	mitochondria DNA
mTOR	mammalian target of rapamycin
NADH&NADPH	Nicotinamide adenine dinucleotide phosphate
$NaHCO_3$	Sodium bicarbonate
ND	Neutral density

NDV	Newcastle disease virus
$-NH_2$	Basic amino group
$-NH_4^+$	Ammonium
NMR	Nuclear magnetic resonance
OAA	Oxaloacetate
OH^-	Hydroxide
−OH	Hydroxy group
OXPHOS	Oxidative phosphorylation
PBS	Phosphate buffered saline
PC	Principal component
PCA	Principal component analysis
PFA	Paraformaldehyde
pHi	Intracellular pH
PLP	Pyridoxal-5'-phosphate
PPP	Pentose phosphate pathway
PYGL/M/B	Glycogen phosphorylase form liver/muscle/brain
Pyr	Pyruvate
RNA	Ribonucleic acid
ROC	Receiver operating characteristic
ROC-AUC	Area under the ROC curve
RPMI	Roswell Park Memorial Institute medium
SCRM	Single-cell Raman micro-spectroscopy
SCRS	Single-cell Raman spectrum
SD	Standard deviation
shCA9	CA9 gene knockdown
SILAC	Amino acids in cell culture
SIMS	Secondary ion mass spectrometry

SIP	Stable isotope probing
SLC	Solute carrier transporters
TCA	Tricarboxylic acid cycle
tRNA	Transfer RNA
UDPG	Uridine diphosphate glucose
UDP-GlcNAc	Uridine diphosphate N-acetylglucosamine
UTP	Uridine triphosphate
UV	Ultraviolet
VR	Virus-resistant
α-KG	α-ketoglutarate

Chapter 1

Introduction

Cancers flourish in a complex tumour microenvironment with various metabolic inter-conversions and dynamic regulation of their metabolic activities. It has remained a challenge to achieve an effective and sensitive assay that can directly elucidate the spatial distribution and quantitative assessments of metabolites in cancer. Raman micro-spectroscopy is a biochemical profiling technology which can reveal intrinsic chemical information of individual cells via detecting inelastic scattering through molecular vibrations[1]. Single-cell Raman micro-spectroscopy (SCRM) has the advantage of semi-quantifying abundancy of some metabolites (e.g., bicarbonate, glycogen, cytochrome c) and mapping their distribution at the single cell and subcellular level without external labels. Therefore, these features make SCRM a potentially useful tool for investigating cancer metabolism at high resolution.

This thesis focuses on the energy metabolism of cancer cells, including the two major sources of energy, glucose and glutamine, and bicarbonate, a by-product of respiratory metabolism and essential to maintain acid-base balance. Cancer cells rely on aerobic glycolysis to synthesise free glucose into glycogen and store it as an energy reservoir[2]. Glutamine is a secondary source of energy for cancer cells and provides important substrates for protein, lipid, and nucleic

acid synthesis. Cellular respiratory metabolism produces large amounts of CO_2, which is hydrolysed to produce HCO_3^-. HCO_3^- plays an important role by regulating cell pH and increasing cell viability.

Energy metabolism is a dynamic process, with rapid anabolic and catabolic metabolism constantly engaged ensuring that cancer cells have sufficient energy and a suitable microenvironment to complete their metabolism and proliferation. The metabolism of cancer cells is so distinctive that scientists have been eagerly studying it for the past century. There remain many unknown scientific questions waiting to be unravelled. Here, taking advantage of Raman single-cell technology, I attempt to answer certain scientific questions about cancer cell metabolism. These scientific questions include: 1) Where do cancer cells store glycogen? 2) How does the structure of glycogen differ between granule sizes? 3) Where does glucose from glycogen go after it has been broken down? 4) How rapidly is glycogen turned over? 5) Is glutamine involved in glycogen synthesis? 6) Where does the intracellular bicarbonate come from? 7) What factors influence HCO_3^- in cells? 8) Where do cancer cells accumulate large amounts of bicarbonate?

1.1 Project aims and objectives

The aim of the project is to apply SCRM to study cancer metabolism involving in bicarbonate, glycogen, and glutamine. The objectives are:

I. To develop a methodology for direct cultivation, SCRM measurements and high-resolution mapping of cancer cells on Raman-grade substrates.
II. To validate the methodology by analysing the compartmentalisation of glycogen at the single-cell level.
III. To investigate the role of glucose and glutamine in glycogen turnover in normoxia and hypoxia by employing Raman–stable isotope probes (SIP).
IV. To dissect variations in bicarbonate flux under CA9 mutation and mitochondria inhibition to the response of hypoxia and normoxia.
V. To apply SCRM and Raman–DIP to investigating metabolic differences within virus-infected Caco-2 cells.

1.2 Structure of the thesis and key findings

This thesis contains seven chapters. Chapter 1 is an overall introduction of the thesis. Chapter 2 provides research background and a literature review. Chapters 3 to 6 present the research work. Chapter 7 is the conclusion and reflection.

Chapter 2 is dedicated to the background of cancer metabolism and an introduction to Raman principles. The section on cancer metabolism focuses on the three subtopics of this thesis, glycogen metabolism, glutamine metabolism, and bicarbonate metabolism. The description of Raman micro-spectroscopy includes the Raman principle and the application of Raman–SIP. The technique of Raman–SIP is an important tool in this thesis and is described in detail in terms of ^{2}H and ^{13}C.

Chapter 3 investigates the metabolic profiles of bicarbonate in human glioblastoma and breast cancer cells in response to carbonic anhydrase IX (CA9) and mitochondria under normoxia and hypoxia. The peak at 1043 cm^{-1} is validated as a marker peak for intracellular HCO_3^- and has the potential to become a new indicator in cancer cells. A new method has been developed to allow cells to grow in appropriate biological conditions on the slides without compromising cell viability by modifying the Raman slide surface with poly-L-lysine. Bicarbonate in cancer cells is found to be mainly derived from cellular HCO_3^- flux in hypoxia and intracellular mitochondrial activity in normoxia.

Chapter 4 is the study of glycogen metabolism in the U87 cell line. The three glycogen biomarkers were confirmed through Raman spectra of pure glycogen: 480 cm^{-1}, 850 cm^{-1} and 940 cm^{-1}, respectively. Glycogen is semi-quantified within each individual cell with location and visualised in the cell mapping images. ^{13}C-glucose isotope probing is used here to trace glycogen turnover. The glycogen spots were found to be randomly distributed in cytoplasm with small sizes in short-term incubation, which are formed by long linear chains with a high Raman signal at 850 cm^{-1}. Glycogen granules enlarge exponentially by 48 hours, and the structure is dominated by branched chains with high intensity at 480 and 940 cm^{-1}.

Chapter 5 investigates the role of glutamine in cancer metabolism by analysing its carbon footprint. Carbons from glutamine can be recycled through the TCA cycle and are likely to be involved in glycogen synthesis again. To determine

the specific carbon contribution from glutamine and glucose to glycogen synthesis, ^{13}C-glutamine and heavy water were applied to trace the band shifts of ^{13}C. The findings suggest that glutamine does not significantly contribute to glycogen synthesis as a supplier of energy and carbon source in addition to glucose.

Chapter 6 is the manuscript of Raman applications on metabolic reprogramming in Caco-2 infected by the Newcastle disease virus. Caco-2 colon cancer cells are a type of virus-resistant cancer. They are able to reprogramme metabolic pathways and divert energy from proliferation to protein synthesis and lipid modulation. This chapter demonstrates a strategy to use Raman–D_2O technique to determine metabolic phenotypes that may be suitable targets to overcome resistance to virotherapy in cancer.

Chapter 7 presents a summary of the main conclusions, reflections, and recommendations.

Chapter 2

Background

Contents

2.1 Cancer metabolism

2.1.1 Glycogen metabolism

2.1.2 Glutamine metabolism

2.1.3 Bicarbonate metabolism

2.2 Single-cell Raman micro-spectroscopy (SCRM) (Published paper 2)

2.2.1 Principles of Raman spectroscopy

2.2.2 Principles of Raman–stable isotope probing (Raman–SIP)

2.2.2 Applications of Raman–SIP in cancer

2.2.4 Raman–SIP monitors intracellular metabolic activities

2.3 Outlook

This chapter introduces the background of the research for this thesis and covers two main sections, cancer cell metabolism and Raman spectroscopy. The description of cancer cell metabolism contains three parts, glycogen metabolism, glutamate metabolism, and bicarbonate metabolism, corresponding to the biological background in Chapters 3, 4 and 5 respectively. In Section 2.2, the principles of Raman are explained, followed by our published

review paper on the applications of Raman stable isotopes in the biological and cancer fields.

2.1 Cancer metabolism

Cancer metabolism has been a longstanding topic of great interest in widespread fields. In the last few decades, a widely observed feature of tumour-associated metabolic alteration is that cancer cells rely on the acquisition of necessary nutrients from the environment to meet the demand for energy and biomass production. This reprogrammed metabolism phenomenon is considered a common hallmark of cancer[3].

The "Warburg Effect" indicated aerobic glycolysis as a characteristic of cancer cells in 1960s[2]. Cancer cells take up large amounts of glucose to provide energy through glycolysis and to provide essential building blocks for cell proliferation[4]. Unlike the high-energy yield of oxidative phosphorylation (OXPHOS), only 2 ATP molecules are yielded with one glucose molecule via glycolysis[5]. However, glycolysis is able to produce ATP at a faster rate and in greater quantities which are comparable with OXPHOS[6].

“Aerobic glycolysis” has been considered as the principal energy production in many cancers. However, glutamine is also a source of energy for the cells, providing a source of nitrogen and a source of carbon. It is heavily involved in the synthesis of nucleotides, proteins, and fatty acids and is an important substrate in the formation of the cancer cell cytoskeleton. Additionally, it has

been shown that carbon from glutamine can contribute to the glycogen carbon skeleton after being converted to glucose[7].

The CO_2 produced by cellular respiratory metabolism is hydrolyzed to produce HCO_3^- and H^+. Bicarbonate has important roles in cancer cells, including regulating intra/extra-cellular pH and assisting cell reproduction and survival.

These metabolic processes have a complicated phenotype in cancer cells. Their relevant metabolic pathways in this thesis are shown in Figure 2.1. In the following, I will present the background of each one.

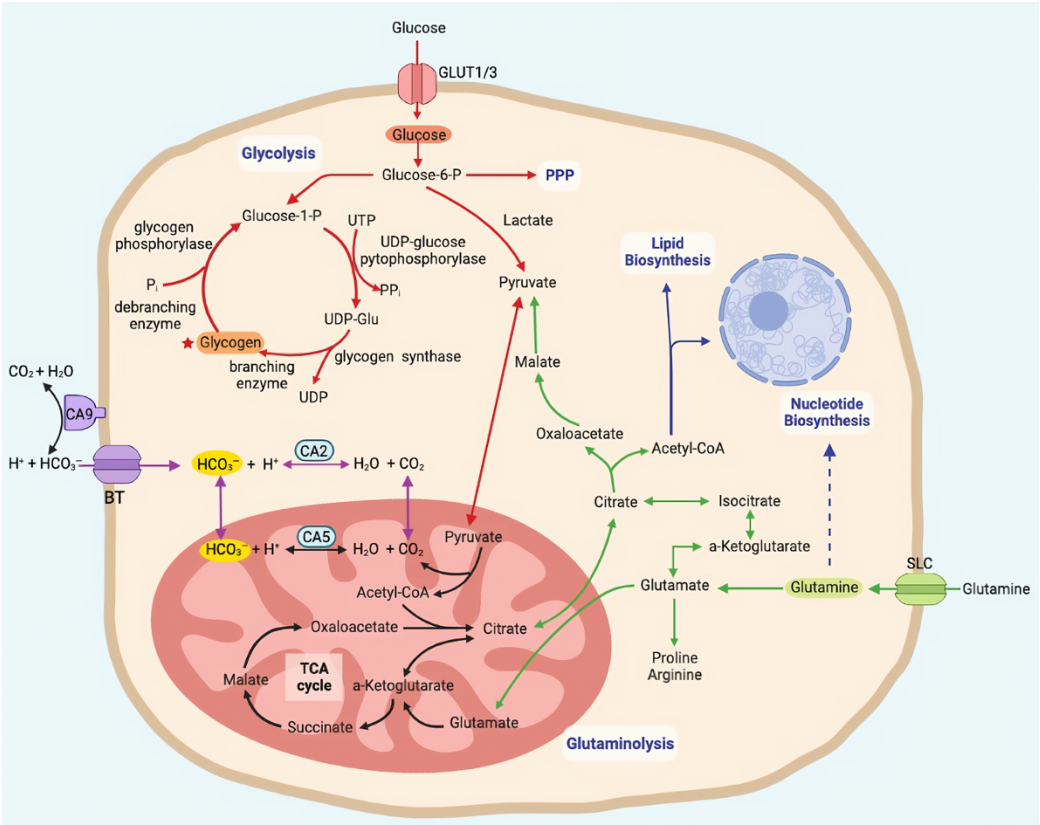


Figure 2.1 The pathway of glycogen, glutamine, and bicarbonate metabolism in cancer cell[8–11]. Abbreviations: BT, bicarbonate transporters; CA, carbonic anhydrase; Glu, glucose; GLUT, glucose transporter; PPP, pentose phosphate pathway; SLC, solute carrier transporters; TCA cycle, tricarboxylic acid cycle;

UDP, uridine diphosphate; UTP, uridine triphosphate.

2.1.1 Glycogen metabolism

Glycogen is a polymer of glucose residues linked together by α-(1,4)-glycosidic bonds, primarily stored in the liver as an energy source and providing a constant supply of glucose to all tissues for later metabolic use[12]. The glycogen granule is a 10-40 nm spheroidal molecule, that contains up to 120,000 glucose residues[13]. Glycogen metabolism involves enzymes and proteins that regulate glycogen breakdown (or glycogenolysis) and glycogen synthesis.

Glycogen synthesis occurs in the cytosol using extracellular glucose transported into the cells through glucose transporters or from an indirect pathway where lactate and amino acids can be used[14,15]. Glycogen breakdown primarily involves phosphorylase and glycogen debranching enzyme, regulated also phosphorylation, resulting in a sensitive regulation process to release glucose residues for energy use[16]. Although the general mechanism of glycogen synthesis and breakdown is the same in all tissues, the regulation of glycogen metabolism differs.

In cancer cells, the regulation of glucose synthesis, storage, mobilization, and catabolism is more sophisticated and elaborate, catering to both immediate and long-term energy needs of the tumours. Cancer cells can take advantage of glycogen under hypoxic environment and regulate several biological processes, including cell proliferation, angiogenesis, metabolism, apoptosis

immortalization and migration[17,18]. The specific mechanism is described in the following sections.

Glycogen synthesis

Figure 2.1 provides a general schematic of the glycogen pathway. When there is an abundance of glucose in cell, glycogen synthesis is stimulated through the action of three enzymes: uridine diphosphate-glucose (UDPG) pyrophosphorylase, glycogen synthase, and glycogen branching enzyme. Glucose-6-phosphate (G6P) is derived from free glucose by hexokinase in muscle or glucokinase in the liver, and then converted to glucose-1-phosphate (G1P) by phosphoglucomutases. As first discovered by Allué in 1975, UDPG is produced when G1P is combined with uridine triphosphate (UTP) and catalysed by UDP-glucose pyrophosphorylase[19]. UDPG is a crucial compound that contributes a glucosyl unit to elongate the glycogen chain.

However, glucosyl units cannot directly link to each other to initiate the glycogen chains. Instead, they require glycogenin, an oligosaccharide primer of the core protein, to initiate the formation of a glucose polymer through self-glycosylation[20]. This leads to a short α (1→4) linked chain of an 8-12 glucose oligosaccharide primer[21–23]. As shown in Figure 2.2, from the protein primer, glycogen synthase then binds UDPG units to the non-reducing ends of the protein primer and elongates the glucose chain through an α (1→4) glycosidic bond. When the elongating chain reaches approximately 8-14 glucose residues,

glycogen branching enzyme (GBE) transfers the long chain into new branches. During this formation, GBE catalyzes the transfer of a 7-residues terminal segment from an α (1→4)-linked glucan chain at the outer non-reducing end into an α (1→6) position of the same or another glycogen chain.

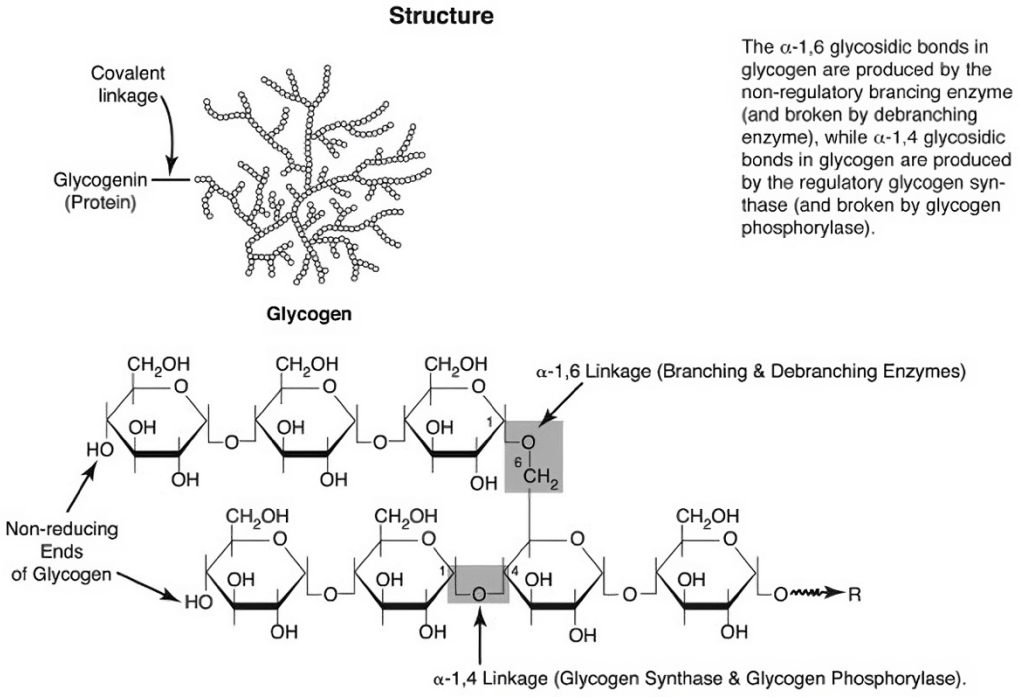


Figure 2.2 The structure of glycogen. Figure from literature[24].

Glycogen breakdown

Glycogen degradation is the opposing process to glycogen synthesis. In mammalian cells, glycogen degradation is regulated through two pathways: the cytosolic pathway and the autophagy and lysosomal pathway[9]. In the cytosol, glycogenolysis requires three enzymes: glycogen phosphorylase, glycogen debranching enzyme and phosphoglucomutase. Glycogen phosphorylase (PYG) was firstly discovered by Coris in the 1940s. It has three isoforms, PYGL (liver), PYGM (muscle) and PYGB (brain)[25–28]. PYGL can serve free glucose

for the whole body, whereas PYGM and PYGB only supply G1P for their tissues[8]. Phosphorylase cleaves glycogen to G1P binding with a vital cofactor pyridoxal-5'-phosphate (PLP). The phosphate group of PLP acts as an acid-base catalyst to facilitate the proton transfer of α-linked terminal glucosyl residue. Therefore, phosphorylase rapidly cleaves the α (1→4)-glycosidic bond to remove glucose residues from the non-reducing ends of glycogen as G1P.

Around 90% G1P is catalyzed through glycogen phosphorylase and then converts into glucose-6-phosphate by phosphoglucomutase, entering glycolysis or the pentose phosphate pathway (PPP). When the glucose unit is less than four or five units away from an α (1→6) branch point, phosphorylase stops releasing glucose, while the glycogen debranching enzyme begins to remove glycogen branches. Glycogen debranching enzyme transfers an α (1→4)-linked trisaccharide unit from the glycogen chain to the non-reducing end of another glycogen chain as a glucosyltransferase.

After that, the remaining glucose residue (about 10%) at the α (1→6) bond is hydrolyzed by further cleavage of the same debranching enzyme to yield free glucose. Glycogen phosphorylase continues to cleave glucose residues from the glycogen chain, producing G1P subsequently.

Glycolysis and hypoxia

Cancer cells are adaptable and can survive and proliferate in hypoxic conditions, which is a reduction in the normal level of tissue oxygen tension (the

hypoxic environment of most cancer cell lines is < 2% O_2 levels)[29]. Under hypoxic conditions, normal cells alter their energy supply method from oxygen-dependent tricarboxylic acid (TCA) cycle to the oxygen-independent glycolysis metabolic pathway.

Cancer cells, on the other hand, rely heavily on glycolysis and metabolize most of their glucose via this pathway even when there is ample oxygen. The earliest research revealed that most types of cancer cells break down glycogen via glycolysis, regardless of whether they are under aerobic or hypoxic conditions. This was reported in 1925 by Otto Warburg based in his first energy metabolism trait[30].

Although TCA cycle generates 36 ATP and glycolysis only yields 2 ATP with one glucose molecule, the rate of ATP production is comparable[6]. Additionally, glycolysis provides many essential building blocks for cell proliferation[4]. As a result, cancer cells compensate for energy by increasing their uptake of glucoses through an important glucose transporter, GLUT1, which substantially conveys glucose into the cytoplasm[31].

Meanwhile, various metabolites, enzymes and cofactors cooperate during the regulation of glycolysis in cancer cells. For example, hypoxia-inducible transcription factor 1 (HIF-1) plays a pivotal role in response to inadequate oxygen tension[32]. HIF-1 binds to hypoxia-response elements (HREs) to activate the expression of a large number of hypoxia-response genes to boost cancer

cells' completion of glycolysis[29]. The remaining glucose accumulates in cancer cells and is converted into glycogen.

Mitochondrial metabolites

Cells contain hundreds of mitochondria, which are important sites for the metabolism of glucose, glutamine and lipids[33]. For many years, it was believed that tumour cells could obtain sufficient ATP from glycolysis alone, and that mitochondria played a limited role in cell progression under optimal growth condition[34]. However, recent advances in technology and methodology have revealed that mitochondria make a significant contribution to cancer cell metabolism[35].

Mutations in mitochondrial genes are common in cancer cells, altering the mitochondrial bioenergetic and biosynthetic state instead of simply inactivating mitochondrial energy metabolism[36]. For example, cancer cells that lack mitochondrial DNA (mtDNA) experience a delay in tumour growth, but can acquire mtDNA from host origin to gradually recover respiratory function from primary to metastatic tumour cells[37]. Key metabolic enzymes in the TCA cycle have been found to be mutated in a variety of cancer cells, and have been the focus of substantial investigation for therapeutic targeting with cancer drugs[38,39].

One controversial aspect of glycogen metabolism in cancer cells is whether they are able to avoid mitochondrial processing of glucose metabolites. Normally, at the last step of glycolysis, pyruvate is imported into the

mitochondria in the presence of oxygen, where it is fully oxidized to CO_2. When oxygen is scarce, however, cells redirect pyruvate away from mitochondrial oxidative phosphorylation. In cancer cells, pyruvate is converted to lactate in the cytosol. Nonetheless, most glucose is broken down in glycolysis, and approximately 10% of glucose in proliferating cells is diverted into biosynthetic pathways upstream of pyruvate production[40]. Studies suggest that mitochondrial gene mutations alter the mitochondrial bioenergetic and biosynthetic state, rather than inactivating mitochondrial energy metabolism[41].

2.1.2 Glutamine metabolism

Glutamine is the most abundant amino acid in the human body. For tumour growth, glutamine is an essential building block of the cell skeleton and is extensively implicated in the synthesis of amino acids, fatty acids and nucleotides[42]. Although it is important for cells, studies on its role in the metabolism of cancer cells have only drawn attention in recent years.

Glutamine was defined as a conditionally essential amino acid by Rose in 1938[43,44]. It is well known that the human body requires 14 amino acids. Nine of these amino acids are unable to synthesis by humans and are therefore considered essential (isoleucine, methionine, leucine, valine, phenylalanine, tryptophan, histidine, threonine and lysine)[45]. The other five amino acids (alanine, aspartic acid, asparagine, glutamate and serine) are considered dispensable because they can be easily synthesized in the human body[46].

In recent years, many studies have found that non-essential amino acids are essential for tumour proliferation and survival[47,48]. Glutamine is now considered as a 'conditionally essential' amino acid [49,50]. The metabolism of cancer cells requires large amounts of glutamine, especially when in a rapid proliferation stage or other stresses[49]. Compared to other organs, tumours are far more dependent on the body's supply of circulating glutamine and act as a "glutamine trap". The addictive feature of cancer cells to glutamine was exposed and then exploited by scientists to develop therapeutic agents for cancer treatment[51]. In glutamate-dependent cancers, reducing glutamine uptake, inhibiting mitochondria, targeting mTOR activation and reducing glutamine metabolizing enzyme activity are all very effective therapies[52]. For example, large glutamine analogues have been verified to deliver anti-CD47 siRNA as carriers for blocking CD47 signalling to kill glutamine-dependent lung cancer A549[51].

Glutamine is transported into cells via transporters. The most well-studied transporter is the solute carrier (SLC), including members of the SLC1, SLC6, SLC7, SLC36, and SLC38 families[10,53]. Driven by the oncogenes of MYC and K-Ras, the expression of the glutamine transporter is upregulated to enhance glutamine uptake[10]. After glutamine enters the cell, it can be employed directly as a substrate by nucleotide synthesis pathways. It promotes the biosynthesis of nucleotides and uridine diphosphate N-acetylglucosamine (UDP-GlcNAc)[54].

Alternatively, glutamine is converted to glutamate by kidney-type glutaminase (GLS) or liver-type glutaminase (GLS2)[55]. Glutamate can be converted to α-

ketoglutarate (α-KG) by two different pathways, glutamate dehydrogenase (GLUD1 or GLD2) or aminotransferases. The main substrate of mitochondria in many cancer cells is glutamine, which is necessary for the integrity and potential of mitochondrial membrane and for formation of NADPH[52].

α-KG enters the TCA cycle to generate ATP via the production of NADH and $FADH_2$ in order to provide energy for cells. The by-product of GLUD is NH_4^+, NADH or NADPH, which contribute to bioenergetics, reducing equivalents and the synthesis of lipids and nucleotides[54,56]. On the other hand, aminotransferase exists both in the mitochondria and in the cytosol[57,58]. The by-product of aminotransferase is other amino acids, which support to nucleotide synthesis, redox control, and integrated stress response (ISR) suppression[59–61].

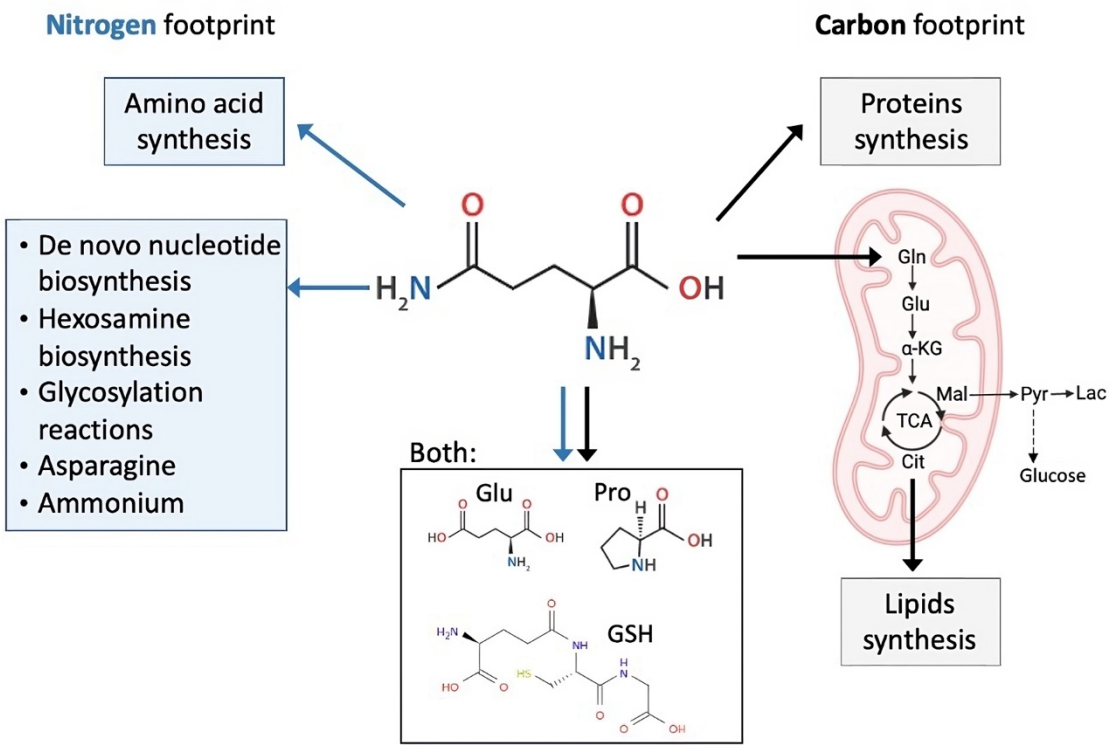


Figure 2.3 The glutamine metabolic footprint of nitrogen and carbon in cancer[62]. Abbreviations: Cit, citrate; GSH, glutathione; α-KG, α-ketoglutarate; Lac, lactate; Mal, malate; OAA, oxaloacetate; Pyr, pyruvate; TCA, tricarboxylic acid cycle.

Glutamine plays an important role in cellular metabolism by supplying nitrogen to the cells and being the second largest source of carbon[50] (Figure 2.3). Glutamine can donate two nitrogen atoms and a five-carbon backbone. Its major function is being the key donor in biosynthetic reactions in cancers. Aminotransferase transfers its nitrogen to generate 'dispensable amino acids', such as asparagine, pyruvate, alanine and α-KG for the production of the extracellular matrix protein collagen and further nucleotide synthesis[54,62].

In addition, glutamine becomes the primary pathway for supplying carbon to the TCA cycle for cell survival when glucose is deficient. It can supplement the TCA cycle and produce other amino acids, act as a precursor for nucleotide and lipid synthesis[62,63]. In plasma, nitrogen from glutamine is directly utilised for the de novo nucleotide synthesis, while carbon from glutamine serves for the synthesis of amino acids and fatty acids[64]. Glutamine can enter the gluconeogenic pathway via the Krebs cycle and be converted to glucose in liver and kidney, predominantly in hepatocytes and renal tubular cells[65]. However, glutamine cannot be directly incorporated into glycogen. Instead, research has shown that its carbon is first converted to glucose before entering the G6P pool and then integrated into the glycogen carbon skeleton[7].

To gain a better understanding of this carbon reuse process, we employed

Raman–SIP to distinguish between glycogen carbon derived from glucose or glutamine in cancer cells. This novel application of SCRM provides valuable insights into the metabolic fate of carbon in cancer cells and have important implications for understanding cancer metabolism.

2.1.3 Bicarbonate metabolism

Cancer cells produce large amounts of metabolic acids through their energy metabolism. There are two major forms of acidic biomasses, either lactate and protons generated via aerobic glycolysis or in the form of HCO_3^-/CO_2 converted through hydration. Although lactic acid is the subject for much cancer research, more recent results have shown that bicarbonate plays an essential role in cancer proliferation[66].

Bicarbonate is a simple single carbon molecule that plays surprisingly important roles in diverse biological processes. Among these are photosynthesis, the Krebs cycle, whole-body and cellular pH regulation, and volume regulation. It has three main functions in cancer: regulating tumour pH, enhancing cell proliferation and survival, and reprogramming mitochondrial function[11,67,68].

Bicarbonate is charged since it needs transporter to facilitate its transport across the cell membrane. There is a large family of bicarbonate transporter. In the human body, there are 14 bicarbonate transport proteins, which can be roughly divided into SLC4 and SLC26 families, anion channels and metal transporters for bicarbonate transport across membranes[67,69,70]. Numerous

studies have focused on carbonic anhydrases (CAs) due to the advantages of therapeutic targeting for cancer treatment[71,72].

Carbonic anhydrases are a big family. In mammals, it includes 16 isoforms which are classified depending on their catalytic activity and expressed localization[73]. Cancer cells primarily express the plasma-membrane-associated isoforms (CA4, CA9, CA12, CA14, CA15), cytosolic isoforms (CA1, CA2, CA3, CA7, CA8), and mitochondrial isoforms (CA5A and CA5B)[74,75]. Under normal circumstances, CO_2 can combine with water to generate HCO_3^- and H^+, but the CAs family accelerates this hydrolysis reaction by up to 1000 times[76]. The CAs active site is a Zn(II) ion coordinated with three histidine residues and a water molecule/hydroxide ion[77]. The CA isoforms catalyze a reversible reaction with the ability to generate CO_2, HCO_3^- and H^+. This process consists of a two-step catalytic mechanism, as demonstrated below (Equation 1 and 2)[78]. In the first step, carbon dioxide is hydrated at the active site to form Zn-bound bicarbonate, following the exchange with H_2O to yield bicarbonate (Equation 1). In the second stage, it is deprotonated with Zn-bound water to generate Zn-bound hydroxyl and hydrogen ions (Equation 2).

$$CO_2 + EZnOH- \leftrightarrow EZnHCO_3^- \leftrightarrow EZnH_2O + HCO_3^- \quad (1)$$

$$EZnH_2O \leftrightarrow EZnOH^- + H^+ \quad (2)$$

Among the cancer-related CAs, CA9 has gained most attention and is strongly upregulated in many tumour tissues. CA9 is induced by hypoxia, functionally

linked to acidosis, implicated in invasiveness, and correlated with therapeutic resistance[79]. Apart from its classical enzyme activity of reversibly hydrating carbon dioxide to form carbonic acid extracellularly to facilitate the net extrusion of protons from inside to outside the cell[67].

Inhibition and activation of CAs assist in provoking alterations in bicarbonate flux in cancer. The classic CA inhibitors (CAIs) are the primary sulfonamides, RSO_2NH_2, with about 30 clinical agents all showing significant CA inhibition[74]. The CAI used in this thesis, U-104 (also known as SLC-001), is a sulfonamide derivative. U-104 has been shown to effectively inhibit CA9 and CA12 enzymatic activity in a variety of different tumors[80–82]. It should be noted that U-104 can only inhibit the catalysed reaction of CA9. CAIs inhibit the reversible hydration and reduces CA-catalyzed HCO_3^- in the extracellular membrane microenvironment. Meanwhile, the non-catalytic mechanism of CA9 can cooperate with bicarbonate transporters to remove H^+ and HCO_3^- crossing the plasma membrane[83].

2.2 Single-cell Raman micro-spectroscopy

Raman spectroscopy technologies present several advantages for the cancer research community. Raman spectroscopy is a label-free spectroscopic method to provide comprehensive biochemical information, the so-called “biomolecular finger-print”, regarding metabolic processes in cells and tissues. In addition, Raman imaging offers high spatial resolution at the sub-cellular

level and is capable of real-time, non-invasive examination of living cells, tissues, and organisms, based on their metabolic profiles. I will emphasis the principles of Raman and applications using Raman and Raman–SIP techniques to investigate metabolism in cancer cells and tissues.

2.2.1 Principles of Raman spectroscopy

Raman spectroscopy is an essential tool for chemists, physicists, biologists, and materials scientists. It was first experimentally observed by C. V. Raman in 1928, for which he was awarded the Nobel Prize in 1930[84]. In Raman spectroscopy, a sample is illuminated with a monochromatic laser beam (Figure 2.4A). The incident laser beam with a frequency of υ_0 interacts with a molecule in the sample that has a vibrational frequency of υ_m. This interaction originates scattered light. The vast majority of the scattered light is elastic scattering, the so-called Rayleigh scattering. However, due to energy exchange between the incident photons and molecular vibration, there is a small fraction of inelastic scattering, which has a different frequency from that of the incident light, collectively called Raman scattering. Raman scattering consists of both Stokes scattering, which has a lower frequency at $\upsilon_0 - \upsilon_m$, and anti-Stokes scattering, which has a higher frequency at $\upsilon_0 + \upsilon_m$ (Figure 2.4B). The Stokes spectrum is often presented as the Raman spectrum, due to its higher intensity, as compared to the anti-Stokes lines.

Raman spectroscopy is now increasingly popular among biologists. A Raman

spectrum can be regarded as a phenotype of a biological system because it provides an overall molecular vibrational profile, containing Raman bands for major cellular building blocks, such as proteins, nucleic acids, lipids, and carbohydrates. Figure 2.5 illustrates a Raman spectrum of a single glioblastoma cell with Raman bands marked with assignments of major biological macromolecules. A biological Raman spectrum can be divided into three regions—the 'fingerprint' region that contains essential bio-information and can be seen as a fingerprint of a cell (400–1800 cm^{-1}); the 'silent' region that usually does not involve vibrational modes contributed by biomolecules formed of naturally occurring isotopes and can involve bands contributed by stable isotopes or triple bonds (1800–2700 cm^{-1}); the high-wavenumber region that is specifically contributed by the stretching vibrations of CH groups, predominantly from lipids and proteins (2700–3200 cm^{-1}).

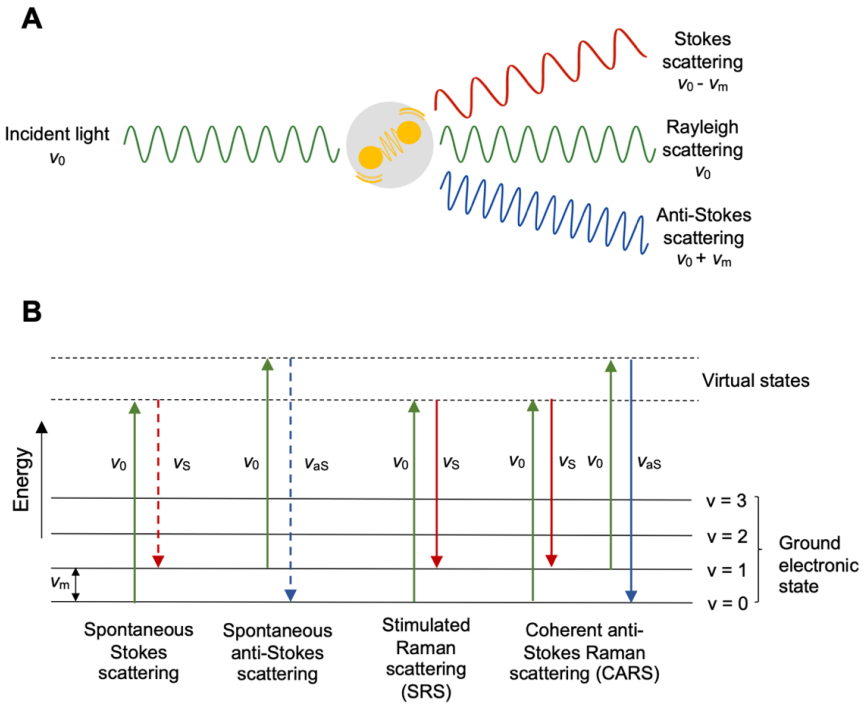


Figure 2.4 (A) Electromagnetic radiation interacting with a vibrating molecule[85]. (B) Schematic energy diagrams of spontaneous Raman scattering and coherent Raman scattering (CRS). The solid arrows indicate laser excitation or stimulated emission; the dashed arrows indicate spontaneous scattering process.

The advantages of using Raman micro-spectroscopy in biological studies are high spatial resolution; ability to detect aqueous samples; intrinsic and label-free characterization; non-contacting and non-destructive analysis; and easy preparation and small sample volume.

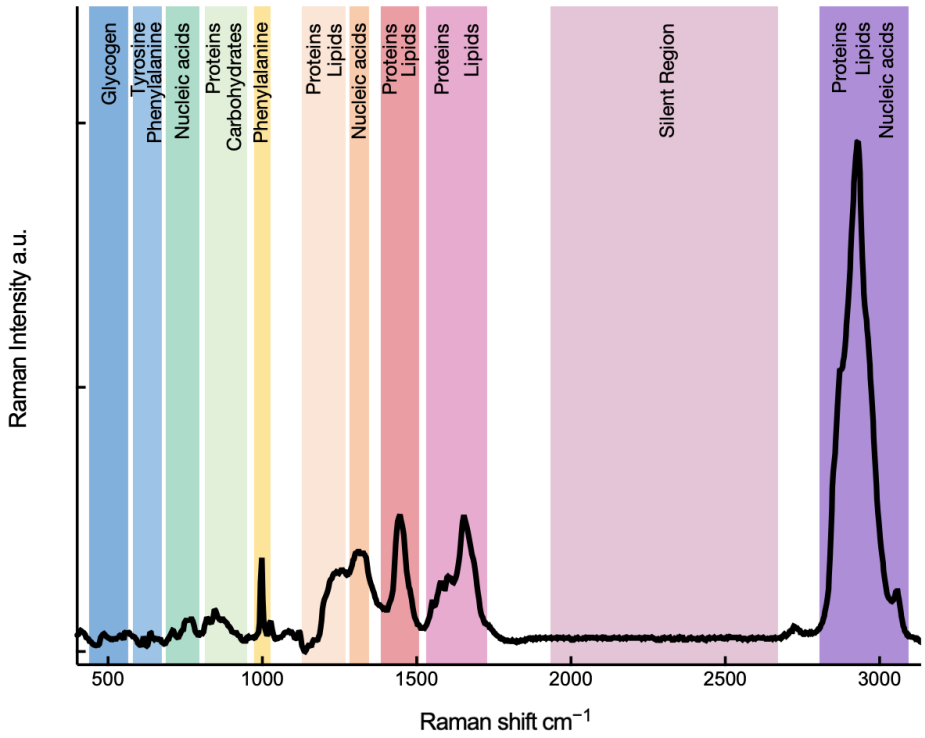


Figure 2.5 Raman spectrum—a cell's fingerprint. Raman spectrum of a single cell of human primary glioblastoma U87 cell line, demonstrating various bands representative of cellular constituents[85].

2.2.2 Principles of Raman–stable isotope probing (Raman–SIP)

As Raman spectroscopy considers changes in vibrational modes of molecules,

a mechanical model can be used to consider a molecular vibration as a spring model. A classical 'two-balls-on-a-spring' approach provides an equivalence of a diatomic molecule with two atoms with masses m_1 and m_2 connected by a chemical bond. The vibrational frequency υ of such a molecule is described as:

$$\upsilon = \frac{1}{2\pi c}\sqrt{\frac{k}{\mu}}$$

where c is the speed of light, k is the force constant of the spring (diatomic bond), and μ is the reduced mass given by:

$$\mu = \frac{m_1 m_2}{m_1 + m_2}$$

Therefore, the vibrational frequency υ is inversely proportional to the square root of the reduced mass μ. When an atom is replaced by its heavier isotope, μ increases, therefore, υ decreases. Taking C–D replacement of C–H as an example, if the ^{1}H atom is replaced by the ^{2}D atom, μ almost doubles and the ratio of the new υ to the old υ is 1.36. Therefore, C–D vibrations usually appear in the silent zone of a Raman spectrum at around 2100–2200 cm^{-1}, shifted from the C–H vibrations at 2800–3000 cm^{-1}. Thus, a strategy to quantify D incorporation is to calculate the percentage of the integrated C–D band area to the sum of the areas of the C–D and C–H bands:

$$\mathrm{D_{incorp}} = \frac{\mathrm{Area_{C-D}}}{\mathrm{Area_{C-D}} + \mathrm{Area_{C-H}}}$$

This type of Raman band shifts can also be observed when replacing ^{12}C, ^{14}N, ^{18}O, or ^{32}S with their heavier analogs. Compared with the C–D shifts, the extent

of the band shift is considerably less dramatic in the ^{13}C and ^{15}N substitutions, due to the comparably low changes in μ. By feeding cells with isotope-labelled substrates, the active cells metabolize these substrates and the isotopic-dependent shifts in Raman spectra can be used as indicators of isotopic incorporation.

2.2.3 Advantages of Raman–SIP in cancer study

By combining the power of optical magnification and direct visualization, Raman micro-spectroscopy can probe biological systems at a subcellular resolution. For large biological systems like tissues, it can collectively produce label-free Raman images with subcellular structural and chemical information. The ability to analyze aqueous samples separates Raman spectroscopy from other vibrational spectroscopies like infrared (IR) spectroscopy. A water molecule has low polarizability; thus, it minimally hinders sample signals in Raman spectroscopy and can be easily subtracted during preprocessing procedures. This is particularly advantageous in biological studies because it avoids laborious sample drying preparation, which might also alter the biochemistry of the samples.

Molecular labelling using genetically encoded reporters (e.g., green fluorescent protein) is used extensively for monitoring cellular events in biological systems[86]. The introduction of unnatural functional groups might risk interfering with the native biological processes. Raman spectroscopy, on the other hand,

is label-free and able to probe biological samples in their natural setting. It also does not require any prior knowledge of the particular substrate for selective labelling. It unbiasedly probes all macromolecules and collectively displays their vibrational modes in one spectrum. Raman spectroscopy is also non-contacting and non-destructive, as opposed to other analytical tools such as gas chromatography and mass spectrometry that destroy the sample to achieve results. This non-invasive, label-free, and spatially resolved nature renders Raman spectroscopy suitable for in vitro and in vivo biological investigations, from investigating a single cancer cell, to producing biochemical maps of cancerous tissues.

SIP to study cell metabolism, in general, shows great advantages over other specific probes that have larger molecular weights, and can disturb the intrinsic metabolic activity of cells. Using isotopes that mimic their naturally abundant counterparts does not alter the natural substrate pool. Among all SIP techniques, Raman spectroscopy has its unique strengths. While modalities like isotope ratio mass spectrometry and NMR spectroscopy require at least 300,000 cells, Raman spectroscopy or secondary ion mass spectrometry (SIMS) coupled with SIP enables an analysis of cell functions at a single-cell level[87]. However, SIMS is limited by its destructive nature and expensive equipment. Raman spectroscopy exceeds other techniques in its non-destructive, sensitive, and relatively cheap nature. While a Raman spectrum already conveys intrinsic and phenotypic in-formation, more insight into cell

functions can be obtained by combining Raman micro-spectroscopy with SIP, using D (^{2}H), ^{13}C, and ^{15}N-containing substrates to replace their primordial isotopes (^{12}C, ^{14}N, and ^{1}H)[88]. Among those stable isotopes, D (^{2}H) and ^{13}C are mostly commonly used due to the stronger C–H bond strength. Heteroatomic X–H bonds such as O–H, N–H, and S–H can be exchanged from nonenzymatic reactions, while C–H bond formation depends solely on enzyme-catalyzed chemical reactions that occurred within the metabolic pathways[89]. This provides unique advantages of D (^{2}H) and ^{13}C for probing the biological metabolism. Providing a wide variety of possible isotopic substrates, Raman–SIP probe the metabolism of most biomolecular constituents of a cell, including proteins, lipids, carbohydrates, and nucleic acids, revealing both molecule specific and general metabolisms, as well as drug–cancer interactions (Figure 2.6).

Although Raman–SIP is now a mature tool to study cell ecology and biology, its application in cancer research is new. Most applications demonstrate the capability of the technique rather than answer specific questions.

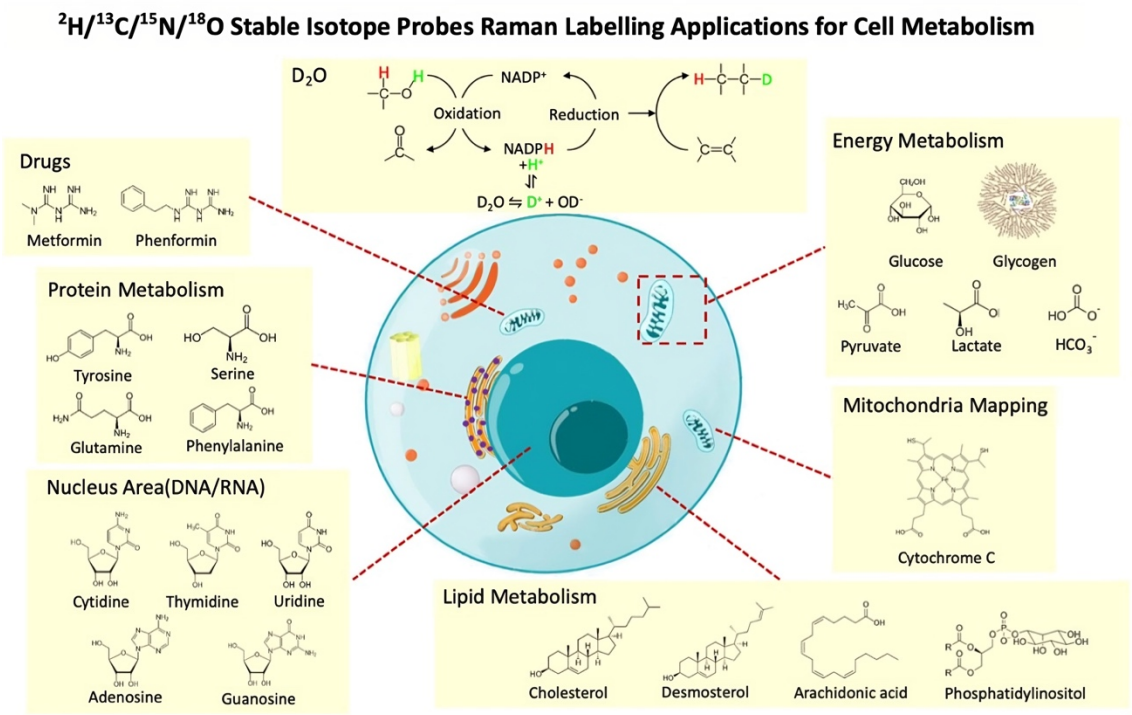


Figure 2.6 Raman–SIP strategies to study cellular metabolism. Heavy water (D_2O) is involved in NADPH regeneration, which is able to indicate the general anabolism activity in cells. Stable isotope labelled sugars, amino acids, nucleic acids, lipid precursors, and drugs can be used to probe the dynamics of metabolic flux and interactions of drugs and cancer cells.

2.2.4 Raman–SIP monitors intracellular metabolic activities

Raman spectroscopy combined with isotopically labelled molecules is used to study the specific metabolic features of cell constituents such as lipids, proteins, and nucleic acids (Figure 2.6). Table 1.1 summarizes a collection of studies using Raman–SIP approaches to study cell metabolism and behaviors, together with their targeted molecules and platform of research.

There is increasing evidence of upregulated demand for fatty acids in cancer cells, compared to their non-malignant counterparts[90]. Lipid uptake, distribution, and metabolism was extensively studied using Raman–SIP approach with

labelled fatty acids in various types of cells[91–97].

Table 1.1 Studies using Raman–SIP to probe metabolism in mammalian cells.

Case studies	Substrate	Target	Platform
Matthäus, C. et al.[91]	d31-palmitic acid d33-oleic acid	Lipids	THP-1 monocytes
Stiebing, C. et al.[93]	d8-arachidonic acid d31-palmitic acid d6-cholesterol-2,2,3,4,4,6	Lipids	Human macrophages
Stiebing, C. et al.[92]	d31-palmitic acid	Lipids	Human macrophages
Majzner, K. et al.[94]	d8-arachidonic acid	Lipids	Endothelial cell line (HMEC-1)
Li, J. & Cheng, J.-X.[95]	d7-glucose d5-glutamine d31-palmitic acid-d31	Lipids	PANC1, A549, MIA PaCa2, MCF7, LNCaP, PC3, HPDE6 and RWPE1 cell lines
García, A. et al.[96]	d38-cholesterol	Lipids	Y1 cell line
Weeks, T. J. et al.[97]	d2-oleic Acid-9,10	Lipids	Human monocytes
Du, J. et al.[98]	d7-glucose d31-palmitic acid d35-stearic acid d33-oleic acid	Lipids	Patient-derived melanoma cell lines
Dodo, K. et al.[99]	d-γ-Linolenic acid	γ-Linolenic acid metabolism and cytotoxicity	WI-38 cell line and VA-13 tumor cell line
Matthäus, C. et al.[100]	1,2-Distearoyl-d70-sn-glycero3-phosphocholine (DSPC-d70)	Liposomal Drug Carrier Systems	MCF-7 cell line
Van Manen, H.-J. et al.[101]	d5-phenylalanine d4-tyrosine d3-methoine	Proteins	HeLa cell line
Wei, L. et al.[102]	d10-leucine	Newly synthesized proteins	Live HeLa cell line Human embryonic kidney HEK293T cell line Neuron-like neuroblastoma mouse N2A cell line
Wei, L. et al.[103]	deuterated amino acids	Proteins	HeLa cell line
Shen, Y. et al.[104]	^{13}C-phenylalanine	Protein degradation	HeLa, HEK293T and PC12 cell lines
Miao, K. & Wei, L.[105]	d5-glutamine	Proteins	HeLa cell line
Zhang, L. et al.[106]	d12-glucose	Glucose metabolism	PC3, HeLa, MCF7, RWPE-1 and U87MG cell lines Mouse model
Lee, D. et al.[107]	d7-glucose	Glucose metabolism; glycogen synthesis	U87 and HeLa cell lines
Hu, F. et al.[108]	3-*O*-propargyl-D-glucose	Glucose metabolism	HeLa cell line U-87 MG tumor xenograft tissue

Long, R. et al.[109]	^{13}C-3-O-propargyl-D-glucose	Glucose metabolism	U87 MG, PC-3, COS-7 and RWPE-1 cell lines
Chen, Z. et al.[110]	^{13}C isotopologues of EdU	DNA	HeLa cell lines
Zhang, L. & Min, W.[111]	d-amino acids d31-palmitate acid d7-glucose	Lipids and proteins	MCF-7 cell lines
Shi, L. et al.[112]	D_2O	Lipids, proteins and DNA	HeLa, COS-7, and U-87 MG cell lines Zebrafish embryos Mouse model
Hekmatara, M. et al.[113]	D_2O	Lipids, proteins and DNA	MCF-7 cell line

De novo lipogenesis in cells can also be studied using deuterated carbon sources such as deuterated glucose or glutamine. Li and Cheng were the first to visualize the direct de novo lipid synthesis that originated from deuterated glucose through imaging[95]. They observed that glucose was largely utilised for lipid synthesis in pancreatic cancer cells, which occurred at a much lower rate in immortalized normal pancreatic epithelial cells. Similarly, de novo synthesis of fatty acids was also studied in undifferentiated and differentiated melanoma cell lines using deuterated glucose with spontaneous Raman spectroscopy[98]. In combination with transcriptomics analysis, the authors identified the fatty acid synthesis pathway as a druggable susceptibility for differentiated melanocytic cells.

Cancer cells exhibit significant metabolic alterations with respect to their primary energy sources, including glucose. Deuterated glucose in Raman–SIP was shown to be valuable for the evaluation and exploration of glucose metabolism in cancer cells. Zhang et al. generated a comprehensive study to visualize the metabolic dynamics of macro-molecules, such as DNA, protein,

lipids, and glycogen, from glucose, in various cancer cell lines, and in an in vivo mouse model with glioblastoma xenografts[106]. The pathway from glucose to glycogen, was also investigated by subcellular visualization of deuterated glycogen from deuterated glucose[107]. Hu et al. developed a protocol for synthesizing deuterated glucose with an alkyne tag, 3-O-propargyl-D-glucose[108]. By using this tag that shows a distinctive Raman band at 2129 cm^{-1}, they quantified the glucose uptake and found different metabolic activities in different cancer cell types. Long et al. further developed this approach to add a second ^{13}C labelling to synthesize ^{13}C-3-O-propargyl-D-glucose[109]. Thus, they demonstrated two-color imaging of glucose uptake and incorporation activity in U-87 MG human glioblastoma cells, PC-3 human prostate cancer cells, COS-7 monkey kidney cells, and RWPE-1 human prostate normal cells, as well as in ex vivo mouse brain tissues.

Just as in SILAC, protein synthesis could be observed in Raman–SIP through the incorporation of isotopically labelled amino acids. Back in 2008, van Manen et al. demonstrated the incorporation of deuterated phenylalanine, tyrosine, and methionine into proteins in single HeLa cells, also observed by the C–D vibrations in the 2100–2300 cm^{-1} spectral region[101]. It was shown that Raman images could be generated by analysing spectra from deuterated amino acids to quantify newly synthesized proteins from deuterated amino acids, in a range of live mammalian cells with high spatial–temporal resolution[102]. Using this approach, subcellular compartments could be identified, revealing fast protein

turnover in HeLa and HEK293T cells, and newly grown neurites in differentiating neuron-like N2A cells. Metabolic changes of proteins and lipids were also studied in cancer cells during epithelial–mesenchymal transition[111]. Compared with approaches like SILAC or fluorescence, this approach with Raman–SIP could examine the proteome of a cell in a spatially resolved, non-destructive manner on living single cells with only minor modifications[114]. This approach could also be used to study protein degradation using ^{13}C labelled amino acids[103,104].

Compared with lipid and protein metabolism, there are fewer studies utilising Raman–SIP approach to study DNA synthesis. Apart from newly synthesized DNA observed from deuterated glucose metabolism, EdU as an analog of thymidine was exclusively used as a DNA metabolic tag, which was incorporated into cellular biomass during cell division[115]. Chen et al. synthesized various designs of ^{13}C isotopologues of EdU and demonstrated three-color chemical imaging of nascent DNA, RNA, and newly synthesized fatty-acids in live HeLa cells[110].

Apart from specifically labelled precursors of cellular constituents, heavy water (D_2O) is suggested to be a unique and universal tool to monitor the synthesis of biomolecules on a global scale. As an isotopologue of water, D_2O can rapidly and freely equilibrate with the total body water inside a cell, and D atoms can exchange with the H atoms to form a variety of X–D bonds. Different from the often non-enzymatic reactions to form heteroatomic X–D bonds, such as O–D,

N–D, and S–D, the C–D bond formation depends solely on enzyme-catalyzed chemical reactions, due to the stronger C–H bond strength[89]. Raman–SIP using D_2O was demonstrated to measure the general metabolic activities of single microbial cells, first reported by Berry et al.[116]. By incubating microbes with D_2O, physiologically active cells could be rapidly and sensitively identified with Raman, by measuring the C–D peak at 2170–2300 cm^{-1}. The metabolic activity could then be semi-quantified and compared by measuring the degree of D incorporation. This approach was extensively applied to study microbial activity and ecology[87,88,117–123].

Although Raman–SIP application in cancer research using heavy water is just coming of age, recent studies exhibit its great potential in metabolic studies, as it is non-invasive, cost-effective, easily accessible, and universally applicable. It can be adapted to a broad range of model systems and cancer research areas to study cancer development, tissue homeostasis, tumor heterogeneity, cancer drug response, and pharmacokinetics. It would be of particular value in diagnosis at surgery, categorizing cancers by their metabolic status, evaluating new drugs, their uptake and metabolism, their antitumor effects, resistance mechanisms, and responses. Characterizing the changes in stroma at the local and distant sites and in premalignant disease, is likely to provide new insights into cancer development.

2.3 Outlook

Monitoring metabolites and understanding the reprogramming pathways are crucial to fully understand cellular metabolism in cancer development and to provide new therapeutic targets. Key questions on tumour metabolic reprogramming have rapidly expanded our understanding of carcinogenesis. In particular, we need to understand 1) how cancer cells reprogram their metabolism and interact with other biological activities to regulate many of these processes, 2) the mechanisms and functions of nutrient acquisition in cancer cells, and 3) what targeted pathways in metabolism can be engaged for the selective development of inhibitors, as well as how to benefit from diagnostics and therapeutic evaluation. However, the challenge remains due to the high complexity and the heterogeneity of intra-tumoral, tissues, and tumour type metabolism.

Raman spectroscopy and Raman imaging are beneficial to cancer research and understanding of metabolic regulation in cancers because they offer single-cell resolution or spatial information about the biochemical composition of nucleic acids, proteins, lipids, and other metabolites. Raman spectroscopy is free of exogenous probes and allows minimal interference with metabolic processes. Offering intrinsic biochemical information and subcellular spatial resolution, the Raman profile of a cancer cell or tissue is an excellent metabolic indicator and an indicator of phenotypic heterogeneity. It can help uncover the molecular basis of the disease and provide comprehensive, objective, and

quantifiable molecular information for diagnosis and treatment evaluation.

Looking into the future, the potential of Raman spectroscopy and imaging in cancer research could be further exploited. Critical improvements and advances are still under development. Raman databases of more metabolites, potentially comparable to a mass spectrometry database, is needed. Advanced chemometric algorithms and machine-learning methods can improve and accelerate current spectral processing and data interpretation, especially in a large, high-dimensional clinical datasets. Instrumentation engineering of advanced fiber optics, detectors, and handheld spectrometers would render Raman tools accessible for clinical translation.

Chapter 3

Regulation of intracellular HCO_3^- by Carbonic Anhydrase 9 and mitochondrial metabolism measured by Raman single cell spectroscopy

Contents

3.1 Introduction

3.2 Experimental section

3.3 Results

- 3.3.1 Spatially resolved Raman mapping of cancer single cells
- 3.3.2 Identification of the Intracellular bicarbonate Raman band
- 3.3.3 Role of CA9
- 3.3.4 Role of hypoxia
- 3.3.5 Effects of bicarbonate and U-104 on mitochondrial metabolism
- 3.3.6 Metformin effects on bicarbonate
- 3.3.7 Effects of metformin and CA9 knockdown on bicarbonate metabolism
- 3.3.8 Metformin effects on cytochrome c
- 3.3.9 Bicarbonate accumulation under different oxygen and glucose concentrations

3.4 Discussion

3.4.1 Bicarbonate band validation

3.4.2 Where does bicarbonate come from?

3.4.3 Mitochondria play a key role in bicarbonate metabolism and regulation

3.4.4 Bicarbonate accumulation and glycolytic activity may be correlated

3.4.5 Cytochrome c has intratumoural heterogeneity

3.4.6 Applications of Raman analysis to bicarbonate metabolism

3.5 Supporting information

This chapter explores the metabolic activity of bicarbonate in cancer cells and its relation to cell membrane-binding transporter and mitochondria. Specifically, inhibitors of carbonic anhydrase IX (CA9) and mitochondria were used to treat cancer cells to investigate the HCO_3^- flux in response to hypoxia and normoxia. The findings of this research have been compiled into a manuscript, which is currently in draft form and ready for submission. The draft manuscript has been attached to this thesis.

TITLE: Regulation of intracellular HCO_3^- by Carbonic Anhydrase 9 and mitochondrial metabolism measured by Raman single cell spectroscopy

Tong Yu[1], Christos E. Zois[2,3], Jiabao Xu[1], Ian P. Thompson[1], Adrian L. Harris[2]* and Wei E. Huang[1]*

1 Department of Engineering Science, University of Oxford, Oxford OX1 3PJ, UK.

2 Molecular Oncology Laboratories, Department of Oncology, Weatherall Institute of Molecular Medicine, John Radcliffe Hospital, University of Oxford, Oxford OX3 9DS, UK.

3 Department of Radiotherapy and Oncology, School of Health Sciences, Democritus University of Thrace, Alexandroupoli, 68100, GR.

* Corresponding to W.E.H and A.L.H.

ABSTRACT

Bicarbonate is known to play a critical role in cancer metabolism, but accurately quantifying its regulation in cancer cells has been challenging. To address this issue, we employed single-cell Raman micro-spectroscopy technology to semi-quantify subcellular bicarbonate and map its distribution in individual cells. Our study identified the 1043-cm^{-1} band as a Raman biomarker for bicarbonate, allowing us to reliably and sensitively track its presence in cancer cells. Using CA9 inhibitor (U-104) to suppress carbonic anhydrase IX (CA9) and using metformin to inhibit mitochondria, we observed a significant reduction of bicarbonate in cancer cells. Furthermore, we found that cancer cells accumulated more bicarbonate under hypoxic and low-glucose microenvironment, where mitochondria and CA9 may have key roles in the metabolism process. The strong and sharp signal of the 1043-cm^{-1} band made it an effective bio- indicator and will provide a valuable tool for future cancer research.

Keywords

Raman, SCRM, single-cell image, bicarbonate, carbonic anhydrase IX (CA9)

3.1 Introduction

Cancer has a complex intracellular environment with various metabolic inter-conversions and dynamic organelles regulating the metabolic activities of the cell. Cancer cells derive their energy metabolism mainly from anaerobic glycolysis and mitochondrial respiration, where vast amounts of metabolic acids are produced. These acidic biomasses are either CO_2 hydrated to HCO_3^- and protons or in the form of lactic acid and protons[124]. Acid-base balance needs to be maintained and regulated. In cancer cells, it is achieved by acid/base exchangers, carbonic anhydrases (CAs) and monocarboxylate transporters[125,126].

Due to glycolytic metabolism, increased expression of lactate transporters, and inadequate vascular clearance[127], cancer cells produce high quantities of lactic acid and excrete it to the extracellular microenvironment[128]. Although previously many researchers have focus on lactate contribution to the acidic microenvironment, recent reports have suggested that the role of CO_2/HCO_3^- equilibrium should be important as a primary pH buffering system in both intracellular and extracellular micro-environments[129]. In cancer cells, HCO_3^- plays a central role in regulating pH values[67], cell proliferation and viability[11,68], and mitochondrial function[11]. Mitochondrial oxidative metabolism is an essential pathway for bicarbonate production in cancer cells[36,130]. Studies have shown that mitochondrial function is also regulated in response to intracellular bicarbonate concentration[11].

HCO_3^- is a base that is converted and transported across the membrane via a large family of bicarbonate transporters[67,77]. The bicarbonate transporters have the capability to affect cancer cell proliferation and growth by regulating the pH of the cell cytosol and extracellular space[131,132]. The hypoxia-inducible carbonic anhydrase IX (CA9) is expressed on the tumour cell surface and catalyses the reversible hydration of carbon dioxide into HCO_3^- and H^+ [124,133]. The HCO_3^- can then be taken up by bicarbonate transporters (BT) to maintain a higher intracellular pH[134] to ensure pH homeostasis and tumour survival[135,136].

To date, it has still remained a challenge to achieve an effective and sensitive assay that directly images the bicarbonate regulation in cancers and different effects of inhibitors on intracelluar localisation and accumulation. Ion-selective electrode (ISE) is a common method for the detection of HCO_3^-, but it is more applicable to liquid samples[137,138]. Other techniques such as ^{13}C NMR assay[139,140], osmotic assay[141] and fluorescence-based transport assays[142] are widely utilised in the research of metabolism and kinetics mechanisms of bicarbonate. However, they are not amenable to measurement at the single-cell level, which could be essential concerning the high heterogeneity in cancer, and do not give spatial information. Therefore, new tools are needed that can overcome these limitations and reflect directly on the metabolic regulation of bicarbonate.

Single-cell Raman micro-spectroscopy (SCRM) has emerged as a powerful label-free tool in the cancer field[85]. SCRM provides comprehensive biochemical

vibrational information that can help understand the metabolic and physiological processes of cellular biomolecules[143]. Biomolecules and organelles can be analysed simultaneously and semi-quantitatively based on a cell's Raman spectrum. Moreover, SCRM possesses single-cell resolution and is able to map biomolecules with high spatial resolution at the sub-cellular level[144]. SCRM is also non-destructive, and samples after Raman measurement could continue to be used for down streaming analysis such as fluorescence spectroscopy or H&E staining. Therefore, SCRM can be considered as a promising method for studying bicarbonate metabolism in cancers.

In this study, we applied SCRM to explore bicarbonate metabolic changes under various pathophysiological conditions, including normoxia and hypoxia, high and low glucose concentrations, and drug inhibition in three cancer cell lines, human glioblastoma U87 cells, human breast cancer MDA-MB-468 and SUM159 cells. The MDA-MB-468 cell line with CA9 knocked out was used to compare the role of CA9, while the wildtype of the U87 and SUM159 cell lines was used to compare the heterogeneity between cell lines. In addition to examining the phenotypic metabolic characteristics of bicarbonate, we also analysed the correlation between intracellular bicarbonate concentration and mitochondrial activity. Moreover, the Raman spatial distribution of bicarbonate at the single-cell level was visualized by Raman mapping images. Based on our findings, we hypothesise that bicarbonate is primarily obtained through

extracellular import and mitochondrial respiratory metabolism. CA9 and mitochondria play critical roles in bicarbonate regulation, with distinct functions under different conditions and the ability to complement each other under stressful conditions. Additionally, we suggest that the easily distinguishable feature of the bicarbonate band has potential as a marker for future Raman applications in cancer cell screening and detection.

3.2 Experimental section

Cell lines and cell culture. U87, MDA-MB-468 (empty vector & CA9 knockdown), HCC1806, MDA-MB-231 and SUM159 cells were maintained in 10-mM Dulbecco's modified Eagle medium (DMEM, Gibco, USA) supplemented with 10% fetal bovine serum (FBS, Gibco, USA). All cells were cultured under 37 ℃ with 5% CO_2. Cells were grown 2-4 days to reach 80% confluence. Cell lines were obtained from American Type Culture Collection (ATCC).

Poly-L-lysine coated slides. We developed a method to seed cells on aluminium slides directly. The 3-well removable chamber (Ibidi, Germany) was attached on the Raman aluminium slide, and then 1 mL 0.01% (v/w) poly-L-lysine solution (Sigma-Aldrich, USA) was added to modify the Raman slide surface. After 5 min incubation, poly-L-lysine solution was removed, and the modified Raman slides were dried for at least 1-2 hours before using.

Stressed sample preparation. Cell suspensions were diluted to a concentration of 5000 cells/ml. 1 mL of cell suspension was pipetted into the poly-L-lysine-coated chamber and then left to incubate for 24 hours at 37 ℃ with 5% CO_2 to allow cells to adhere to the surface of the Raman slide. The two groups of U87 cells and SUM159 were then moved to 21% (normoxia) and 1% (hypoxia) oxygen concentrations for 24 hours separately. The medium for rest groups was quickly changed to 22.5-mM glucose and glucose-free Dulbecco's modified Eagle medium (Gibco, USA) correspondingly, and cells were incubated for 24 hours. When cells were cultured to optimal confluence, the cell chamber was quickly washed with cold phosphate buffered saline (PBS, Life Technologies, UK) and 1 ml of 4% paraformaldehyde (PFA, ThermoFisher Scientific, USA) solution was added to fix the cells for further Raman application.

Western blot assay[145]**.** Cells were lysed using radioimmunoprecipitation assay (RIPA) buffer (R0278, Sigma-Aldrich, USA) containing phosphatase (PhosSTOPTM inhibitor cocktail, Roche, Switzerland) and protease (cOmpleteTM, Mini, EDTA-free Protease Inhibitor Cocktail, Roche, Switzerland). The DC Protein Assay kit (Bio-Rad, USA) was used to calculate total protein concentrations. 15 μg of protein samples were loaded onto NuPAGE gradient 4-12% Bis-Tris gels (Invitrogen, USA) and then transferred overnight at 20 V to PVDF membranes (Millipore Corp, USA). The membranes were incubated with 5% non-fat dried milk in 150 mM NaCl, 10 mM Tris, and 0.1% Tween-20 pH 7.5 for 2 hours at room temperature. After that, primary

antibodies were applied to the membranes and hybridize overnight at 4 °C. The secondary antibody was then used to hybridize the membranes for 2 hours at room temperature. Antibodies used were β-actin conjugated to HRP (Sigma, USA), H1alpha67 to HIF-1α (Novus, USA) and NB100-417H to CA9 (Novus, USA). Membrane immunoreactivity was discovered using ECL Prime (GE Healthcare, USA). An ImageQuant LAS4000 was used for visualization (GE Healthcare, USA).

CA9 inhibitor activity. U87 and SUM159 cells were seeded on the poly-L-lysine coated Raman slides at a density of 3000 cells/well. At 24 hours post-plating, cells were treated with 25- and 50-μM CA9 inhibitor SLC-0111 (U-104, Sigma-Aldrich, USA) or DMSO (Insight Biotechnology, UK) and transferred to either 21% O_2 or 1% O_2 for 24 hours. After the drug incubation time, cells were fixed with 4% PFA solution at room temperature for at least one hour. Samples were rinsed three times with Milli-Q water to remove excess PFA for further Raman measurements.

Metformin treatment. 1mL of U87 and SUM159 cell suspensions were seeded on the poly-L-lysine-coated chamber respectively and incubated overnight. Glucose-free DMEM was supplemented with a range of glucose (Gibco, USA) concentrations of 0, 1, 5 and 10 mM. The MDA-MB-468 EV and shCA9 cells were cultured in advance using the same method in 0- and 10-mM glucose DMEM. Cells were grown in prepared DMEM and divided into control groups without drug treatment, and experimental groups containing 0.5-, 1- and 2-mM

metformin (1,1-dimethylbiguanide hydrochloride, Sigma-Aldrich, USA). After 24 hours of incubation, cells were quickly washed with cold PBS and fixed by 4% PFA solution.

Spontaneous Raman spectra measurement. The poly-L-lysine coated slides with cell samples were washed three times with Milli-Q water to remove the salts. Samples were allowed to dry at room temperature before Raman measurements. Spontaneous Raman spectra were obtained by a confocal Raman microscope (LabRAM HR Evolution, Horiba Scientific, UK) equipped with an integrated microscope (BX41, Olympus, Japan), motorized XYZ stage and a 532-nm neodymium-yttrium aluminium garnet laser. For single-cell measurements, spectra were acquired using a 50× objective lens (numerical aperture 0.5, spatial resolution ~2 μm), a 3-s acquisition time and 300 grooves/mm diffraction grating for an 80-mW input laser power through a 25% neutral density (ND) filter. All cells were randomly selected and scanned by the Mapping method to obtain spectra of individual cells.

Pure chemical Raman spectra. Sodium bicarbonate (≥99.7%, Sigma-Aldrich, USA) powder was measured with a 1.5-s acquisition time with a 40-mW input laser power through a 0.1% filter.

Raman mapping. Raman mapping measurement was done using Raman software (HORIBA, LabSpec6, UK). Single-cell samples were detected by point-to-point acquisition scanning with 2-μm resolution. The parameters of the test were set as described in the Raman Spectra Measurement section. Raman

bands associated with bicarbonate (1043 cm^{-1}) and cytochrome c (750 cm^{-1}, 1128 cm^{-1}) were selected to produce in mapping window with x and y axes to represent each test laser point location. The mapping figure was overlayed correspondingly on its cell image and finally gave the Raman mapping image.

Raman spectral data processing and analysis. Raman spectra were processed by the LabSpec6 software (HORIBA, UK) for baseline correction and normalization. Cosmic spikes were first removed, and baselines were subtracted by a polynomial correction at degree 9. The baselines were zeroed and the whole range Raman spectra were normalized by the area under the curve. The averaged spectra files obtained from the original map data were corrected for normalization and calibration using LabSpec6 software. This step aimed to eliminate any potential influence from variations in the measurement time on the experimental results. To perform semi-quantitative calculations of peak areas, MATLAB 2019b (MathWorks, USA) was utilised. The “findpeaks” function was employed to identify the local maxima and minima of the target peaks within a set of spectra data. The maximum value identified represented the peak, while the minimum value on either side serves as the valleys. The area of the peak was then calculated, taking into account the background value. Peak area calculations were further refined using a Gaussian model to exclude interference from neighbouring peaks. The threshold of the band area at 1043 cm^{-1} was set as 0.2 (critical intensity of the signal background) for sub-setting positive or negative bicarbonate in MDA-MB-468 CA9 knockdown cells. Data

analysis and visualization was done using MATLAB 2019b (MathWorks, USA), GraphPad Prism 9.0.2 (GraphPad, USA) and R (3.5.1, USA) using in-house scripts. All experiments were repeated with three biological replicates. Numerical data values are represented as mean ± standard deviation (SD).

3.3 Results

3.3.1 Spatially resolved Raman mapping of cancer single cells

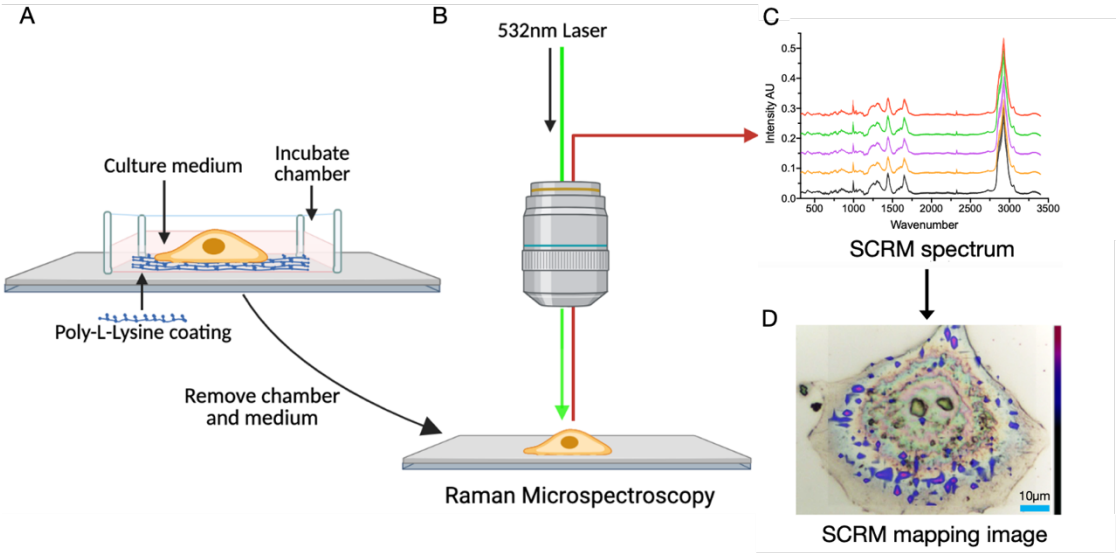


Figure 3.1 Schematic of subcellular spatial Raman mapping of single cells based on poly-L-lysine modified Raman slides. (A, B) Schematic of single-cell Raman measurement after cells being seeded on a poly-L-lysine coated Raman slide. (C) Example of SCRM spectra of single cells. (D) An example of an SCRM mapping image with heatmap intensities of bicarbonate signal overlayed.

We developed a method of Raman imaging of cells which involves seeding cells directly on Raman-grade Aluminium slides (Figure 3.1). The surface of the slide was coated with poly-L-lysine to promote cell adhesion by enhancing the

electrostatic interaction between the cells and slide surface[146]. To verify the practicality of the method, different cancer cell lines were cultured on the modified slides, including U87, SUM159, HCC1806, MDA-MB-468, MDA-MB-231 cell lines. In this thesis, cells were fixed with 4% PFA before Raman measurement. Compared to other chemical fixation methods such as ethanol or formaldehyde, PFA is more suitable for cell structure, cytoskeleton and image studies as it does not alter the structures of proteins while providing high quality cell images[147–149]. The PFA can be easily washed away by water and does not produce a background signal (Figure 3S1A and B).

As a result, this new method offers three advantages consistent among multiple cell lines: high biocompatibility without affecting the cell viability; a clear Raman spectrum without background interference; and maintenance of native morphologies of the cells (Figure 3S1). This methodology enables production of Raman mapping image of cancer cells with high spatial resolution (Figure 3.1C).

3.3.2 Identification of the intracellular bicarbonate Raman band

Intracellular bicarbonate monitoring remains a challenge via traditional biochemical assays while a unique Raman band at 1043 cm^{-1} can be attributed to bicarbonate, as identified by measuring pure sodium bicarbonate ($NaHCO_3$) as shown in Figure 3S2 and confirmed by a reference database[150]. We have utilised this distinctive feature of bicarbonate to monitor its metabolism in cancer cells with subcellular spatial resolution.

3.3.3 Role of CA9

CA9 is a membrane-bound enzyme which converts CO_2 into bicarbonate and protons[151]. In addition, HCO_3^- ions are imported by BT and interconverted with CO_2 under the maintenance of CA9[126] (Figure 3S3A). Because CA9 is hypoxia-induced[152], we incubated the cells under a hypoxic environment (1% oxygen concentration).

To assess the effect of inhibiting the extracellular CA9 we used two methods. The first was a knockdown of the protein. Figure 3.2A and 3.2B show an intensive Raman band at 1043 cm^{-1} in the fingerprint region, which was higher in empty vector of MDA-MB-468 (MDA-MB-468 EV) than the MDA-MB-468 with a CA9 knockdown (MDA-MB-468 shCA9). We calculated the Raman spectra for both bicarbonate by integrating the area, shown as box plots in Figure 3.2C and 3.2D. The production of bicarbonate was over 10 times higher in MDA-MB-468 EV cells than that in the MDA-MB-468 shCA9.

The second was the inhibition of the CA9 catalyst function. A CA9 inhibitor, U-104 was used to depress the functions of CA9. The intensity of 1043-cm^{-1} band decreased in MDA-MB-468 EV with the addition of U-104 (Figure 3.2A). Consistently, the intensity of bicarbonate decreased significantly under hypoxic conditions with 25- and 50-μM U-104 (Figure 3.2C). For CA9 knockdown cells, the addition of CA9 inhibitor was ineffective. No significant bicarbonate signal was detected in Raman spectra (Figure 3.2B). Semi-quantitative calculations showed relatively low levels of bicarbonate in both the knock-out and the

inhibitor-added cells. However, a statistically significant effect on bicarbonate levels was observed in the group treated with 50-μM U-104 (Figure 3.2D).

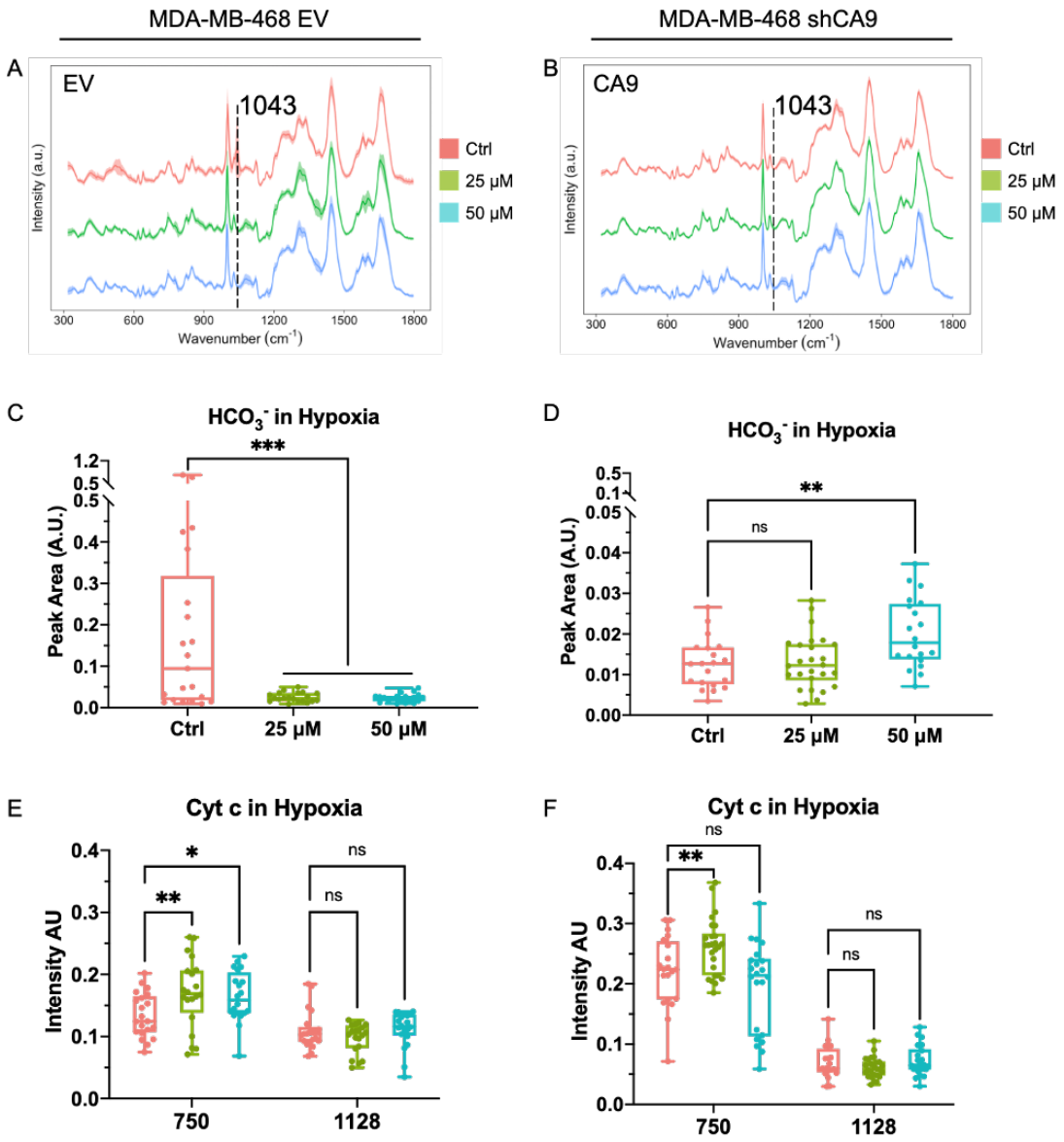
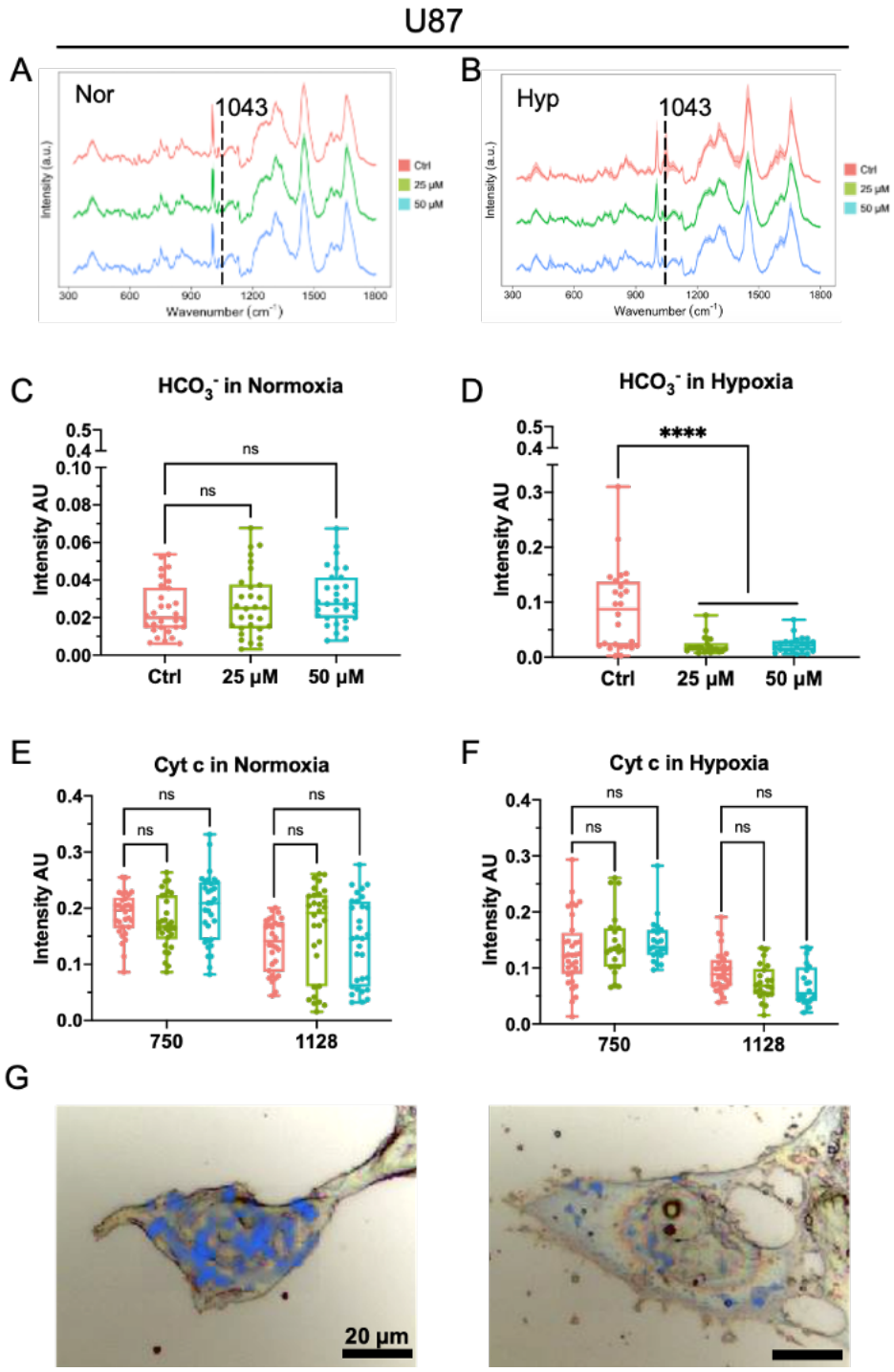


Figure 3.2 Bicarbonate production and mitochondria activity in response to MDA-MB-468 CA9 mutants under effect of an CA9 inhibitor in hypoxic condition. (A, B) Averaged single-cell Raman spectra showing (A) MDA-MB-468 empty vector (EV) and (B) MDA-MB-468 CA9 knockdown (shCA9) at 0-, 25- and 50-μM U104 added in hypoxic conditions for 24 hours. (C, D) Bicarbonate quantification in the band region at 1043 cm^{-1} of MDA-MB-468 (C) EV and (D) shCA9, in corresponding to A and B. (E, F) Cytochrome c quantification of

MDA-MB-468 (E) EV and (F) shCA9 at peaks 750 and 1128 cm^{-1}, in corresponding to A and B. 20-26 cells were measured for each group. For each cell, around 300 spectra were measured.

3.3.4 Role of hypoxia

We observed high levels of bicarbonate (as indicated by a Raman band at 1043 cm^{-1}) in U87 and SUM159 cell lines under hypoxic conditions, compared to normoxia (Figure 3.3A, 3.3B, 3.3H and 3.3I). Remarkably, when U-104 was added to the growth medium under hypoxia, the bicarbonate Raman band disappeared in U87 and SUM159 (Figure 3.3B and 3.3I), indicating that the inhibitor was effective in suppressing CA9 activity. Calculations of the bicarbonate band indicated a significant reduction of bicarbonate after inhibition of CA9 in U87 and SUM159 with 25- and 50-μM U-104 under hypoxia (Figure 3.3D and 3K). However, under normoxia (21% O_2 level), the bicarbonate remained at low levels following the addition of the CA9 inhibitor (Figure 3.3C and 3J).


U87
A
Nor
1043
Intensity (a.u.)
Wavenumber (cm⁻¹)
Ctrl
25 μM
50 μM
B
Hyp
1043
C
HCO3- in Normoxia
Intensity AU
ns
Ctrl
25 μM
50 μM
D
HCO3- in Hypoxia
****
E
Cyt c in Normoxia
750
1128
F
Cyt c in Hypoxia
G
20 μm

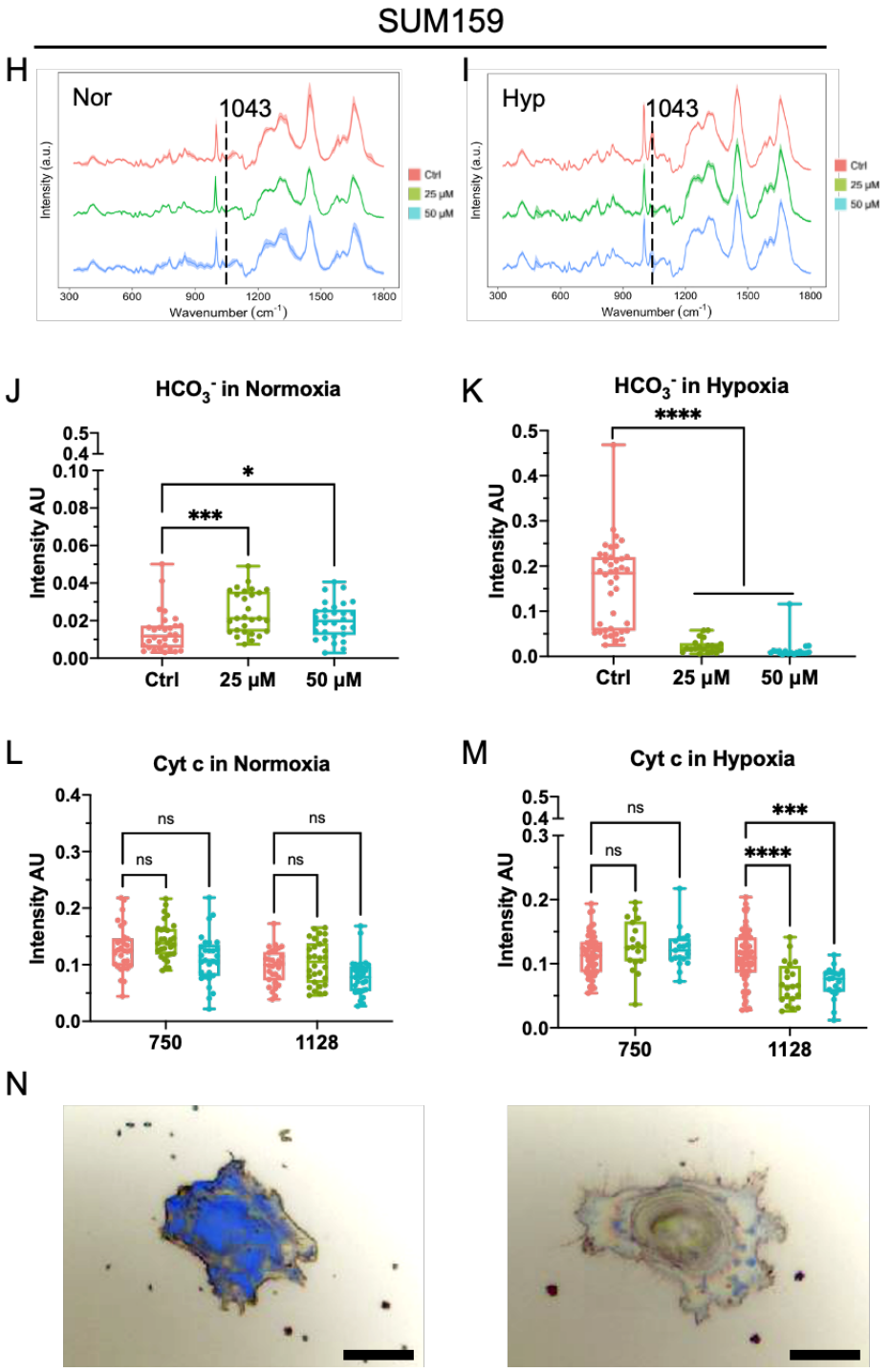


Figure 3.3 Bicarbonate expression of U87 & SUM159 with the effect of CA9 inhibitor in 10-mM DMEM culture. (A, B) Averaged single-cell Raman spectra of U87 with 0-, 25- and 50-μM U104 added at beginning of experiment and maintained for 24 hours in normoxia and hypoxia. (C, D) The corresponding bicarbonate quantification of U87 cultured under normoxia (C) and hypoxia (D). (E, F) Semi-quantification of cytochrome c bands at 750 and 1128 cm^{-1} of U87

cultured under normoxia (E) and hypoxia (F). (G) Raman cell images of single hypoxic control and 50-μM U-104 of U87 at bicarbonate (blue, 1043 cm^{-1}). Scale bar = 20 μm. (H, I) Averaged single-cell Raman spectra of SUM159 with 0-, 25- and 50-μM U-104 added over 24 hours in hypoxic and normoxic conditions. (J, K) The corresponding bicarbonate quantification of SUM159 cultured under normoxia (J) and hypoxia (K). (L, M) Semi-quantification of cytochrome c bands at 750 and 1128 cm^{-1} of SUM159 cultured under normoxia (L) and hypoxia (M). (N) Raman cell images of single hypoxic control and 50-μM U104 of SUM159 with bicarbonate intensities overlayed (blue, 1043 cm^{-1}). 20-30 cells were measured for each group. For each cell, around 300 spectra were measured. Scale bar = 20 μm.

Raman mapping images showed the distribution of bicarbonate at the subcellular level. U87 and SUM159 cells exhibited high levels of bicarbonate across the cells, but treatment with U-104 under hypoxic conditions significantly reduced the level of bicarbonate (Figure 3.3G and 3.3N). In U87, large bicarbonate spots were mainly distributed in the cytoplasm surrounding the nucleus, whereas in SUM159, the hypoxic control showed a large amount of bicarbonate diffused throughout the cytoplasm (Figure 3.3G and 3.3N).

The results demonstrate that the U-104 inhibitor effectively reduced the bicarbonate band at 1043 cm^{-1} under hypoxia, in contrast to CA9 knockdown, and suggest that CA9 plays a critical role in regulating bicarbonate metabolism in cancer cells.

3.3.5 Effects of bicarbonate and U-104 on mitochondrial metabolism

Cytochrome c is abundantly found in the mitochondrial intermembrane[153]. Its Raman scattering can be detected with high sensitivity. It exhibits distinctive peaks at 750 and 1128 cm^{-1}, making it a valuable marker for the label-free monitoring for mitochondrial activity using resonance or non-resonance Raman spectroscopy[154,155]. In this study, the characteristic bands of cytochrome c were used in conjunction with mitochondrial analysis to compare the mitochondrial activity in cancer cell lines under hypoxia and U-104 treatment.

The intensity of the band at 750 cm^{-1} was found to be significantly increased in MDA-MB-468 EV and shCA9 cells treated with 25-μM U104 compared to the control group (Figure 3.2E and 3.2F). The enhancement of cytochrome c was most pronounced when shCA9 cells were in hypoxia with 25-μM U-104 (Figure 3.2F). In contrast, the mitochondrial activity of the 1128-cm^{-1} band did not appear significantly different to the effects of CA9 inhibitor (Figure 3.2E and 3.2F). The intensity of 1128-cm^{-1} band did not show a significant difference under any condition.

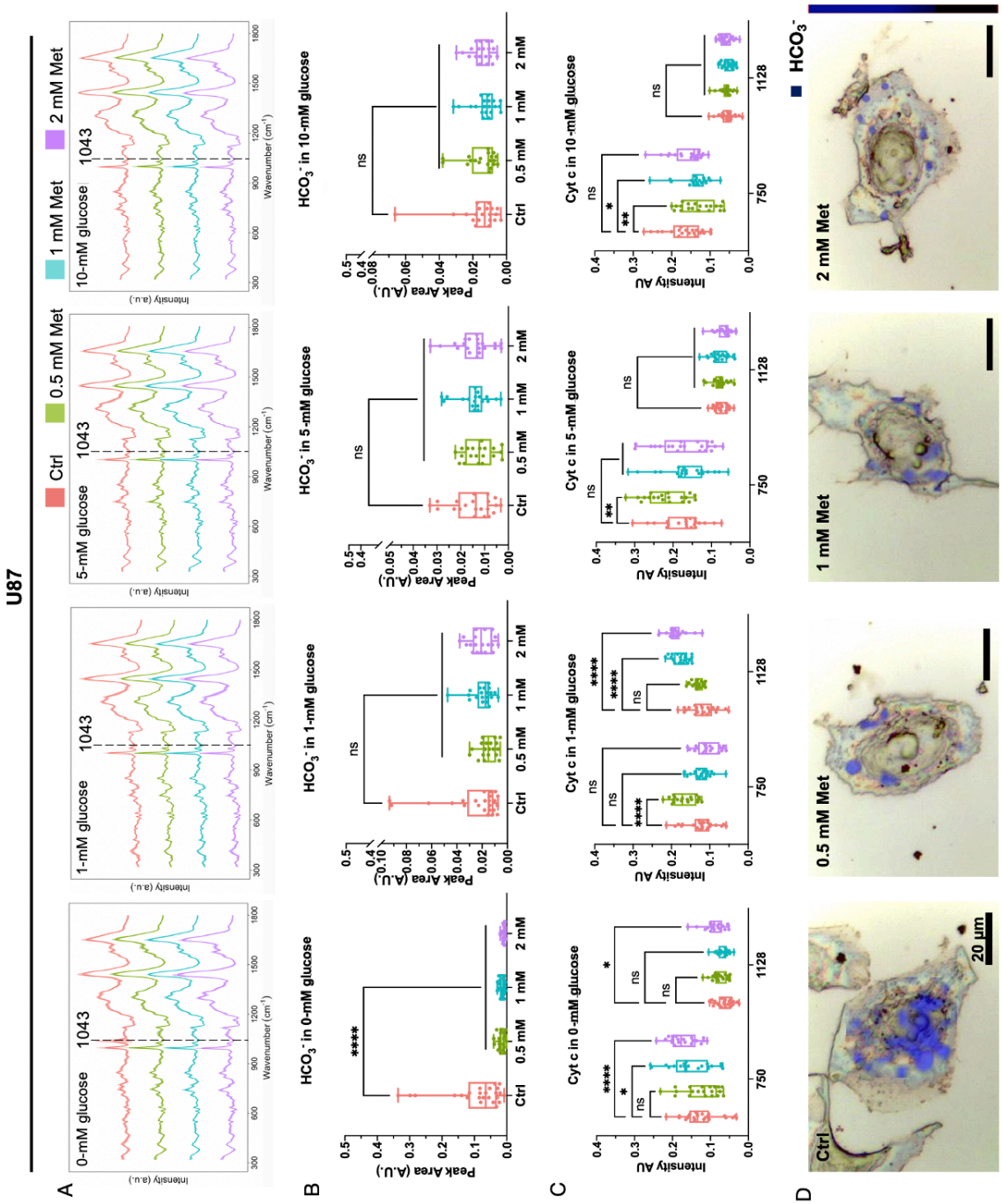
Unlike MDA-MB-468, the level of cytochrome c showed no significant differences in U87 cells with increasing concentrations of added U-104 regardless of normoxia or hypoxia (Figure 3.3E and 3.3F). The 750-cm^{-1} intensity of SUM159 cells neither presented an obvious difference due to the change in oxygen (Figure 3.3L and 3.3M). Except for the 1128-cm^{-1} band

significantly reduced under hypoxia when SUM159 cells were inhibited by U-104 (Figure 3.3M).

3.3.6 Metformin effects on bicarbonate

Mitochondrial carbonic anhydrases play a significant role in the metabolism of bicarbonate, which catalyses the interconversion between CO_2 and HCO_3^- [75,156]. The hydrolytic conversion may be affected by giving specific mitochondrial inhibitors. Here metformin was used to inhibit mitochondrial respiratory [157,158] to examine the flux shifts of bicarbonate. Metformin was added into the growth medium DMEM with 0-, 1-, 5- or 10-mM glucose to assess the effects of mitochondrial metabolism on bicarbonate production in U87 and SUM159.

For U87 cells, as shown in Figure 3.4A, a strong Raman signal of bicarbonate at 1043 cm^{-1} was detected in the cells under glucose-free conditions. However, this effect was not seen in the experimental group cultured in 1-, 5- and 10-mM glucose of DMEM (Figure 3.4A). After the addition of metformin, the bicarbonate signal was not detected when cells were incubated with DMEM containing 0-mM glucose, as shown in Figure 3.4A. Interestingly, even in glucose-containing culture conditions without the addition of metformin, the bicarbonate Raman signal was absent, as indicated in Figure 3.4A. This suggests that the presence of glucose alone did not result in the detection of bicarbonate signal, and the absence of the signal may be attributed to factors other than the addition of metformin.


U87
A
B
C
D
Ctrl
0.5 mM Met
1 mM Met
2 mM Met
0-mM glucose
1-mM glucose
5-mM glucose
10-mM glucose
1043
Intensity (a.u.)
Wavenumber (cm-1)
HCO3- in 0-mM glucose
HCO3- in 1-mM glucose
HCO3- in 5-mM glucose
HCO3- in 10-mM glucose
Peak Area (A.U.)
Cyt c in 0-mM glucose
Cyt c in 1-mM glucose
Cyt c in 5-mM glucose
Cyt c in 10-mM glucose
Intensity AU
Ctrl
0.5 mM Met
1 mM Met
2 mM Met
HCO3-
20 µm

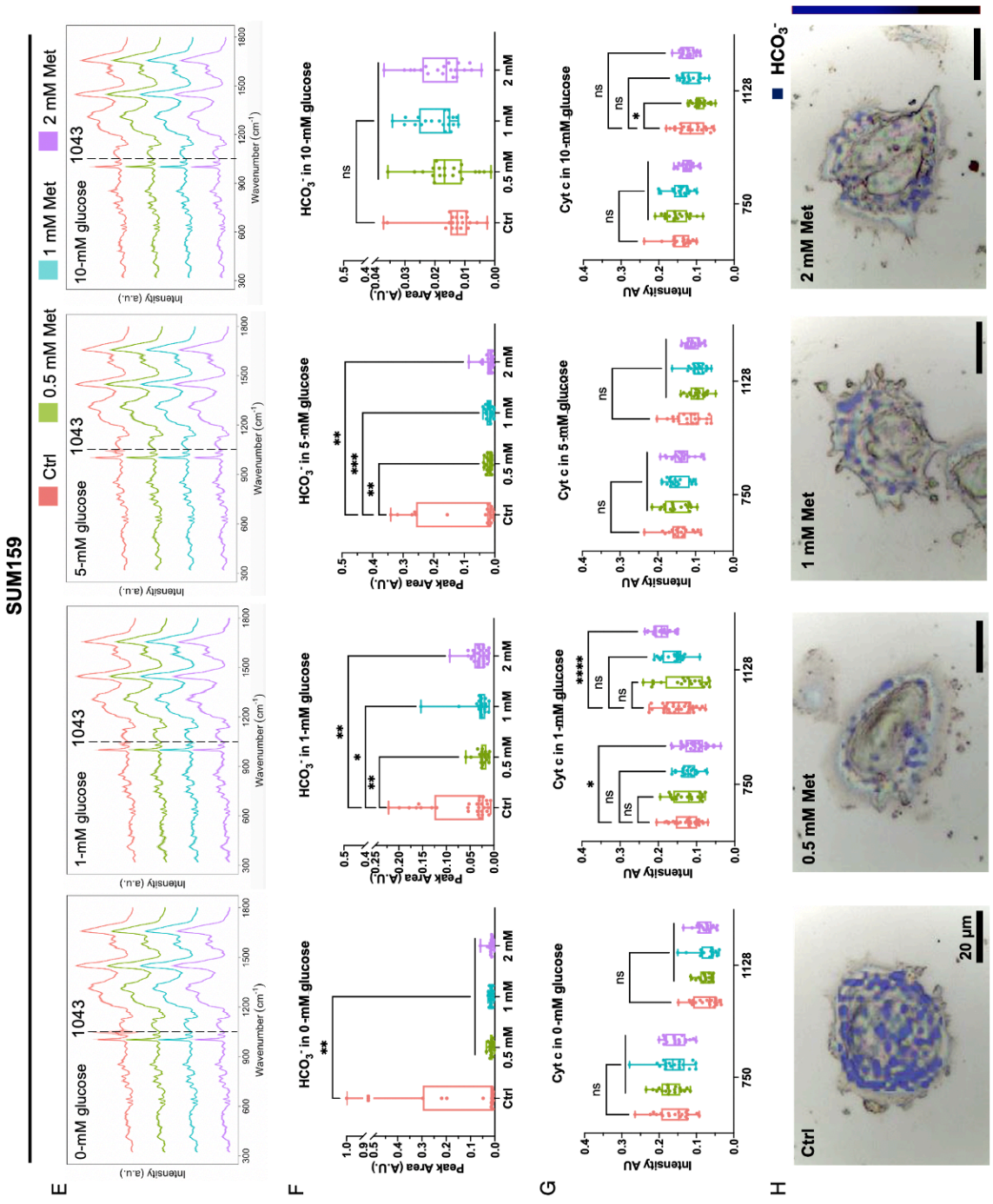


Figure 3.4 Comparison of the inhibitory effect at different concentrations of metformin on bicarbonate. (A) Raman spectra of the effects of different concentrations of metformin on U87 cells. (B) Quantification by integration of bicarbonate band area of U87 cells. (C) Quantitative comparison of cytochrome c band areas of U87 cells. (D) Bicarbonate profile images of U87 cells at different metformin concentrations in 0-mM DMEM (blue, 1043 cm^{-1}). Scale bar = 20 μm. (E) Raman spectra of the effects of different concentrations of

metformin on SUM159 cells. (F) Quantification by integration of bicarbonate band area of SUM159 cells. (G) Quantitative comparison of cytochrome c band areas of SUM159 cells. (H) Bicarbonate profile images of SUM159 cells at different metformin concentrations in 0-mM DMEM (blue, 1043 cm^{-1}). 18-20 cells were measured for each group. For each individual cell, approximately 300 spectra were measured. Scale bar = 20 μm.

Figure 3.4B shows the quantitative bicarbonate levels in the four treatments with metformin (0, 0.5, 1 and 2 mM) in culture conditions with different concentrations of glucose DMEM. The level of intracellular bicarbonate significantly decreased in U87 cells following the addition of metformin (0.5, 1 and 2 mM) to the glucose-free DMEM. The low concentration, 0.5 mM of metformin, was sufficient to inhibit the production of bicarbonate in all groups (Figure 3.4B). As shown in the single-cell Raman images (Figure 3.4D), U87 produced large amounts of intracellular bicarbonate in the glucose-free medium and this was present throughout the cytoplasm, whereas no such large accumulation of bicarbonate was found in the cells treated with metformin.

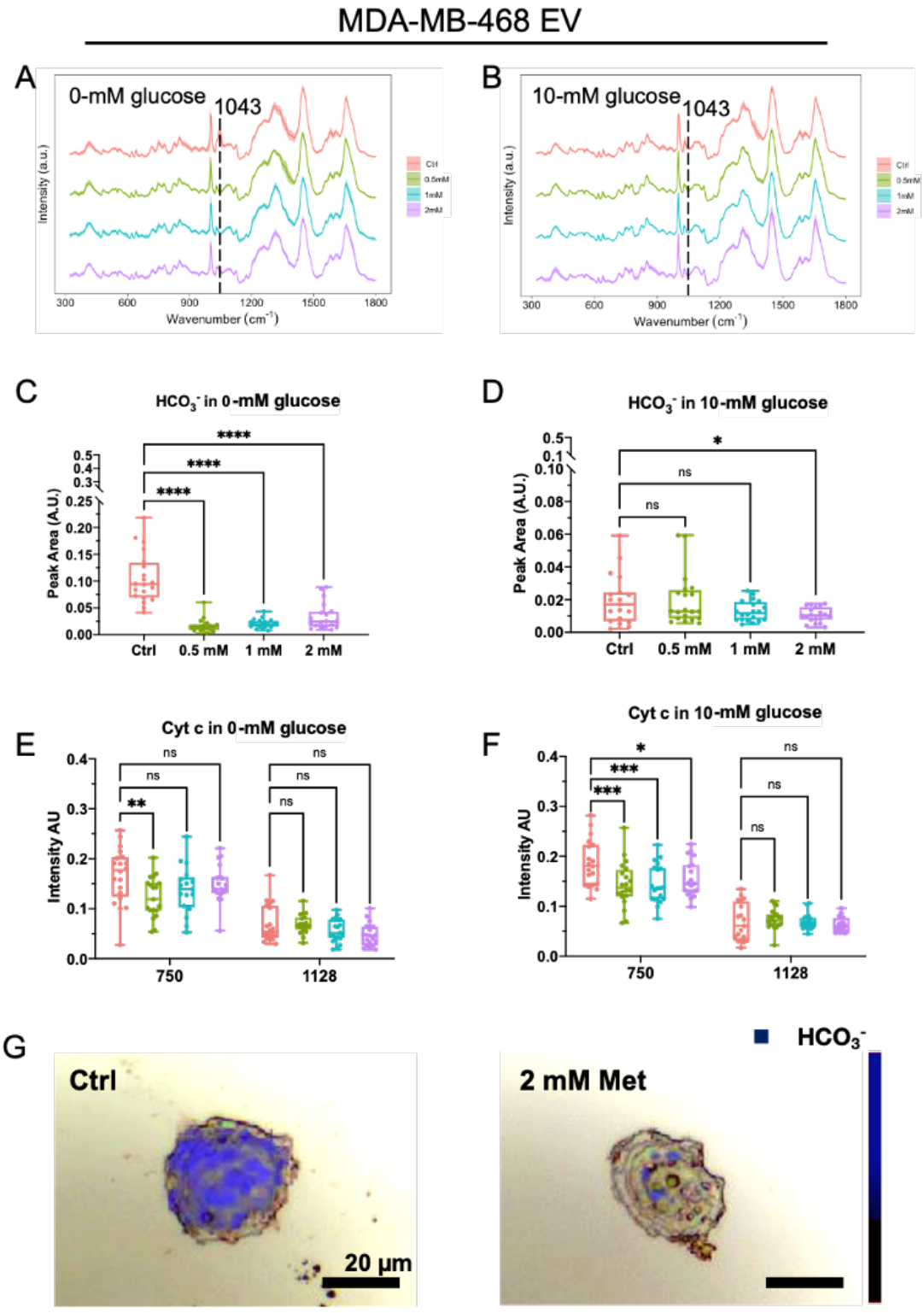
By Raman analysis, the inhibitory effect of metformin on intracellular bicarbonate was similar in SUM159 and U87. A very high bicarbonate Raman signal could be detected in the SUM159 cells when the glucose in the medium was low (below 5-mM glucose), but the signal was significantly reduced in cells to which metformin was added (Figure 3.4E and 3.4F). Figure 3.4H demonstrated the inhibitory effect of metformin on bicarbonate in SUM159,

which appeared less distributed and formed smaller patches compared to the control cells.

3.3.7 Effects of metformin and CA9 knockdown on bicarbonate metabolism

We first inhibited the mitochondrial activity with metformin on U87 and SUM159 cells. In parallel, CA9 mutants were then inhibited for mitochondrial activity to observe the effect of mitochondria and CA9 on bicarbonate production.

Raman results for MDA-MB-468 EV have the similar results for U87 and SUM159. As shown in Figure 3.5A, a sharp Raman band of bicarbonate at 1043 cm^{-1} was detected in the cells cultured in glucose-free medium. After the addition of metformin, the bicarbonate band was absent in all spectra (Figure 3.5A). The addition of metformin (0.5, 1 and 2 mM) to glucose-free DMEM resulted in a significant decrease in the bicarbonate in MDA-MB-468 EV (Figure 3.5C). None of the MDA-MB-468 EV cells cultured in 10-mM DMEM had visible high bicarbonate band (Figure 3.5B). Interestingly, high concentration of metformin inhibition (2 mM) led to significantly lower bicarbonate production in MDA-MB-468 EV (Figure 3.5D). Figure 3.5G presents a clear difference in the distribution of bicarbonate in the MDA-MB-468 EV under control and 2-mM metformin inhibition. In these, bicarbonate in the control cell was diffused throughout the cells, whereas it was barely visible in the mitochondria-inhibited MDA-MB-468 EV (Figure 3.5G).


MDA-MB-468 EV
A
0-mM glucose
1043
Intensity (a.u.)
Wavenumber (cm-1)
B
10-mM glucose
1043
C
HCO3- in 0-mM glucose
Peak Area (A.U.)
Ctrl
0.5 mM
1 mM
2 mM
D
HCO3- in 10-mM glucose
E
Cyt c in 0-mM glucose
Intensity AU
750
1128
F
Cyt c in 10-mM glucose
G
Ctrl
20 μm
2 mM Met
HCO3-

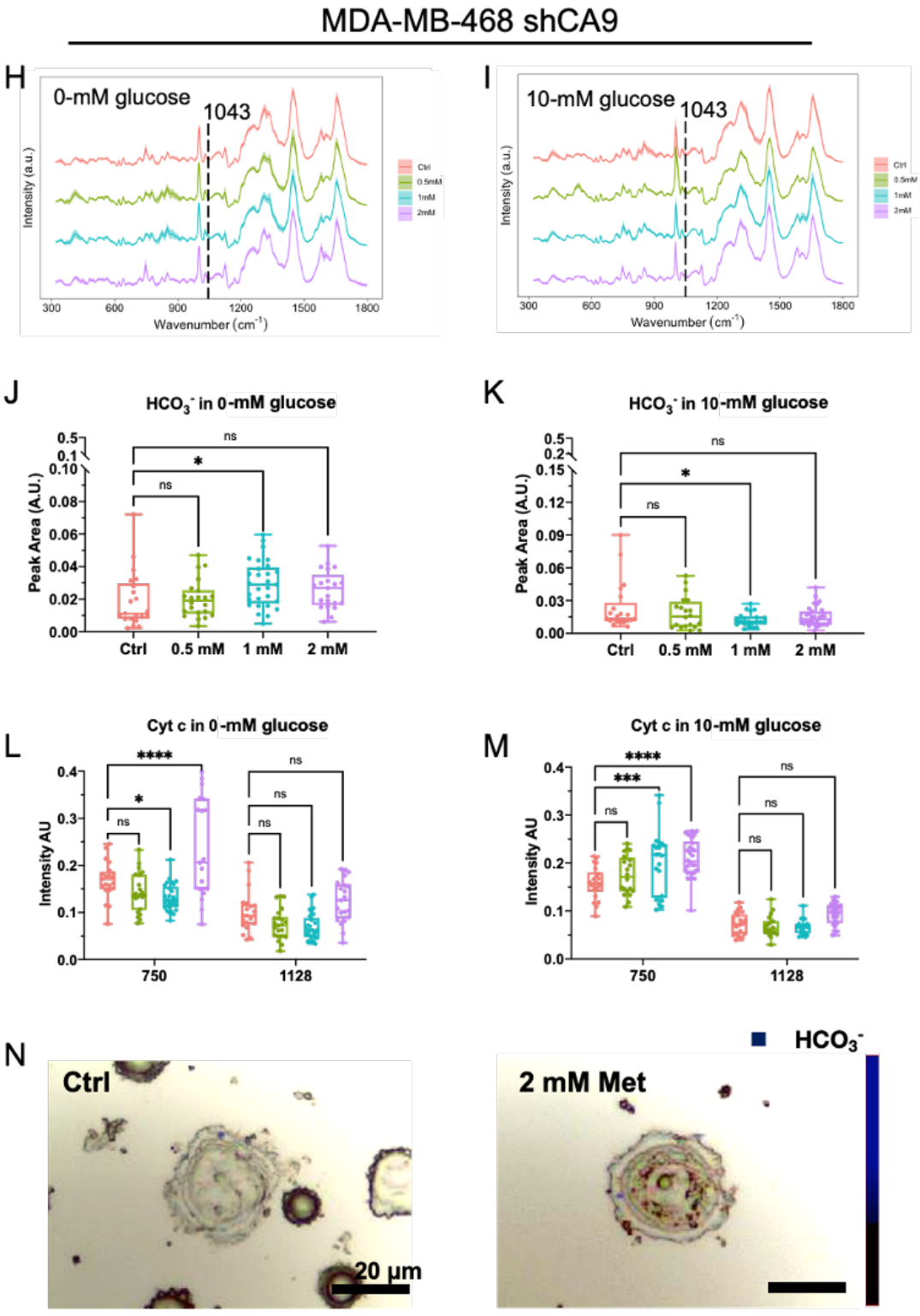


Figure 3.5 Effect of metformin on bicarbonate production in MDA-MB-468 EV and shCA9. (A, B) Comparison of averaged Raman spectra of MDA-MB-468 EV by incubating under (A) 0-mM and (B) 10-mM glucose DMEM. (C, D) Quantification of bicarbonate band areas in MDA-MB-468 EV cells in the

corresponding A, B respectively. (E, F) Quantification of cytochrome c bands in the corresponding A and B respectively. (G) Raman map of bicarbonate (blue, 1043 cm^{-1}) in control and 2-mM metformin-incubated MDA-MB-468 EV cells. Scale bar = 20 μm. (H, I) Comparison of averaged Raman spectra of MDA-MB-468 shCA9 by incubating under (A) 0-mM and (B) 10-mM glucose DMEM. (J, K) Quantification of bicarbonate band areas in MDA-MB-468 shCA9 cells in the corresponding H and I respectively. (L, M) Quantification of cytochrome c bands in MDA-MB-468 shCA9 cells in the corresponding H and I respectively. (N) Raman map of bicarbonate (blue, 1043 cm^{-1}) in control and 2-mM metformin-incubated MDA-MB-468 shCA9 cells. Between 20 and 29 cells were measured for each group in this study. For each individual cell, approximately 300 spectra were measured. Scale bar = 20 μm.

High bicarbonate bands were not seen in MDA-MB-468 deficient of CA9 function, either in a culture environment with or without glucose (Figure 3.5H and 3.5I). Their control cells had low levels of bicarbonate, whereas the addition of metformin resulted in an even lower concentration of bicarbonate (Figure 3.5J and 3.5K). MDA-MB-468 shCA9 were most sensitive to 1-mM metformin concentrations, showing statistically significant decline in the quantification by integration of bicarbonate band (Figure 3.5J and 3.5K). Figure 3.5N demonstrates that bicarbonate is virtually absent from the spatial distribution of CA9 KD cells, whether or not mitochondria are inhibited by metformin.

3.3.8 Metformin effects on cytochrome c

The 750 and 1128 cm^{-1} Raman bands of cytochrome c were calculated for each treatment to see the effect of metformin on the mitochondria.

For U87 in 0-mM glucose DMEM, the cytochrome c band at 750 cm^{-1} became

significantly stronger with increased concentrations of metformin (Figure 3.4C). When U87 cells could obtain free glucose from the external environment (1- and 5-mM glucose DMEM), 0.5 mM of metformin showed a significantly higher intensity of 750-cm^{-1}-band versus control, whereas a decrease in 10-mM glucose DMEM with the effects of 0.5- and 1-mM metformin. 1128-cm^{-1} band showed a remarkable increase in low glucose medium (0- and 1-mM glucose DMEM) added with a higher concentration of metformin (1- and 2-mM metformin). There was no significant difference in the intensity of 1128-cm^{-1} band between the 5- and 10-mM glucose medium.

Differently, the cytochrome c levels of SUM159 were not as variable as that of U87. For most of the SUM159 cells treated with metformin, the cytochrome c Raman band did not display a significant difference from the control (Figure 3.4G).

The mitochondrial activity of MDA-MB-468 EV was significantly reduced by metformin inhibition (Figure 3.5E and 3.5F). In particular, the reduction in the 750-cm^{-1} band was much dramatic under 10-mM glucose conditions (Figure 3.5F).

In contrast, the intensity of 750-cm^{-1} band of MDA-MB-468 shCA9 was significantly enhanced with increasing metformin (Figure 3.5L and 3.5M). The same results were obtained with both 0- and 1-mM glucose incubations. However, the band at 1128 cm^{-1} did not show a mathematical statistical difference (Figure 3.5L and 3.5M).

3.3.9 Bicarbonate accumulation under different oxygen and glucose concentrations

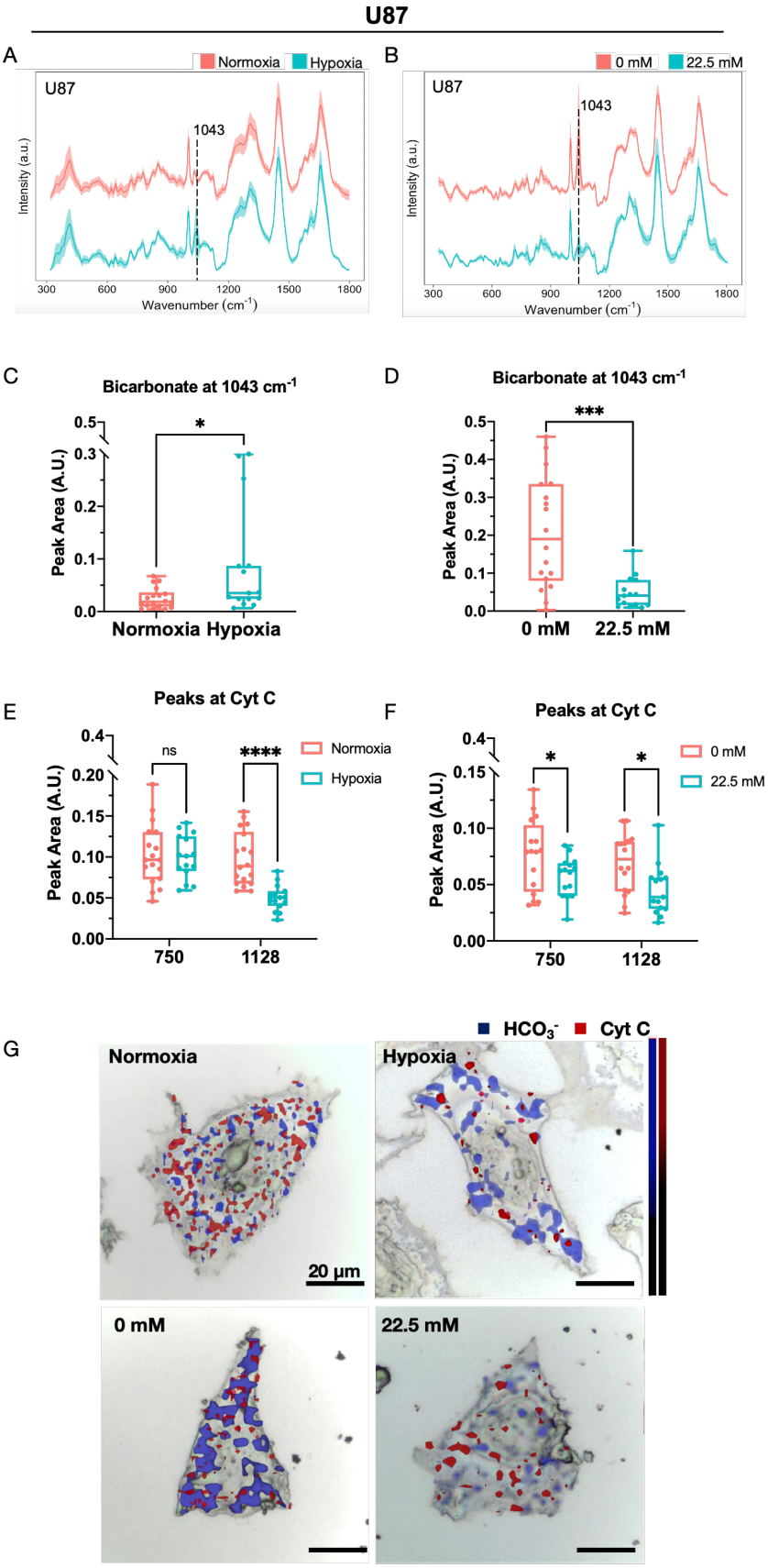
We then adjusted the concentrations of oxygen and glucose to investigate the bicarbonate response under stressful conditions. Raman spectra of cells were obtained under stress in hypoxia (1% oxygen concentration) vs. normoxia (20% oxygen concentration) and glucose-free DMEM (0 mM) vs. high glucose DMEM (22.5 mM).

In Figure 3.6A, the red spectra represent the U87 cells after 24 hours of incubation under normoxic conditions, while the blue spectra represent the cells under hypoxic conditions. All the cells were incubated in a 10-mM glucose concentration. In Figure 3.6B, the plots depict the U87 cells after 24 hours of incubation in 0-mM and 22.5-mM glucose concentrations, respectively, under normoxia.

Figure 3.6C and E present the semi-quantitative calculation of the bicarbonate and cytochrome c peaks in Figure 3.6A. Figure 3.6D and F correspond to the semi-quantitative calculations of the bicarbonate and cytochrome c peaks in Figure 3.6B. In Figure 3.6G, the cell maps display the co-localization of bicarbonate and cytochrome c for the four conditions. Additionally, the experiments and data processing were conducted on another cell line, SUM159, and the results are shown in Figure 3.6H to N, following the same order as U87.

As shown in Figure 3.6A and 3.6B, the fingerprint regions for both cells under hypoxia and in glucose-free medium, displayed a strong characteristic Raman band of bicarbonate at 1043 cm^{-1}. These groups produced significantly more bicarbonate than their respective controls with normal oxygen and glucose levels (Figure 3.6C and 3.6D). When U87 cells were grown in hypoxic conditions, their mitochondria were downregulated and the two Raman bands of cytochrome c both significantly decreased (Figure 3.6E). When U87 cells lack a supply of glucose, their cytochrome c signals were strengthened (Figure 3.6F).

To explore the bicarbonate turnover, we mapped both bicarbonate and mitochondria in U87 cells. The cytochrome c was displayed as numerous small heat spots distributed in the cytoplasm in normoxia, and it had fewer in hypoxia condition (Figure 3.6G). However, the sizes of the bicarbonate spots were dramatically larger in hypoxia than that in normoxia. The most noticeable change was in the 0-mM glucose group, where large bicarbonate spots appeared to be diffused throughout the cytoplasm (Figure 3.6G).


U87
A
Normoxia
Hypoxia
U87
1043
Intensity (a.u.)
300
600
900
1200
1500
1800
Wavenumber (cm-1)
B
0 mM
22.5 mM
U87
1043
Intensity (a.u.)
Wavenumber (cm-1)
C
Bicarbonate at 1043 cm-1
Peak Area (A.U.)
*
Normoxia
Hypoxia
D
Bicarbonate at 1043 cm-1
Peak Area (A.U.)
***
0 mM
22.5 mM
E
Peaks at Cyt C
Peak Area (A.U.)
ns
****
Normoxia
Hypoxia
750
1128
F
Peaks at Cyt C
Peak Area (A.U.)
*
*
0 mM
22.5 mM
750
1128
G
HCO3- Cyt C
Normoxia
20 µm
Hypoxia
0 mM
22.5 mM

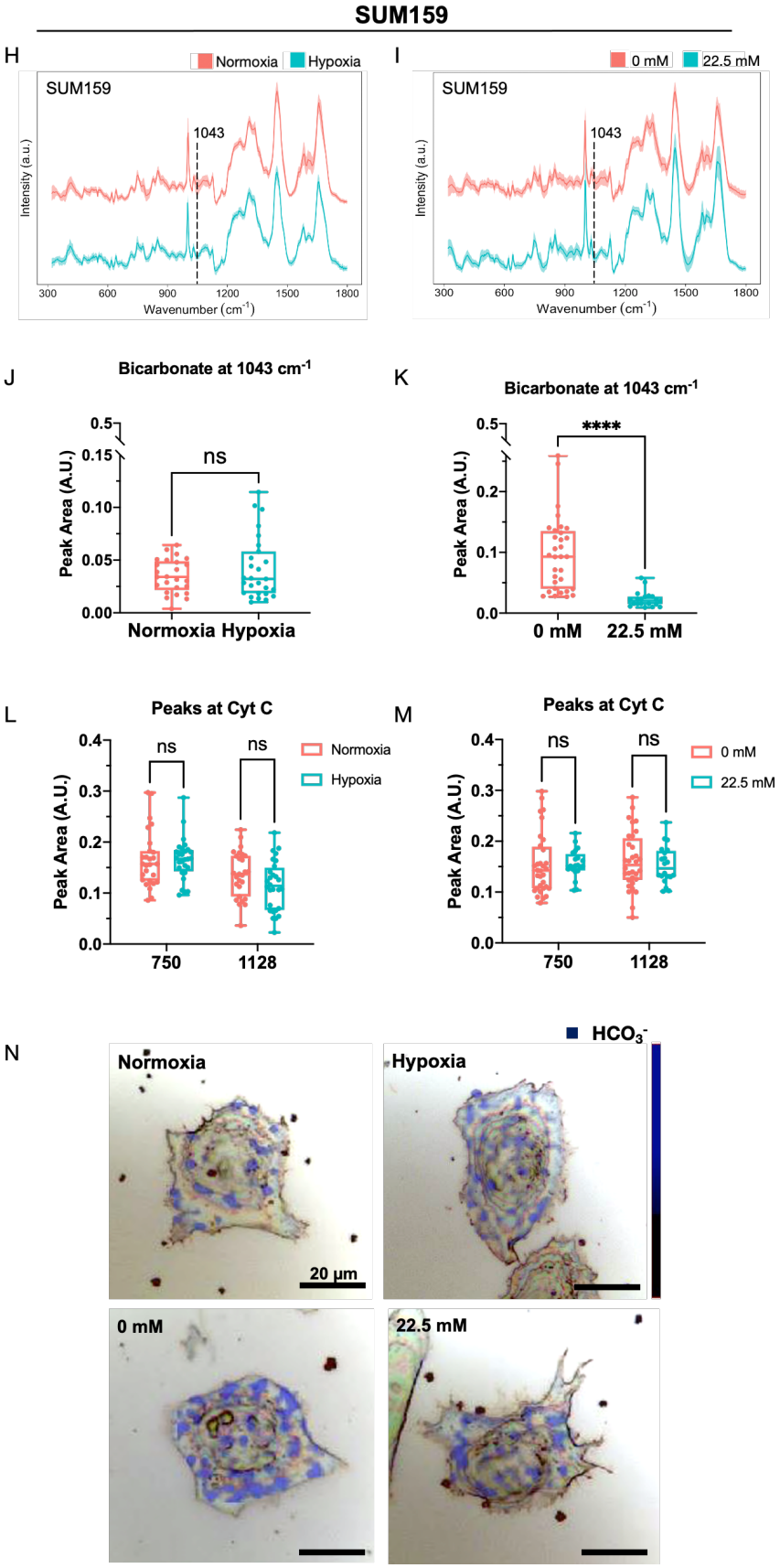


Figure 3.6 Variations in bicarbonate production in cells under different

concentrations of oxygen and glucose. (A) Comparison of averaged Raman spectra of U87 by incubating under normoxia and hypoxia in 10-mM glucose DMEM. (B) Comparison of averaged Raman spectra of U87 by incubating in 0-mM and 22.5-mM glucose DMEM under normoxia. (C, D) Quantification of bicarbonate band areas in U87 cells in the corresponding A, B respectively. (E, F) Quantification of cytochrome c bands in U87 cells in the corresponding A and B respectively. (G) The cell images of bicarbonate (blue, 1043 cm^{-1}) and cytochrome c (red, 750 cm^{-1}, 1128 cm^{-1}). Scale bar = 20 μm. (H) Comparison of averaged Raman spectra of SUM159 by incubating under normoxia and hypoxia in 10-mM glucose DMEM. (I) Comparison of averaged Raman spectra of SUM159 by incubating in 0-mM and 22.5-mM glucose DMEM under normoxia. (J, K) Quantification of bicarbonate band areas in SUM159 cells in the corresponding H and I respectively. (L, M) Quantification of cytochrome c bands in SUM159 cells in the corresponding H and I respectively. (N) The SUM159 Raman mapping images of bicarbonate (blue, 1043 cm^{-1}). 15-27 cells were measured for each group. For each cell, around 300 spectra were measured. Scale bar = 20 μm.

Figures 3.6H and 3.6I illustrate the average Raman spectra of cells under normoxia and hypoxia, zero and high glucose media, respectively, in the other cell line SUM159. In hypoxia culture for 24 hours, intracellular bicarbonate increased slightly but without statistical significance (Figure 3.6J). However, it was notable that the accumulation of bicarbonate in SUM159 cells incubated in the glucose-free medium changed significantly (Figure 3.6K, $p<0.0001$). No obvious variations in cytochrome c signals were detected in any of these conditions (Figure 3.6L and 3.6M). As shown in the Raman mapping images (Figure 3.6N), SUM159 cells grown in 0-mM DMEM had a large amount of

bicarbonate in the cytoplasm, which is much greater than that in the other cell images, where there were merely a few spots of bicarbonate.

3.4 Discussion

3.4.1 Bicarbonate band validation

Although previous studies have used Raman spectroscopy to measure bicarbonate ions in seawater[159] and supercritical water[160], there have been no studies on bicarbonate in mammalian cells. Our findings demonstrated that the 1043-cm^{-1} band is the characteristic band for intracellular HCO_3^-. We measured pure sodium bicarbonate chemicals (Figure 3S2) and utilised CA9 mutation and CA9 inhibitor to identify the bicarbonate marker band (Figure 3.2 and Figure 3.3).

3.4.2 Where does bicarbonate come from?

We hypothesise that bicarbonate in cancer cells is mainly derived from cellular HCO_3^- flux and intracellular mitochondrial activity. On the one hand, the loss of CA9 function in cancer cells was reflected by a significant decrease in intracellular bicarbonate. On the other hand, intracellular bicarbonate was also eliminated from cells after mitochondrial inhibition with metformin.

1. CA9 mutation and inhibition in relation to HCO_3^- flux

In hypoxia, it was previously shown that CA9 was upregulated and overexpressed on the cell surface[161,162]. In accordance with those studies, our results also show that CA9 is induced by hypoxic factors to upregulate

expression at the single cell level. The level of CA9 protein expression in MDA-MB-468 cells has been successfully confirmed in the previous publication[163]. The CA9 and HIF-1α protein expression induced by hypoxia in U87 and SUM159 can be found in Figure 3S4. It has been found that transcription of CA9 can be enhanced by stabilization of HIF-1α in MDA-MB-231, in agreement with our results[164].

CA9 is induced to be expressed abundantly on the cell surface under hypoxia. Extracellular CO_2 is continuously converted into HCO_3^-, which is then transferred to the cell via bicarbonate transporters (Figure 3S3B)[11]. When the CA9 protein is knocked out, most extracellular CO_2 cannot be converted to HCO_3^-, leaving the intracellular environment devoid of substantial HCO_3^- accumulation (Figure 3S3C). This implies a major role in promoting HCO_3^- efflux, with the increase potentially due to continued import (Figure 3S3C).

2. Mitochondrial respiratory metabolism is an essential endogenous source of HCO_3^-

Our work showed that cancer cells accumulated large amounts of bicarbonate when they were unable to intake glucose from the environment (Figure 3.4B, 3.4F, 3.5C, 3.6D and 3.6K). This is because when glycolysis ceases in cancer cells, the mitochondria will step up their function to provide enough energy. Researchers have found that cancer cells increase their dependence on mitochondrial respiration when cultured in reduced glucose circumstances[165]. The primary target of metformin is the mitochondrial respiratory-chain complex 1 in result of mitochondrial function shutdown. A previous study have proved

that metformin is more effective under reduced glucose conditions[166]. Consistently, our results also show that metformin is most effective in inhibiting bicarbonate under low-sugar conditions (Figure 3.4 and 3.5).

As a result, the respiratory metabolism of the mitochondria produces large amounts of CO_2. CO_2 in cytoplasm is hydrated by intracellular carbonic anhydrases (CAi) to HCO_3^-, increasing its concentration inside the cell (Figure 3S3D). Inhibited by metformin, the bicarbonate band can no longer be seen as the mitochondrial respiratory metabolism is blocked (Figure 3.4B, 3.4F and 3.5C). This indicates that most of the bicarbonate produced inside the cancer cell may come from mitochondrial respiratory metabolism.

3.4.3 Mitochondria play a key role in bicarbonate metabolism and regulation

For a long time mitochondrial dysfunction was considered to be a hallmark of cancer cells[167,168]. In recent decades, it has been recognized that cancer cells do not obey the Warburg effect and that they possess active, functional mitochondria[169,170]. Our findings also reveal that mitochondria play a key role in the metabolism of bicarbonate in cancer cells.

We have demonstrated with metformin that mitochondrial oxygen consumption leads to a large accumulation of bicarbonate in the cancer cells under normoxic conditions. In hypoxia, Figures 3.2 and 3.3 show that HCO_3^- flux is mainly regulated by CA9. Besides, studies have indicated that the mitochondrial

bicarbonate production was reduced in hypoxia [40,171]. However, we find that if the mitochondria are inhibited with metformin under hypoxic conditions, the signal from bicarbonate was also significantly reduced (Figure 3S5).

We hypothesize that mitochondria are involved in respiratory metabolism and bicarbonate production under both normoxic and hypoxic conditions. The roles of CA9 and mitochondria for HCO_3^- flux is significant in hypoxia. However, more research is needed to clarify the mechanism of their specific actions in the future work.

3.4.4 Bicarbonate accumulation and glycolytic activity may be correlated

The inhibition of CA9 with U-104 resulted in a down-regulation of bicarbonate conversion and its concentrations in hypoxia. We suggest this difference may also be relevant to the breakdown of glycogen. A comparison of the changes in glycogen concentrations of U87 and SUM159 after the addition of U-104 under normoxia revealed varying degrees of decrease in the intensity of the characteristic glycogen peaks (480, 850 and 940 cm^{-1}) (Figure 3S6). Confirmation of glycogen signature peaks is provided in Chapter 4. In Figure 3S6A and B, U87 cells exhibited a significant decrease at the 480 and 850-cm^{-1} peaks due to the effects of U-104. Conversely, the reduction of glycogen in SUM159 was primarily observed at 940 cm^{-1} (Figure 3S6C and D). The glycogen bands showed a decline when CA9 was inhibited by U-104 in both U87 and SUM159, with hypoxia having a more significant effect than normoxia (Figure 3S6A, B, C and D).

Generally, hypoxia induces glycolysis to produce more glycogen[9,172]. However, our experimental results show that U-104 may trigger an acceleration in glycogen degradation in human cancer cells. Bicarbonate has been shown to facilitate the shift from respiration to anaerobic glycolysis by acting as a substrate for t6A biogenesis and slowing down mitochondrial tRNA translation[11].

Inhibiting CA9 enzymatic activity with U-104 has no impact on monocarboxylate transporters (MCTs) transport activity since it is a non-catalytic transport[173]. The "proton antenna" of CA9 can cooperate with BT and MCT to help acid and lactate achieve transmembrane transport[83,126]. Additionally, CA functional deficiency does not affect glucose transporter activity[76].

Anaerobic glycolysis in cancer cells produces large amounts of lactic acid and H^+, which is a main mechanism by which tumours lower their pH[29]. Hence the intracellular HCO_3^- was consumed to neutralize the excess acidic metabolites, and the reaction product CO_2 diffused out of the cell (Figure 3S6E). CA9 potentially cycles substrates of water, CO_2, HCO_3^- and protons to maintain the pHi because of cellular acidification resulting from excessive excretion of glycolytic byproducts[174].

It is noticeable that cancer cells accumulate HCO_3^- under stress rather than converting it to CO_2 and releasing it (Figure 3.6). Researchers have shown that bicarbonate can support cell viability and prevent acidification to help cancer cells survive[11,68]. Cancer cells may maintain large amounts of bicarbonate to neutralize acidic metabolites generated from glycolysis. This evidence

suggests that glycolysis may play a key role in intracellular pH regulation and the metabolism of bicarbonate.

3.4.5 Cytochrome c has intratumoral heterogeneity

In this work, we compared the cytochrome c levels of different treatments in cancer cell lines. Both in the U-104 inhibition effects and stress conditions sections, U87 cells showed a significant decrease at cytochrome c bands during hypoxia, compared to normoxia. It suggests that hypoxia triggers a downregulation of mitochondria in cancer cells (Figure 3.6E). In addition, our results demonstrate that glucose-free culture increases the mitochondrial activity of the U87 cells. It is because the glycolysis is inhibited without glucose intake and cancer cells have to obtain energy through mitochondrial respiration, which upregulates mitochondria function.

Interestingly, however, we did not see a significant change in the mitochondria of SUM159 under these conditions (Figure 3.6L and 3.6M). Although the variability of the signal intensity of other Raman bands is relatively low, the mitochondrial dynamics of SUM159 always stay at a similar level. SUM159 shows a higher tumour heterogeneity, perhaps contributing to their resistance to the restrictive environment[175].

In addition, the release of cytochrome c is considered a sign of cell apoptosis and the band intensity in the early apoptotic stage is maintained at a similar level to that of control cells[176]. Here, the cytochrome c of cancer cells cultured

in the different gradients of glucose medium was at a similar level in the data of the metformin effect (Figure 3.4C and 3.4G). Metformin did not down-regulate cytochrome c signalling in cells cultured in the glucose-free medium. We assume that it is a signal for the early stage of cell death under stress. We tried feeding the cells with higher concentrations of metformin, and the cells became very weak and massive death was observed. When a suitable concentration of glucose is given, this situation is relieved, and the cytochrome c Raman signal no longer shows a rising form. Previous studies have illustrated that increasing glucose metabolism in neurons and cancer cells can inhibit cytochrome c-mediated apoptosis and facilitates anti-apoptotic cell death[177,178].

There is intertumoural heterogeneity in cytochrome c bands between the different cell lines. Our results point out that the cytochrome c bands of U87 cells are much more sensitive to stress conditions, but those of SUM159 cells were not significantly identified (Figure 3.4C, 3.4G, 3.6E and 3.6L). It is possible to combine Raman mitochondria-associated labelled bands with other tools, such as fluorescent labelling. This combination enables a more accurate indication of the location of mitochondria and allows for exploration of mitochondrial function in cancer cells for the future research.

3.4.6 Application of Raman analysis to bicarbonate metabolism

Many bicarbonate metabolism studies have mainly focused on pH regulation[79,151,162,179] and cell growth inhibition[180,181]. It is still challenging to directly detect the metabolic phenotype of bicarbonate in mammalian cells.

Here we developed a novel method to study sub-cellular bicarbonate by Raman imaging and spectral analysis. In addition, this method allows cells to be grown directly on the slide, maintaining the morphology, without affecting the bioactivity and viability of the cells. It is possible to control cell number and confluence, and the researcher can easily obtain the required single cells based on the cell growing density and growth rate. In combination with Raman data analysis, the bicarbonate can be semi-quantified, and its high-resolution single-cell mapping can be generated.

The characteristic Raman band of bicarbonate could be a good biomarker for cancer cells. The 1043-cm^{-1} band is distinguishable and easy to analyse, which enables a rapid indication of intracellular bicarbonate by Raman analysis. Bicarbonate band may have the potential to become a new indicator in cancer cells. Some clinical studies have also treated sodium bicarbonate in anti-cancer treatment[182] and clinical cancer care[183,184]. However, blood and urine samples have to be collected to test changes in levels of key cations and anions to analyse bicarbonate. Our findings provided great advantages to non-invasive and direct-quantitative bicarbonate detection. In the future, portable Raman technology in conjunction with bicarbonate detection, might open up non-invasive diagnostic applications in cancer clinical trials.

Authors contributions

T.Y. performed the experiments and wrote the manuscript. J.X. and S.H.

supported the mitochondrial pellet sample preparation and Raman measurement. J.X. and W.E.H. designed the work and assisted in the data analysis. A.L.H and W.E.H. supervised the research and designed the experiments for cancer metabolism. A.L.H. and C.Z. interpret the data for cancer metabolism. All authors contributed to discussion, data interpretation and editing of this paper.

Acknowledgements

We thank Dr Mira Kreuzer and Dr Marina Petrenko for providing MDA-MB-468 WT and MDA-MB-468 shCA9 cells. Created with BioRender.com.

Supporting information

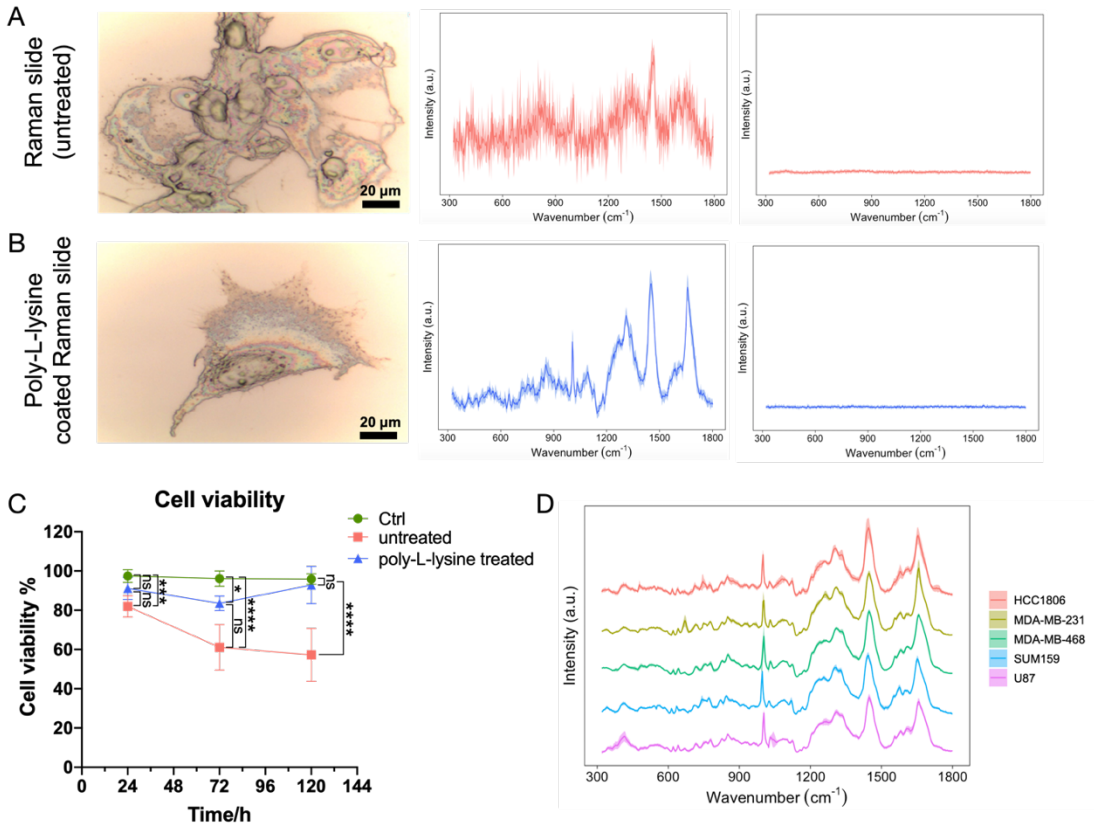


Figure 3S1 Comparison of poly-L-lysine-modified and untreated Raman slides

and its applications on different cancer cell line. (A) Cell images of U87 cells on untreated Raman slide, along with their single-cell Raman signal and background signal of untreated Raman slide (red). (B) Cell images of U87 cells on poly-L-lysine modified Raman slide, along with their Raman signal and background signal of coating Raman slide (blue). (C) Comparison of the cell viability of U87 cells on plastic slides (Ctrl, green), untreated (red) and poly-L-lysine treated (blue) Raman slides. (D) Raman profiles of several cell lines after culture on poly-L-lysine coated Raman slides. 6-10 cells were measured for each group. For each cell, around 150 spectra were measured.

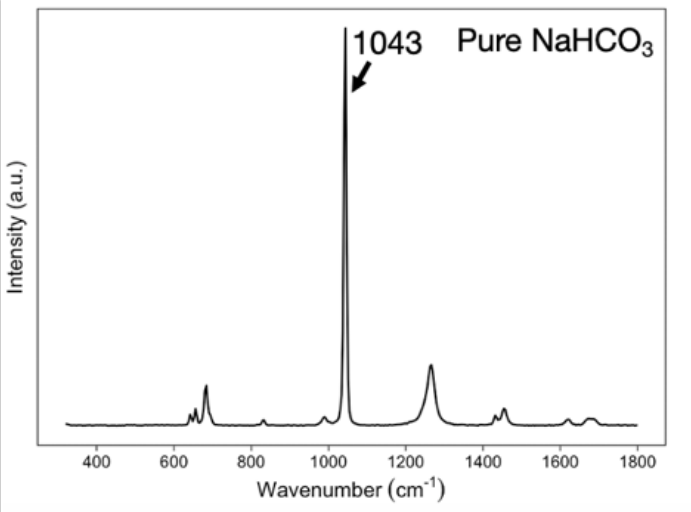


Figure 3S2 Raman spectra of pure $NaHCO_3$ with a characteristic 1043-cm^{-1} peak.

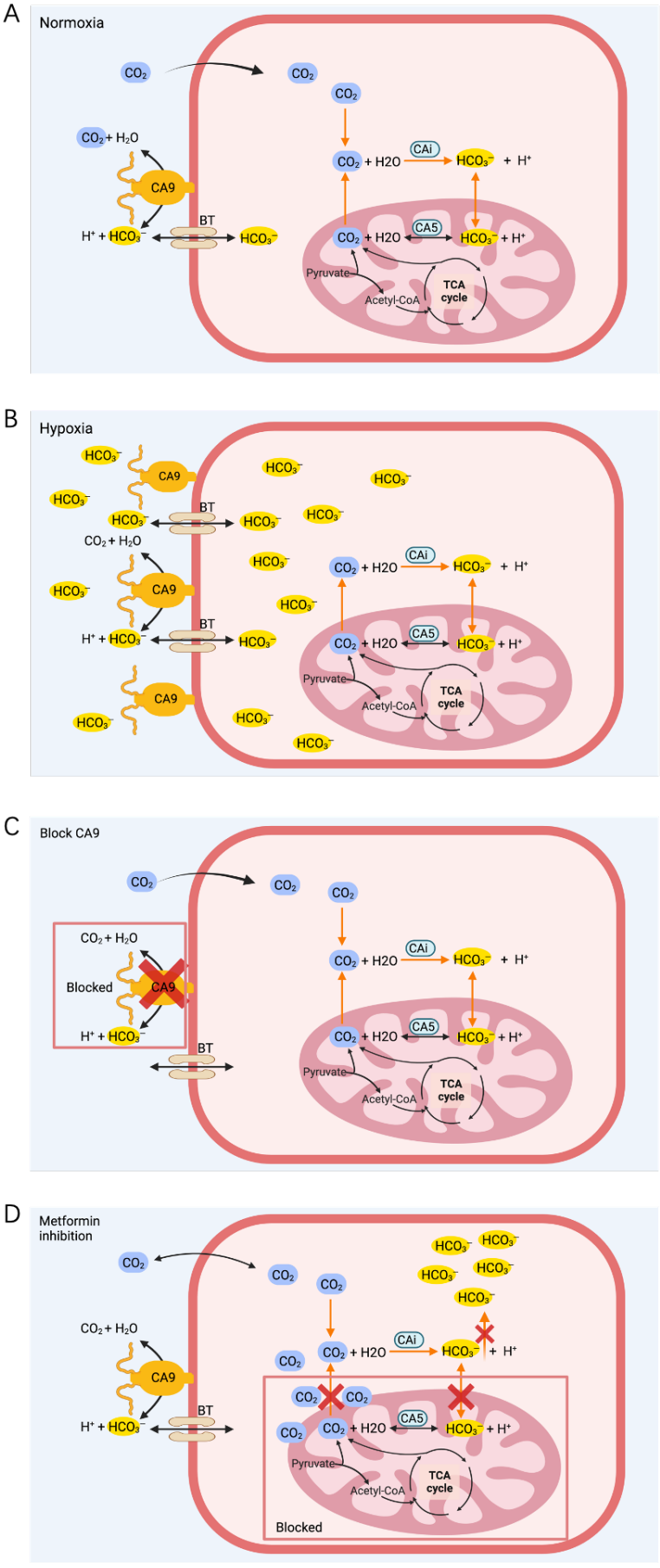

A
Normoxia
CO2
CO2 + H2O
CA9
H+ + HCO3−
BT
HCO3−
CO2 + H2O
CAi
HCO3− + H+
CA5
Pyruvate
Acetyl-CoA
TCA cycle
B
Hypoxia
C
Block CA9
Blocked
D
Metformin inhibition
Blocked

Figure 3S3 Metabolism of bicarbonate in cytoplasm and mitochondria in cancer cells. (A) A schematic of bicarbonate metabolism under normoxia. Mitochondrial respiratory metabolism produces CO_2, which is hydrated to HCO_3^- by carbonic anhydrase V (CA5). Additionally, imported and mitochondrial CO_2 are hydrated to from HCO_3^- by intracellular CAs (CAi) in cytoplasm. (B) CA9 is abundantly expressed in the cell membrane under hypoxia. Extracellular CO_2 is converted into HCO_3^- which then enters the cell via BT. (C) When CA9 is blocked, extracellular CO_2 cannot be hydrated to HCO_3^-. (D) Increased mitochondrial activity under low glucose produces large amounts of CO_2, which are then hydrated to HCO_3^- by CAi. This metabolic process is halted when mitochondrial respiratory metabolism is blocked by metformin.

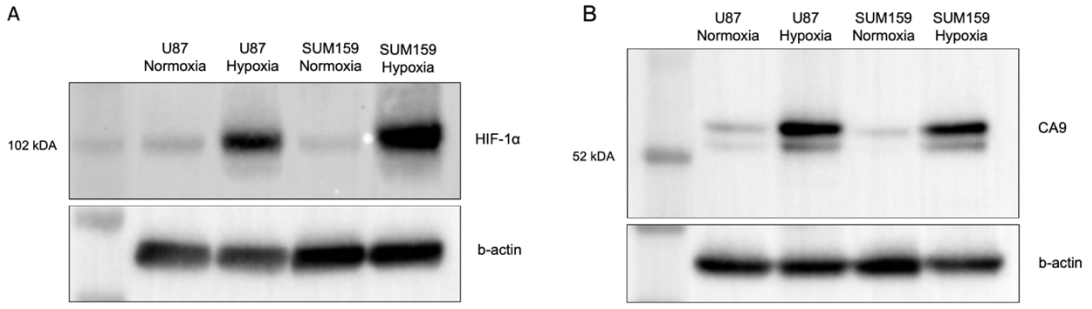


Figure 3S4 Validation of hypoxia-induced expression of hypoxia-inducible factor 1-alpha (HIF-1α) enzyme and CA9 protein. (A, B) Western blot images of HIF-1α (A) and CA9 (B) in U87 cells and SUM159 cells under normoxic and hypoxic conditions respectively. b-actin was used as a control.

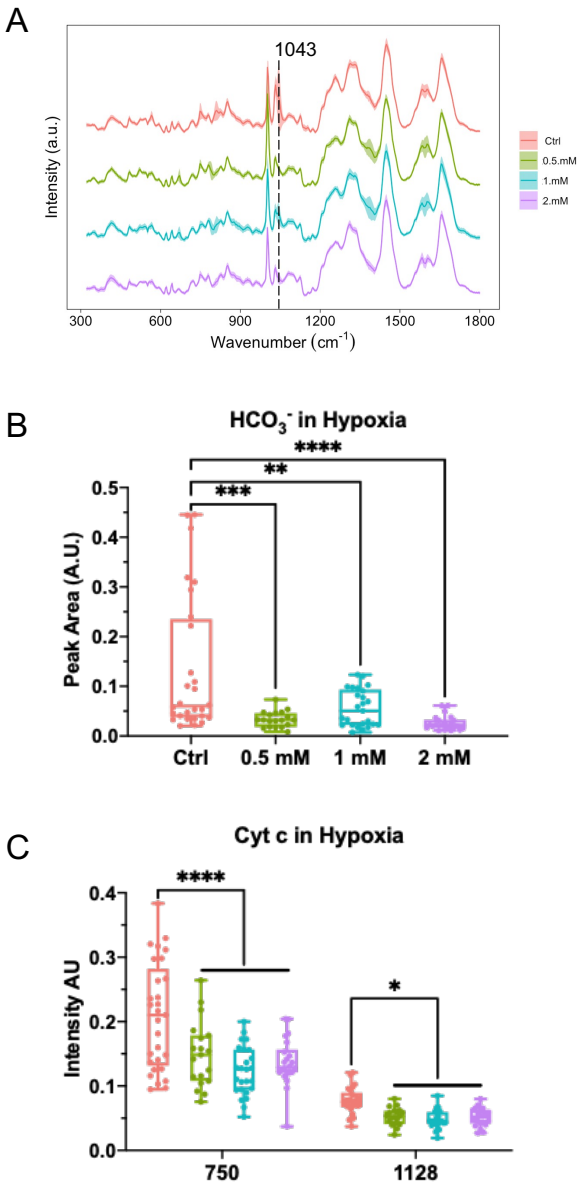


Figure 3S5 Comparison of the inhibitory effect of metformin on bicarbonate under hypoxia in MDA-MB-468 EV. (A) Raman spectra of the effects of different concentrations of metformin on MDA-MB-468 EV. (B) Quantification by integration of bicarbonate peak area. (C) Quantitative comparison of cytochrome c peaks at 750 and 1128 cm^{-1}. 22-29 cells were measured for each group. For each cell, around 300 spectra were measured.

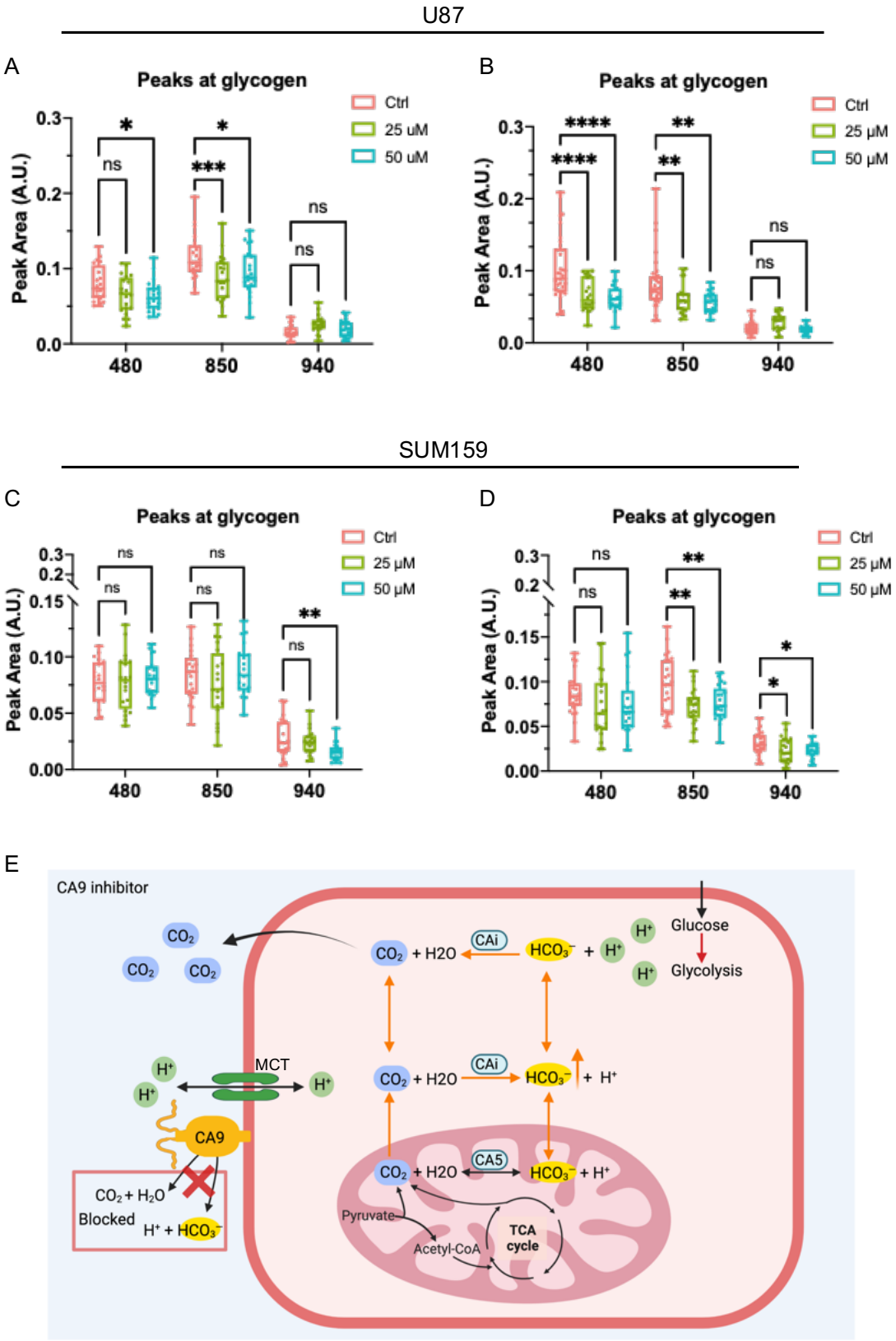


Figure 3S6 Glycogen changes in response to U-104 inhibition. (A, B) Quantification of the characteristic glycogen peak (480, 850 and 940 cm^{-1}) in U87 under (A) normoxic and (B) hypoxic conditions. (C, D) Quantification of the

characteristic glycogen peak (480, 850 and 940 cm^{-1}) in SUM159 under (C) normoxic and (D) hypoxic conditions. (E) CA9 inhibitors affect only the conversion of CO_2 to HCO_3^-, but not the transport of protons through the cell membrane. The glycogen level in cancer cells suppressed by CA9 inhibitor is significantly reduced. Glycogen degradation produces large amounts of lactic acid and protons. The intracellular HCO_3^- is used to neutralize the excess acids and generate CO_2 which excretes out of the cell directly. 20-30 cells were measured for each group. For each cell, around 300 spectra were measured.

Chapter 4

Application of SCRM–SIP using ^{13}C-glucose to study glycogen metabolism in cancer cells

Contents

4.1 Introduction

4.2 Materials and method

4.3 Results and discussion

4.3.1 Glycogen extraction and identification of Raman characteristic bands of glycogen

4.3.2 Glycogen semi-quantitative analysis and high-resolution Raman mapping of glycogen and DNA distribution

4.3.3 ^{13}C-glucose stable isotope probing

4.3.4 Glycogen metabolic profiles in ^{12}C and ^{13}C-glucose medium

4.3.5 Metabolic phenotyping of other bio-components with ^{13}C-glucose stable isotope probing

4.3.6 Acute breakdown of glycogen in short-term glucose-free incubations

4.4 Conclusions

In this chapter, Single-cell Raman micro-spectroscopy (SCRM) was used to study the time-course of glycogen metabolism and turnover in cancer cells, primarily the human glioblastoma cell - U87. I showed that SCRM was able to detect the three glycogen characteristic Raman bands and visualize glycogen location and distribution at the sub-cellular level. SCRM also combined ^{13}C stable isotope probing (SIP) technology to distinguish structural assignments of glycogen, and to evaluate the short-term turnover of glycogen in cancer cells.

4.1 Introduction

Cancer cells largely rely on metabolism of glucose through the glycolysis pathway, even when exposed to normal oxygen conditions. Glycogen, the storage form of glucose in cells, is essential for energy supply and glucose homeostasis[8]. This is because glycolysis generates many metabolites needed for synthesis of proteins, lipids and nucleotides. ATP is still generated by the Krebs cycle in cancer cells.

Glycogen metabolism includes glycogen breakdown (or glycogenolysis) and glycogen synthesis. This metabolism also involves several enzymes and kinases that regulate these processes (Figure 4.1). The glucose transporter delivers free glucose into the cytosol, enabling glycogen synthesis[18,5]. Free glucose is converted to glucose-6-phosphate (G6P) by the action of hexokinase in muscle or glucokinase in the liver, followed by conversion to glucose-1-phosphate (G1P) by phosphoglucomutases[185]. Uridine diphosphate glucose

(UDP-Glucose or UDPG) stretches glucose chains by binding UDP-glucose units at the non-reducing ends and glycogen branching enzymes (GBE) catalyse the long glucose chains to branched chains, which forms glycogen granules[19,20,186,187]. Glycogen breakdown proceeds mainly by phosphorylase (PYGL/M/B)[26–28] and glycogen debranching enzyme[188], resulting in an extremely sensitive regulation process to release glucose residues for energy use.

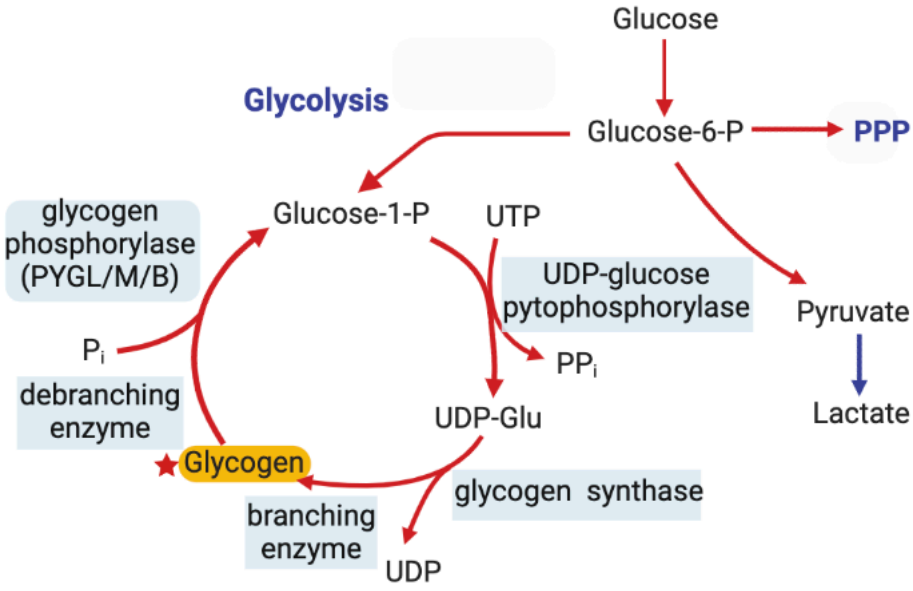


Figure 4.1 Key pathways for glycogen metabolism process in cancer cells[8,9]. PPP, pentose phosphate pathway; UTP, uridine triphosphate; UDP, uridine diphosphate; Glu, glucose; P, phosphatase; Pi, intracellular inorganic phosphate; PPi, pyrophosphate; PYGL/M/B, glycogen phosphorylase for liver (L), muscle (M) and brain (B).

SCRS is a reliable and high resolution technology for studying cells, which has been applied in many fields, including gene regulation and expression[189], function of microbial communities[120,190], stem cell differentiation and

development[191], brain tumour and necrosis[192,193]. Raman spectroscopy has been used previously to study glycogen in cancer cells [194]. For example, it detected the radiation-induced accumulation of intracellular glycogen[195] in several cell lines. The results showed that the increase in glycogen post-irradiation was highest in lung (H460) and breast (MCF7) cell lines. Moreover, another group[195] treated MCF7 cells with metformin, which is an oral anti-diabetic drug that inhibits the generation of ATP by inhibiting complex I in the electron transport chain[196,197]. They found that Raman spectroscopy detected a significant reduction in glycogen levels for irradiated MCF7 cells treated with metformin for 2 to 3 days[195]. Another study indicated that the glycogen band at 850 cm^{-1} is one of the main differences between normal and tumour subtypes when comparing spectra from the normal brain cells to those of tumours by using attenuated total reflection Fourier-transform IR (ATR–FTIR) and Raman[198].

Raman-stable isotope probing (Raman–SIP) is able to link a specific substrate with its metabolism in a complex cellular microenvironment. The quantitative estimation of the stable isotopic atom (^{13}C, ^{15}N and ^{2}H) labelled biomolecules can be calculated by Raman band shift ratio. When stable isotopic atoms are taken by the cells, the replacement of the 'heavy' atoms (stable isotope) changes the vibration energy, leading to a shift of Raman bands[88]. Based on these isotope-dependent band shifts, stable isotope probes are widely used to

trace atoms, indicating how organisms assimilate a stable isotope substrate and how biomolecules change in the metabolic pathway.

The most commonly used isotope markers are ^{2}H, ^{13}C and ^{15}N. Various pathways have been analysed using Raman–SIP in microbial communities and mammalian tissues, including DNA transcription/translation[199], protein biosynthesis[200] and lipid degradation[93]. In this chapter, I utilised SCRM to track ^{13}C-fully labelled glucose in glycogen granules and its turnover in human cancer cell lines.

Here I present that Raman technology detects biomolecules at the single-cell level and identifies molecules at subcellular resolution. In this study, SCRM revealed characteristic bands of glycogen at the subcellular level in cancer cells. I used it to visually map the distribution of biological components such as glycogen, DNA/RNA and cytochrome c within a cancer cell. Remarkably, glycogen images and ^{13}C isotope labelling showed rapid glycogen turnover in hypoxic conditions.

4.2 Materials and methods

Cell lines and cell culture. The human U87 and SUM159 cell lines were grown in Dulbecco's modified Eagle medium (DMEM, Gibco, USA) supplemented with 10-mM glucose and 10% fetal bovine serum (Gibco, USA). All cells were cultured in a water-saturated incubator under 37℃ and 5% CO_2. Cell lines were obtained from American Type Culture Collection (ATCC).

Poly-L-lysine coated slides. The three well-removable chambers (Ibidi, Germany) were pressed on the Raman slide, and then 0.01% (v/w) poly-L-lysine solution (Sigma, USA) was added to modify the Raman slide surface. After 5 minutes incubation, the slide surface was washed thoroughly with sterile tissue culture grade water (Gibco, USA) to remove poly-L-lysine. The modified Raman slides were put back in the incubator to dry for at least 1-2 hours before use.

Sample preparation. The cell suspension was diluted to a concentration of 5000 cells/mL seeded on poly-L-lysine-coated Raman slides and then incubated overnight. The cells were washed in phosphate buffered saline (PBS, Life Technologies, UK) and then added to the required culture medium for incubation. At the culture time points, the cells were washed quickly with cold PBS and immediately fixed with 4% paraformaldehyde (PFA, ThermoFisher Scientific, USA) at room temperature. Samples were washed twice with Milli-Q water to remove the salts and dried at room temperature before Raman spectroscopy measurement.

Spontaneous Raman spectra. Spontaneous Raman spectra were obtained by a confocal Raman microscope (LabRAM HR Evolution, Horiba Scientific, UK) equipped with an integrated microscope (BX41, Olympus, Japan). A 532 nm neodymium-yttrium Aluminum garnet laser was used to excite cells. A 50× objective lens (numerical aperture 0.5, spatial resolution ~2 μm) was used to visualize cells and collect Raman spectra from about 1 μm diameter spots on

cells. The acquisition parameters were set as 3-s acquisition time, 4.5-mW laser power exposure and 300 grooves/mm diffraction grating through a 25% filter.

^{13}C-glucose labelled cell viability assay. The human U87 cells were cultured in 10%, 25%, 50%, 75%, 90% ^{13}C-glucose DMEM (Gibco, USA) for 24 hours separately. Trypan blue exclusion was used to evaluate total cell counts and viability by LUNA-IITM automated cell counter (Logos Biosystems, South Korea).

Glycogen extraction standard method. This chapter used the classic KOH-ethanol method to extract glycogen from U87 cells[201]. Cells were incubated in 30% KOH (Sigma, USA) at 95°C for 30 minutes. After incubation, cells were placed on ice for rapid cooling and three times the volume of cold pure ethanol (Sigma, USA) added. The centrifugation of the cell suspension was repeated three times at 1500 rpm with cold pure ethanol to precipitate the white glycogen pellets. The extracted glycogen was then placed and dried on the Raman slide for Raman spectra acquisition.

Raman spectral data processing and analysis. Raman spectral data processing and analysis. The Raman spectra were processed by the LabSpec 6 software (HORIBA, LabSpec6, UK) for baseline correction and calibration. Data analysis and visualization was done using MATLAB 2019b (MathWorks, USA), GraphPad Prism 9.0.2 (GraphPad, USA) and R (3.5.1, USA) using in-house scripts. The specific data processing method is the same

as Chapter 3. All experiments were repeated with at least three biological replicates. Numerical data values are represented as mean ± standard deviation (SD)

4.3 Results and discussion

4.3.1 Glycogen extraction and identification of Raman characteristic bands of glycogen

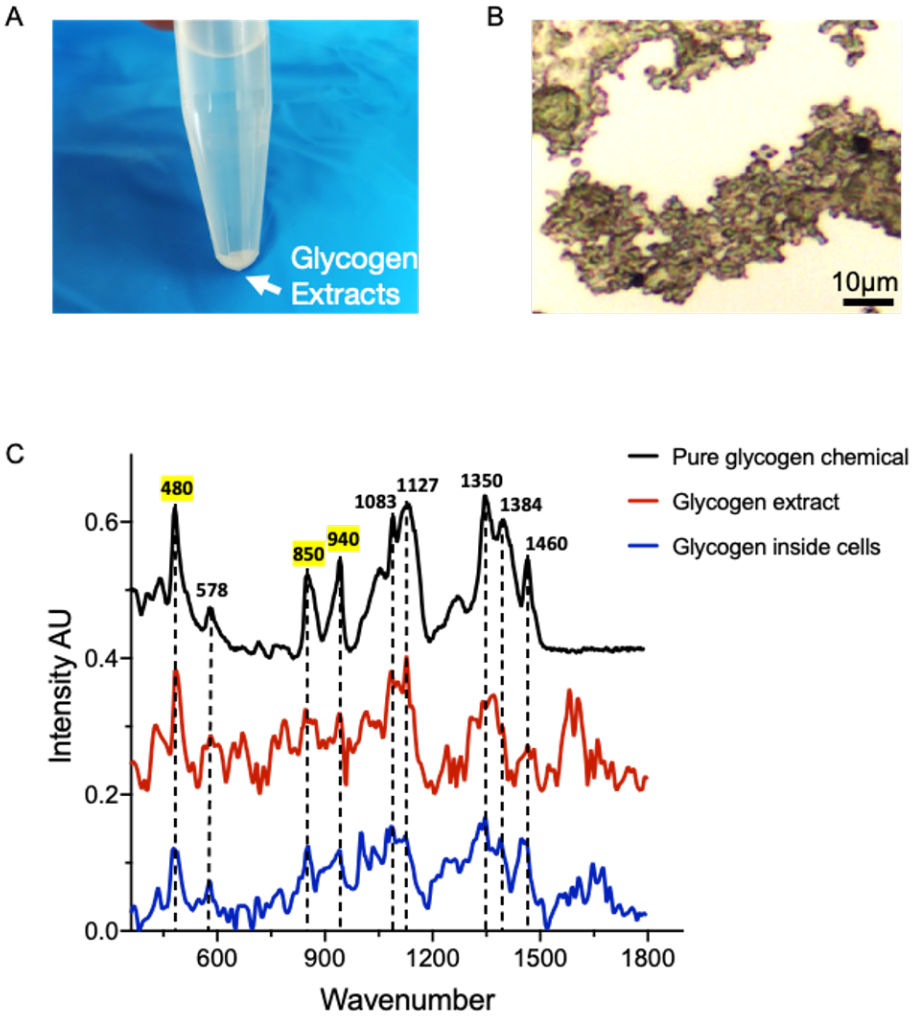


Figure 4.2 Identification of glycogen characteristic Raman bands. (A) The glycogen white powder extracted from U87 cells and stored in pure ethanol. (B) The cellular extracted glycogen crystals observed under Raman microscopy. (C) The averaged spectrum of pure glycogen chemical from Sigma-Aldrich Co.

(black), the extracted glycogen from U87 cancer cells (red), and glycogen inside cancer cells (blue).

To confirm the characteristic Raman bands of glycogen, we examined both pure glycogen from Sigma-Aldrich Co. and extracted glycogen from U87 cancer cells. Both pure glycogen and glycogen extract from U87 cells are white solid powders, which were stored in pure ethanol as shown in Figure 4.1A. The glycogen extracts were washed by Milli-Q water, resuspended, and dropped on the Raman slide for Raman analysis. The Figure 4.1B shows the image of large, extracted glycogen granules observed under Raman Spectroscopy.

In the Figure 4.1C, the averaged Raman spectra of pure glycogen, the glycogen extracts and intra-cellular glycogen match well. In most studies, glycogen is extracted from liver tissues as this has far higher yields than cancer cells. The Raman features of glycogen in tissue have been identified at 484, 856, 941, 1130, 1337 and 1460 cm^{-1} [202]. 480 cm^{-1} is associated with skeletal and α(1 → 4) glycosidic links vibrations[203]. A strong signal at 850 cm^{-1} is associated with the modes of C—H bending[204]. 940 cm^{-1} is relevant with modes related to the glycosidic COC vibrations[205]. 1130 cm^{-1} is assigned to the stretching of C—O bonds[204]. 1337 and 1460 cm^{-1} are associated with the bending of CH_2 and the deformation of CCH[204]. The Raman spectrum from our extracted glycogen is highly consistent with the reported glycogen spectra identified from tissues[202].

However, there are a large amount of DNA/RNA, lipid, and protein bands in the range of 1080 to 1460 cm^{-1}. The glycogen bands in this range overlap with the

Raman bands from other biomolecules. Hence, the Raman spectra in this range cannot be used as indicator bands for glycogen. Through comparison with the Raman spectral database of substances, it was finally determined that 480, 850 and 936 cm^{-1} are unique bands of glycogen. Interestingly, these Raman bands also reflect typical chemical properties of glycogen, such as linkage, branch, and length of glycogen chains. The vibrations of the α-D-(1→4) glycosidic linkages is assigned to 480 cm^{-1} [206]. The band at 850 cm^{-1} is attributed to the C(1)—H(α) bending mode and in α-configuration of the glycosidic bond [203]. It has been proposed as a marker band to the skeletal mode involving the α-D-(1→4) glycosidic linkage[207]. The 940-cm^{-1} band contributes to the symmetric COC vibration of α-D-(1→6) glycosidic linkages[203]. As a result, these three bands were confirmed to characterize glycogen in the subsequent data statistics.

In this chapter, I used the same Raman mapping mode measurements as in Chapter 3. Single cancer cells were randomly selected, then a square grid of 2-μm pixels was set up to scan each cell. The mapping spectra were then processed into glycogen signal imaging to obtain glycogen signal intensity and location information.

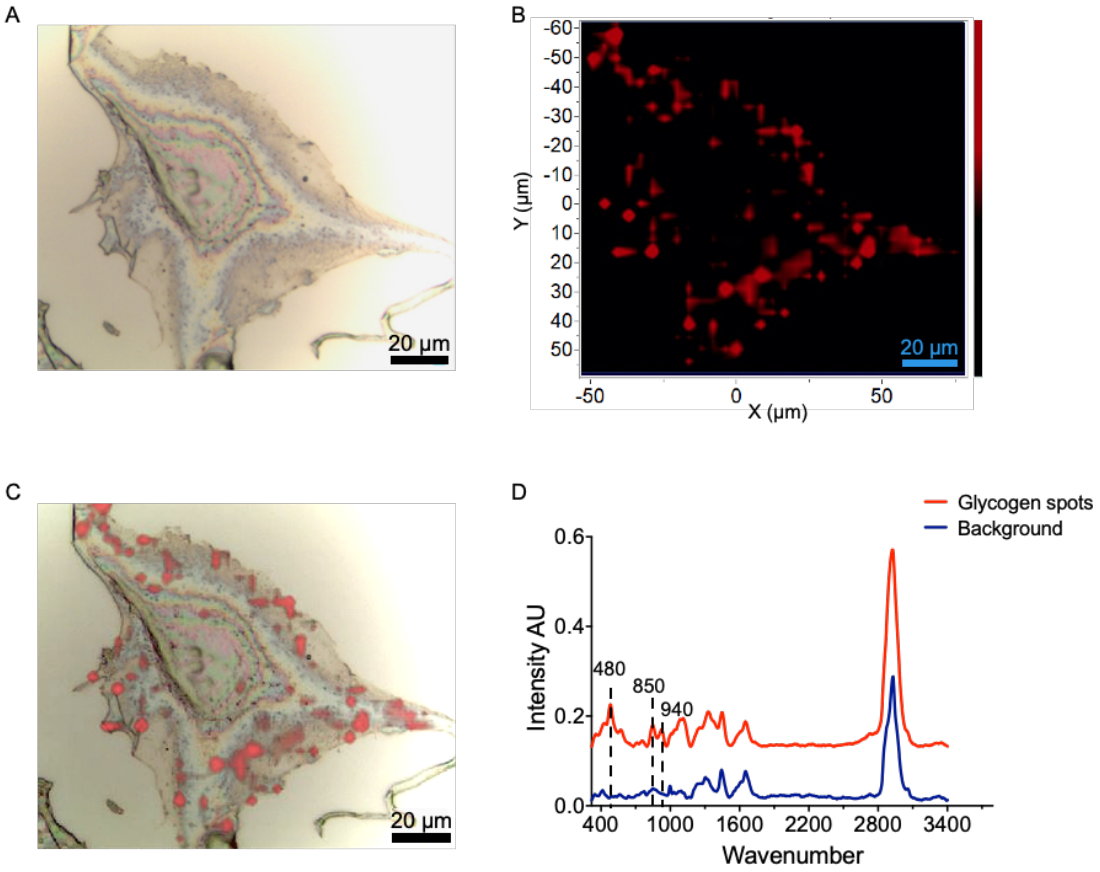


Figure 4.3 Comparison of glycogen characteristic Raman bands with cellular background in Raman mapping within a single cell. (A)The cancer cell microscopic image. (B) Raman mapping image of glycogen in the single cell. (C) The overlapping Raman image of glycogen distribution and image of the cancer cell. (D) The averaged Raman spectra of sub-cellular glycogen hot pots (red) and cellular background (blue).

In Figure 4.3 for U87 cell Raman mapping, glycogen distribution (red) and its Raman mapping image are shown, respectively. In Figure 4.3B, the extent of red color corresponds to the glycogen signal intensity. The red spots are high signals of glycogen; and the background is black, i.e., non-glycogen signaling. Their Raman profiles are shown in Figure 4.3D. The red spectrum is the

averaged Raman spectrum of glycogen spots, in contrast, the cellular background is shown as the blue spectrum below.

By comparison, it can be seen that the Raman spectra of the high glycogen expression region demonstrates three clear glycogen characteristic bands. At the same time, the location and distribution of glycogen are also shown within the single cell by imaging overlapping (Figure 4.3C).

4.3.2 Glycogen semi-quantitative analysis and high-resolution Raman mapping of glycogen and DNA distribution

Liver glycogen phosphorylase (PYGL) is one isoform of glycogen phosphorylase acting in glycogen breakdown (Figure 4.1)[11,35]. PYGL mutations induce a deficiency of hepatic phosphorylase with resulting glycogen storage disease (GSD) type VI[36]. PYGL knockdown results in the accumulation of glycogen in GBM cells, which subsequently reduces flux of PPP and increases the production of reactive oxygen species (ROS), triggering premature senescence, markedly impaired tumourigenesis and radiosensitivity[37,38].

U87 wild type (WT) and PYGL knockdown (PYGL KD) cells were cultured under three conditions, normoxia, hypoxia and with γ radiation. The cells were scanned by SCRS, and the band areas of glycogen were calculated separately. Glycogen concentrations were semi-quantified within each individual cell with location.

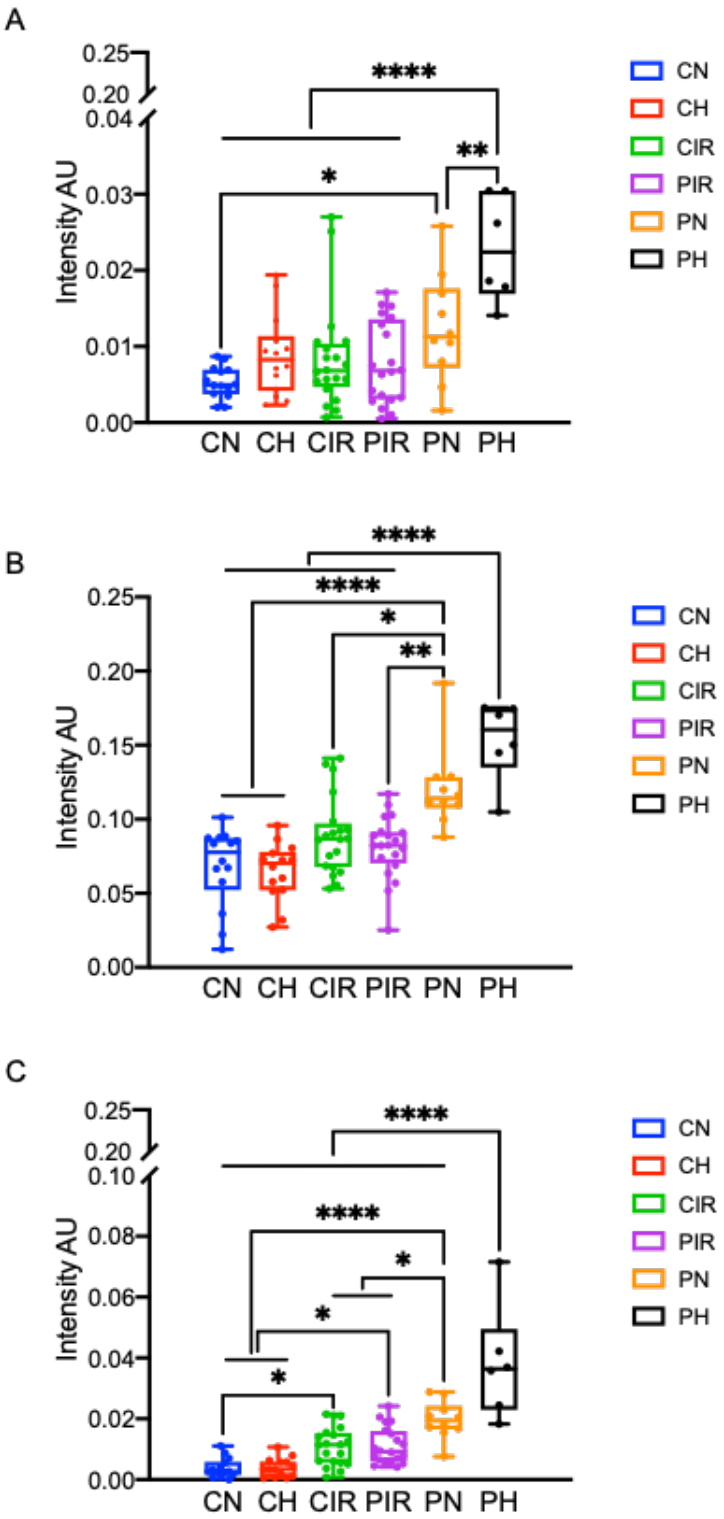


Figure 4.4 Single-cell Raman micro-spectroscopy detects intensity of glycogen in U87 WT and PYGL KD cells under normoxia, hypoxia and γ radiation treatment. The intracellular glycogen levels measured at (A) 480 cm^{-1}, (B) 850 cm^{-1} and (C) 940 cm^{-1} band. CN: WT cells under normoxia; CH: WT cells under hypoxia; CIR: WT cells under γ radiation; PIR: PYGL KD cells under γ radiation;

PN: PYGL KD cells under normoxia; PH: PYGL KD cells under hypoxia. 6-20 cells in each group and around 300 spectra were measured in each cell. Data are presented as mean values ± S.D., two-way ANOVA test, *p<0.05, **p<0.01, ***p<0.001 and ****p<0.0001.

In Figure 4.4, three bar plots display the intensity of the three characteristic peaks of glycogen in U87 cells under different conditions. Figure 4.4A shows the peak intensity at 480 cm^{-1}, Figure 4.4B presents the peak intensity at 850 cm^{-1}, and Figure 4.4C depicts the peak at 940-cm^{-1}. The six experimental groups correspond to U87 WT cells in normoxia (CN, blue), hypoxia (CH, red), γ irradiation treatment (CIR, green), PYGL KD cells with γ irradiation treatment (PIR, purple), and PYGL KD cells in normoxia (PN, orange) and hypoxia (PH, black), respectively.

In Figure 4.4A, the PYGL KD cells showed a stronger glycogen signal at the 480-cm^{-1} band compared to control cells, and this signal increased significantly in hypoxia compared to normoxia ($p < 0.01$). Glycogen levels were higher under hypoxia compared to normoxia in wide-type U87 cells, but the difference did not reach statistical significance. Cells irradiated with gamma rays did not show significant differences at the 480-cm^{-1} peak.

The 850-cm^{-1} band had the highest signal of the three bands and showed a similar pattern as the 480-cm^{-1} band. Similar to the data from the 480-cm^{-1} group, the PYGL KD cell showed the highest glycogen signal at 850 cm^{-1} compared to the controls. However, there was no significant difference

observed between hypoxia and normoxia (Figure 4.4B). Additionally, there was no significant difference in the intensity of the 850-cm^{-1} peak among the other four groups (Figure 4.4B).

For the 940-cm^{-1} band, both gamma-irradiated and PYGL-knockout cells had higher signals than their WT counterparts (Figure 4.4C, $p < 0.01$ and $p < 0.0001$ respectively). The 940-cm^{-1} peaks of control cells exhibited no significant changes under both normoxic and hypoxic conditions (Figure 4.4C).

Overall, the highest glycogen signal was observed in the PYGL KD U87 cells cultured under hypoxic conditions. Gamma-irradiated cells did not show a significant change in glycogen signal in any of the three bands, and PYGL gene knockout did not have a significant effect. In subsequent experiments, the irradiation was omitted.

Here, we further identified 480, 850 and 940 cm^{-1} as the three characteristic bands of glycogen by knocking out one of the genes to block the glycogen degradation in metabolic pathway. The highest 850 cm^{-1}-band suggests that glycogen granules in these cancer cells are predominantly synthesized to form linear chains, with α-D-(1 → 4) glycosidic linkages.

It can be seen that the PYGL mutant cells exhibit an exceptionally high glycogen level. Glycogen in PYGL KD cells has the high level of 480 and 940 cm^{-1} which implies that glycogen formed as a large number of both α-D-(1 → 4) and -(1 → 6) branched structures. Glycogen phosphorylase only acts on the

non-reducing end of α (1 → 4) glycosidic bonds to release G1P[208]. Expressed in the Raman spectrum, PYGL knockdown would affect the 480 and 850 peaks associated with the α (1 → 4) bonds. This is consistent with our results. The area of the 480 and 850 peaks was significantly higher in PYGL-inhibited cells than in wild-type U87 cells (Figure 4.4A and B). PYGL plays an important role in glycogen shunt and energy use in cancers. A study using a ^{13}C tracking assay showed that G6P/G1P produced by glycogenolysis was shunted to PPP which could be blocked by PYGL siRNA[209]. Several studies have showed that glycogen phosphorylase is able to promote metastatic phenotypes and participate in tumour growth[210–212]. In our data, PYGL mutant gives a great contribution to glycogen accumulation and it may be a promising target for cancer treatment in the future[213,214].

Hypoxia induces an increase in glycogenolysis. In particular, the 480 peak of PYGL knockout cells were significantly higher under hypoxia than under normoxic conditions (Figure 4.4A). However, there was no significant difference between normoxic and hypoxic conditions for the controls in Figure 4.4. PYGL knockdown caused massive aggregation of glycogen that far exceeded hypoxia-induced glycogenesis. Statistically, this resulted in the hypoxic group being unable to show a significant difference in the data.

In conclusion, SCRM is a powerful, state-of-the-art tool for tracking glycogen metabolism and its heterogeneous interaction in response to different microenvironment conditions in cancer cells.

4.3.3 ^{13}C-glucose isotope probing

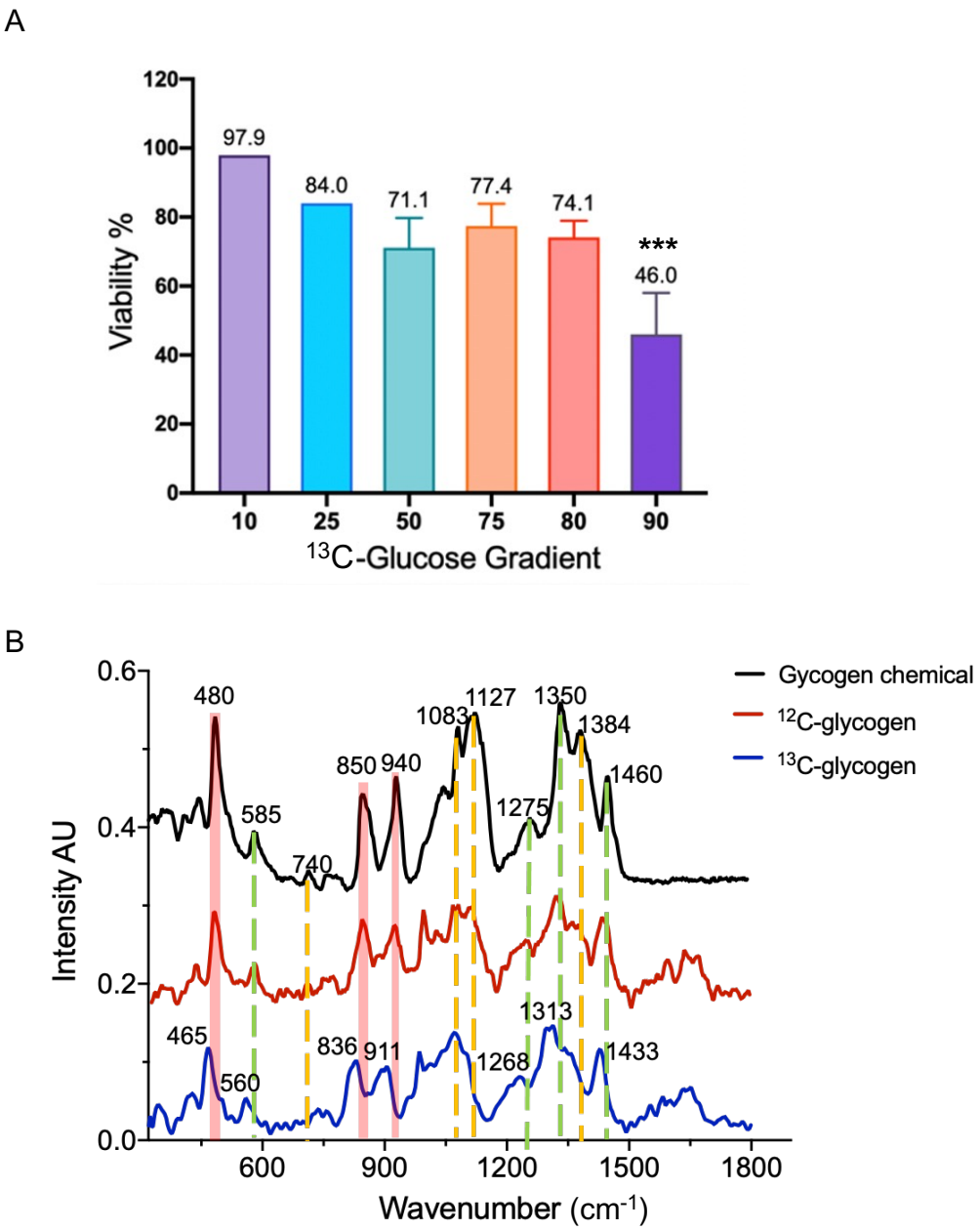


Figure 4.5 Effect of different gradients of ^{13}C-glucose medium on cellular activity and comparison of ^{12}C and ^{13}C-labelled glycogen peak positions. (A) Effects of different 13C-glucose gradients from 10% to 90% of the culture medium on the cell activity of U87. Test repeated at least three times. (B) Comparison of Raman profiles of standard glycogen chemical (black) and intracellular detection of ^{12}C (red) vs ^{13}C (blue) labelled glycogen. 6 cells were

measured for each group and approximately 300 spectra were measured in every individual cell.

Here, ^{13}C-glucose was used to track the turnover of glycogen in cancer cells. Different concentration ratios of ^{12}C and ^{13}C glucose-DMEM were added to culture U87 cells. The viability of the cells under different conditions is shown in Figure 4.5A. Our results indicate that U87 cancer cells tolerated up to 80% ^{13}C-glucose without significantly effect on cell growth (Figure 4.5A). However, when the concentration of ^{13}C glucose exceeded 75%, the cells became fragile, and most of them lysed and died. Therefore, we considered 75% ^{13}C glucose-DMEM as the optimal condition for stable isotope probing in cancer cells and was used as the experimental concentration.

U87 cells were incubated with a mixture of 25% ^{12}C glucose and 75% ^{13}C glucose-DMEM for 48 hours. The cells were then fixed for subsequent Raman measurements, and the resulting Raman spectrum is shown in Figure 4.5B. The top spectrum (black) represents the averaged Raman spectra of pure glycogen chemicals (Sigma-Aldrich Co., USA); the middle spectrum (red) shows the glycogen identified within a U87 cell cultured with ^{12}C-glucose; and bottom spectrum (blue) shows the glycogen within a U87 cells cultured with 75% ^{13}C-glucose.

The red glycogen band spectrum matches well with the standard glycogen Raman band spectrum. Notably, the spectrum of ^{13}C-labeled glycogen band has shifted significantly, which was consistent with the prediction of Raman–

SIP[88]. Specifically, the 480-cm^{-1} band has shifted to 465 cm^{-1}, the 850-cm^{-1} band to 836 cm^{-1}, and the 940-cm^{-1} band to 922 cm^{-1} (the band shifts are labelled in red).

In addition to this, a clear change in several other glycogen bands is also evident. The 585-cm^{-1} band has shifted to 560 cm^{-1}, the 1275-cm^{-1} to 1268 cm^{-1}, 1350-cm^{-1} to 1313 cm^{-1}, and 1460 cm^{-1} to 1433 cm^{-1} (labelled in green). In addition, several other bands that typically overlap with those of other biomolecules also shifted to lower wavenumbers, for example 740-cm^{-1}, 1083-cm^{-1}, 1127-cm^{-1} and 1384-cm^{-1} band (labelled in yellow).

This indicates that the original ^{12}C-glycogen has been replaced by newly synthesized ^{13}C-glycogen, which was detected in cancer cells within 48 hours. It suggests that stable isotope probing of ^{13}C-glucose is a feasible method to study the glycogen turnover of cancer cells. It shows that Raman–SIP is a useful method to reveal the chemical properties and structural modifications of glycogen due to the biological metabolism processes. Therefore, I designed a set of ^{13}C labelling experiments which are discussed in the following section.

4.3.4 Glycogen metabolic profiles in ^{12}C and ^{13}C-glucose medium

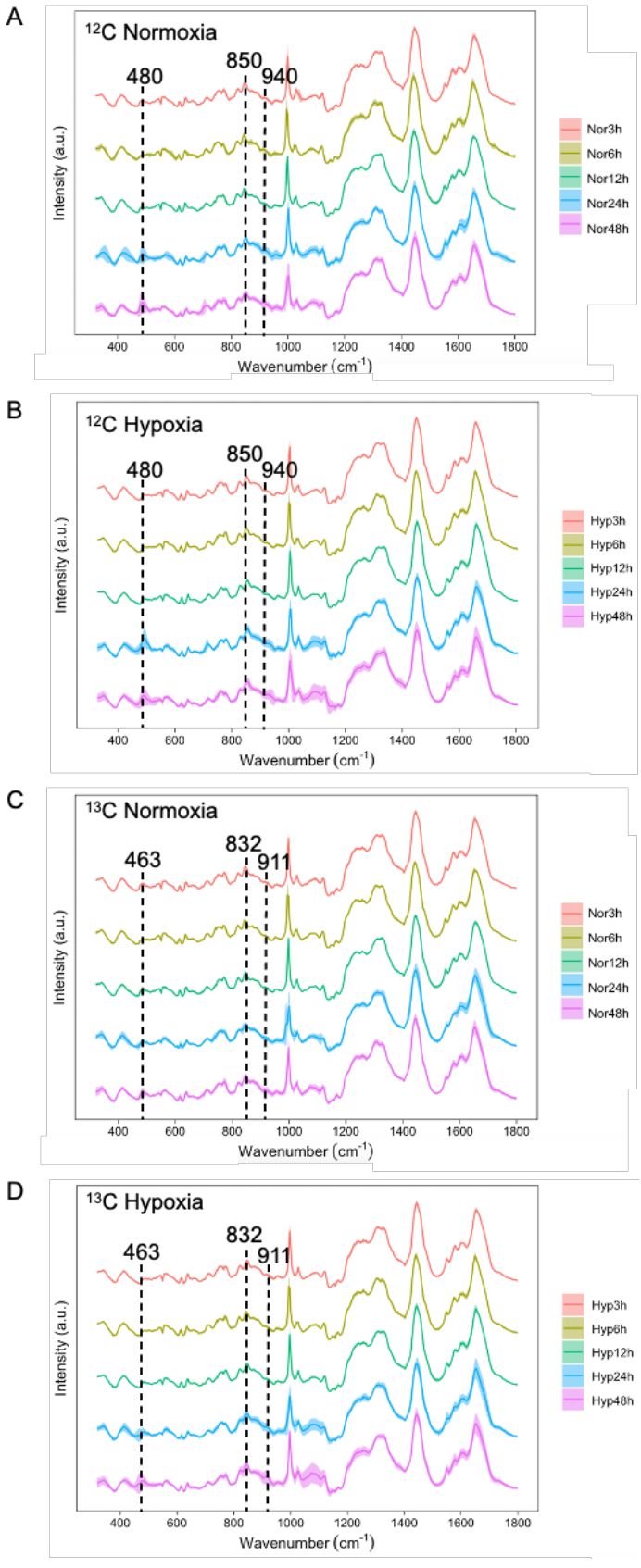
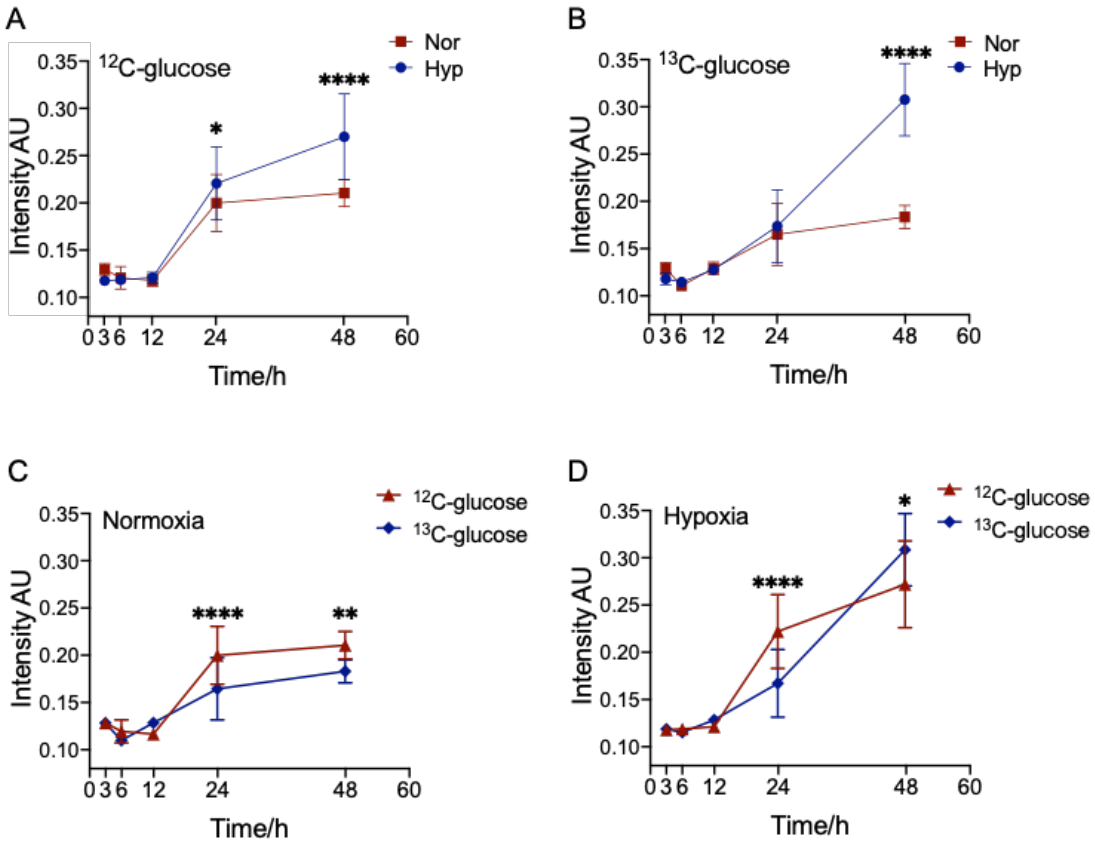


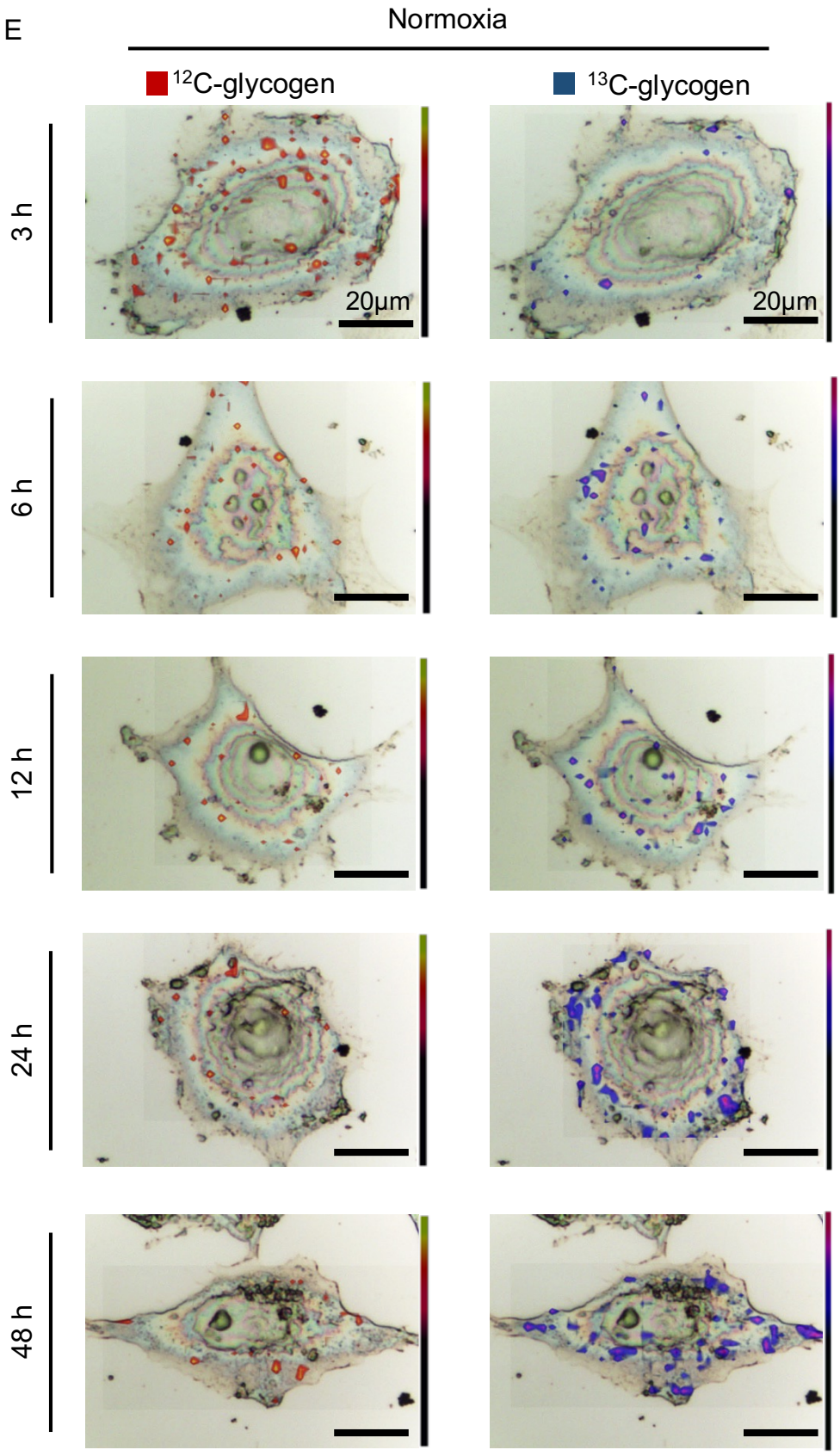
Figure 4.6 Raman profiles of ^{12}C and ^{13}C-glucose labelled U87 cells cultured in normoxia and hypoxia for 3, 6, 12, 24 and 48 hours. The averaged spectra of U87cells cultured with ^{12}C-glucose media under (A) normoxia and (B) hypoxia. The averaged spectra of U87cells cultured with 75% ^{13}C-glucose media under (C) normoxia and (D) hypoxia. 15-16 cells were measured for each time point. For each cell, around 300 spectra were measured.

To investigate the rapid synthesis and breakdown of glycogen in U87 cancer cells, a time course experiment using ^{13}C-glucose labelling was conducted. U87 cells were seeded directly onto poly-L-lysine modified slides and treated with gradients of 0% and 75% ^{13}C-glucose. Sampling time points were set at 3, 6, 12, 24 and 48 hours after growth under normoxia or hypoxia, respectively.

By comparing ^{12}C and ^{13}C-glucose experimental groups, clear shifts were detected in the glycogen band from 480 to 463 cm^{-1}, 850 to 832 cm^{-1}, and 940 to 911 cm^{-1} (Figure 4.6), which is consistent with the data from the previous section (Figure 4.5B).

In Figure 4.6, the signals for both 480 and 940-cm^{-1} band had low levels at the beginning and increased significantly after 24 hours, except for ^{13}C-480 cm^{-1} under normoxia. The intensity of the 850-cm^{-1} band in hypoxic conditions also increased, but not as pronounced as the other two bands. In the normoxic group, the 850-cm^{-1} band labelled by ^{12}C did not continue to increase at 48 hours, while the proportion of ^{13}C-850-cm^{-1} band decreased after 24 hours. At 48 hours, the intensity of the three glycogen bands was almost at the same level.


A
^{12}C-glucose
Nor
Hyp
Intensity AU
Time/h
B
^{13}C-glucose
C
Normoxia
^{12}C-glucose
^{13}C-glucose
D
Hypoxia


E
Normoxia
^{12}C-glycogen
^{13}C-glycogen
3 h
6 h
12 h
24 h
48 h
20μm
20μm

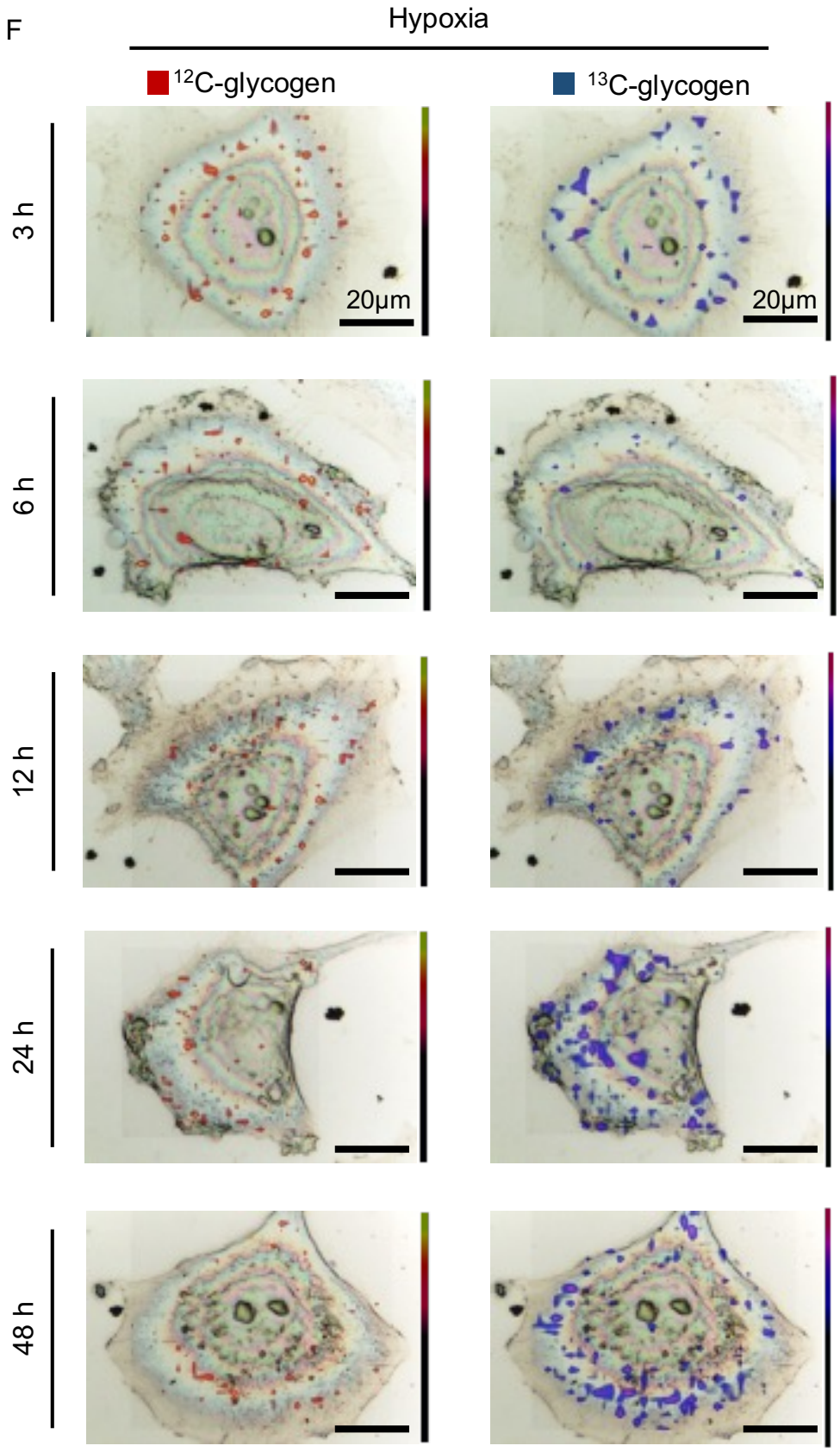


Figure 4.7 Comparation of Raman mapping and statistical analysis of glycogen labelled by ^{12}C and ^{13}C-glucose. (A) Band area comparisons of total glycogen

(three peaks together) cultured in ^{12}C-glucose media under normoxia and hypoxia. (B) Band area comparisons of total glycogen cultured in 75% ^{13}C-glucose media under normoxia and hypoxia. (C, D) Glycogen accumulation curves of ^{12}C and ^{13}C-labelled glycogen under normoxia (C) and hypoxia (D). (E, F) SCRM mapping images of ^{12}C and ^{13}C glycogen in normoxic (E) and hypoxic (F) conditions. 10-24 cells were measured for each time point. For each cell, approximately 300 spectra were measured. Data are presented as mean values ± S.D., two-way ANOVA test, *p<0.05, **p<0.01, ***p<0.001 and ****p<0.0001. Scale bar = 20 μm.

The effect of high (Nor) and low (Hyp) oxygen levels on glycogen production is present in Figure 4.7A and B. Figure 4.7A represents the ^{12}C-labelled glycogen, while Figure 4.7B represents the ^{13}C-labelled glycogen. The red curve indicates normoxia, and the blue curve indicates hypoxia. The X-axis represents time, with timepoints ranging from 3, 6, 12, 24 to 48 hours.

As shown in Figure 4.7A, when cancer cells were cultured in ^{12}C-glucose media, the amount of glycogen under normoxia or hypoxia was no different in the first 12 hours. At 24 hours, glycogen concentrations were higher under hypoxic conditions than under normoxic conditions ($p < 0.01$). By 48 hours, the gap had increased significantly ($p < 0.0001$). For ^{13}C-glucose incubation, low oxygen concentrations did not show an increase in glycogen production for 3 to 24 hours (Figure 4.7B). At 48 hours, the glycogen level under hypoxia became significantly higher compared to the normoxia group (Figure 4.7B, $p < 0.0001$).

Figure 4.7 C and D show a comparison of the glycogen content of ^{12}C and ^{13}C

labelling under normoxia (C) and hypoxia (D), respectively. The red curve represents ^{12}C-labelled glycogen, and the blue curve represents ^{13}C-labelled glycogen.

In Figure 4.7C and D, the amount of ^{12}C and ^{13}C glycogen remained stable for 3 to 12 hours, with no difference between new and old glycogen pellets. At 24 hours, the amount of ^{12}C glycogen was significantly higher than its ^{13}C counterpart under both normoxia and hypoxia ($p < 0.0001$). In normoxia, the gap narrowed rapidly but ^{13}C-glycogen remained slightly lower than ^{12}C-glycogen (Figure 4.7C, $p < 0.01$). In contrast, the ^{13}C-labelled glycogen rapidly boosted and exceeded ^{12}C-glycogen at 48 hours under hypoxia (Figure 4.7D, $p < 0.05$).

By overlaying microscopic and Raman images of the same cell, subcellular location, distribution, and concentrations of the glycogen were mapped and compared between the ^{12}C and ^{13}C groups, and between hypoxia and normoxia groups.

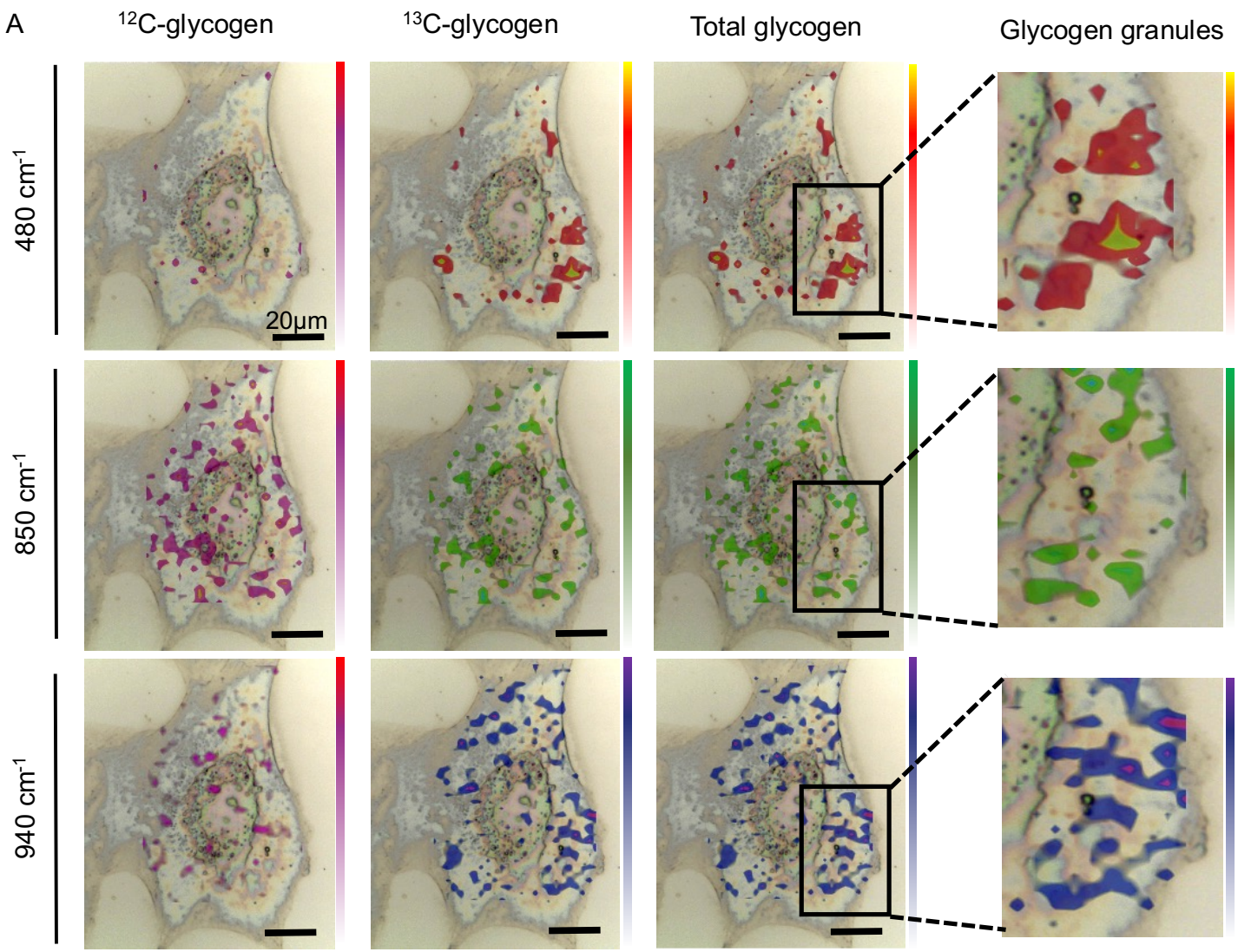
As shown in Figure 4.7E and F, the glycogen spots were found to be randomly distributed in cytoplasm with small sizes at 3-hours. Small glycogen spots were also observed in ^{13}C groups, indicating that glycogen synthesis can occur rapidly within a few hours. The distribution of glycogen in the cells was similar at 6 and 12 hours of incubation, and the dominant band of glycogen was 850-cm^{-1}. At 24 hours, the glycogen granules grew larger in size and cells hoarded

glycogen in both normoxia and hypoxia.

New glycogen granules continued to appear throughout the incubation period and were significantly larger after 24 hours. There is an intensity variation in the three glycogen biomarker bands as they represent different structural components of glycogen, and their ratio can reflect the molecular structure of the new glycogen pellets being synthesized.

Based on the above results, it is evident that the formation of large glycogen granules is most visible in the cells at 48 hours. In this study, U87 cells cultured for 48 hours under hypoxic conditions were used as an example to demonstrate the relationship between the structure of the granules of glycogen and the three characteristic Raman bands.

In Figure 4.8A, the three columns represent the visualization of glycogen distribution. The ^{12}C-glycogen is labelled in purple, while ^{13}C-glycogen is labelled in red, blue, and green corresponding to the bands at 480, 850 and 940 cm^{-1}, respectively. The last column displays a magnified view of the glycogen granules within the cell.


A
^{12}C-glycogen
^{13}C-glycogen
Total glycogen
Glycogen granules
480 cm^{-1}
850 cm^{-1}
940 cm^{-1}
20μm

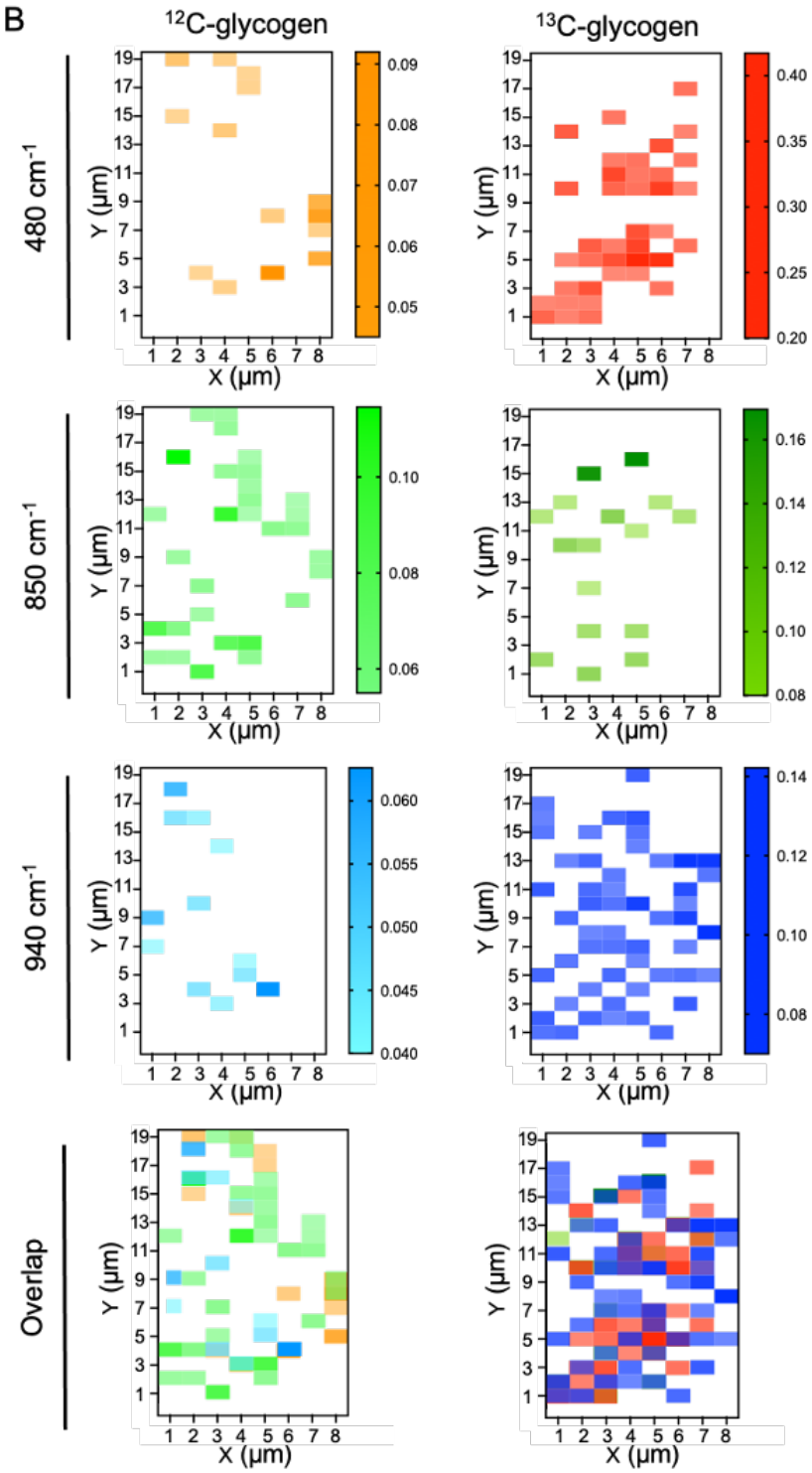


Figure 4.8 Intracellular distribution of the three characteristic bands of large glycogen granules at 48 hours timepoint. (A) SCRM Images of 480, 850 and 940 cm^{-1} band of ^{12}C and ^{13}C -glycogen after 48 hours of incubation under hypoxic condition. (B) The relationship between the locations of 480, 850 and 940 cm^{-1} bands of extra-large glycogen particles cultured in 75% ^{13}C-glucose

media. The location of the heat map corresponds to the black square in Figure 4.8A. The X and Y axes represent the distance to the position of each detection point. Scale bar = 20 μm.

In the Raman mapping of 850-cm^{-1} band, both ^{12}C and ^{13}C-glycogen displayed almost equivalent amounts (Figure 4.8A). This indicates that the previous 850-cm^{-1} band was not replaced by the new glycogen. New glycogen of 850-cm^{-1} was added to the original. In contrast, the majority of the 480 and 940-cm^{-1} glycogen bands were ^{13}C-labelled. This suggests that the freshly supplied glucose was used to synthesize new glycogen chains and branches, as indicated by the 480 and 940-cm^{-1} bands.

It can also be seen from the zoomed image that the 850 and 940 cm^{-1} bands were more loosely distributed and with smaller particles, whereas the clusters of the 480 cm^{-1} band were much larger and there was a significant overlap with both other bands.

To obtain a clear view of the relationship between the structure of the glycogen granules and the three Raman bands, the distribution of the corresponding positions in the black square was plotted, as shown in Figure 4.8B. The ^{12}C and ^{13}C-glycogen were divided into two columns, with the 480, 850 and 940-cm^{-1} glycogen bands in red, blue, and green respectively.

The new glycogen of 850-cm^{-1} band was found to overlap and extended mainly at the end of the old chain. The new 480-cm^{-1} band glycogen formed a large number of chains in the space around 850-cm^{-1} glycogen and was the main

component of the glycogen granules. The 940-cm^{-1} band of glycogen, on the other hand, mostly appeared at the ends, forming an encircling distribution.

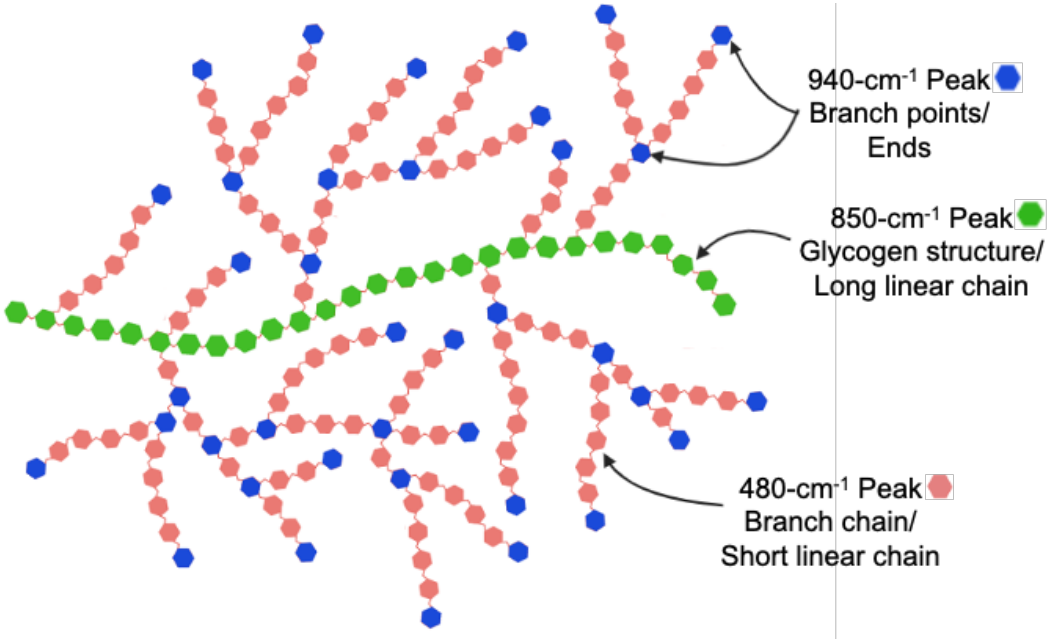


Figure 4.9 Schematic diagram of the relationship between the Raman characteristic band of glycogen and its structure.

Raman spectroscopy has shown that the characteristic bands of glycogen correspond with different molecular structures. Specifically, the 480-cm^{-1} band is associated with the branch chain of glycogen, the 850-cm^{-1} band with the long linear chains that make up the main structure of glycogen, and the 940-cm^{-1} band with the branch points and end points.

To illustrate the relationship between the Raman bands and the molecular structure of glycogen, Figure 4.9 shows a section of the glycogen structure in three colours representing different glucose units: red represents the 480-cm^{-1} band assigned to the branch chain, blue represents the 850-cm^{-1} band signed to the linear chain, and green represents the 940-cm^{-1} band corresponding to the branch point and end position.

As dispicted in Figure 4.9, in the middle is the long straight chain structure, also assigned as the chemical structure of 850 cm^{-1}. This structure forms the basic skeleton of glycogen granules. Extending from this skeleton are numerous branched chains, which are associated with the 480-cm^{-1} peak. At the ends of these branched chains, the branch points are placed around the glycogen skeleton, corresponding to the 940-cm^{-1} peak.

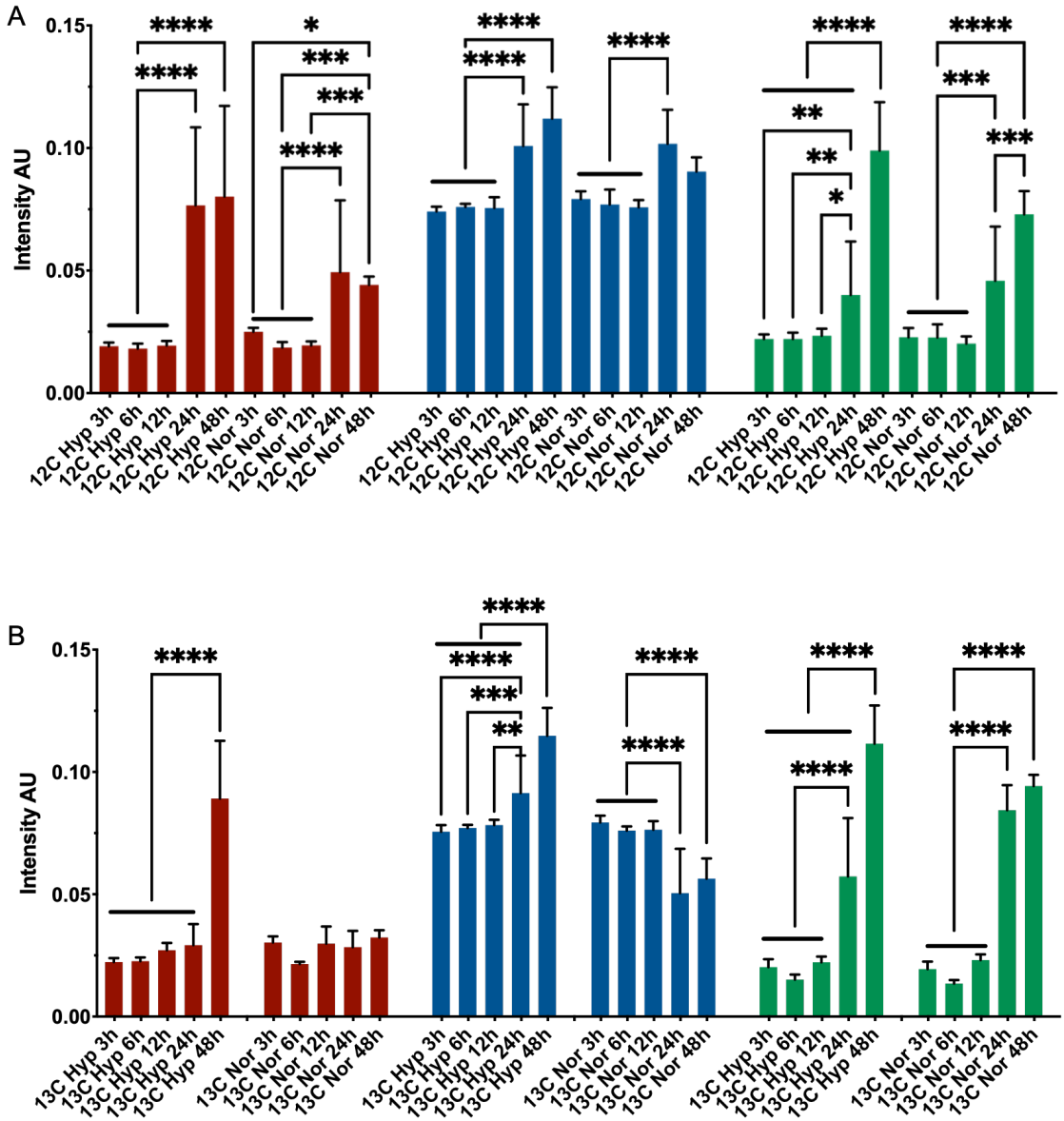


Figure 4.10 Band area comparisons of (A) ^{12}C glycogen and (B) ^{13}C glycogen

in U87 cells cultured for 3, 6, 12, 24 and 48 hours under normoxia and hypoxia. 10-24 cells were measured for each time point. For each cell, around 300 spectra were measured.

The results of the semi-quantitative analysis of the data in 4.7A are shown in Figure 4.10. In Figure 4.10, A represents the incubation condition for ^{12}C-glucose, and B represents the incubation condition for ^{13}C-glucose. The bar charts display the intensities of three glycogen peaks, with the 480 peak shown in red, 850 peak in blue and 940 peak in green.

In Figure 4.10, the dominant peak for the first 12 hours for both ^{12}C and ^{13}C glycogen is the 850 peaks. After 24 hours, there is a significant increase in signal for all three peaks, with the 480 and 940 peaks showing the most significant increase.

These results suggest that glycogen in cancer cells is dynamic and can become larger in size over time during glycogen synthesis. The structure of glycogen has been observed by electron microscopy and is divided into three types: α-, β- and γ-particles, from large to small size[215,216]. The β-particles consist of several γ-particles, with a diameter of 20-30 nm, which can be rapidly broken down to feed the cells with energy[217,218]. A large number of individual γ-particles make up an α-granule, with a diameter of 300 nm, and is a spare energy source for cancer cells[218].

The resolution of Raman microscopy limits what we can see in the glycogen mapping to basically an α-granule. Nanoscale resolution images can be

observed with electron microscopy, but most studies use muscle biopsy, and the distribution of glycogen cannot be fully visualised in the cell images. It is difficult to observe the position of glycogen in relation to other cellular components[219–221].

We have described the relationship between the structure of glycogen and the three Raman marker peaks. The large glycogen granules allow for the visualisation of three peaks in relation to the straight and branched chains of glycogen. Initially, linear chains are formed as 850-cm^{-1} bands, and when there is sufficient glucose, the new chain continues to extend at the end of the old straight chain (Figure 4.10A). After 24 hours, numerous branched chains begin to form around the straight chains of glycogen, as indicated by the 480-cm^{-1} band. At the same time, the branch point and end point of the branched chain are detected as the signal of the 940-cm^{-1} band (Figure 4.10B). The strong 480 and 940-cm^{-1} bands appear almost simultaneously and are the signature of large glycogen granules.

In Figure 4.8A, it can be seen that cells formed large glycogen granules after 48 hours of incubation. Large clusters of glycogen particles are common in individual cancer cells or staining tissue in glycogen metabolism studies[209,222]. Glycogen serves as storage energy source, and it is stored in the cell in large volumes instead of small quantities with small dimensions. Saving cell space may be one of the reasons for this. Glycogen forming a sphere-like three-dimensional structure is more volume-efficient than dispersed smaller

particles[223]. Our results shows that cells are initially full of small glycogen pellets in short culture time and mainly large granules after longer incubation (Figure 4.7E and F). Similar results have been observed using fluorescence microscopy, where small glycogen droplets can fuse with each other and form larger droplets over time[224].

4.3.5 Metabolic phenotyping of other bio-components with ^{13}C-glucose stable isotope probing

SCRM is very sensitive in detecting biomolecules such as carbohydrates[225], lipids[226], proteins[227] and nucleic acids[228]. In addition to glycogen, I have also labelled the Raman shifts of other biological components in the plots.

In Figure 4.11, the top black spectrum represents the averaged WT U87 cells without any band shifts (Ctrl). The middle set of five spectra represents the Raman profiles of U87 cells incubated with 75% ^{13}C-glucose media under normoxic conditions. The spectra correspond to U87 cells cultured for 3 hours (Nor 3h) shown in the first red curve, 12 hours (Nor 12h) shown in the second curve, 24 hours (Nor 24h) shown in the third curve, and 48 hours (Nor 48h) shown in the fifth dark purple curve.

The bottom set of five spectra represents the Raman profiles of U87 cells incubated with 75% ^{13}C-glucose media under hypoxia for different time durations. The spectra are indicated by Hyp 3h (pink), Hyp 6h (violet), Hyp 12h (indigo), Hyp 24h (green) and Hyp 48h (purple), respectively.

In Figure 4.11, no detectable band shifts are observed for other large biomolecules within a short period (up to 24 hours), except for Nor 48h and Hyp 48h. For DNA (780 cm^{-1}), lipids and proteins (1448, 1556 and 1657 cm^{-1}), apparent band shifts occurred after 24 hours (Nor 24h, Nor 48h, Hyp 24h and Hyp 48h). Small biomolecules, such as phenylalanine (620 and 1001 cm^{-1}) and tyrosine (642 cm^{-1}), started exhibiting bands at three hours. The shifts in the peaks positions can be seen in the spectra of all other groups when compared to the topmost control group.

There are two types of Raman band shift [229]. In the type I shift, the position of the peak labelled by the heavier atom remains unchanged, and only the intensity of the peak changes. The ratio of the shifted band intensity to the original band intensity increases with a higher content of stable isotope atoms. Glycogen (480, 850 and 940 cm^{-1}), DNA/RNA (780 cm^{-1}), cytochrome c (750 and 1128 cm^{-1}), tyrosine (642 cm^{-1}) and phenylalanine (620 and 1001 cm^{-1}) are type I shift, as shown in Figure 4.11. New bands are generated due to the labelling of stable isotope atoms, whilst the original Raman band remains. In the second shift pattern, the introduction of stable isotope atoms leads to bands gradually shifting towards lower wave numbers as the content of stable isotope atoms increases. In the type II shift, the higher content of stable isotope atoms, the lower wavenumber of the shifted band. Lipids and proteins (1448, 1556 and 1657 cm^{-1}) are type II shift (Figure 4.11).

This gives an idea of how glycogen metabolism relates to the metabolism of

other substances with the detection of ^{13}C incorporation. The differences in red-shift patterns are due to different biosynthetic pathways. Glucose first goes in large quantities to generate glycogen. Meanwhile, it can also be used to synthesize small amino acids. For them, ^{12}C and ^{13}C-glucose is an easy-to-use source and is rapidly involved into their building processes. However, it takes more than 24 hours before a signal can be detected for the large biomolecules. It shows that lipid/protein biosynthesis is slower, more complex, and has a more diverse range of isotopomers.

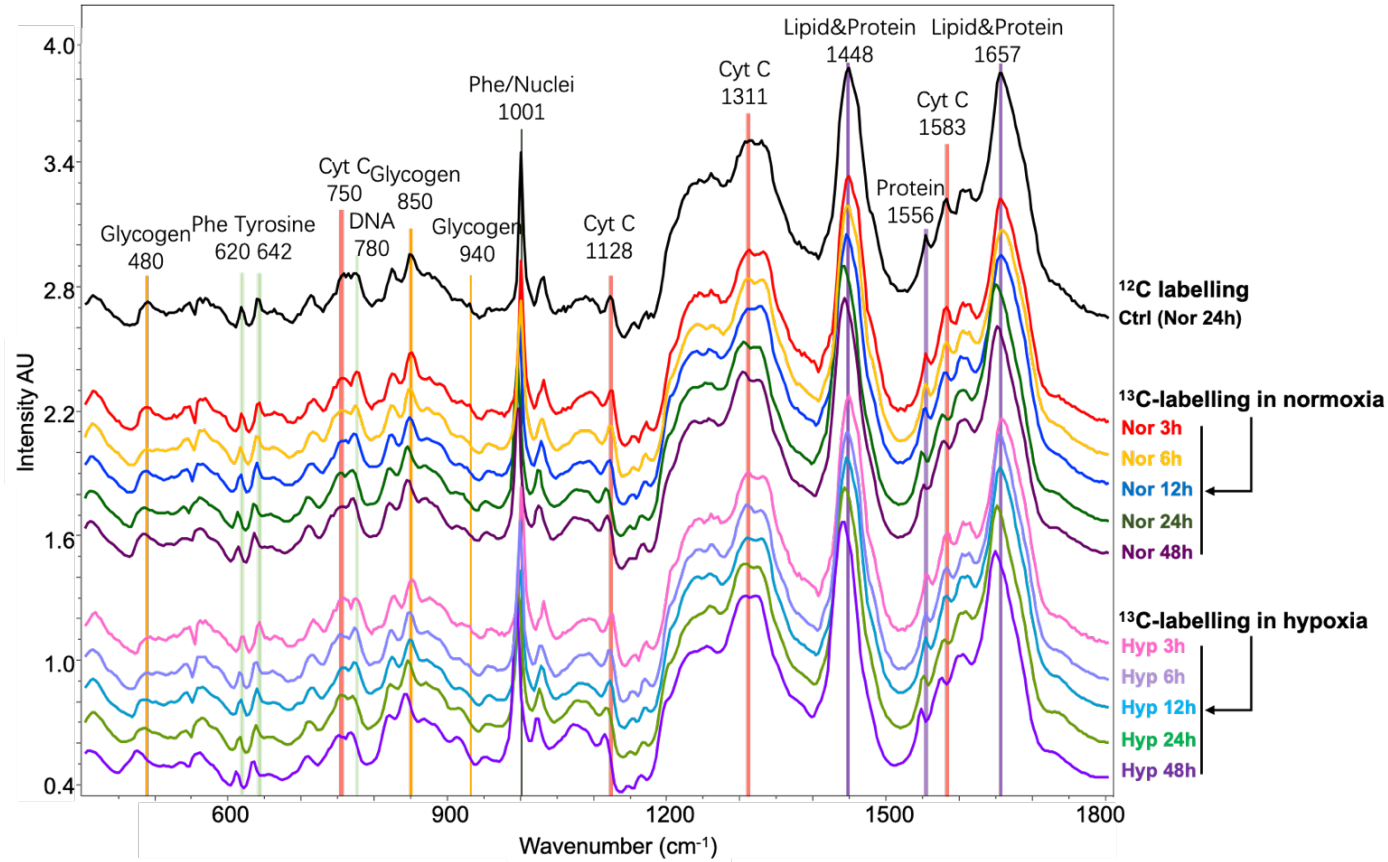


Figure 4.11 Comparison of Raman band shifts after different times of incubation with ^{12}C and ^{13}C-glucose. The top black curve is the Raman spectra of U87 cells after 24 hours of incubation in ^{12}C-glucose medium under normoxia. The middle set of five curves shows the Raman spectra of U87 after incubation in 75% ^{13}C-glucose medium under normoxia (Nor) for 3, 6, 12, 24 and 48 hours (from top to bottom). The third set of five curves shows the Raman spectra of U87 after incubation in 75% ^{13}C-glucose medium under hypoxia (Hyp) for 3, 6, 12, 24 and 48 hours (from top to bottom). Around 10-24 cells were measured for each time point, and approximately 300 spectra were measured for each cell.

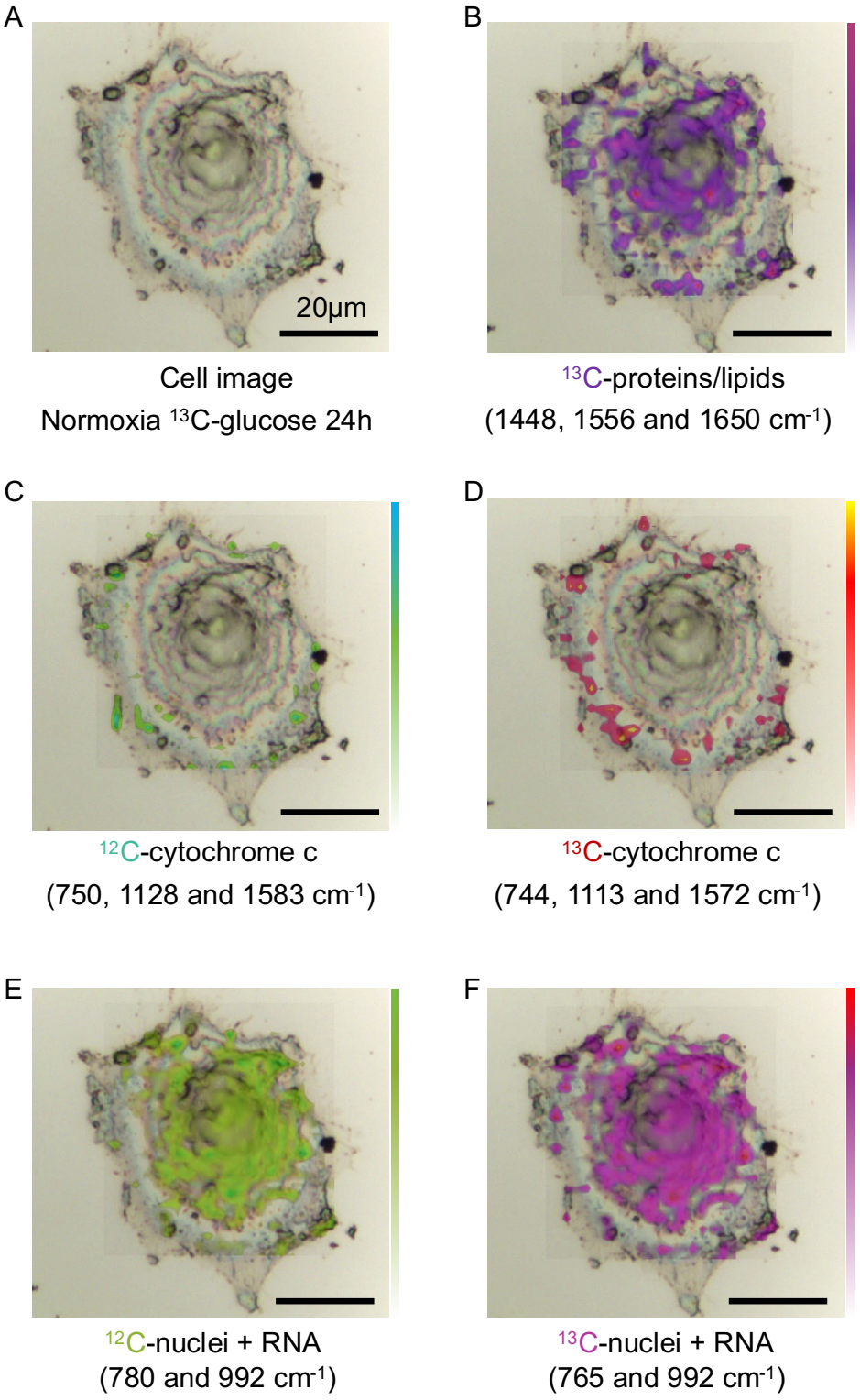


Figure 4.12 SCRM mapping images of the main biochemicals after 24 hours-^{13}C labelling. (A)The images of U87 cell incubated in 75% ^{13}C-glucose media

for 24 hours under normoxia. (B) The SCRM image of ^{13}C-lablled lipids and proteins. (C, D) The SCRM image of ^{12}C- (C) and ^{13}C- (D) cytochrome c. (E, F) SCRM mapping images of ^{12}C- (E) and ^{13}C- (F) nuclei and RNA. Scale bar = 20 μm.

I generated the distribution maps of lipids, cytochrome c and nuclei/RNA on U87 cells, as shown in the Figure 4.12. Figure 4.12A represents the original cell image, B is the ^{13}C-labelled lipids (purple), C and D are the ^{12}C and ^{13}C-cytochrome c respectively (dark green and red), and E and F show the distribution of ^{12}C and ^{13}C-labelled nuclei and RNA (bright green, pink).

The protein and lipid bands shifted progressively toward lower wavenumbers with increasing ^{13}C content. Thus, only one shifted position is shown in the Figure 4.12B, with Raman bands taken at 1448, 1559 and 1650 cm^{-1}. The majority of lipids surrounded the nucleus this is likely to be the nuclear envelope. The inner and outer membranes of the nuclear envelope consist of more than 60 different membrane proteins with complex roles and functions[230]. One study found that glycogen activities could be detected in co-purified nuclear envelope extracts from rat liver cells, although glycogen was not distributed in the nucleus on cell images[231].

There was more cytochrome c labelled by ^{13}C than in ^{12}C, suggesting that a new glucose source was used for cytochrome c synthesis. Both ^{12}C and ^{13}C were dispersed in the cytoplasm, and many of the sites overlapped with each

other (Figure 4.12C and D). In Raman images, the signal of cytochrome c is usually used to characterise mitochondria. The ^{13}C-containing signalling mitochondria suggest that they are involved in the metabolism of ^{13}C-glucose. Mitochondria play a role downstream in glycose metabolism. A small number of lipid droplets were randomly distributed in the cytoplasm, and they were near mitochondria (Figure 4.12B, C and D).

The distribution of ^{12}C and ^{13}C-labelled DNA in the cells was consistent with what was expected for the nuclear compartment (Figure 4.12E and F). This might suggest that the carbon source from ^{13}C-glucose is involved in DNA metabolism after 24 hours of incubation. Most of the ^{12}C and ^{13}C-RNA positions were also very close to each other, with much overlap occurring. Some new RNA could be found in the Figure 4.12F.

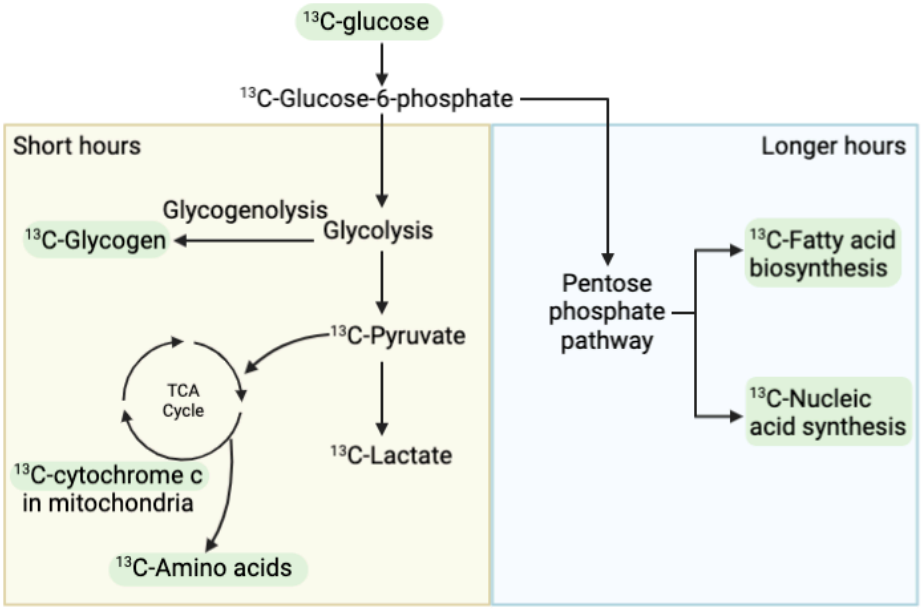


Figure 4.13 The tracing pathway of ^{13}C-glucose metabolic activity.

The ^{13}C-glucose metabolic profile is depicted in Figure 4.13. Glycogen synthesis is the primary metabolic pathway of glucose, and ^{13}C-labelled glycogen can be detected in human muscle cells by ^{13}C NMR within 2 hours[232,233]. However, we did not observe the two major glycolytic intermediates, pyruvate and lactate, in our data as their Raman bands overlapped with the other chemicals, resulting in no distinctive peaks. The insignificant shifts of metabolic intermediates in the TCA cycle are due to the fact that the majority of the carbons used in the metabolic cycle are derived from glutamine, with only the two carbons in citrate labelled from ^{13}C-glucose[234,235]. Although small amino acids exhibit ^{13}C-labelled band shifts after 3 hours, the movements were not pronounced (Figure 4.11). Researchers have used magnetic enhancement technique to measure [1-^{13}C] lactate metabolic signalling in ^{13}C-glucose cultured MCF7 and PC3 cells [236]. The pentose phosphate pathway plays a crucial role in meeting the needs of proliferating cells, producing new lipogenesis or generating ribose for nucleic acid synthesis. Although metabolic products of ^{13}C-glucose enter the PPP, the movements of lipids and nucleic acids are relatively minor and occurs after 24 hours (Figure 4.11). The ^{13}C flux through the PPP is considerably lower than that of glycolysis, as calculated from the ^{13}C-glucose fate[236,237].

4.3.6 Acute breakdown of glycogen in short-term glucose-free incubations

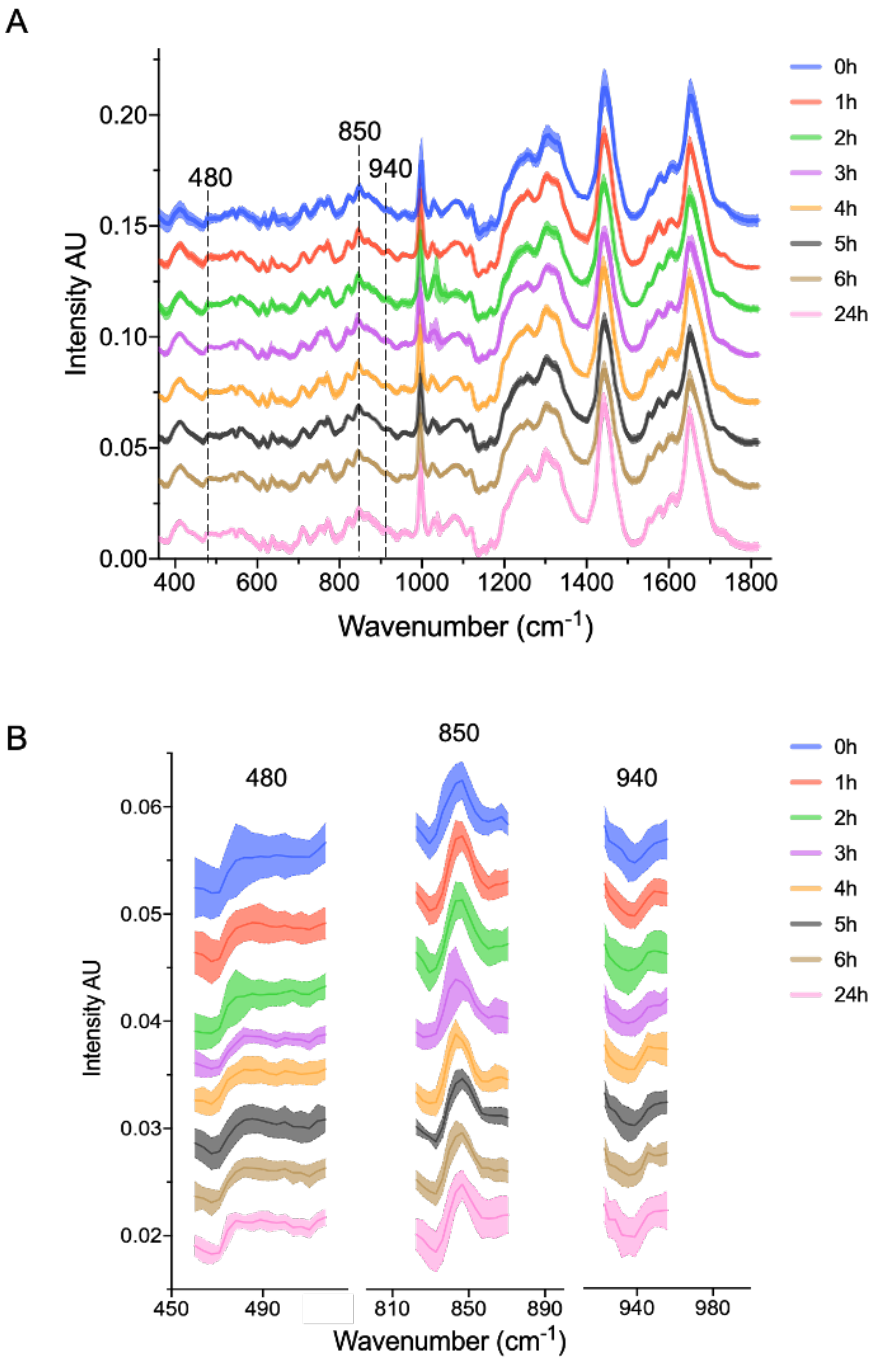


Figure 4.14 The averaged Raman spectra of U87 cell incubated in glucose-free media at different time points under normoxia. (A) The whole Raman

profiles of eight timepoints. (B) The averaged Raman spectra of glycogen at 480 (show the range from 460 to 520 cm^{-1}), 850 (show the range from 820 to 870 cm^{-1}) and 940 cm^{-1} (show the range from 920 to 960 cm^{-1}) obtained by zooming in from Figure 4.14A. 10 cells were measured for each time point. For each cell, around 300 spectra were measured.

I investigated glycogen degradation in cancer cells by culturing U87 cells in 10-mM glucose DMEM for 24 hours and then replacing the medium with glucose-free culture medium. Samples were fixed at 0, 1, 2, 3, 4, 5, 6 and 24 hours and then their fingerprint signals were detected by Raman spectroscopy.

As shown in Figure 4.14A, the averaged Raman spectra of U87 at 0, 1, 2, 3, 4, 5, 6 and 24 hours are listed in order from top to bottom. However, since the variation of the glycogen peaks was not clearly visible in the fingerprint region, we magnified the spectra of the three peaks as shown in Figure 4.14B. The 480-cm^{-1} peak was taken as the region from 460 to 520 m^{-1}, the 850 peak from the region 820 to 870 m^{-1}, and the 940 peak from the region 920 to 960 m^{-1}. The spectra are sorted from top to bottom according to the timepoints corresponding to Figure 4.14A.

Figure 4.14A shows the whole Raman spectra for the eight time points, and Figure 4.14B shows the three characteristic band bands of glycogen taken from Figure 4.14A. At 480 cm^{-1}, there were distinct bands in the spectra at 0,

1 and 2 hours. The signal of the 850-cm^{-1} band decreased with time. The band remained insignificant at 940 cm^{-1}, and no obvious difference could be observed.

Next, we semi-quantify the intensities of glycogen and glucose. The bands for glucose are 452, 842, 914 and 1074 cm^{-1}. The calculation results of the glycogen and glucose are illustrated in Figure 4.15A and B.

In Figure 4.15B, the change of three bands was not much significant. The intensity of 480-cm^{-1} band was highest at 0 and 1 hour and then decreased. The 850-cm^{-1} band increased during the first 2 hours and then decreased until it reached a minimum at 24 hours. The band intensity of 940 cm^{-1} remained very low level without significant difference.

The glucose shows the opposite result of glycogen. In the early stages, the concentration of glucose decreased but increased significantly at 24 hours. This is related to the breakdown of glycogen. It shows that 480 and 940-cm^{-1} bands as branched chains and end points are the first to be broken down (Figure 4.15). As the main structure, the glucose preferentially forms the straight chain of glycogen which is the 850-cm^{-1} band when the glucose source is not abundant. The high 850-cm^{-1} and the low 480 and 940-cm^{-1} bands are spectral feature of small glycogen particles.

Unfortunately, we did not see extra-large glycogen particles in this set of experimental data. I assume that it may be that there was no large glycogen formation in the cells tested, or more likely, that the large glycogen broke down into smaller glycogen pellets. In most of the cells, there was no significant difference in the level of glycogen concentration for the small glycogen spots.

If the glucose source is still severely lacking at this point, glycogen degradation will continue. The evidence is the start of degradation of the straight chains, which is reflected in the weakening of the 850-cm^{-1} band on the Raman spectrum (Figure 4.14). Meanwhile, an increase of glucose in the cancer cells can be detected. At this point, the cancer cells have to break down the glycogen into glucose to supply them with energy.

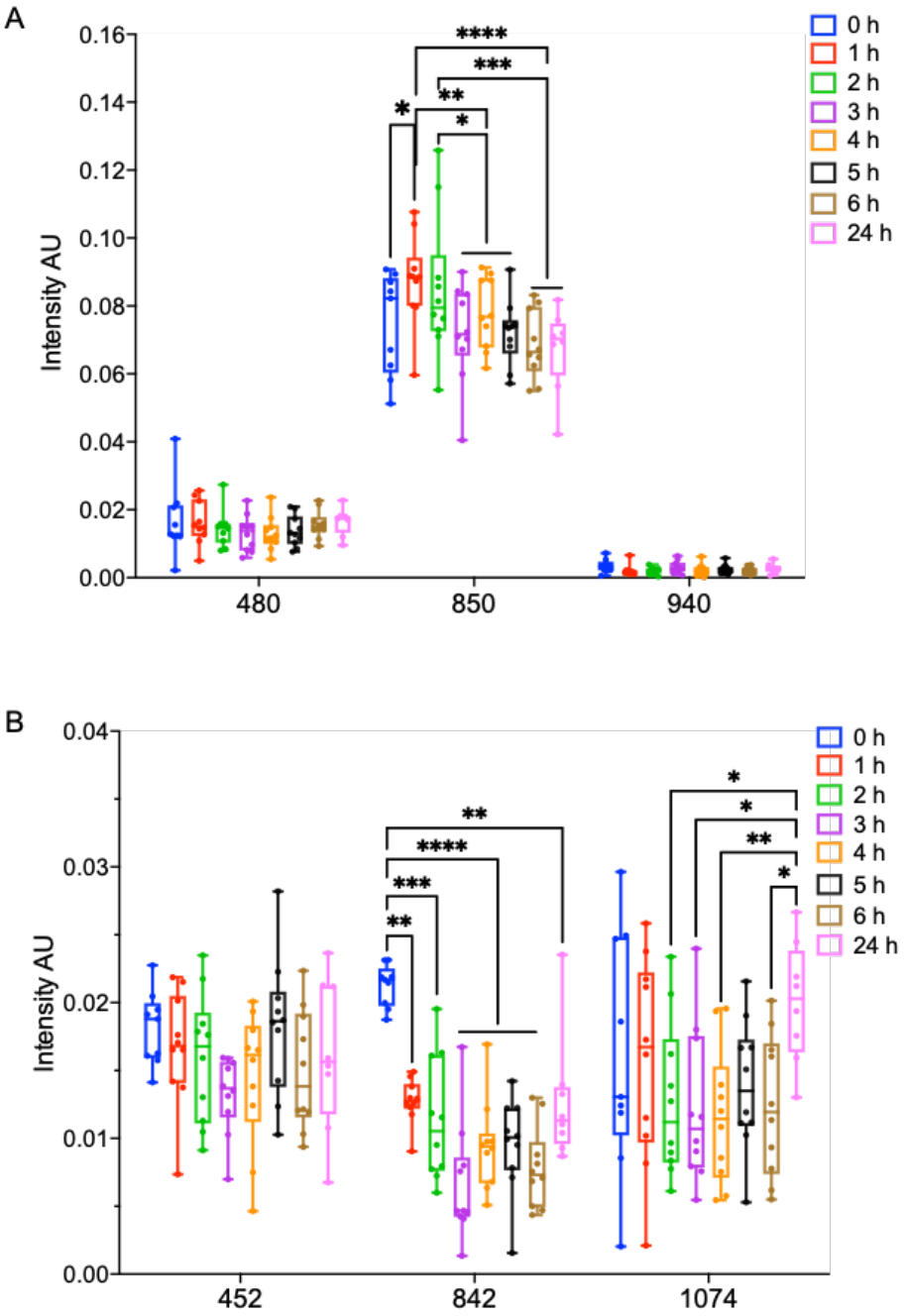


Figure 4.15 Metabolic analysis of the rapid degradation of glycogen in the short term (data from Figure 4.14). (A) Comparison of the band areas between the three bands of glycogen at different time points. (B) Comparison of band areas of glucose in U87 cells in the absence of glucose at different time points. 10 cells were measured for each time point. For each cell, around

300 spectra were measured. 10 cells were measured for each time point. For each cell, around 300 spectra were measured. Data are presented as mean values ± S.D., two-way ANOVA test, *p<0.05, **p<0.01, ***p<0.001 and ****p<0.0001.

4.4 Conclusions

Using single-cell Raman spectroscopy, it is possible to identify the characteristic bands of glycogen at 480, 850 and 940 cm^{-1}, as well as the location of sub-cellular glycogen spots with high resolution. Raman–SIP experiments show that glycogen has been labelled and replaced by the supplement of ^{13}C-glucose. The 480-cm^{-1} band shifted to 465 cm^{-1}, the 850-cm^{-1} band shifted to 836 cm^{-1}, and the 940-cm^{-1} band shifted to 922 cm^{-1}. The mapping images demonstrates the distribution of glycogen spots under single-cell level.

Glycogen marker band assignments are related to its structure. The 480-cm^{-1} band represents the linear branched chain, 850-cm^{-1} band is the skeletal structure, and 940-cm^{-1} band is the branch points and end points of glycogen. The high expression at 850 cm^{-1} is for small glycogen granules. The enlargement of glycogen increases branched chains, resulting in simultaneous high signals of 480 and 940-cm^{-1} bands. Glycogen degrades the branched chains first, as shown by the reduced intensity of the 480 and 940 -cm^{-1} bands.

Glucose is preferentially synthesized into glycogen when it enters cancer cells. If sufficient glucose is continuously supplied for more than 24 hours, glycogen is abundantly stored and forms large glycogen granules. New lipids and proteins take longer to build up and may contain more complex isomers.

Single-cell Raman spectroscopy is a powerful tool for revealing the metabolism of glycogen in cancer cells. In combination with isotope probing, it is possible to explore the timing, location, and association with other biocomponents of glycogen metabolism. We propose that this might provide insight into how glycogen metabolism enters glycolysis and contribute to the future of cancer therapy.

Chapter 5

Phenotypic alterations in the metabolism of cancer cells labelled with ^{13}C-glutamine and deuterium isotope probing

Contents

5.1 Introduction

5.2 Materials and Methods

5.3 Results and Discussion

5.3.1 Validation of ^{13}C-glutamine labelling in cancer cells

5.3.2 Changes in Raman band shifts of cancer cells after ^{13}C-glutamine labelling

5.3.3 Intracellular metabolic activities revealed by SCRM–DIP and ^{13}C-isotope probing

5.4 Conclusions

In the previous chapter, I labelled glycogen using ^{13}C-glucose probing to investigate the biological metabolism of glycogen synthesis and breakdown. However, cancer cells require two main carbon sources-glucose and glutamine (Figure 2.3 illustrates the carbon footprint of glutamine). Therefore,

in this chapter, SCRM–SIP was applied to study the impact of glutamine on glycogen metabolism. I used two isotope probing, ^{13}C-glutamine, and deuterium from heavy water, to probe U87 and SUM159 cells, revealing the destination of ^{13}C in glutamine and their spatial distribution within the single cells.

5.1 Introduction

Cancer cells have a special reprogrammed metabolism to meet their energy demands, and the programming of energy metabolism has been added to the list of next-generation hallmarks of cancer by Hanahan and Weinberg [238]. Glucose, as a major energy supplier, has been a focus of cancer research for over a century[2,165]. In contrast, glutamine has received less attention and has been on the fringes of cancer research for a long time. However, recent years have brought new insights into the metabolism of glutamine in cancer cells[239].

Glutamine is initially considered a nonessential (dispensable) amino acid because it can be rapidly synthesized in all tissues in 1938[43,44]. With the recent appreciation of the importance of glutamine, glutamine is now referred to as a “conditionally essential” amino acid[49,50]. Cancer cells exhibit glutamine addiction, a glutamine-dependent increase in feeding the tricarboxylic acid cycle (TCA cycle or Krebs cycle) [240]. Glutamine serves four

main functions: 1) nitrogen transport; 2) regulation of the cellular redox state; 3) acting as a metabolic intermediate; and 4) serving as an energy source[50,241]. In rapid proliferation, cancer cells take up most of the available glutamine to build proteins and nucleotides[242].

Glutamine is transported into the cell via a number of transporters, the best known being SLC1A5[243]. It can be exported extracellularly via antiporters in exchange for other amino acids[244]. Glutamine is converted to glutamate by glutaminase, and then glutamate is converted to α-ketoglutarate (α-KG) by either glutamate dehydrogenase or by non-ammonia-producing aminotransferases[245]. The aminotransferases are the key enzymes for the transfer of nitrogen from glutamate[246]. α-KG enters the TCA cycle to provide energy to cancer cells. As an alternative, α-KG is able to go backwards through the TCA cycle to generate citric acid, which is necessary for the acetyl-CoA and lipid synthesis[247]. This is the pathway of glutamine metabolism, which is called reductive carboxylation[54]. TCA cycle intermediates can either yield pyruvate and NADPH or be converted to aspartate to facilitate nucleotide synthesis[56,234].

As the key energy source for cancer cells, glutamine is the main mechanism for transporting nitrogen into the cell, and glucose is the main carbon source contributor via anaerobic glycolysis[248]. But at the same time, glutamine acts

as an additional carbon source apart from glucose in cancers[249]. The metabolic processes in cancer cells are complex, and both glucose and glutamine serve as cellular biomass building blocks[250]. It has been argued that glutamine contributes its carbon backbone particularly under conditions of carbon transfer to the glycolytic pathways[249,251,252].

We showed that the glycogen in cancer cells is built from extracellular uptake of glucose. However, there is no clear evidence to prove whether the carbon in glutamine enters the carbon cycle of glycogen metabolism as demonstrated in chapter 4. To distinguish the carbon source in glycogen, we used ^{13}C-glutamine and deuterium double isotope labelling method. Cancer cells were incubated in ^{13}C fully labelled glutamine and 35% heavy water for 24 and 48 hours, followed by Raman measurement of single cells.

The results indicate that all glycogen in cancer cells is derived from glucose. The carbon in glutamine is not involved in the carbon cycle of glycogen and glucose metabolism. This ensures the accuracy and reliability of our previous data on glycogen metabolism. In addition, we found that glutamine is metabolized rapidly in cells. Glutamine plays a key role in the synthesis of amino acids, lipids, proteins, and nucleic acids in cells. However, it is challenging for Raman to distinguish an effective signal for glutamine at the single cell level. We propose to refine the metabolic reprogramming process

of glutamine in conjunction with other analytical approaches.

5.2 Materials and methods

Cell culture. The 10-mM Dulbecco's modified Eagle medium (DMEM, Gibco, USA) supplemented with 10% fetal bovine serum (Gibco, USA) was used to culture the human U87 and SUM159 cell lines. All cells were grown in a water-saturated incubator with 5% CO_2 at 37°C. Cell lines were obtained from American Type Culture Collection (ATCC).

Sample preparation. Cells were seeded on the poly-L-lysine pre-treated Raman slides overnight. The previous medium was quickly changed to the required media and samples were incubated continuously for 24 or 48 hours. Samples were washed with cold phosphate buffered saline (PBS, Life Technologies, UK) at the appropriate culture time points, and then they were instantly fixed with 4% paraformaldehyde (PFA, ThermoFisher Scientific, USA) at room temperature.

Raman–fluorescence *in situ* hybridization (FISH)[117]**.** The cell suspension was diluted to a concentration of 5000 cells/mL seeded on the 6-well plate (Corning, USA). U87 cells were incubated for 24 hours in media with 0%, 70%, 80% and 100% ^{13}C-glutamine. Cells were washed with PBS and stained with neutral red stain (Sigma, USA). Samples were fixed by 4% PFA for at least one hour. All autofluorescence images were acquired using a

LabRAM UV light source (Horiba, Japan) with an epifluorescence microscope (Olympus, Japan). FITC and CY3 filter blocks were applied, and the exposure time was 30 s. The Raman parameter settings were kept constant during the fluorescence image acquisition.

Cell viability. Two standard cell viability methods were examined in this chapter. The first was trypan blue assay. LUNA-IITM automatic cell counter evaluated total cell counts and viability using trypan blue exclusion (Logos Biosystems, South Korea). The second was resazurin assay. Media was replaced with 200µL / well of resazurin blue dye (Invitrogen, USA) for one hour incubation continuously protected from light. A multi-mode microplate reader (BMG Labtech, Germany) was employed to expose samples to an excitation wavelength of 560 nm and a tracking emission wavelength of 590 nm.

Heavy water time-course metabolic activity. 99% Heavy water (D_2O) (Sigma, USA) was diluted to 35% with glutamine-free DMEM. U87 and SUM159 were seeded in the poly-L-lysine pre-treated Raman slides at $1x10^5$ cells per well in complete DMEM and then were incubated at 37 ℃ with 5% CO_2. Once cell confluence was 70%, the medium was replaced with required DMEM feeding for 24 and 48 hours. The samples were washed and then immersed in 500 µL cold 4% PFA for fixation. Samples were stored at 4 ℃

until Raman measurement.

Spontaneous Raman spectra. The specific experimental method is as described in Chapters 3 and 4. A confocal Raman microscope (LabRAM HR Evolution, Horiba Scientific, UK) with an integrated microscope (BX41, Olympus) was used to acquire spontaneous Raman spectra. Samples were excited using a 532 nm neodymium-yttrium aluminium garnet laser. A 1-μm diameter spot on cells was utilised to gather the Raman spectra via a 50-objective lens (numerical aperture 0.5, spatial resolution~2 μm). The parameters were: 3-s acquisition time, 4.5-mW laser power exposure, 300 grooves/mm diffraction grating and 25% filter. The grating setting used for ^{12}C and ^{13}C-glutamine substance was 600 grooves/mm.

Raman spectral data processing and analysis. For baseline correction and calibration, the Raman spectra were analysed using the LabSpec 6 software (HORIBA, LabSpec6, UK). Data analysis and visualization were carried out using MATLAB 2019b (MathWorks, USA), GraphPad Prism 9.0.2 (GraphPad, USA), and R (3.5.1, USA). Every experiment was repeated at least three additional biological replicas. The mean and standard deviation are used to represent numerical data values (SD).

5.3 Results and discussion

5.3.1 Validation of ^{13}C-glutamine labelling in cancer cells

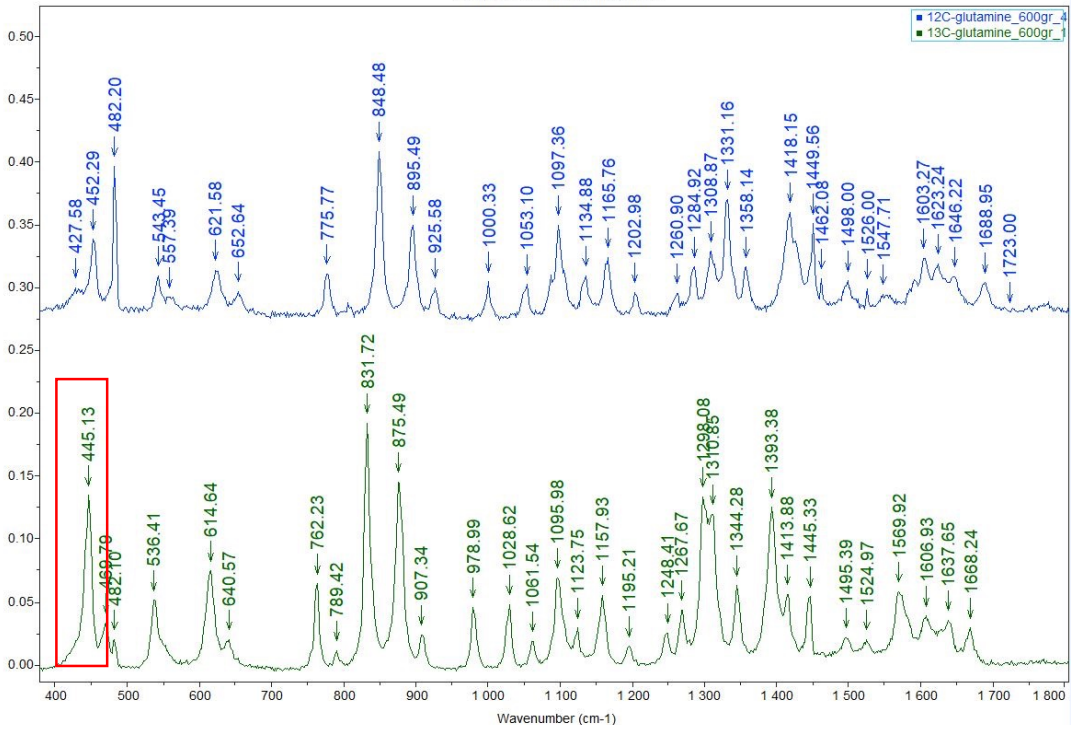


Figure 5.1 Raman spectra of glutamine and ^{13}C-lablled glutamine. ^{12}C-glutamine is the blue curve and ^{13}C-glutamine is the green curve.

Firstly, we tested pure ^{12}C- and ^{13}C- glutamine and the Raman spectra are shown in Figure 5.1. Neither the ^{12}C nor the ^{13}C glutamine had a particularly sharp, characteristic, and easily distinguishable feature band. The major bands of ^{12}C-glutamine are: 452, 482, 848, 895, 1097, 1331, 1418 and 1496 cm^{-1}. Of these, the peaks at 452, 482, 848, 895 and 1331 cm-1 are associated with C–related bonds, bending of the skeleton, C–C bending, stretch of C–H, and C–O bending, respectively[253]. It is noticeable that the

positions of these peaks are shifted by the replacement of carbon by ^{13}C (Figure 5.1). There were some peaks whose positions had not changed, including 1097, 1418 and 1496 cm^{-1}. Their structure is not related to carbon, but rather to the $–NH_2$ or $–NH_3$ functional groups[253].

Many of the bonds are in the protein and lipid region and are difficult to distinguish from these large biomasses. 445 cm^{-1} is the only peak with a relatively strong signal, while no other substrate signals overlap.

Based on our previous experience with ^{13}C fully labelled glucose, it may have a certain degree of cytotoxicity. Hence, I first conducted 24-hour labelling experiments in U87 containing 60%, 70%, 75%, 80%, 90% and 100% of ^{13}C-glutamine. SUM159 was the complementary cell line and treated with 60%, 80% and 100% ^{13}C-glutamine media.

Figure 5.2A and B present the Raman average spectrum of the ^{13}C-glutamine labelling experiment for U87 and SUM159 separately. Interestingly, the peak at 445 cm^{-1}, the characteristic ^{13}C-glutamine peak, could be detected in U87 cells under 80% and 90% of ^{13}C-glutamine incubation (Figure 5.2A). However, in the other experimental groups, we did not see a strong signal for this band.

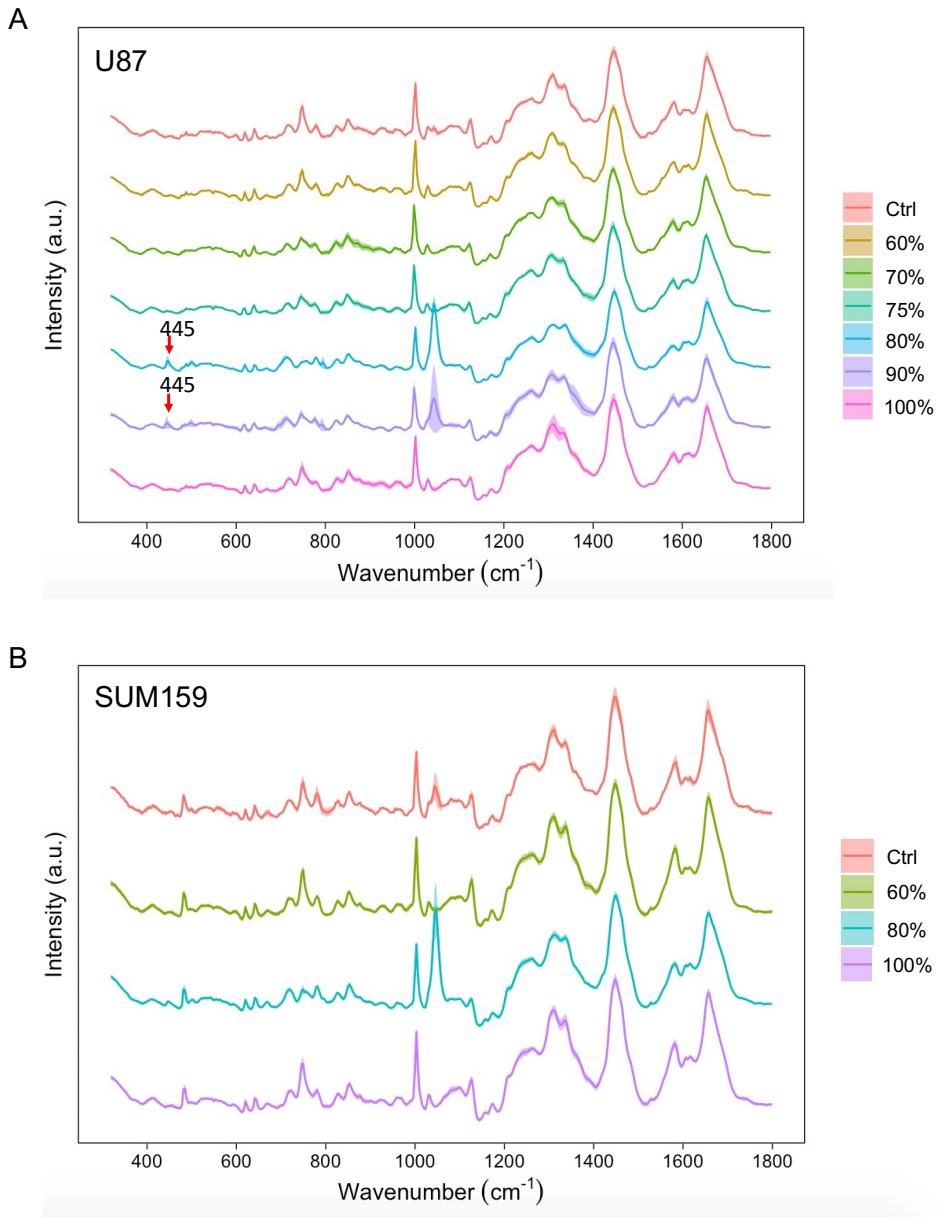


Figure 5.2 The averaged Raman spectra of (A) U87 and (B) SUM159 cultured at different gradients of ^{13}C-glutamine for 24 hours. 7 cells were measured for each group, and around 200 spectra were measured for each cell.

Glutamine enters the cell and is quickly utilised by the cancer cell in metabolic synthesis processes in periods of rapid growth[254]. Therefore, the glutamine

is degraded in metabolism, and no longer maintaining its original chemical structure. This explains why Raman spectra of the cancer cells did not show the same original glutamine bands as those in the pure chemical.

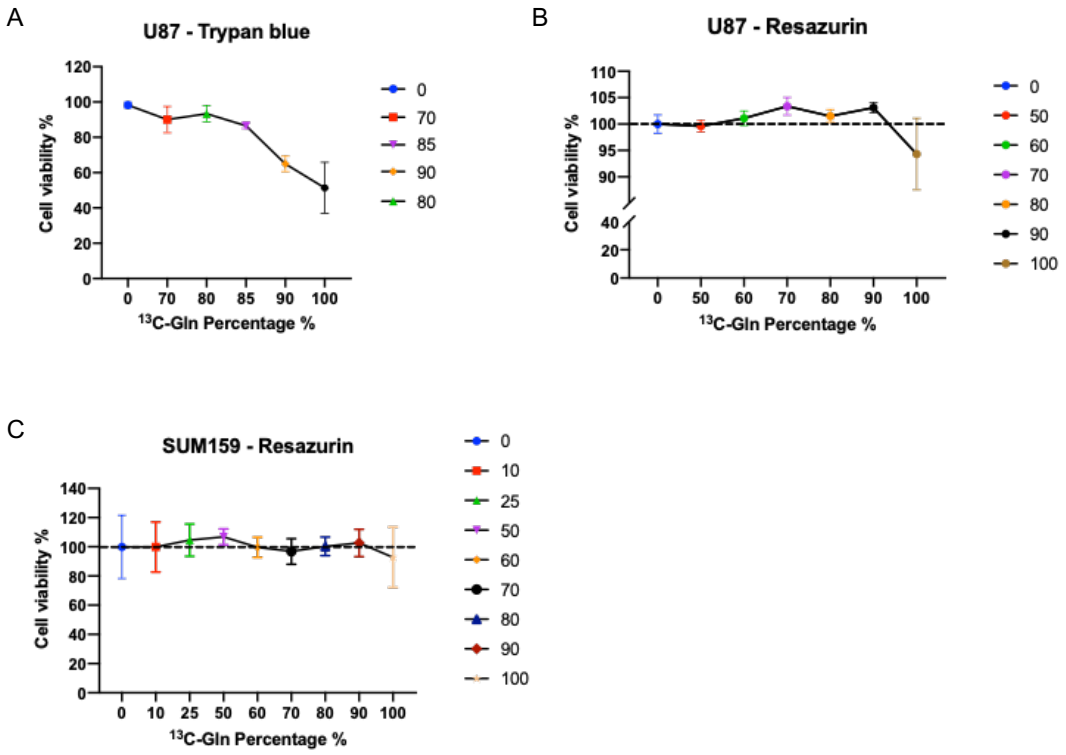


Figure 5.3 Cell activity under different rates of ^{13}C-glutamine incubation. (A) Cell activity of U87 using the trypan blue staining method. (B, C) Cell activity of (B) U87 and (C) SUM159 using the resazurin assay. Data are presented as mean values ± S.D., n = at least 20 cells, repeated 3 times, one-way ANOVA test, *p<0.05 and ****p<0.0001.

Glutamate enters the Krebs cycle and undergoes metabolic processes to produce CO_2[65]. This CO_2 is then hydrolysed by carbonic anhydrases to produce HCO_3^-. However, the specific reason for the observed increase in intracellular bicarbonate in 80% ^{13}C-glutamine groups remains unclear.

I conducted two methods to test cell viability. Trypan blue staining demonstrated that using more than 85% concentration of ^{13}C-glutamine caused massive cell death in U87 cells (Figure 5.3A). The resazurin results showed no significant difference in the biological activity of surviving U87 cells 24 hours after ^{13}C-glutamine labelling (Figure 5.3B). SUM159 had better cellular bioactivity than U87, as ^{13}C-glutamine did not affect its cytotoxicity much and SUM159 cells grew normally under 100% ^{13}C-glutamine culture (Figure 5.3C).

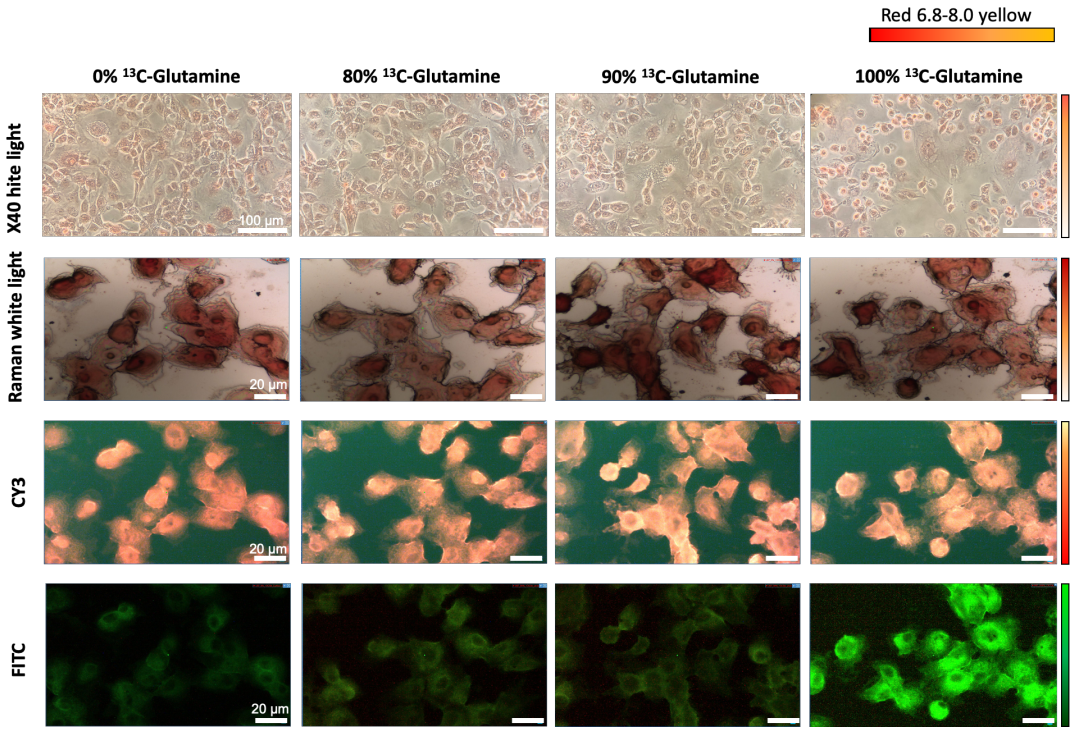


Figure 5.4 Raman fluorescence imaging of U87 cells stained with neutral red. U87 cells were incubated in media containing 0%, 80%, 90% and 100% concentrations of ^{13}C-glutamine for 24 hours before being stained with neutral red. The stained cells were then observed under optical microscope

and Raman microscope, with fluorescence images captured using CY3 and FITC channels, respectively.

Afterwards, I performed neutral red staining of U87 for 24-hour incubation with 80%, 90% and 100% ^{13}C-glutamine. Neutral red is a common stain that stains live cells red and acts as a light-up fluorescent probe[255].

Figure 5.4 illustrates images of U87 cells, after incubation at 0%, 80%, 90% and 100% ^{13}C-glutamine. The first row shows the cells observed under a 40-x microscope after being stained with neutral red. The second row is composed of images of cells captured under Raman microscopy with white light illumination. The third and fourth rows show are the corresponding images of cells under CY3 and FITC channels, respectively.

The number of U87 cells in 100% ^{13}C-glutamine culture was reduced. Cells labelled with ^{13}C exhibited slightly higher fluorescence background under the CY3 compared to the control. It is worth noting that the cells showed a strong FTIC fluorescence signal under the 100% ^{13}C-glutamine condition.

The peak wavelengths of absorption and emission of FTIC are 495 nm and 519 nm, which is a green colour [256]. The CY3 has its absorption and emission peak wavelengths of 554 nm and 560 nm, giving a red colour[257]. The fluorescence of neutral red is enhanced by a lowering of intracellular pH (pHi). The strong signal of the FTIC channel means that the absorption peak of

neutral red is located at about 500 nm. The corresponding pH range at this point is approximately 6.0-6.5[258]. The mechanism by which high concentrations of ^{13}C-glutamine lead to cell acidification is not yet fully understood. Furthermore, during the early stages of apoptosis, both mitochondrial-matrix pH and cytosolic pH decrease[259], which makes it challenging for Raman spectroscopy to differentiate the pH change caused by each factor. Additionally, neutral red may not be an optimal indicator for intracellular pH measurement in SCRM. It may be worthwhile to consider alternative pH-sensitive indicators like pH-GFP$_{mito}$ or ECFP$_{mito}$ for future work.

5.3.2 Changes in Raman band shifts of cancer cells after ^{13}C-glutamine labelling

In Figure 5.2, the characteristic Raman bands of glutamine were not observed, and no obvious Raman band shifts from ^{13}C were detected. I therefore separated the Raman spectra of ^{13}C-glutamine-labelled cells by the four main components, glycogen, mitochondria, nucleus, and cytoplasm, and then averaged the spectra as shown in Figure 5.5. In all plots, the ^{12}C-labelled spectra are in red, and the ^{13}C-labelled spectra are in blue.

We found that there was no spectral difference between ^{12}C and ^{13}C-glutamine labelled cells. The three characteristic peaks of glycogen in U87, 480, 850 and 940 cm^{-1}, were not shifted (Figure 5.5A). Other glycogen peaks,

for example, 1130, 1337 and 1460 cm^{-1} were also not seen to be shifted (Figure 5.5A). The glycogen in U87 showed a standard glycogen spectrum, which was in agreement with the peaks of the standard glycogen chemical in the Chapter 4. Both 480 and 940-cm^{-1} bands were sharp, indicating that the glycogen in U87 exited as large granules containing a large number of branched chain structures.

The glycogen signal in SUM159 was not as strong as in U87 (Figure 5.5E). Its results were consistent with U87 in that neither underwent a significant band shift. The dominant peak for glycogen in SUM159 was 850 cm^{-1}, and both 480 and 940 cm^{-1} were relatively weak. This indicated that in SUM159, the glycogen granules were comparatively small and dominated by the main structure of the straight chain.

The mitochondria have four main characteristic peaks. The same band shifts can be seen in U87 and SUM159. All four characteristic peaks were shifted to a minor degree. 750 cm^{-1} moved to 747 cm^{-1}, 1128 cm^{-1} moved to 1124 cm^{-1}, 1311 cm^{-1} moved to 1306 cm^{-1}, and 1580 cm^{-1} moved to 1577 cm^{-1} (Figure 5.5B and F). In Chapter 4, we used ^{13}C-glucose to label U87 for 24 hours after which we found that the Raman shift of the mitochondrial bands was 744, 1113 and 1572 cm^{-1}. The carbon flux of intracellular mitochondria was labelled more with ^{13}C-glucose than with ^{13}C-glutamine. The Raman

shifts observed in U87 and SUM159 cells labelled with ^{13}C-glutamine were relatively minor, while the Raman shifts observed in U87 cells labelled with ^{13}C-glucose were more pronounced. This suggests that ^{13}C-glucose is a better substrate for labelling intracellular mitochondria than ^{13}C-glutamine.

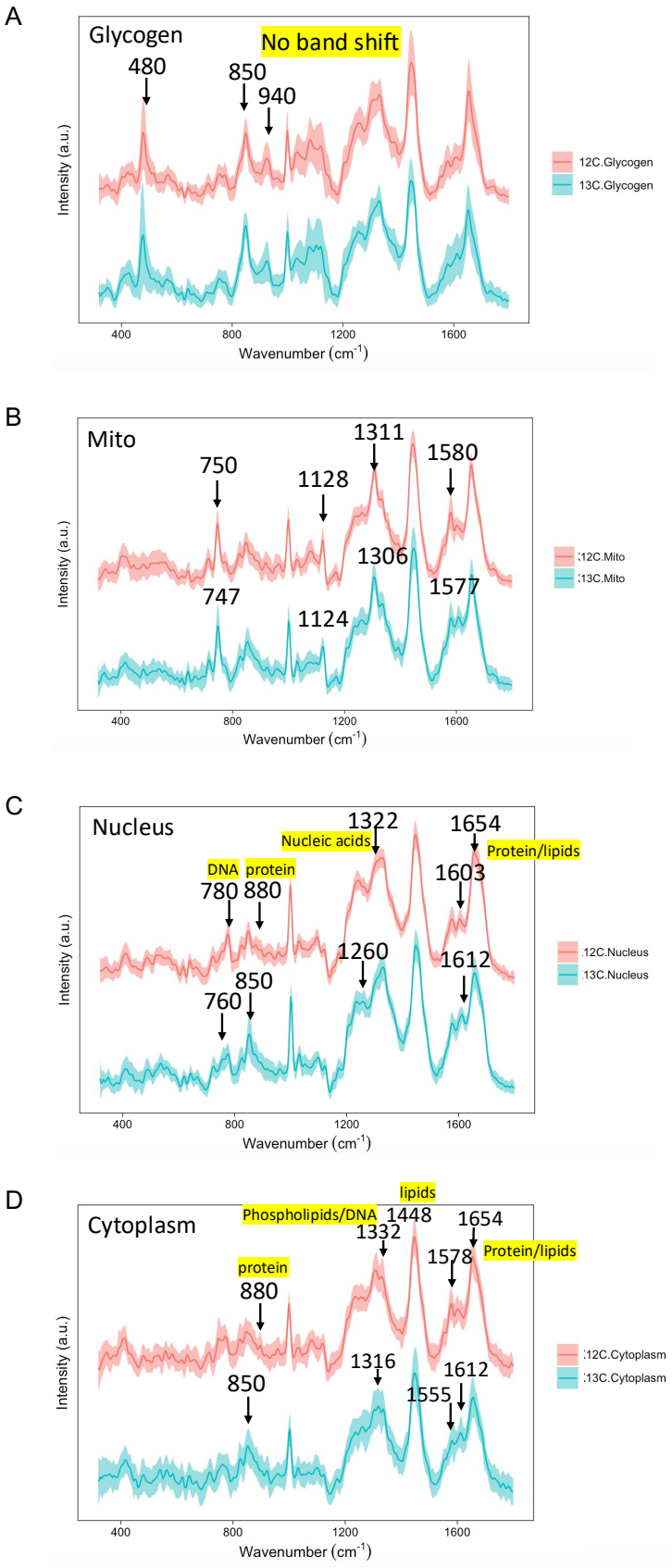
There is a clear Raman band shift in the nucleus, with the most obvious shift observed at the 780-cm^{-1} peak, which is characteristic of nucleic acids. This peak shifted to 760 cm^{-1}, a movement of 20 wavenumbers (Figure 5.5C). Changes in the strength of other nucleic acid peak signals were also easily visible, such as the weakening of the 1322-cm^{-1} peak signal and the enhancement of the 1260-cm^{-1} peak of the ^{13}C spectrum (Figure 5.5C). It is possible that the signal of the nucleic acid near 1322 cm^{-1} moved to 1260 cm^{-1}. However, further studies are needed to confirm the exact nature of these changes and their biological significance.

This variation in the signal strength of bands was pronounced in the Raman spectra of the cytoplasm. It mainly appeared in the range of 1200-1660 cm^{-1}, which was mainly in the protein and lipid regions (Figure 5.5D and H). The band that intensified at 1332, 1448, 1578 and 1654 cm^{-1} were diminished after ^{13}C-glutamine labelling (Figure 5.5D and H). At the same time, new bands occurred near 1316, 1555 and 1612 cm^{-1} (Figure 5.5D and H). This is because proteins and lipids contain two modes of band shift. One is the band

shift to the left when the ^{12}C is replaced by ^{13}C, and the other is a weakening of the signal intensity with no change in the position of the peak[229]. The band shifts and changes in signal intensity were discussed in Chapter 4 and will not be repeated here.

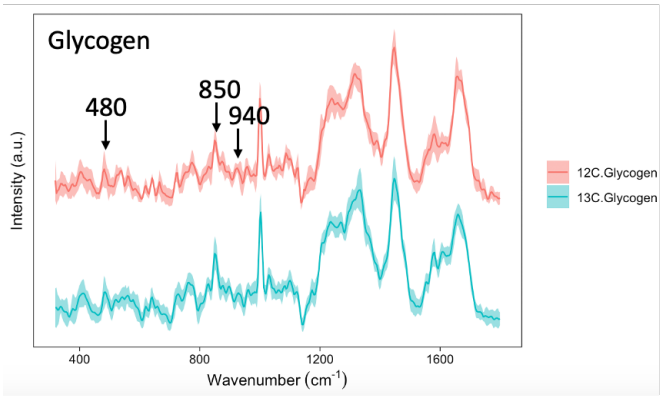
Glutamine is an important source of carbon and nitrogen for many cancer cells, and it is known to be metabolized in the mitochondria[260]. When ^{13}C-glutamine is infused into cells, the carbon from glutamine can be transferred to other molecules such as glutamate, TCA cycle intermediates, amino acids, fatty acids, and proteins[261,262]. The metabolic intermediate ^{13}C-glutamate of ^{13}C-glutamine can be detected in mitochondria[263]. Studies by the DeBerardinis group have shown that when ^{13}C-glutamine is infused into mice, all tumours displayed labelling in glutamate and TCA cycle intermediates[250]. The carbon from ^{13}C-glutamine can also be used to labelled nucleic acids, which can be distinguished as markers in pathways of glutamine metabolism using gas chromatography-mass spectrometry (GC–MS)[250].

U87

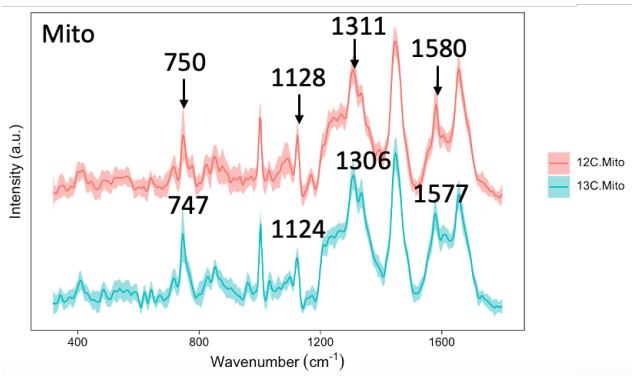

A
Glycogen
No band shift
480
850
940
Intensity (a.u.)
12C.Glycogen
13C.Glycogen
400
800
1200
1600
Wavenumber (cm-1)
B
Mito
1311
1580
750
1128
1306
1577
747
1124
Intensity (a.u.)
:12C.Mito
:13C.Mito
400
800
1200
1600
Wavenumber (cm-1)
C
Nucleus
1322
1654
Nucleic acids
Protein/lipids
DNA
protein
780
880
1603
1260
1612
850
760
Intensity (a.u.)
:12C.Nucleus
:13C.Nucleus
400
800
1200
1600
Wavenumber (cm-1)
D
Cytoplasm
lipids
Phospholipids/DNA
1448
1654
1332
1578
Protein/lipids
protein
880
1316
1612
850
1555
Intensity (a.u.)
:12C.Cytoplasm
:13C.Cytoplasm
400
800
1200
1600
Wavenumber (cm-1)

SUM159

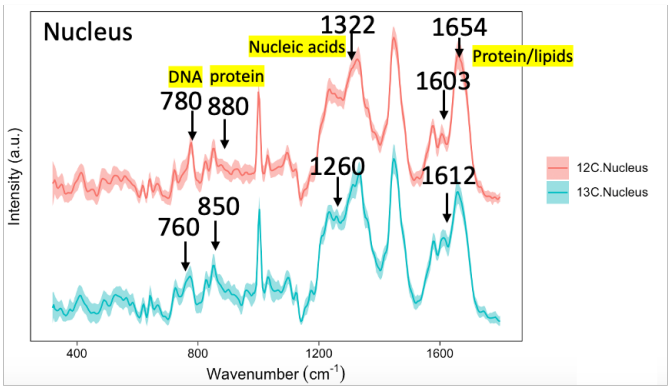
E


Glycogen
480
850
940
Intensity (a.u.)
400
800
1200
1600
Wavenumber (cm-1)
12C.Glycogen
13C.Glycogen

F


Mito
750
1128
1311
1580
1306
1577
747
1124
Intensity (a.u.)
400
800
1200
1600
Wavenumber (cm-1)
12C.Mito
13C.Mito

G


Nucleus
1322
Nucleic acids
1654
Protein/lipids
DNA
protein
780
880
1603
1260
1612
850
760
Intensity (a.u.)
400
800
1200
1600
Wavenumber (cm-1)
12C.Nucleus
13C.Nucleus

H

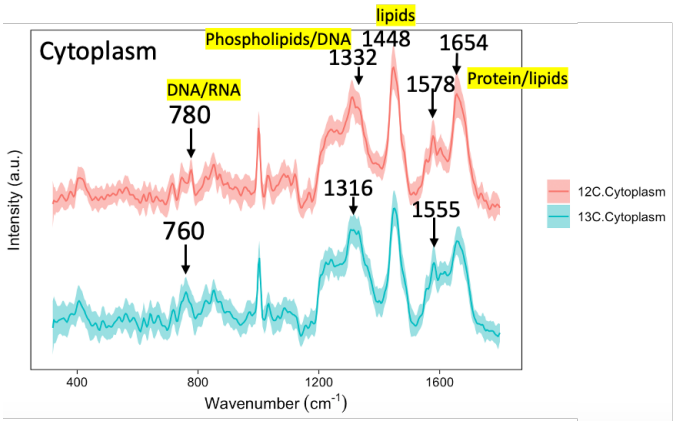

lipids
Cytoplasm
Phospholipids/DNA
1448
1332
1654
1578
Protein/lipids
DNA/RNA
780
1316
1555
760
Intensity (a.u.)
400
800
1200
1600
Wavenumber (cm-1)
12C.Cytoplasm
13C.Cytoplasm

Figure 5.5 Band shifts of different biocomponents in cancer cells after labelling with ^{13}C-gulamine for 48 hours. (A, E) The averaged spectra of glycogen in (A) U87 and (E) SUM159. (B, F) The averaged spectra of mitochondria in (B) U87 and (F) SUM159. (C, G) The averaged spectra of nucleus in (C) U87 and (G) SUM159. (D, H) The averaged spectra of cytoplasm in (D) U87 and (H) SUM159. The spectrum of cells cultured with ^{12}C-glutamine is coloured in red and the spectrum of cells cultured with ^{13}C-glutamine is coloured in blue. 8 cells were measured for each group and around 200 spectra were measured for each cell.

5.3.3 Intracellular metabolic activities revealed by SCRM–DIP and ^{13}C-isotope probing

The above results suggest that since the ^{13}C-glutamine molecule is small and metabolized rapidly, its distribution within the cell is difficult to observe. Hence, we attempted to probe the cells by adding heavy water with deuterium. In this section, U87 and SUM159 cells were fed with a combination of 35% heavy water (D_2O) and 4mM ^{13}C-glutamine, creating a double-labelling experiment with both ^{2}H and ^{13}C.

Deuterium isotope probing (DIP) is an important indicator used to measure the metabolic activity of single cells[264]. The deuterium in heavy water is incorporated during synthesis through the action of H/D exchange reactions[120]. The H in the C–H band is replaced with deuterium, causing the Raman peak to shift to the left, where the C−D bond appears in the 2100-

2300 cm^{-1} region[120,121].

Firstly, I conducted a series of cell tolerance experiments on U87 and SUM159. The culture medium contained 35% heavy water and varying amounts of ^{13}C-glutamine, including 0, 70, 80, 85, 90 and 100%.

The Raman spectra of U87 and sum159 cells are shown in Figure 5.6 A and C respectively. The spectrum after 24 hours of incubation in heavy water for demonstrated a clear C−D band in the 2100–2300 cm^{-1} (Figure 5.6A and C). Calculation of the C−D band area revealed a significant increase in the labelled cells compared to the control group (Figure 5.6B and D).

However, in the group that was 100% labelled with ^{13}C-glutamine, SUM159 showed a decrease in the region of the C−D band. These results suggest that they had decreased cellular activity at high concentrations of ^{13}C-glutamine and D_2O dual labelling[120].

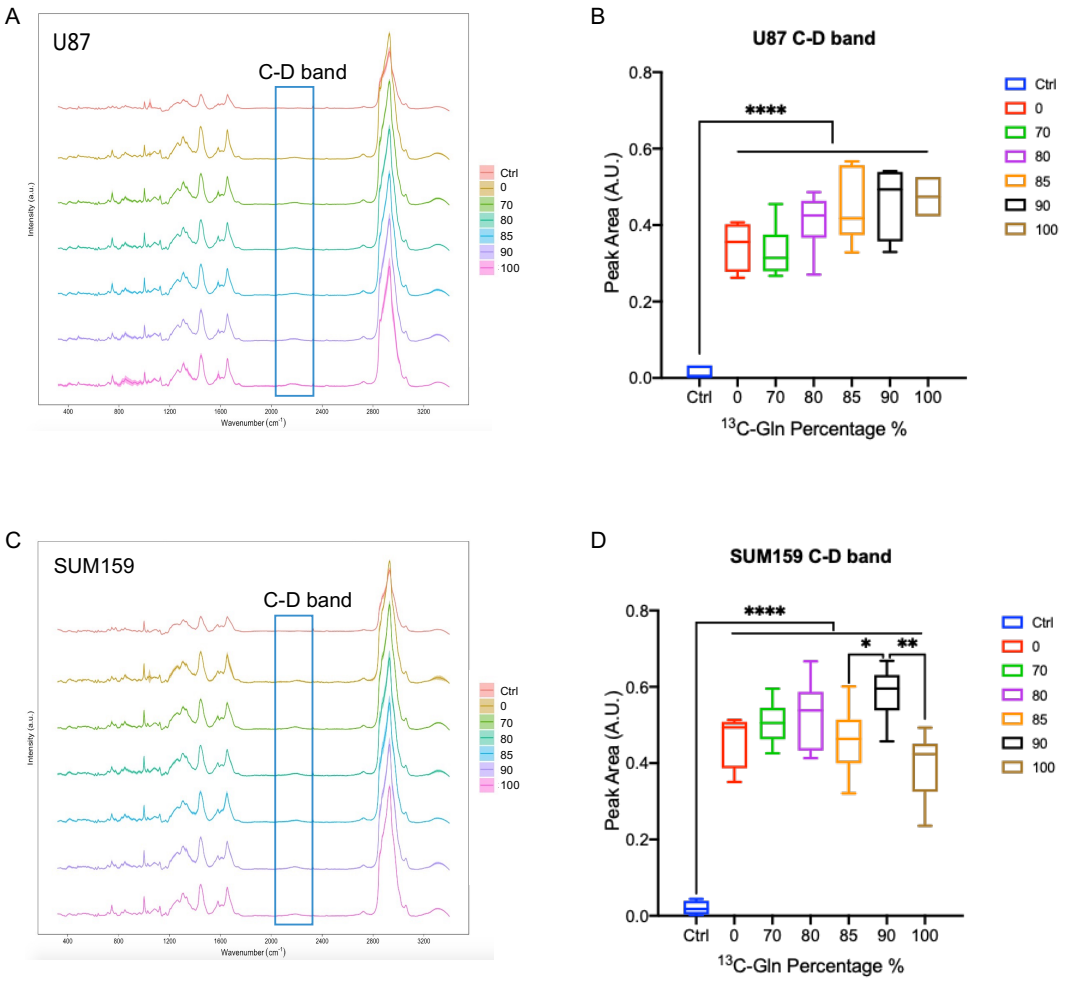


Figure 5.6 SCRM of U87 and SUM159 for 24 hours in a culture medium with 35% D_2O and increasing gradients of ^{13}C-glutamine. (A, C) The Raman profiles of (A) U87 and (C) SUM159 grown. (B, D) Comparison of the areas of the C−D band corresponding to A and C. 6-8 cells were measured for each group. For each cell, around 200 spectra were measured. Data are presented as mean values ± S.D., two-way ANOVA test, *p<0.05, **p<0.01 and ****p<0.0001.

I attempted to compare the other peak movements of the cells, but I found that the 24-hour labelling time was not long enough for cancer cell metabolism. Although the C−D band was clearly visible, the shift of the other

C−H bands was not so obvious as in bacteria[118]. This is because the cellular biochemical metabolism of mammalian cells is not as fast as that of bacterial cells[85,265]. 2-7 days is an acceptable incubation time for cancer cells[266]. Considering that double labelling may magnify cytotoxicity, a 48-hour incubation is probably the optimal condition. SUM159 demonstrated more sensitivity to D_2O, and for repeat experiments, I chose only U87.

U87 cells were cultured in a media containing 35% heavy water and 0%, 80% and 100% ^{13}C-glutamine for 48 hours. The cells were successfully labelled with ^{2}H, and a clear C−D band was observed in the Raman spectrum (Figure 5.7A). Compared to the control group, the C−D band was more pronounced in U87 cells grown in heavy water ($p<0.0001$, Figure 5.7B). Interestingly, the metabolic activity of the cells in the 80% ^{13}C-glutamine group was higher than that of the cells in the absence of ^{13}C-glutamine ($p<0.05$, Figure 5.7B).

Unsupervised principal component analysis (PCA) was used to minimize the high dimensional Raman dataset and identify the critical information causing single-cell variations because one SCRM contains hundreds of Raman bands. PCA plots along the first two principal components (PC1 and PC2) separate the control from the experimental group of cells. The control cells are on one side and the cells labelled by ^{13}C-glutamine and heavy water are overlaid (Figure 5.7C). This suggests that the labelling of ^{13}C and ^{2}H gives

U87 cells a unique phenotypic profile.

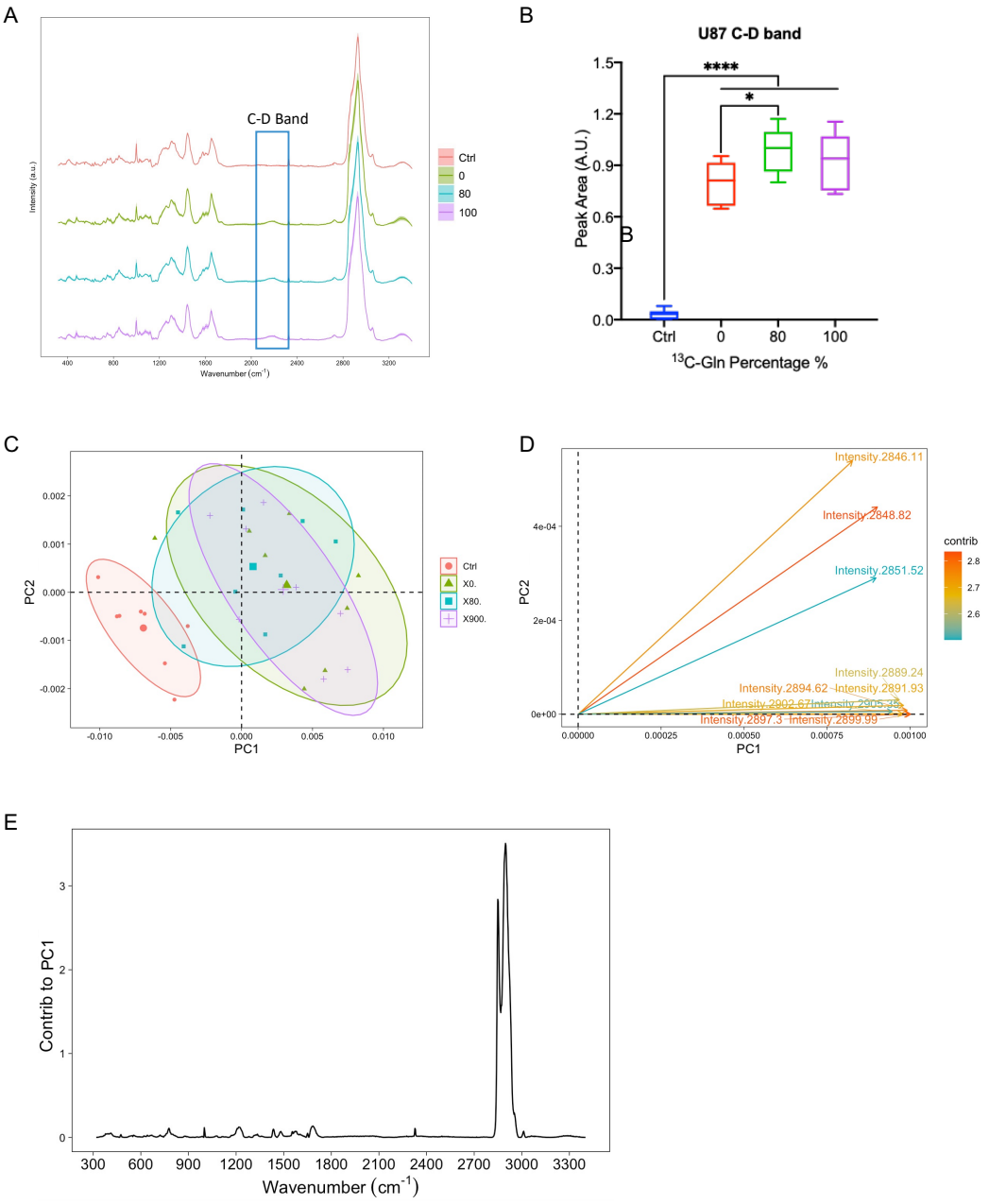


Figure 5.7 SCRM of U87 grown for 48 hours within 35% D_2O and high gradients of ^{13}C-glutamine. (A) The whole Raman spectra of U87 under double labelling. (B) Comparison of the areas of the C−D band corresponding to A. (C, D) PCA and peak contribution plots displaying the distinctive metabolic features of U87 grown in D_2O and ^{13}C-glutaime in the Raman

fingerprint region. (E) Loading plot of SCRM of double-labelled U87, with Raman wavenumbers against their contributions to PC1 of the PCA. 8 cells were measured for each group. For each cell, around 200 spectra were measured. Data are presented as mean values ± S.D., one-way ANOVA test, *p<0.05 and ****p<0.0001.

The most significant differences were observed in 2850–2990 cm^{-1}, which are C−H stretching bands (Figure 5.7D). The maximum variance between control and experimental cells was accounted for by the Raman contribution of PC1 to PCA, which explained these differences. The two peaks with the largest differences occurred at 2851 and 2990 cm^{-1} (Figure 5.7E). Both peaks are from C−H stretching[267].

The phenotypic differences in this group of cells were more in the deuterium labelling than in the ^{13}C-glutamine. Neither the ^{12}C nor the ^{13}C-labeled cells could be distinguished by PCA (Figure 5.7C). The high expression of the C−D band indicates that D_2O is heavily involved in the bio-metabolism of the U87 cells.

To further observe the specific band shifts, I separated the cells into two major components, nucleus and cytoplasm. U87 cells cultured with 35% D_2O and 0% and 80% ^{13}C-glutamine were selected for comparative data.

Figure 5.8 represents the analysis of the nucleus and cytoplasm of U87 after double labelling with deuterium and ^{13}C. For the plots of the Raman spectra,

^{12}C is labelled as the red curve and ^{13}C as the blue curve.

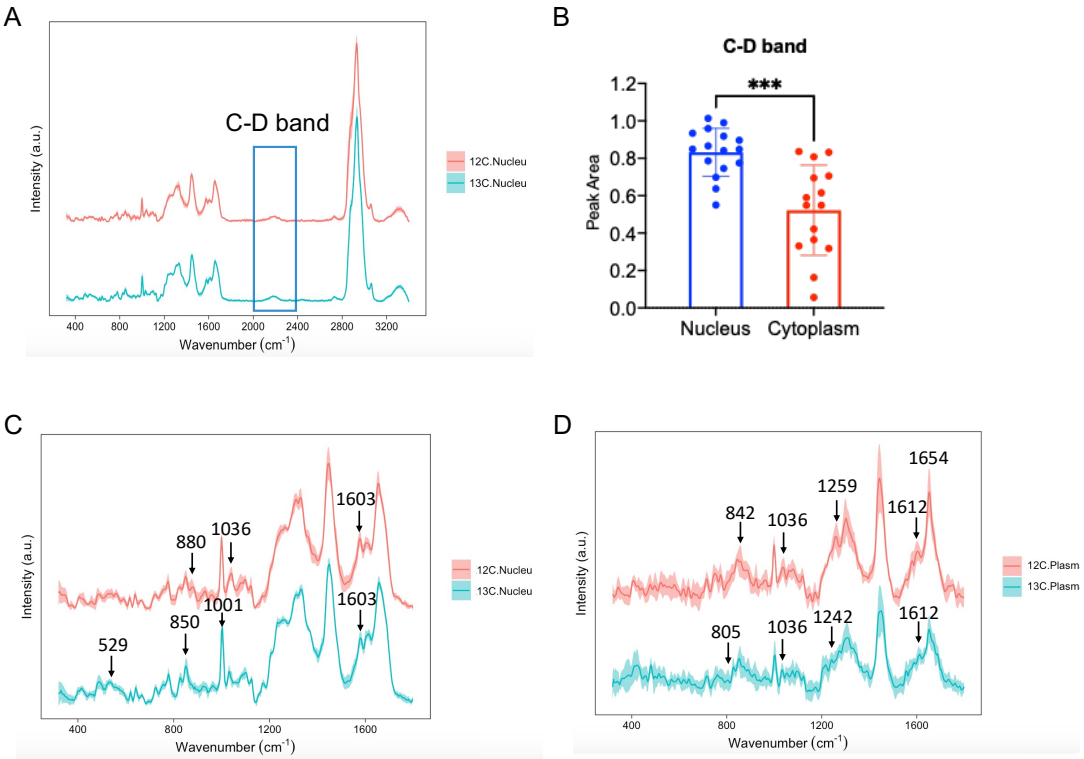


Figure 5.8 Raman–SCRM band shifts of U87 cells under double labelling with deuterium and ^{13}C. (A) The Raman spectra of nuclei area labelled by ^{12}C (red) and ^{13}C (blue) separately. (B) Raman spatial distribution of C−D bands in U87 single cell. (C, D) The fingerprint profiles of (C) nuclei and (D) cytoplasm. The spectrum of cells cultured with ^{12}C-glutamine is coloured in red and the spectrum of cells cultured with ^{13}C-glutamine is coloured in blue. 15-16 cells were measured for each group. For each cell, around 200 spectra were measured. Data are presented as mean values ± S.D., one-way ANOVA test, ***p<0.001.

A distinct C−D band was seen in the whole Raman spectra of both ^{12}C and ^{13}C-glutamine groups of U87 (Figure 5.8A). The C−D band was significantly higher in the nucleus than in the cytoplasm (p<0.001, Figure 5.8B).

Interesting findings were also obtained by looking at the fingerprint area of the U87 cells. There were some bands of nuclei that disappeared or diminished after labelling. 880 and 1361-cm^{-1} bands were missing, while peaks at 1036 and 1603 cm^{-1} were clearly reduced (Figure 5.8C). Likewise, the 1036-cm^{-1} band of the cytoplasm was attenuated (Figure 5.8D). The signal of the 842, 1612 and 1654-cm^{-1} band of the cytoplasm also decreased, and the peak at 1259 cm^{-1} shifted to 1242 cm^{-1} (Figure 5.8D). The variation in these peaks was dominated by a second type of band shifts. In the nucleus, nucleic acids and amino acids were labelled by ^{2}H, while in the cytoplasm, it was the proteins and amino acids that were labelled[268].

5.4 Conclusions

In conclusion, this chapter demonstrated the usefulness of combining ^{13}C and ^{2}H isotope probing with Raman–FISH for investigating the metabolic activity and phenotypic features of U87 and SUM159 cells.

The experiments revealed that glutamine is rapidly metabolized in the synthesis of cellular endogenous molecules and that Raman has difficulty in detecting its sub-cellular spatial distribution. Cells did not show significant band shifts on the averaged Raman spectra after 24 hours of ^{13}C-glutamine incubation. However, by separating the different cellular components, proteins, lipids, and nucleic acids were successfully labelled with ^{13}C.

The results show that the carbon in glutamine is not directly involved in glycogen synthesis within 48 hours in the presence of sufficient glucose.

Raman–DIP was shown to be an effective method for detecting cellular metabolic activity, although excessive levels of ^{13}C-glutamine may inhibit cellular metabolic activity. The shift of the C−H band allowed for the identification of cellular phenotypic metabolic features, providing insight into the turnover of metabolites and positional information. H/D exchange reactions were found to be mainly involved in nucleic acid metabolism in the nuclei and protein metabolism in the cytosol.

Chapter 6

Metabolic reprogramming in colon cancer cells persistently infected by Newcastle disease virus

Contents

6.1 Introduction

6.2 Materials and methods

6.3 Results and discussion

6.3.1 Cell line screening for establishing an NDV-susceptible cancer cell system

6.3.2 Identification of persistently infected VR Caco-2 cells

6.3.3 Persistent VR Caco-2 can be identified by metabolic profiles at single-cell level

6.3.4 Raman profiles differentiates VR Caco-2 and Caco-2 cells

6.3.5 Raman–DIP reveals metabolic reprogramming via newly synthesised biomolecules

6.4 Conclusions

This chapter describes a research paper that has been published in the journal *Cancers*. The project was a collaborative effort between myself, Dr Archana Chandrabhan Jadhav, and Dr Jiabao Xu. The technique of Raman–

DIP was applied to investigate the metabolism differences between virus infected and non-infected Caco-2 cells. While the data in sections 6.3.1 and 6.3.2 were provided by Dr Jadhav, and I completed the remaining data in sections 6.3.3, 6.3.4 and 6.3.5. Dr Xu and I have contributed to the data curation. The full manuscript is attached here.

This chapter focuses on the utilisation of Newcastle disease virus (NDV) to establish persistently infection in Caco-2 colon cancer cells. A specific subset of Caco-2 cells demonstrated resistance to NDV reinfection and were identified as persistently infected cells (VR Caco-2). The study employed Single-cell Raman micro-spectroscopy (SCRM) and stable isotope techniques to investigate the metabolic reprogramming of VR Caco-2 cells. The linear discriminant analysis (LDA) model was particularly effective in distinguishing VR Caco-2 from regular Caco-2 cells at the single-cell level. Comparative analysis of metabolic profiles using deuterium labelling at different time points revealed an increase in *de novo* synthesis of proteins and lipids, accompanied by a decrease in DNA synthesis in VR Caco-2 cells. The findings suggests that VR Caco-2 cells undergo metabolic reprogramming, redirecting energy resources from proliferation towards protein synthesis and lipid regulation.

This chapter serves as a demonstration of the application of SCRM in studying cancer cell metabolism within the context of this thesis.

Metabolic reprogramming in colon cancer cells persistently infected by Newcastle disease virus

Tong Yu[1,†], Archana Chandrabhan Jadhav[2,3,†], Jiabao Xu[1,*], Adrian L. Harris[4], Venugopal Nair[3] and Wei E. Huang[1,*]

1 Department of Engineering Science, University of Oxford, Parks Road, Oxford OX1 3PJ, UK

2 Beamline B24, Diamond Light Source, Harwell Science and Innovation Campus, Didcot, Oxfordshire OX11 0DE, UK

3 Viral Oncogenesis Group, The Pirbright Institute, Surrey, GU24 0NF, UK

4 Molecular Oncology Laboratories, Department of Oncology, Weatherall Institute of Molecular Medicine, John Radcliffe Hospital, Oxford University, Oxford OX3 9DS, UK

5 Department of Biology, University of Oxford, 11a Mansfield Road, Oxford OX1 3SZ, UK

* Authors to whom correspondence should be addressed.

† The authors contributed equally to this work.

Abstract: Newcastle disease virus (NDV) is an oncolytic agent protecting against various types of mammalian cancers. As in all cancer therapies, the development of cancer resistance, both innate and acquired, is becoming a challenge. In this study, we investigated persistently NDV-infected Caco-2 colon cancer cells, designated as virus-resistant (VR) Caco-2 cells, which were then able to resist NDV-mediated oncolysis. We applied single-cell Raman spectroscopy and combined it with deuterium isotope probing (Raman-DIP) techniques to investigate the metabolic adaptions and dynamics in VR Caco-2 cells. A linear discriminant analysis (LDA) model demonstrated excellent performance in differentiating VR Caco-2 from Caco-2 cells at the single-cell level. By comparing the metabolic profiles in a time-resolved manner, the de novo synthesis of proteins and lipids was found upregulated, together with a decrease in the DNA synthesis in VR Caco-2. The results suggest that VR Caco-2 cells might reprogram their metabolism and divert energy from proliferation to protein synthesis and lipidic modulation. The capability of identifying and characterising single resistant cells among a population of cancer cells would help a deeper understanding of the resistance mechanisms and better tactics for developing effective treatment for cancer.

Keywords: Newcastle disease virus; Raman spectroscopy; cancer resistance; drug resistance; single cells

6.1 Introduction

Newcastle disease virus (NDV) is a single-stranded RNA avulavirus causing Newcastle disease. Over the last five decades, NDV has been known to have oncolytic properties and is a potential candidate for oncovirotherapy due to its tumour-selective replication sparing healthy cells[269]. Tumours provide a favourable environment for NDV replication and spread due to compromised antiviral defences related to the weaker sensitivity and expressions of type 1 interferon (IFN), as well as developing resistance to cell death pathways[270]. Since in 1957 when the antitumour potential of NDV was first demonstrated in NDV-coated ascitic cancer cells[271], both preclinical and clinical research have made substantial use of NDV as an oncolytic drug, with its non-pathogenic strains (e.g. Hitchner B1, LaSota, Ulster and V4UPM), mildly-pathogenic strains (e.g. PV701 and 73T) and highly-pathogenic strains (e.g. AF2240) all proven to be potent anti-cancer agents.

Despite promising responses observed in clinical studies, persistent NDV infections have been reported in a range of in vitro cancer cell infections[272–274]. In colorectal cancer, the persistently infected cells were discovered to harbour viral offspring that formed smaller plaques, in contrast to the uninfected cancer cells[272]. Hyperfusogenic NDV activity and the emergence of persistence infection were linked by two alterations in the glycoproteins of NDV, F and HN proteins in persistently infected ovarian cancer[273]. Upregulation of genes associated with cell growth, pro-survival, and anti-apoptosis have also been reported during the development of persistently infected bladder cancer cells[274]. Persistent NDV infections in cancer cells result in reduced NDV-induced oncolysis and therefore hinders the development and translation of NDV as an

oncolytic virotherapy. As the mechanism of NDV persistent infection in cancer cells remains poorly understood, further investigation and identification of the persistency in cancer cells is critical.

Here, we apply label-free single-cell Raman spectroscopy for investigating cellular resistance at a single-cell level. This spectroscopic technique can provide a comprehensive 'biomolecular fingerprint' of a biological system[85]. In combination with advanced confocal microscopy, the biomolecular fingerprint of a single cell can be obtained as a single-cell Raman spectrum (SCRS)[275]. In addition, Raman techniques can be integrated with deuterium isotope probing (DIP) to map the general metabolic activity of a cell[116]. By incubating cells with heavy water (D_2O), the D atoms in D_2O can exchange with H atoms and form a variety of C–D bonds mediated by NADPH. By quantifying the C–D band at 2170–2300 cm^{-1} in the Raman spectrum, the degree of D incorporation can be used to estimate the anabolic activity. This method has been widely used to research the ecological and microbiological activity of microbes[88,116,123,276]. Recently, Raman-DIP using D_2O has also been reported to study the metabolism of cancer cells[112,113]. Raman-DIP has many advantages over other targeted probes, for example, fluorophores, that are invasive and may interfere with a cell's inherent metabolic activity.

In this study, we unintentionally observed the emergence of infection-persistent Caco-2 cells, initially the most sensitive to the NDV strain, after infection in a succession of cancer cell lines with a non-pathogenic strain of NDV, B1-GFP. The persistently infected cells were isolated and named virus-resistant (VR) Caco-2. We employed single-cell Raman spectroscopy and Raman-DIP to explore the metabolic differences within the VR Caco-2 cells and compared

them to the parental uninfected Caco-2 cells. Raman spectral profiles of the VR Caco-2 cells were found to be distinctly different from those of the uninfected Caco-2 cells, suggesting significant metabolic reprogramming in those persistently infected cells.

6.2 Materials and methods

Virus strain and cell lines used in this study The virus strain used in this study was a non-pathogenic strain of NDV Hitchner B1-GFP, obtained from the Department of Microbiology, Mount Sinai School of Medicine, New York. Human cancer lines used include lung adenocarcinoma A549, hepatocellular Hep G2, prostate adenocarcinoma PC3, cervical adenocarcinoma HeLa, colorectal adenocarcinoma Caco-2 and virus-resistant Caco-2 (VR Caco-2). A non-cancer human lung fibroblast cell line MRC5 was also used. A549, Hep G2, HeLa, Caco-2, PC3 and MRC cell lines were obtained from the cell line inventory run by the Pirbright Institute's cell services unit. A549, MRC5, PC3, Caco-2 and VR Caco-2 cells were authenticated using short tandem repeat (STR) profiling from ECACC. For VR Caco-2 cells, Caco-2 cells were first infected with undiluted stock of B1-GFP virus, resulting in an estimated multiplicity of infection (MOI) of 50. About >98% cells were infected within 24 h and >95% of infected cells were dead within 48 h post-infection. A few cells survived 12 days post-infection and were identified by cultivation and further isolated as VR Caco-2 cells.

Cell culture and virus infection The complete media used for culturing each cell line are as follows. For culturing Caco-2 and VR Caco-2 cells, minimum essential medium eagle (MEM) with Earle's salts and sodium bicarbonate

without L-Glutamine (Sigma-Aldrich, Gillingham, Dorset, UK) was supplemented with 1.0 mg/mL D-glucose, 1% penicillin-streptomycin (10,000 U/mL), 1 x NEAA, 4 mM L-glutamine, 1 µg/mL amphotericin B and 20% foetal bovine serum (FBS). For culturing Hep G2 and MRC cells, MEM was used, supplemented with 1.0 mg/mL of D-glucose, 1% penicillin-streptomycin, 4 mM L-glutamine, 1 µg/mL amphotericin B and 10% FBS. Roswell Park Memorial Institute (RPMI) (2.2 mg/mL of D-glucose) medium (Sigma-Aldrich, UK) and Ham's F-12K (Kaighn's) (1.26 mg/mL of D-glucose) medium (Gibco, Thermo Fisher Scientific, Loughborough, UK) were used for culturing HeLa cells and PC3 cells, respectively, both supplemented with 1% penicillin-streptomycin, 1 µg/mL amphotericin B and 10% FBS. For culturing A549 cells, Dulbecco's modified eagle's medium (DMEM) with high glucose of 4.5 µg/mL, L-glutamine and sodium bicarbonate without sodium pyruvate (Sigma-Aldrich) was supplemented with 1% penicillin-streptomycin, 1 mM sodium pyruvate, 1 µg/mL amphotericin B and 10% FBS. The cell culture media was changed every 48 h during the prolonged cell-culturing process.

Cell viability and toxicity assay CellTiter-Blue® Cell Viability Assay (Promega, Southampton, UK) was used to compare the viability of NDV-infected cells to mock-infected control cells. The manufacturer's instructions were followed. The reduction reaction of the resorufin to the fluorescent product was done by incubating the metabolically active cells at 37 °C and 5% CO_2 for up to 4–6 h. A Promega GloMax® Explorer Multimode Microplate Reader was used to measure the fluorescence generated at an excitation of 560 nm and emission at 590 nm. The measured viability fraction was computed by dividing the normalised fluorescence reading of the infected cells by that of the uninfected

cells.

CellToxTM green cytotoxicity assay The DNA-binding cyanine dye was only taken up by dead cells due to a breakdown of cell membrane integrity and the fluorescent signal was detected at 520–530 nm. The manufacturer's instructions were followed when performing the end-point cytotoxicity assay at day 4 of infection by B1-GFP (MOI~0.1) to Caco-2 and VR Caco-2 cells. The fold change in cytotoxicity was calculated by cytotoxicity of NDV-infected cells divided by cytotoxicity of mock-infected cells.

Cell proliferation assay CellTrace™ CFSE Cell Proliferation Kit (Invitrogen™, Thermo Fisher Scientific, Loughborough, UK) and flow cytometry analysis of CFSE-labelled cells at 488 nm were used to measure cell proliferation in Caco-2 and VR Caco-2 cells. Cells were cultured in complete growth media at 37 °C inside a 5% CO_2 incubator until 80–90% confluence was reached. Cells were then trypsinised with 0.25% trypsin-EDTA solution, centrifuged at 325 g, and washed and resuspended with serum-free MEM media. CFSE buffer was added to the resuspended cells to reach 1×10^6 cells/mL in 2.5 μM CFSE buffer. The mixture was then incubated in a water bath at 37 °C for 15 min to label DNA. Following a serum-free MEM medium wash, CFSE-labelled cells were resuspended in complete growth media at 37 °C for 1 hour. After washing and resuspending, 5×10^5 cells per well were seeded into 24-well plates, which were then cultured at 37 °C with 5% CO_2. Using a MACSQuant Analyzer (Miltenyi Biotec, Bisley, Woking, UK), the fluorescence of the CFSE-labelled cells was monitored at five different time intervals (0, 12, 24, 48 and 72 h) after labelling. The Incucyte Live-Cell Analysis system (Sartorius, Epsom,UK) was used to monitor the proliferation of Caco-2 and VR Caco-2 cells seeded at

different densities (5 k/well, 10 k/well and 15 k/well) in real time.

Caco-2 and VR Caco-2 cells for Raman and Raman-DIP measurements Non-infected parental Caco-2 and VR Caco-2 cells were grown for up to 5–6 days until 80–90% confluence was attained. In Raman-DIP experiments, Caco-2 complete media with 30% D_2O (Sigma-Aldrich) were used for culturing Caco-2 and VR Caco-2 cells, with cells obtained at different time points at 0, 12, 24, 48 and 72 h. The 30% D_2O Caco-2 media was formulated by using 10 mL of 10 x MEM (10 mg/mL of D-glucose) without L-glutamine and sodium bicarbonate (Sigma-Aldrich), 30 mL of 99% D_2O (Sigma-Aldrich), 1 mL of 100 x NEAA (Gibco), 1 mL of 200 mM L-glutamine (Gibco), 3 mL of 7.5% sodium bicarbonate solution (Sigma-Aldrich), 1 mL of penicillin-streptomycin (10,000 U/mL) (Gibco), 0.04 mL of Amphotericin B (Gibco), 20 mL of heat-inactivated FBS and 33.6 mL of sterile deionised water. The cells were washed with PBSa and trypsinised. Trypsin was neutralised using serum-containing media and cells were washed with PBSa at 325 g for 5 min. Following that, cells were resuspended with cold solution of 4% paraformaldehyde (PFA) in PBSa and fixed for 1 hour at room temperature. The PFA-fixed cells were then washed once with PBSa and twice with Milli-Q water, following which the cell suspensions were dropped onto an aluminium-coated Raman slide and air dried before the measurements.

Single-cell Raman spectroscopic measurements and analysis A LabRAM HR Evolution Raman microscope (Horiba Scientific, UK) was used for spectroscopic measurements, equipped with a 532-nm neodymium-yttrium aluminium garnet laser. Raman spectra were acquired via a 50× objective lens and 300 grooves/mm diffraction grating using 90-mW input laser power through

a 25% neutral density (ND) filter and 3-s acquisition time. Raman scattering was detected by a charge-coupled device (CCD) cooled at –68 °C. The spectra were acquired in the range of 300 to 3400 cm^{-1}. For VR Caco-2 and Caco-2 cells, 218 and 92 single cells were measured, respectively. In Raman-DIP experiments, >30 cells were measured for each time point. For each cell, around 30 spectra were measured. As the dried cells lost the original spatial distribution, spectra were averaged into one spectrum per single cell, which was used in the following analysis.

All spectra were pre-processed by cosmic ray correction and polyline baseline fitting using LabSpec 6 (Horiba Scientific, Montpellier, France). The entire spectrum region was vector normalised. Data analysis, statistics and visualisation were carried out in an R environment. Intracellular biomolecules were semi-quantified by quantifying corresponding band areas. The C–D (2070–2300 cm^{-1}) and C–H (2800–3030 cm^{-1}) band areas were quantified to determine deuterium content originating from incubation with D_2O, while the metabolic rate was calculated by the ratio of C–D / C–D + C–H. Performance of the statistics was done between single cells of VR Caco-2 and Caco-2 at each Raman wavenumber by comparing their intensities with Student's t-test (ns: $p > 0.05$; *: $p < 0.05$; **: $p < 0.01$; ***: $p < 0.001$; ****: $p < 0.0001$).

6.3 Results and discussion

6.3.1 Cell line screening for establishing an NDV-susceptible cancer cell system

A non-pathogenic reporter strain of NDV, Hitchner B1-GFP, was introduced to infect various cancer/non-cancer cell lines for screening and establishing an

NDV-susceptible system. Six different human cell lines were used, including five cancer cell lines derived from various tissues, the colon (Caco-2), prostate adenocarcinoma cells derived from a metastatic site in bone (PC3), the lung (A549), the liver (Hep G2), the cervix (HeLa) and a non-cancerous fibroblast cell line developed from lung tissue (MRC5). All cell lines were infected with B1-GFP neat virus (MOI of 50) and its ten-fold dilutions. Time- and NDV dose-dependent cell viability was monitored during a nine-day period (Figure 6.1).

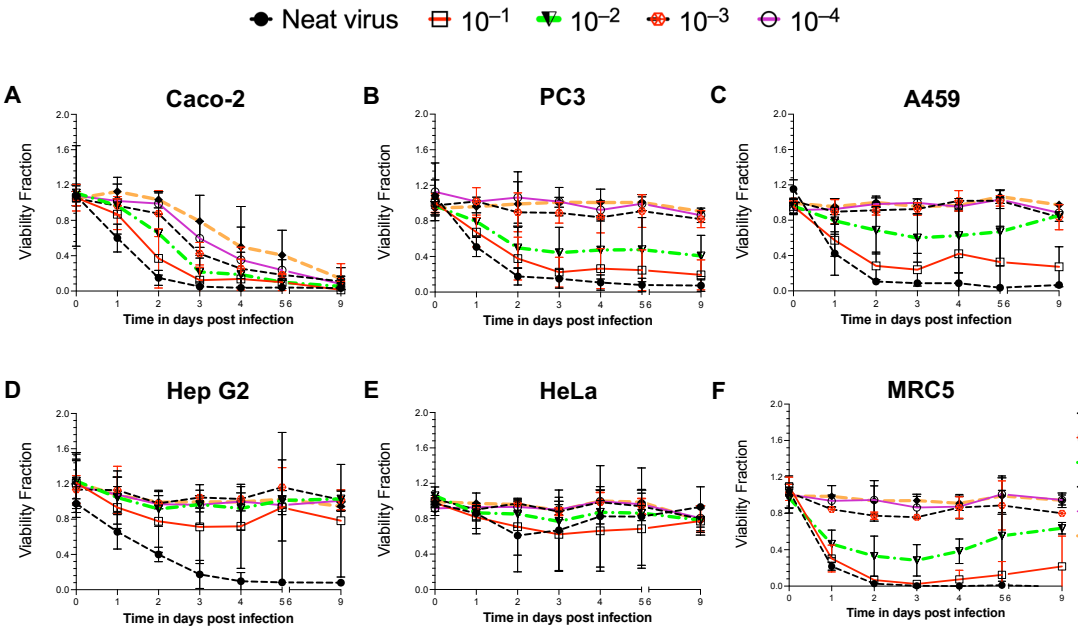


Figure 6.1 Time- and NDV dose-dependent cell viability assay in different human cancer cells. Cell lines were infected with a neat virus (MOI of 50) of a non-pathogenic reporter strain of NDV B1-GFP and its 10-fold dilutions. Cell lines derived from different cancerous tissues such as (A) the colon (Caco-2), (B) prostate adenocarcinoma cells derived from the metastatic site in bone (PC3), (C) lung (A549), (D) liver (Hep G2), (E) cervix (HeLa) and (F) non-cancerous human lung fibroblast cells (MRC5) were used for the study. Cell viability was measured throughout nine days of infection study. Data (mean ± SD) represented here is the combination of three repeats for each cell line. Viability Fraction = Normalised fluorescence reading of infected cells at (560 Ex/590 Em)/Normalised fluorescence reading of uninfected cells at (560 Ex/590

Em).

A consistent decrease in cell viability was only observed in the infected Caco-2 cells with all concentrations of virus (Figure 6.1A). The B1-GFP virus infection reduced cell viability by more than 90% within 48 h of neat virus infection. A gradual decrease in cell viability with more diluted virus was observed in successive 10-fold dilutions of the virus after 48 h post-infection in Caco-2 cells. PC3 (Figure 6.1B) and A549 (Figure 6.1C) cells were found to be moderately susceptible to the B1-GFP infection only at higher viral doses (neat virus, 10^{-1} and 10^{-2} dilutions for PC3 cells; neat virus and 10^{-1} dilution for A549 cells). Liver cancer Hep G2 cells were susceptible only to the B1-GFP neat virus infection within 72 h (Figure 6.1D), whereas HeLa cells remained unaffected by the viral infection regardless of viral dose or duration of the infection (Figure 6.1E). Within 48 h post-infection (neat virus and 1:10 dilution), the non-cancerous MRC5 cells showed a reduction in cell viability. However, with a 1:10 dilution of B1-GFP, an increase in the cell viability of MRC5 cells was observed after 5 days (Figure 6.1F).

Oncolytic viruses acquire oncotropism by favourably infecting and replicating in cancer cells, as cancer cells have deficient cell death pathways and weaker antiviral responses. On the contrary, non-cancer cells' antiviral responses and cell death pathways are intact, hence non-cancer cells like MRC5 when infected with NDV at higher viral load are susceptible to death. However, with decreasing viral doses, MRC5 cells recovered from the infection and regained cell viability. The oncolytic efficacy of the virus is dependent on multiple factors, such as the efficiency of infection in cancer cells, type of virus, and natural and induced viral tropisms leading to the types of cell deaths, hence cancer cells

like HeLa, Hep G2, PC3 and A549 cells showed varying degrees of response to NDV doses in a time-dependent manner.

6.3.2 Identification of persistently infected VR Caco-2 Cells

After examining the susceptibility of Caco-2 cells to B1-GFP virus, further study focused on the Caco-2 cells. With the neat virus, which resulted in an estimated MOI of 50, most cells were infected and consequently died after 48 h post-infection. A small number of surviving cells (<1%) were unintentionally found after 12 days under microscopic examination, despite a high level of oncolysis, named as virus-resistant Caco-2 (VR Caco-2) cells. The VR Caco-2 cells that initially survived required 4–6 weeks to form colonies and ~4 months to reach 80–90% confluence. Infected and mock-infected Caco-2 cells were observed routinely under a conventional inverted bright-field microscope to assess the cell morphology and cytopathic effects of NDV infection. Under the microscope, the VR Caco-2 cells proliferated much more slowly than the uninfected Caco-2 cells.

NDV reinfection experiments with B1-GFP demonstrated a significant difference in the cell viability of the infected Caco-2 and VR Caco-2 cells (Figure 6.2A, B). While Caco-2 cells responded to B1-GFP infection in a dose-dependent manner (Figure 6.2A), no viral doses had an effect on VR Caco-2 cells at any time point, resulting in constant cell viability (Figure 6.2B). The cell cytotoxicity was measured in the infected Caco-2 and VR Caco-2 cells at low MOI of 0.1; Caco-2 cells showed significantly higher cytotoxicity than the VR Caco-2 cells upon infection, as illustrated in Figure 6.2C. Both tests confirmed the resistance of VR Caco-2 cells to NDV reinfection and NDV-induced

oncolysis.

The resistance to NDV superinfection and NDV-mediated cell death was acquired only in persistently infected (VR Caco-2) cells. VR Caco-2 cells produced a significantly low titre of replicating virus continuously. There are many possible reasons why only a small population of the cells sustained persistent infection. For instance, one possible explanation could be that Caco-2 is a heterogenous cell line known to differentiate spontaneously into different intestinal epithelial cells. Therefore, it is possible that some cells are more likely to inhabit persistent infection than others. The difference in the metabolic remodelling of parental wild-type Caco-2 cells relative to persistently NDV-infected VR Caco-2 cells is not substantial, as VR Caco-2 cells harbour a significantly low level of virus and do not become reinfected by NDV in the continuous cell culture. Although more research is required, it is possible that either receptor alteration of VR Caco-2 cells or the induction of an antiviral state in VR Caco-2 cells accounted for the resistance to reinfection.

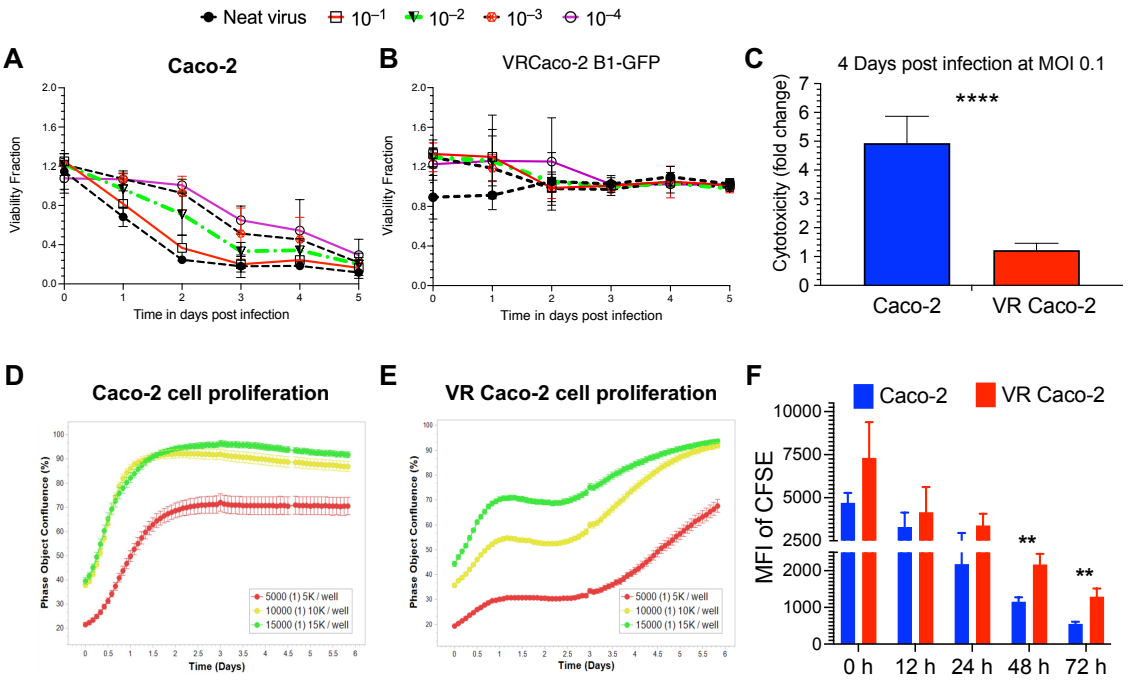


Figure 6.2 Characterisation of VR Caco-2 and Caco-2 cells. Cell viability

measured in NDV B1-GFP neat virus and 10-fold virus dilutions infected (A) Caco-2 and (B) VR Caco-2 cells in a 5-day virus killing curve assay. NDV reinfection experiments demonstrated resistance in VR Caco-2 cells. (C) Cell cytotoxicity assay of 0.1-MOI NDV B1-GFP-infected Caco-2 and VR Caco-2 cells 4 days post-infection demonstrated reduced cytotoxicity of VR Caco-2 cells. Cell proliferation assays showing (D) Caco-2 and (E) VR Caco-2 cell confluence monitored in real time using the Incucyte imaging system at different seeding densities. Phase object confluence (%) represents the surface area covered by cell monolayer in the culture plate. (F) Mean fluorescence intensity (MFI) of CFSE-stained Caco-2 and VR Caco-2 cells at different proliferation time points. CFSE dilution is significant at 48 h and 72 h in Caco-2 cells, indicating greater numbers of cell divisions than VR Caco-2 cells. Data (mean ± SD) shown here are from three independent experiments and analysed using multiple non-parametric t-tests (****: $p < 0.0001$; **: $p < 0.01$).

Similar to the microscopic observation of slower VR Caco-2 cell growth compared to the uninfected Caco-2 cells, cell proliferation assays by real-time monitoring of the cell confluence confirmed the slower proliferation of VR Caco-2 cells (Figure 6.2D and E). Caco-2 cells entered the log phase after less than 12 h in the lag phase and reached more than 90% confluence in 1.5 days after being seeded at 10,000 and 15,000 cells/well, at which point they entered the stationary phase. A similar pattern was seen in 5000 cells/well that had reached 70% confluence and had begun stationary development (Figure 6.2D). Contrarily, VR Caco-2 cells entered the exponential phase after around three days in the lag phase across all three densities, regardless of confluence. At all cell densities, VR Caco-2 cells displayed a distinct growth phase curve from Caco-2 cells. It took VR Caco-2 cells 5.5 days to reach >90% cell confluence at seeding densities of 10,000 and 15,000 cells/well (Figure 6.2E). The CFSE cell proliferation experiment confirmed that the growth of VR Caco-2 cells was

twice as slow as that of Caco-2 cells at 48 and 72 h after CFSE labelling (Figure 6.2F). Notably, VR Caco-2 cells displayed similar morphology in the cell culture monolayers as the Caco-2 cells.

6.3.3 Persistent VR Caco-2 can be identified by metabolic profiles at single-cell level

Despite initially being the most susceptible cell line for NDV-induced oncolysis, Caco-2 cells developed infection persistence in a small population of VR Caco-2 cells. To understand whether the metabolic profiles can be discriminated in the two groups of cells responsible for distinct infection manifestations, we employed single-cell Raman spectroscopy to investigate Caco-2 and VR Caco-2 cells. The averaged Raman spectra for VR Caco-2 and Caco-2 cells are shown in Figure 6.3A, averaged from 218 and 92 single cells, respectively. The fingerprint region (300–1800 cm^{-1}) illustrates biomolecular vibrational modes within a single cell, and the high wavenumber region (2800–3100 cm^{-1}) shows the intensive C–H stretching vibrations from lipids, proteins and nucleic acids.

First, an unsupervised t-distributed stochastic neighbour embedding (tSNE) analysis was used to visualise the high-dimensional Raman dataset in a two-dimensional space (Figure 6.3C). Interestingly, a degree of heterogeneity within populations was observed, especially in the VR Caco-2 cells. Three clusters were identified via k-means clustering. Cluster I was comprised mostly of the wild-type Caco-2 cells (73%); some of the VR Caco-2 cells in this cluster might still have had phenotypic resemblance to the wild-type cells. Cluster II was mostly made up of VR Caco-2 cells (97%) while cluster III, the most distant from the other two clusters, was the most heterogeneous (34% Caco-2 wild type and

66% VR Caco-2).

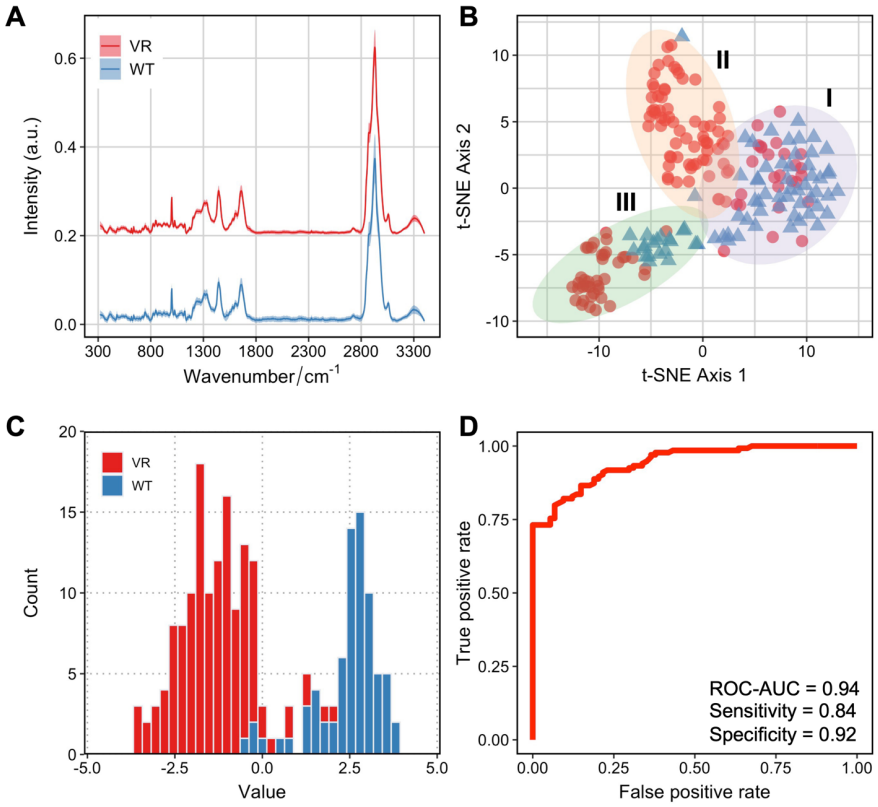


Figure 6.3 Distinct Raman profiles of Caco-2 and VR Caco-2 cells. Raman spectra of VR Caco-2 and Caco-2 cells averaged from 218 and 92 single cells, respectively. The shaded area represents standard deviation at each wavenumber from single-cell measurements. Raman spectra from each group was shifted and scaled in intensity to aid visualisation and the intensity is expressed in arbitrary unit (a.u.). (B) Unsupervised tSNE visualisation observes three distinct clusters I, II and III comprised of heterogeneous Caco-2 and VR Caco-2 single cells. (C) Histogram of values of a linear discriminant analysis (LDA) model to differentiate Caco-2 and VR Caco-2 based on their Raman spectra. (D) A receiver operating characteristic (ROC) curve was used to evaluate the LDA model performance. The area under the ROC curve (ROC-AUC) was 0.94 where 1 indicates perfect classification.

We then visualised the Raman profiles of the two groups in a supervised manner via linear discriminant analysis (LDA). The histogram of the LD values from the LDA clearly separates the VR Caco-2 and Caco-2 cells (Figure 6.3C).

In a binary classification task using LDA for differentiating VR Caco-2 and Caco-2 cells based on their SCRS, a receiver operating characteristic (ROC) curve was used to evaluate the model performance (Figure 6.3D). The area under the ROC curve (ROC-AUC) achieved 0.94 at single-cell level, where 1 indicates perfect classification. The supervised machine learning model demonstrates that the Raman profiles of the VR Caco-2 cells are distinctly different from those of the uninfected parental Caco-2 cells, suggesting significant metabolic reprogramming in those persistently infected cells. The development of persistent infections for oncolytic viruses may result in reduced oncolytic potential and compromised therapeutic outcomes[277]. Importantly, the persistent cancer cells are able to proliferate and produce populations that are resistant to the viruses. The ability to identify the subpopulations of resistant cells from the wild-type cancer cells is imperative in clinical settings.

6.3.4 Raman profiles differentiate VR Caco-2 and Caco-2 cells

Based on the most important variables selected by the LDA model, differential biomolecules were semi-quantified by integrating corresponding Raman bands and compared between VR Caco-2 and Caco-2 cells (Figure 6.4 and Table 6.1). Assignment of a Raman band is most accurate for the corresponding vibrational modes; nevertheless, assignments to biomolecules with specific vibrations are possible. A number of changes related to DNA/RNA, lipids and proteins are colour-coded in green, orange and blue, respectively, in Figure 6.4 Raman bands related to DNA/RNA at 680 cm^{-1}, which can be assigned to ring breathing modes in the DNA bases, were significantly lower in the resistant cells compared to the uninfected parental cells. This is consistent with the observation in the cell proliferation experiments that VR Caco-2 cells had a

much slower replication rate than Caco-2 cells. A number of Raman biomarkers related to protein synthesis were significantly lower in the VR Caco-2 cells, including Amide III at 1200–1300 cm^{-1}, Amide I at 1600–1690 cm^{-1} and C–C vibrations of tryptophan and phenylalanine at 1210 cm^{-1} (Figure 6.4). An increase in protein synthesis and a decrease in nucleic acids in the VR Caco-2 cells suggest that energy could be redirected from proliferation to anabolism in those resistant cells for synthesising more proteins and metabolic reprogramming.

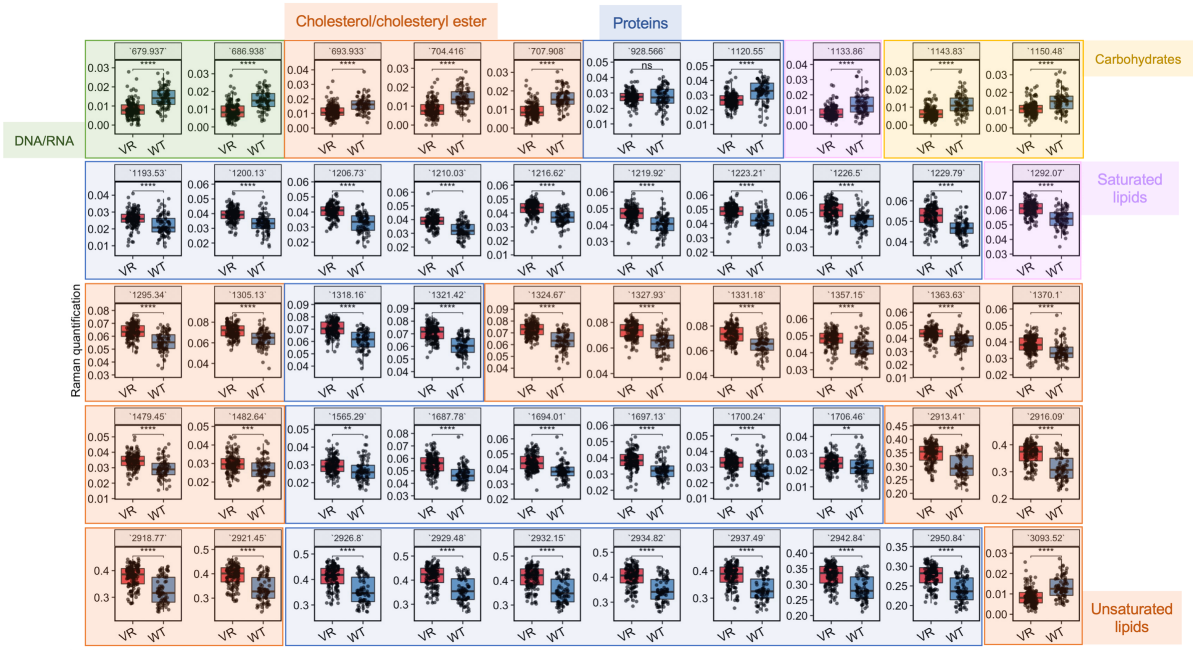


Figure 6.4 Quantification of biomolecules in Caco-2 and VR Caco-2 based on their SCRS. Differential Raman bands selected based on the LDA model were quantified and compared between Caco-2 and VR Caco-2 cells. All Raman bands are colour-coded as green (DNA/RNA), orange (lipids) or blue (proteins). Statistics was done with Student's *t*-test (ns: $p > 0.05$; **: $p < 0.01$; ***: $p < 0.001$; ****: $p < 0.0001$). VR: VR Caco-2; WT: Caco-2.

The lipidic profiles were also significantly modified in the VR Caco-2 cells. Several bands of saturated lipids exhibited an increase in the VR Caco-2 cells; for example, 1295 cm^{-1} for CH_2 deformation, 1370 cm^{-1} for CH_3 stretching,

1480 cm^{-1} for CH_2 bending and 2913 cm^{-1} for CH_2 stretching. On the other hand, =CH stretching for unsaturated lipids and vibrations in cholesterols and cholesteryl esters demonstrated significant decreases in the VR Caco-2 cells compared to the parental Caco-2. Production of phospholipids in combination with deceased proliferation rates suggests the development of a more saturated and robust plasma membrane. A plasma membrane is made up of lipids, particularly phospholipids and cholesterol, which function as integral pump proteins for multidrug efflux transporters from the ATP-binding cassette (ABC) superfamily. It has been shown that efflux pump activity could be modulated via the development of a more robust plasma membrane for favourable drug binding and release, thus conferring resistance to anti-cancer agents[269]. A decrease in the C–C and C–O ring breathing in the carbohydrates at 1150 cm^{-1} was also observed, suggesting that utilisation of carbohydrates might not be advantageous, and the resistant Caco-2 cells might use alternative nutrients, such as lipids.

6.3.5 Raman-DIP reveals metabolic reprogramming via newly synthesised biomolecules

We next sought to use Raman-DIP to probe the general and specific metabolic activities of VR Caco-2 and Caco-2 cells. SCRS of cells incubated with D_2O showed a distinguishable C–D band centred at 2170 cm^{-1}, with its intensity gradually increased from 0 h to 72 h in both VR Caco-2 and Caco-2 cells (Figure 6.5A). This band was shifted from the C–H stretching from 2800–3100 cm^{-1} due to the incorporation of D via C/D exchange during active metabolism. Hence, the D incorporation in cells can be used as a universal indicator of

metabolic activity and was calculated as the ratio of (C–D) / (C–D) + (C–H).

Figure 6.5B shows the comparison of D incorporation, hence the metabolic activities, between the two groups of cells at 0, 12, 48 and 72 h. At 12 h, Caco-2 cells exhibited a higher metabolic rate compared to the VR Caco-2 cells, in agreement with the cell proliferation assay showing that the Caco-2 cells replicated much faster than the VR Caco-2 cells and had a much shorter lag phase (Figure 6.2D and E). Intriguingly, metabolism at 24 and 48 h suggested opposite results to the proliferation assay. Despite being two times slower in proliferation at 48 h and 72 h (Figure 6.2F), VR Caco-2 showed a significantly higher metabolic activity at 24 and 48 h (Figure 6.5B). At 72 h, the Caco-2 cells caught up and the 2 groups of cells had similar metabolic activities.

Due to the statistical significance at 48 h in both the proliferation assay and DIP experiment, the C–D band at 48 h was selected for further analysis. Previous studies have shown the C–H signal is a linear overlap of C–H stretching from lipids, proteins and DNA; therefore, the C–D signal is a combination of de novo lipid synthesis (I_{2190}), de novo protein synthesis (I_{2150}) and DNA replication (I_{2125})[278106]. The C–D band can therefore be resolved into individual components of newly synthesised biomolecules via a linear unmixing algorithm (Figure 6.5C). At 48 h, both the de novo protein and de novo lipid synthesis in the VR Caco-2 cells increased, while the newly synthesised DNA was significantly lower than the control Caco-2 cells. Together with the decreased DNA/RNA content and increased protein synthesis (Figure 6.4), the DIP experiments suggest that the escape strategy of the resistant VR Caco-2 cells from the viral infection might be slowing down their replication and redirecting the energy to protein synthesis and metabolic reprogramming, such as forming

a more robust plasma membrane. Notably, this finding should be tested in other cell lines to determine if it is one of the universal mechanisms to generate resistance. In future studies, it should also be confirmed using other technologies, such as measurements of cellular respiration or lipidomic mass spectroscopy.

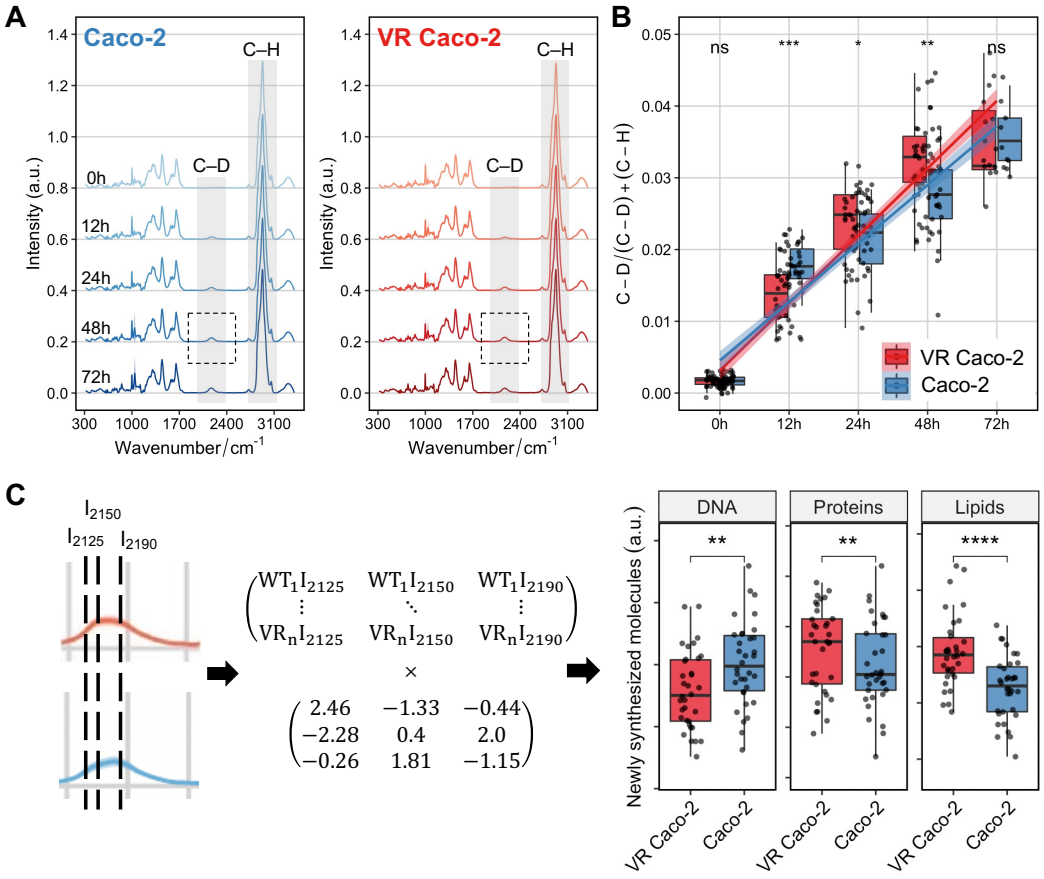


Figure 6.5 Raman-DIP of newly synthesised DNA, proteins and lipids. (A) Raman spectra of VR Caco-2 and Caco-2 cells cultured with 30% D_2O at different incubation time points. The Raman band of C–H vibrations was shifted to a C–D band at 2070–2300 cm^{-1}, highlighted in the grey box. (B) Metabolic activities of VR Caco-2 and Caco-2 cells were quantified and compared at each time point by calculating the ratio of C–D/(C–D) + (C–H). (C) Linear unmixing algorithm for calculating newly synthesised DNA at 2125 cm^{-1}, proteins at 2150 cm^{-1} and lipids at 2190 cm^{-1}. WT: Caco-2; VR: VR Caco-2. Statistics was done with Student's *t*-test (ns: $p > 0.05$; *: $p < 0.05$; **: $p < 0.01$; ***: $p < 0.001$; ****: $p < 0.0001$).

Resistance to chemotherapy and targeted small molecule inhibitors has been found in multiple cancer types[279–282]. It has been proposed that a sizeable proportion of "idling" cells contribute to the persistent disease in BRAF-mutated melanoma patients after targeted inhibitor therapy[279]. Persisters' observed nonquiescent and antiproliferative properties matched well with our persisters' slower proliferation but more active metabolism. It has also been found that upregulation of antioxidant genes and metabolic engineering towards fatty acid oxidation are associated with persisters across multiple cancer types[283], which may correlate with the observation of increased fatty acid synthesis in VR Caco-2 cells. Our study provides phenotypic and metabolic evidence of cancer cells' resistance to viral infection, while little is known about the mechanisms of resistance to viral therapy. Moreover, the emerging reservoir of heterogeneous drug-resistance cells and mechanisms[282] highlights the importance of single-cell techniques in investigating drug-tolerant cancer persister cells. By combining the power of optical magnification and confocality, Raman micro-spectroscopy even has the potential to explore biological processes at subcellular level. It may collectively provide label-free Raman images with subcellular structural and chemical information. In future studies, spatially resolved Raman images could be generated to locate biomolecules within a specific cellular compartment and therefore further pin down the underlying mechanistic pathways.

Table 6.1 Molecular vibrations and biological assignment of Raman wavenumbers of importance via LDA model.

Raman Wavenumber (cm^{-1})	Molecular Vibrations and Biological Assignment	Reference

680	Guanine; ring breathing modes in the DNA bases/C-2′-endo-anti	284
700	Cholesterol, cholesterol ester	285
929	Proline, hydroxyproline, ν(C–C) skeletal of collagen backbone	286
1121	C–N stretching of proteins	268
1134	ν(C–C) skeletal of acyl backbone in lipid (trans conformation)	287
1150	C–C, C–O ring breath, glycogen	288
1200	Amide III and CH_2 wagging vibrations	289
1210	Tryptophan and phenylalanine ν(C–C6H5) mode	290
1230–1300	Amide III (arising from coupling of C–N stretching and N–H bonding)	291
1295	CH_2 deformation in lipids	292
1320	Amide III, C–H deformation	291
1370	CH_3 stretching in phospholipids	292
1479	CH_2 bending mode of proteins and lipids	293
1483	CH_2 bending mode of proteins and lipids	293
1480–1580	Amide II of proteins	268
1600–1690	Amide I of proteins	268
2913	CH_3 stretching of lipids	285
2950	CH_3 stretching of proteins	284
3010	Unsaturated =CH stretching	285

6.4 Conclusions

Resistance of cancer cells to NDV is a major obstacle to the development of the oncolytic virus as a promising cancer treatment. Upon infection of a non-pathogenic strain of NDV to a range of cancer cell lines, Caco-2 cells were found to be most susceptible to NDV killing. However, a subpopulation of Caco-2 cells with persistent infection was identified as VR Caco-2. Compared to their non-infected counterpart, VR Caco-2 cells grew much more slowly and demonstrated resistance towards NDV reinfction and NDV-induced cell death. To understand the metabolic adaptations of the resistant VR Caco-2 cells, single-cell Raman spectroscopy and Raman-DIP techniques were employed to

identify the persistent NDV infection in cancer cells. The LDA model has achieved high performance in distinguishing VR Caco-2 and Caco-2 cells at single-cell level with an ROC-AUC of 0.94. Furthermore, the metabolism of those resistant cells was investigated. The Raman profiling and Raman-DIP experiments unveiled an increased de novo synthesis of proteins and lipids, accompanied by a decreased DNA/RNA synthesis. Despite having a much slower replication rate, the VR Caco-2 cells exhibited more active metabolism at 24 and 48 h after infection. The results suggest that the resistant VR Caco-2 cells might employ an escape mechanism from the viral infection to slow down their replication and redirect the energy to protein synthesis and metabolic reprogramming.

As with other cancer therapies, treatments based on oncolytic viruses like NDV face the challenge of resistance. The existence of a subpopulation of drug-resistant cancer cells poses difficulty and complexity in identifying them due to their small number, <1% in the case of Caco-2. Being able to recognise them at single-cell level with high accuracy would be hugely beneficial in the process of developing new cancer treatment. Applying the methods in combinational and personalised medicine, Raman and Raman-D_2O techniques can quickly identify and characterise resistant cells that are still metabolically active based solely on their metabolic phenotypes, thus helping equip better strategies and improve efficacy for fighting treatment resistance in cancer.

Supplementary Materials: The following supporting information can be downloaded at: www.mdpi.com/xxx/s1.

Author Contributions: Conceptualisation and design: V.N. and W.E.H.; data curation: T.Y. and A.C.J.; data analysis and visualisation: A.C.J. and J.X.; supervision: A.L.H., V.N. and W.E.H.; original manuscript writing: J.X. and W.E.H. All authors have read and agreed to the published version of the manuscript.

Funding: The authors thank EPSRC (EP/M002403/1 and EP/M02833X/1) and NERC (NE/M002934/1) for finance and instrumentation support. This research was also supported by the Biotechnology and Biological Sciences Research Council (BBSRC) grants BBS/E/I/00007032, BBS/E/I/00007039 and BB/R007896/1, the BBSRC Newton Fund which supported Joint Centre Awards on “UK-China Centre of Excellence for Research on Avian Diseases” (BBS/OS/NW/000007) and UK-India Joint Centre on Animal Technology. We also thank the international collaboration project between the University of Oxford and Suzhou Institute of Biomedical Engineering and Technology, Chinese Academy of Sciences.

Data Availability Statement: Data is available from Figshare at 10.6084/m9.figshare.21960743.

Conflicts of Interest: The authors declare no conflict of interest.

Chapter 7

Summary and Perspectives

7.1 Work summaries

SCRM is a novel technique in cancer cell metabolism research, and its application has been gradually explored in the last few years. This thesis describes an application of SCRM and Raman–SIP to study the alterations and profiles of cancer cell metabolism. The results of this thesis fully demonstrate the advantages of SCRM, which are 1) reliable quantitative data analysis, 2) non-destructive measurement, 3) sensitive monitoring and 4) high-resolution spatial mapping.

I optimized the Raman imaging method for cells by seeding cells on poly-L-lysine modified aluminium slides. The traditional method of drop-casting cell suspension onto aluminium slides leads to cell aggregation and folding due to the highly hydrophobic and charged nature of the surface. The improved method enables control over cell numbers and confluency while preserving cell viability, resulting in high-resolution Raman images. This method can be further optimized by developing cell growth protocols.

The significance of SCRM and Raman–SIP techniques are demonstrated across the four research chapters, which involve the use of isotopic labelling

using ^{2}H in heavy water, ^{13}C-glucose, and ^{13}C-glutamine. Through analysis of Raman spectra, key scientific questions related to 'what, when, where, and how' can be answered.

- **What is it?**

The Raman spectra are highly informative and can provide extensive data on numerous substances. Chapter 3 of the research identified the characteristic peak of bicarbonate at 1043 cm^{-1} through CA9 knockdown and inhibitor. In chapter 4, glycogen's three characteristic peaks (480, 850, and 940 cm^{-1}) were determined through glycogen extract analysis. The same glycogen peak pattern was observed in PYGL knockout cells. Upon ^{13}C labelling, the glycogen peaks shifted to 465, 836, and 922 cm^{-1}, and the glycogen structure was found to correlate with its characteristic Raman peaks. The 480-cm^{-1} band corresponds to short, branched structures present in large glycogen granules, the 850-cm^{-1} band contributes to the straight chain glycosidic linkage of α-D-(1 → 4), which forms the basic framework of glycogen, and is the dominant peak in small spots. The 940-cm^{-1} band, in contrast to the former, represents the branching point or branched end in glycogen, α-D-(1 → 6) glycosidic linkage.

Through years of research, a database of Raman spectra has been established, which allows for the identification of characteristic peaks for various biomolecules. In this thesis, the mitochondria, nucleic acids, proteins, and fatty acids marker peaks were all identified based on the information from the Raman database.

- **Where is it?**

A key finding of this thesis is the illustration of the distribution of glycogen at single-cell level, which has been a challenge in previous research. Traditional imaging techniques such as electron microscopy, fluorescence microscopy, mass spectrometry, and nanoparticles targeting have the inevitable limitations of labelling, complex sample preparation, sample damages, and low resolution[294–299]. However, the advantages of SCRM can largely overcome these issues.

Chapter 4 demonstrates the application of Raman mapping technique to investigate glycogen distribution at the single-cell level. The results showed that high glycogen spots were randomly distributed in the cytoplasm, while no obvious glycogen granules were detected in the nuclear region. Most of the glycogen sizes were relatively small, and large glycogen granules were formed by the gradual expansion of small glycogen from the centre outwards. By altering the extratumoural microenvironment, such as glucose and oxygen availability, it is possible to compare the two sets of cell images and observe changes in glycogen metabolism. The study revealed that glycogen spots were much larger in hypoxia than in normoxia, providing impressive localization of the massive production of glycogen in the cell plasma induced by hypoxia.

In addition, this thesis also presents the distribution maps of proteins, lipids, DNA/RNA and mitochondrial using a combination of SCRM to confirm substance peaks and Raman imaging techniques. These maps enable the

visualization of different substances at the cellular level and give compelling insights for the phenotypic discoveries of cancer metabolism.

- **When is it?**

In both Chapter 4 and Chapter 6, I conducted time-course labelling experiments. SCRM is able to detect metabolic changes and rates in cells from cell samples taken at different time points.

In Chapter 4, ^{13}C probing is an important indicator in the process of glycogen synthesis. By calculating the quantity and distribution of ^{12}C and ^{13}C-glycogen, it allows us to trace the metabolic footprint of glycogen in the cell. Glycogen is synthesized rapidly in cancers, and a 3-hour incubation is sufficient for Raman microscopy to detect the presence of glycogen in single cells. During the period of rapid cell growth, glycogen is constantly being synthesized and degraded to provide energy for the cells. It is only 24 to 48 hours later that the cells begin to store glycogen as a backup energy source.

In Chapter 6, the Raman profiling and Raman–DIP discovered that VR Caco-2 cells had a more active metabolism after 24 and 48 hours, even though their rate of replication was substantially slower. Deuterium incorporation quickly identifies resistant cells that are still metabolically active based solely on their metabolic phenotypes. The new biomolecular synthesis has gone towards proteins and lipids, while DNA/RNA synthesis has decreased over the same period.

One advantage of the Raman spectroscopy over other techniques is that it is non-invasive and can be used with isotopic labelling to track the metabolism of cancer cells over time. Raman spectroscopy can detect the appearance, transformation, and disappearance of specific molecules, and can provide information on the rates of these processes at different time points.

- **How is it?**

SCRM allows for the identification and analysis of various biomolecules, including proteins, lipids, nucleic acids, and mitochondria, based on their characteristic Raman spectra. This can provide valuable insights into the metabolic processes occurring in cells and their associated functional information. The high spectral resolution of Raman spectroscopy also allows for semi-quantitative analysis, providing information about the relative abundance of different molecules in a sample. Raman–SIP is implicated in specific metabolic reactions, thereby uncovering functional information about the metabolism of substrates.

Chapter 3 discusses the role of CA9 in controlling HCO_3^- fluxes, particularly the import of extracellular HCO_3^- under hypoxia. Mitochondrial respiratory metabolism is a major endogenous source of HCO_3^-. By blocking the import of HCO_3^- into the cell during hypoxia, the mitochondria can still provide HCO_3^- by hydrolysing CO_2. The metabolism of bicarbonate is also thought to be related to glycolysis and the regulation of cellular pH.

In the Chapter 4 and 5, ^{13}C labelling was used to the investigation of glycogen and glutamate metabolism. Single-cell Raman is an effective method for elucidating the location of glycogen and its association with other biological components in combination with isotopic detection. When ^{13}C-glucose entered the cancer cells, it was preferentially converted into glycogen and amino acids. With a continuous supply of sufficient glucose, glycogen was stored and formed large glycogen granules. Cancer cells required additional time to generate more complex isomers for the synthesis of new lipids and proteins. The ^{13}C-glutamine labelling activity implicated that it was converted preferentially to nucleic acids, amino acids and fatty acids, and was not involved in glycogen synthesis in short incubation.

Chapter 6 is an application of Raman-DIP technique to the metabolic activity of virus-infected cancer cells. In virus-infected Caco-2, it was discovered that the synthesis of proteins and lipids increased while DNA synthesis was downregulated. According to the findings, virus-infected Caco-2 cells might rewire their metabolism so that energy is instead directed toward protein synthesis and lipidic regulation instead of proliferation.

7.2 Limitations

This thesis presents preliminary results on the energy metabolism of cancer cells. Due to the pandemic, my experimental work was interrupted for eight months. This resulted in a part of my project lacking supporting data, especially

in chapter 5 on glutamine metabolism. Due to time pressure, I did not complete ^{13}C-glutamine and heavy water time-course labelling experiments, and the work on the effects of different glucose concentrations has not been replicated. This part of the data is not shown in this thesis.

The project still has some issues that could be improved. In chapter 3 on glycogen metabolism, it would be a good idea to expand on the effects of gene knockdown on glycogen synthesis. Further work can be done to investigate the role of glycogenin, the core protein of glycogen[300]. The glycogenin-1 (GYG1) for glycogen synthase can be blocked down to detect the expression of glycogen[301]. This section could be added to the manuscript on glycogen metabolism in the future.

Raman has the merit of providing whole-window information, but it loses the benefit of fast acquisition time. The testing time for a single U87 cell is approximately 20-40 minutes, making it impossible to measure large numbers of cell samples.

The lengthy acquisition times posed a challenge in conducting measurements on the same day, leading to potential errors in the data due to variations across different test days. Although efforts were made to address these errors through data processing, it was not possible to completely eliminate the influence of time on molecular structure, dynamic changes, and metabolic activity. Enhancing acquisition times stands as a crucial aspect to consider for the future

advancement of Raman spectroscopy.

Studies have been successfully undertaken to enhance and denoise Raman signals to speed up measurements via machine learning[302]. I have done measurements on U87 cells at 0.5, 1 and 3-s acquisition time, and I may collaborate with other colleagues in the future to help reduce the Raman acquisition time via machine learning.

An additional limitation is the accuracy of the data processing method employed. A significant number of semi-quantitative calculations were utilized, involving the calculation of peak areas using a code program. The Gaussian model was employed to simulate the curve of the target peak and integrate it to determine the area under the curve. However, due to the overlapping nature of Raman peaks, the target peak area often includes contributions from neighbouring peaks. While the Gaussian model captures the shape of individual peaks, it does not account for the presence of overlapping peaks, leading to a reduction in data accuracy. It is important to note that all peak intensities or areas presented in this thesis are semi-quantitative, and the current data processing methods have limitations in achieving a high level of quantitative analysis.

7.3 Perspectives

SCRM and Raman–SIP provide a wealth of data information on cancer cell metabolism, enabling simultaneous semi-quantitative analysis and distribution imaging. When applied to samples treated with anti-cancer drugs and inhibitors,

Raman technique can indicate the reprogramming response of metabolic activities and related anabolisms. In the future, it has the potential to aid in studying metabolic pathways, cancer drug screening, and improving the efficacy of cancer therapy.

Moreover, the combination of SCRM and AI technology is a promising research direction in cancer research. Raman spectra contain a large amount of information that can be useful for big data analysis. Unsupervised deep learning neural networks can automatically denoise Raman images, allowing for instant training on other datasets or images[303]. Additionally, automatic Raman imaging can be achieved through k-means clustering algorithms, convolutional neural networks, or least squares analysis, resulting in image segmentation[303–305]. It is also possible to enhance the pixel count of an image through computational algorithms while simultaneously analysing the different components on the Raman spectrum and visualising their spatial position[306].

Recently, time-gated Raman spectroscopy has been applied to proteomics studies to capture protein signatures[307]. Combining SCRM with genome sequencing can establish phenome-genome links by calculating genomic assemblies with high coverage and sensitivity[308]. The benefits of mechanistic learning allow Raman technology to improve imaging, gene expression prediction, medical diagnosis, digital histopathology and tumour subtype classification in cancers[309–312]. The combination of Raman spectroscopy and AI offers significant advantages for the future cancer metabolism research and

clinical diagnosis, including high-speed detection, workload reduction, and cost-effectiveness.

While this thesis focuses on cellular metabolism, Raman technology can also be used for tissue and non-invasive clinical detection. SCRM technique has the potential to bridge the gap between tissue and cells, as cells are the basic structural and functional unit of organisms. Understanding the rules of cancer biology requires measuring phenotype and molecular signatures from single-cell resolution to tumour tissue analysis and clinical diagnosis.

References

1. Huang WE, Griffiths RI, Thompson IP, Bailey MJ, Whiteley AS. Ra man microscopic analysis of single microbial cells. *Anal Chem*. 200 4;76(15):4452-4458.

2. Warburg O. On the origin of cancer cells. *Science (80-)*. 1956;123 (3191):309-314.

3. Pavlova NN, Thompson CB. The Emerging Hallmarks of Cancer M etabolism. *Cell Metab*. 2016;23(1):27-47.

4. Liberti M V, Locasale JW. The Warburg effect: how does it benefit cancer cells? *Trends Biochem Sci*. 2016;41(3):211-218.

5. Nelson DL, Lehninger AL, Cox MM. *Lehninger Principles of Bioche mistry*. Macmillan; 2008.

6. Shestov AA, Liu X, Ser Z, et al. Quantitative determinants of aerob ic glycolysis identify flux through the enzyme GAPDH as a limiting step. *Elife*. 2014;3:e03342.

7. Shulman GI, Landau BR. Pathways of glycogen repletion. *Physiol Rev*. 1992;72(4):1019-1035.

8. Zois CE, Favaro E, Harris AL. Glycogen metabolism in cancer. *Bio chem Pharmacol*. 2014;92(1):3-11.

9. Zois CE, Harris AL. Glycogen metabolism has a key role in the ca ncer microenvironment and provides new targets for cancer therapy. *J Mol Med*. 2016;94(2):137-154.

10. Yoo HC, Yu YC, Sung Y, Han JM. Glutamine reliance in cell meta bolism. *Exp Mol Med*. 2020;52(9):1496-1516.

11. Lin H, Miyauchi K, Harada T, et al. CO2-sensitive tRNA modificatio n associated with human mitochondrial disease. *Nat Commun*. 201 8;9(1).

12. Young FG. Claude Bernard and the discovery of glycogen. *Br Med J*. 1957;1(5033):1431.

13. Calder PC. Glycogen structure and biogenesis. *Int J Biochem*. 199 1;23(12):1335-1352.

14. Rousset M, Dussaulx E, Chevalier G, Zweibaum A. Growth-related glycogen levels of human intestine carcinoma cell lines grown in vit ro and in vivo in nude mice. *J Natl Cancer Inst*. 1980;65(5):885-88

9.

15. Witney TH, Carroll L, Alam IS, et al. A novel radiotracer to image glycogen metabolism in tumors by positron emission tomography. *C ancer Res*. 2014;74(5):1319-1328.

16. Apaoblaza A, Galaz A, Strobel P, Ramírez-Reveco A, Jeréz-Timaur e N, Gallo C. Glycolytic potential and activity of adenosine monoph osphate kinase (AMPK), glycogen phosphorylase (GP) and glycoge n debranching enzyme (GDE) in steer carcasses with normal (< 5. 8) or high (> 5.9) 24 h pH determined in M. longissimus dorsi. *Me at Sci*. 2015;101:83-89.

17. Jope RS, Johnson GVW. The glamour and gloom of glycogen synt hase kinase-3. *Trends Biochem Sci*. 2004;29(2):95-102.

18. Dauer P, Lengyel E. New roles for glycogen in tumor progression. *Trends in cancer*. 2019;5(7):396-399.

19. Allué LAQ, Belocopitow E, Maréchal LR. Glycosyl transfer to an ac ceptor lipid from insects. *Biochem Biophys Res Commun*. 1975;66 (4):1201-1208.

20. Smythe C, Cohen P. The discovery of glycogenin and the priming mechanism for glycogen biogenesis. *EJB Rev 1991*. Published onli ne 1991:149-155.

21. Whelan WJ. The initiation of glycogen synthesis. *Bioessays*. 1986;5 (3):136-140.

22. Pitcher J, Smythe C, Campbell DG, Cohen P. Identification of the 38-kDa subunit of rabbit skeletal muscle glycogen synthase as glyc ogenin. *Eur J Biochem*. 1987;169(3):497-502.

23. Khan T, Sullivan MA, Gunter JH, et al. Revisiting glycogen in canc er: a conspicuous and targetable enabler of malignant transformatio n. *Front Oncol*. 2020;10:592455.

24. Rocha Leão MHM. GLYCOGEN. *Encycl Food Sci Nutr*. Published online 2003:2930-2937.

25. Cori GT, Colowick SP, Com CF. The activity of the phosphorylating enzyme in muscle extract. *J Biol Chem*. 1939;127:771-782.

26. Newgard CB, Nakano K, Hwang PK, Fletterick RJ. Sequence analy sis of the cDNA encoding human liver glycogen phosphorylase rev eals tissue-specific codon usage. *Proc Natl Acad Sci*. 1986;83(21):8 132-8136.

27. Newgard CB, Littman DR, van Genderen C, Smith M, Fletterick RJ.

Human brain glycogen phosphorylase. Cloning, sequence analysis, chromosomal mapping, tissue expression, and comparison with the human liver and muscle isozymes. *J Biol Chem*. 1988;263(8):3850-3857.

28. Burke J, Hwang P, Anderson L, Lebo R, Gorin F, Fletterick R. Intr on/exon structure of the human gene for the muscle isozyme of gl ycogen phosphorylase. *Proteins Struct Funct Bioinforma*. 1987;2(3): 177-187.

29. Harris AL. Hypoxia—a key regulatory factor in tumour growth. *Nat Rev cancer*. 2002;2(1):38-47.

30. Warburg O. The metabolism of carcinoma cells. *J Cancer Res*. 192 5;9(1):148-163.

31. Jones RG, Thompson CB. Tumor suppressors and cell metabolism: a recipe for cancer growth. *Genes Dev*. 2009;23(5):537-548.

32. Patiar S, Harris AL. Role of hypoxia-inducible factor-1α as a cancer therapy target. *Endocr Relat Cancer*. 2006;13(Supplement_1):S61-S75.

33. Newmeyer DD, Ferguson-Miller S. Mitochondria: releasing power for life and unleashing the machineries of death. *Cell*. 2003;112(4):48 1-490.

34. King MP, Attardi G. Human cells lacking mtDNA: repopulation with exogenous mitochondria by complementation. *Science (80-)*. 1989; 246(4929):500-503.

35. Grasso D, Zampieri LX, Capelôa T, Van de Velde JA, Sonveaux P. Mitochondria in cancer. *Cell Stress*. 2020;4(6):114.

36. Wallace DC. Mitochondria and cancer. *Nat Rev Cancer*. 2012;12(1 0):685-698.

37. Tan AS, Baty JW, Dong LF, et al. Mitochondrial genome acquisitio n restores respiratory function and tumorigenic potential of cancer c ells without mitochondrial DNA. *Cell Metab*. 2015;21(1):81-94.

38. Liu Y, Chen C, Wang X, et al. An epigenetic role of mitochondria i n cancer. *Cells*. 2022;11(16):2518.

39. Jeena MT, Kim S, Jin S, Ryu J-H. Recent progress in mitochondri a-targeted drug and drug-free agents for cancer therapy. *Cancers (Basel)*. 2019;12(1):4.

40. Heiden MGV, Cantley LC, Thompson CB. Understanding the warbu rg effect: The metabolic requirements of cell proliferation. *Science*

(80-). 2009;324(5930):1029-1033.

41. Wallace DC. Mitochondria and cancer. *Nat Rev Cancer*. 2012;12(10):685-698.

42. Medina MA. Glutamine and cancer. *J Nutr*. 2001;131(9):2539S-2542S.

43. Rose WC. The nutritive significance of the amino acids. *Physiol Rev*. 1938;18(1):109-136.

44. Rose WC. The nutritive significance of the amino acids and certain related compounds. *Science (80-)*. 1937;86(2231):298-300.

45. Lopez MJ, Mohiuddin SS. Biochemistry, essential amino acids. Published online 2020.

46. Hou Y, Yin Y, Wu G. Dietary essentiality of “nutritionally non-essential amino acids” for animals and humans. *Exp Biol Med*. 2015;240(8):997-1007.

47. Combs JA, DeNicola GM. The non-essential amino acid cysteine becomes essential for tumor proliferation and survival. *Cancers (Basel)*. 2019;11(5):678.

48. Hope HC, Salmond RJ. The Role of Non-essential Amino Acids in T Cell Function and Anti-tumour Immunity. *Arch Immunol Ther Exp (Warsz)*. 2021;69(1):1-9.

49. Lacey JM, Wilmore DW. Is glutamine a conditionally essential amino acid? *Nutr Rev*. 1990;48(8):297-309.

50. Labow BI, Souba WW. Glutamine. *World J Surg*. 2000;24(12):1503-1513.

51. Wu J, Li Z, Yang Z, et al. A glutamine-rich carrier efficiently delivers anti-CD47 siRNA driven by a “glutamine trap” to inhibit lung cancer cell growth. *Mol Pharm*. 2018;15(8):3032-3045.

52. Wise DR, Thompson CB. Glutamine addiction: a new therapeutic target in cancer. *Trends Biochem Sci*. 2010;35(8):427-433.

53. Yoo HC, Park SJ, Nam M, et al. A variant of SLC1A5 is a mitochondrial glutamine transporter for metabolic reprogramming in cancer cells. *Cell Metab*. 2020;31(2):267-283.

54. Altman BJ, Stine ZE, Dang C V. From Krebs to clinic: glutamine metabolism to cancer therapy. *Nat Rev Cancer*. 2016;16(10):619-634.

55. Matés JM, Campos-Sandoval JA, de Los Santos-Jiménez J, Márquez J. Dysregulation of glutaminase and glutamine synthetase in can

cer. *Cancer Lett*. 2019;467:29-39.

56. DeBerardinis RJ, Mancuso A, Daikhin E, et al. Beyond aerobic glyc olysis: transformed cells can engage in glutamine metabolism that exceeds the requirement for protein and nucleotide synthesis. *Proc Natl Acad Sci*. 2007;104(49):19345-19350.

57. Cooper AJL, Jeitner TM. Central role of glutamate metabolism in th e maintenance of nitrogen homeostasis in normal and hyperammon emic brain. *Biomolecules*. 2016;6(2):16.

58. Hertz L, Rothman DL. Glutamine-glutamate cycle flux is similar in c ultured astrocytes and brain and both glutamate production and oxi dation are mainly catalyzed by aspartate aminotransferase. *Biology (Basel)*. 2017;6(1):17.

59. Sullivan LB, Gui DY, Hosios AM, Bush LN, Freinkman E, Vander Heiden MG. Supporting aspartate biosynthesis is an essential functi on of respiration in proliferating cells. *Cell*. 2015;162(3):552-563.

60. Zhang J, Fan J, Venneti S, et al. Asparagine plays a critical role i n regulating cellular adaptation to glutamine depletion. *Mol Cell*. 20 14;56(2):205-218.

61. Ye J, Fan J, Venneti S, et al. Serine catabolism regulates mitocho ndrial redox control during hypoxia. *Cancer Discov*. 2014;4(12):1406 -1417.

62. Cluntun AA, Lukey MJ, Cerione RA, Locasale JW. Glutamine meta bolism in cancer: understanding the heterogeneity. *Trends in cance r*. 2017;3(3):169-180.

63. Filipp F V, Ratnikov B, De Ingeniis J, Smith JW, Osterman AL, Sc ott DA. Glutamine-fueled mitochondrial metabolism is decoupled fro m glycolysis in melanoma. *Pigment Cell Melanoma Res*. 2012;25(6): 732-739.

64. Lane AN, Fan TWM. Regulation of mammalian nucleotide metabolis m and biosynthesis. *Nucleic Acids Res*. 2015;43(4):2466-2485.

65. Stumvoll M, Perriello G, Meyer C, Gerich J. Role of glutamine in h uman carbohydrate metabolism in kidney and other tissues. *Kidney Int*. 1999;55(3):778-792.

66. Ali ES, Lipońska A, O'Hara BP, et al. The mTORC1-SLC4A7 axis stimulates bicarbonate import to enhance de novo nucleotide synth esis. *Mol Cell*. 2022;82(17):3284-3298.

67. Gorbatenko A, Olesen CW, Boedtkjer E, Pedersen SF. Regulation and roles of bicarbonate transporters in cancer. 2014;5(April):1-15.

68. Geyer RP, Chang RS. Bicarbonate as an essential for human cells in vitro. *Arch Biochem Biophys*. 1958;73(2):500-506.

69. Alka K, Casey JR. Critical Review Bicarbonate Transport in Health and Disease. *IUBMB Life*. 2014;66(9):596-615.

70. Romero MF. Molecular pathophysiology of SLC4 bicarbonate transp orters. *Curr Opin Nephrol Hypertens*. 2005;14(5):495-501.

71. Giatromanolaki A, Harris AL, Banham AH, Contrafouris CA, Koukou rakis MI. Carbonic anhydrase 9 (CA9) expression in non-small-cell l ung cancer: correlation with regulatory FOXP3+ T-cell tumour strom a infiltration. *Br J Cancer*. 2020;122(8):1205-1210.

72. Guan S-S, Wu C-T, Liao T-Z, et al. A novel 111indium-labeled dua l carbonic anhydrase 9-targeted probe as a potential SPECT imagi ng radiotracer for detection of hypoxic colorectal cancer cells. *Eur J Pharm Biopharm*. 2021;168:38-52.

73. Paškevičiūtė M, Petrikaitė V. Application of carbonic anhydrase inhi bitors to increase the penetration of doxorubicin and its liposomal f ormulation into 2D and 3D triple negative breast cancer cell culture s. *Am J Cancer Res*. 2020;10(6):1761.

74. Supuran CT. Carbonic anhydrase inhibitors. *Bioorg Med Chem Lett*. 2010;20(12):3467-3474.

75. Supuran CT. How many carbonic anhydrase inhibition mechanisms exist? *J Enzyme Inhib Med Chem*. 2016;31(3):345-360.

76. Mboge MY, Chen Z, Khokhar D, et al. A non-catalytic function of c arbonic anhydrase IX contributes to the glycolytic phenotype and p H regulation in human breast cancer cells. *Biochem J*. 2019;476(1 0):1497-1513.

77. Supuran CT. Carbonic anhydrases-an overview. *Curr Pharm Des*. 2 008;14(7):603-614.

78. Nocentini A, Supuran CT. Carbonic anhydrases: An overview. *Carb on Anhydrases*. Published online 2019:3-16.

79. Lee SH, McIntyre D, Honess D, et al. Carbonic anhydrase IX is a pH-stat that sets an acidic tumour extracellular pH in vivo. *Br J Ca ncer*. 2018;119(5):622-630.

80. Güttler A, Theuerkorn K, Riemann A, et al. Cellular and radiobiolog ical effects of carbonic anhydrase IX in human breast cancer cells. *Oncol Rep*. 2019;41(4):2585-2594.

81. Lou Y, McDonald PC, Oloumi A, et al. Targeting Tumor Hypoxia:

Suppression of Breast Tumor Growth and Metastasis by Novel Carbonic Anhydrase IX InhibitorsTargeted Inhibition of CAIX Suppresses Breast Cancer ProgressionTargeted Inhibition of CAIX Suppresses Breast Cancer Progression. *Cancer Res*. 2011;71(9):3364-3376.

82. Mussi S, Rezzola S, Chiodelli P, Nocentini A, Supuran CT, Ronca R. Antiproliferative effects of sulphonamide carbonic anhydrase inhibitors C18, SLC-0111 and acetazolamide on bladder, glioblastoma and pancreatic cancer cell lines. *J Enzyme Inhib Med Chem*. 2022;37(1):280-286.

83. Pastorekova S, Gillies RJ. The role of carbonic anhydrase IX in cancer development: links to hypoxia, acidosis, and beyond. *Cancer Metastasis Rev*. 2019;38(1-2):65-77.

84. RAMAN C V., KRISHNAN KS. A New Type of Secondary Radiation. *Nat 1928 1213048*. 1928;121(3048):501-502.

85. Xu J, Yu T, Zois CE, et al. Unveiling cancer metabolism through spontaneous and coherent raman spectroscopy and stable isotope probing. *Cancers (Basel)*. 2021;13(7):1-24.

86. Thorn K. Genetically encoded fluorescent tags. *Mol Biol Cell*. 2017;28(7):848-857.

87. Abraham W-R. Applications and impacts of stable isotope probing for analysis of microbial interactions. *Appl Microbiol Biotechnol*. 2014;98(11):4817-4828.

88. Wang Y, Huang WE, Cui L, Wagner M. Single cell stable isotope probing in microbiology using Raman microspectroscopy. *Curr Opin Biotechnol*. 2016;41:34-42.

89. Miyagi M, Kasumov T. Monitoring the synthesis of biomolecules using mass spectrometry. *Philos Trans R Soc A Math Phys Eng Sci*. 2016;374(2079):20150378.

90. Ackerman D, Simon MC. Hypoxia, lipids, and cancer: surviving the harsh tumor microenvironment. *Trends Cell Biol*. 2014;24(8):472-478.

91. Matthäus C, Krafft C, Dietzek B, Brehm BR, Lorkowski S, Popp J. Noninvasive imaging of intracellular lipid metabolism in macrophages by Raman microscopy in combination with stable isotopic labeling. *Anal Chem*. 2012;84(20):8549-8556.

92. Stiebing C, Meyer T, Rimke I, et al. Real-time Raman and SRS imaging of living human macrophages reveals cell-to-cell heterogeneity and dynamics of lipid uptake. *J Biophotonics*. 2017;10(9):1217-1226.

93. Stiebing C, Matthäus C, Krafft C, et al. Complexity of fatty acid distribution inside human macrophages on single cell level using Raman micro-spectroscopy. *Anal Bioanal Chem*. 2014;406(27):7037-7046.

94. Majzner K, Tott S, Roussille L, Deckert V, Chlopicki S, Baranska M. Uptake of fatty acids by a single endothelial cell investigated by Raman spectroscopy supported by AFM. *Analyst*. 2018;143(4):970-980.

95. Li J, Cheng J-X. Direct visualization of de novo lipogenesis in single living cells. *Sci Rep*. 2014;4(1):1-8.

96. García AA, Pfisterer SG, Riezman H, Ikonen E, Potma EO. D38-cholesterol as a Raman active probe for imaging intracellular cholesterol storage. *J Biomed Opt*. 2015;21(6):61003.

97. Weeks TJ, Schie IW, Rutledge JC, Huser TR, den Hartigh LJ. Lipid-cell interactions in human monocytes investigated by doubly-resonant coherent anti-Stokes Raman scattering microscopy. *J Biomed Opt*. 2011;16(2):21117.

98. Du J, Su Y, Qian C, et al. Raman-guided subcellular pharmaco-metabolomics for metastatic melanoma cells. *Nat Commun*. 2020;11(1):1-16.

99. Dodo K, Sato A, Tamura Y, et al. Synthesis of deuterated γ-linolenic acid and application for biological studies: metabolic tuning and Raman imaging. *Chem Commun*. 2021;57(17):2180-2183.

100. Matthäus C, Kale A, Chernenko T, Torchilin V, Diem M. New Ways of Imaging Uptake and Intracellular Fate of Liposomal Drug Carrier Systems inside Individual Cells, Based on Raman Microscopy. *Mol Pharm*. 2008;5(2):287-293.

101. van Manen H-J, Lenferink A, Otto C. Noninvasive Imaging of Protein Metabolic Labeling in Single Human Cells Using Stable Isotopes and Raman Microscopy. *Anal Chem*. 2008;80(24):9576-9582.

102. Wei L, Yu Y, Shen Y, Wang MC, Min W. Vibrational imaging of newly synthesized proteins in live cells by stimulated Raman scattering microscopy. *Proc Natl Acad Sci*. 2013;110(28):11226-11231.

103. Wei L, Shen Y, Xu F, et al. Imaging Complex Protein Metabolism in Live Organisms by Stimulated Raman Scattering Microscopy with Isotope Labeling. *ACS Chem Biol*. 2015;10(3):901-908.

104. Shen Y, Xu F, Wei L, Hu F, Min W. Live-Cell Quantitative Imaging of Proteome Degradation by Stimulated Raman Scattering. *Angew Chemie Int Ed*. 2014;53(22):5596-5599.

105. Miao K, Wei L. Live-Cell Imaging and Quantification of PolyQ Aggr egates by Stimulated Raman Scattering of Selective Deuterium Lab eling. *ACS Cent Sci*. 2020;6(4):478-486.

106. Zhang L, Shi L, Shen Y, et al. Spectral tracing of deuterium for im aging glucose metabolism. *Nat Biomed Eng*. 2019;3(5):402-413.

107. Lee D, Du J, Yu R, Su Y, Heath JR, Wei L. Visualizing Subcellula r Enrichment of Glycogen in Live Cancer Cells by Stimulated Ram an Scattering. *Anal Chem*. 2020;92(19):13182-13191.

108. Hu F, Chen Z, Zhang L, Shen Y, Wei L, Min W. Vibrational Imagi ng of Glucose Uptake Activity in Live Cells and Tissues by Stimula ted Raman Scattering. *Angew Chemie Int Ed*. 2015;54(34):9821-982 5.

109. Long R, Zhang L, Shi L, et al. Two-color vibrational imaging of glu cose metabolism using stimulated Raman scattering. *Chem Commu n*. 2018;54(2):152-155.

110. Chen Z, Paley DW, Wei L, et al. Multicolor Live-Cell Chemical Ima ging by Isotopically Edited Alkyne Vibrational Palette. *J Am Chem Soc*. 2014;136(22):8027-8033.

111. Zhang L, Min W. Bioorthogonal chemical imaging of metabolic chan ges during epithelial-mesenchymal transition of cancer cells by stim ulated Raman scattering microscopy. *J Biomed Opt*. 2017;22(10):1-7.

112. Shi L, Zheng C, Shen Y, et al. Optical imaging of metabolic dyna mics in animals. *Nat Commun*. 2018;9(1):2995.

113. Hekmatara M, Heidari Baladehi M, Ji Y, Xu J. D2O-Probed Raman Microspectroscopy Distinguishes the Metabolic Dynamics of Macro molecules in Organellar Anticancer Drug Response. *Anal Chem*. 20 21;93(4):2125-2134.

114. Azemtsop Matanfack G, Rüger J, Stiebing C, Schmitt M, Popp J. I maging the invisible—Bioorthogonal Raman probes for imaging of c ells and tissues. *J Biophotonics*. 2020;13(9):e202000129.

115. Yamakoshi H, Dodo K, Okada M, et al. Imaging of EdU, an Alkyn e-Tagged Cell Proliferation Probe, by Raman Microscopy. *J Am Ch em Soc*. 2011;133(16):6102-6105.

116. Berry D, Mader E, Lee TK, et al. Tracking heavy water (D2O) inco rporation for identifying and sorting active microbial cells. *Proc Natl Acad Sci*. 2015;112(2):E194-E203.

117. Huang WE, Stoecker K, Griffiths R, et al. Raman-FISH: combining

stable-isotope Raman spectroscopy and fluorescence in situ hybridi zation for the single cell analysis of identity and function. *Environ Microbiol*. 2007;9(8):1878-1889.

118. Song Y, Cui L, López JÁS, et al. Raman-Deuterium Isotope Probin g for in-situ identification of antimicrobial resistant bacteria in Tham es River. *Sci Rep*. 2017;7(1):1-10.

119. Hong W, Karanja CW, Abutaleb NS, et al. Antibiotic Susceptibility Determination within One Cell Cycle at Single-Bacterium Level by Stimulated Raman Metabolic Imaging. *Anal Chem*. 2018;90(6):3737-3743.

120. Xu J, Zhu D, Ibrahim AD, et al. Raman Deuterium Isotope Probing Reveals Microbial Metabolism at the Single-Cell Level. *Anal Chem*. 2017;89(24):13305-13312.

121. Wang Y, Xu J, Kong L, et al. Raman–deuterium isotope probing to study metabolic activities of single bacterial cells in human intestin al microbiota. *Microb Biotechnol*. 2020;13(2):572-583.

122. Li H-Z, Zhang D, Yang K, et al. Phenotypic Tracking of Antibiotic Resistance Spread via Transformation from Environment to Clinic b y Reverse D2O Single-Cell Raman Probing. *Anal Chem*. 2020;92(2 3):15472-15479.

123. Wang Y, Xu J, Kong L, et al. Raman-activated sorting of antibiotic-resistant bacteria in human gut microbiota. *Environ Microbiol*. 2020; 22(7):2613-2624.

124. Swietach P, Vaughan-Jones RD, Harris AL. Regulation of tumor pH and the role of carbonic anhydrase 9. *Cancer Metastasis Rev 200 7 262*. 2007;26(2):299-310.

125. Schulze A, Harris AL. How cancer metabolism is tuned for prolifera tion and vulnerable to disruption. *Nature*. 2012;491(7424):364-373.

126. Becker HM. Carbonic anhydrase IX and acid transport in cancer. *B r J Cancer*. 2020;122(2):157-167.

127. Gullino PM, Clark SH, Grantham FH. The interstitial fluid of solid t umors. *Cancer Res*. 1964;24(5):780-797.

128. Gatenby RA, Gillies RJ. Why do cancers have high aerobic glycoly sis? *Nat Rev cancer*. 2004;4(11):891-899.

129. Alka K, Casey JR. Bicarbonate transport in health and disease. *IU BMB Life*. 2014;66(9):596-615.

130. Zong W-X, Rabinowitz JD, White E. Mitochondria and cancer. *Mol*

Cell. 2016;61(5):667-676.

131. Song L-J, Liu R-J, Zeng Z, et al. Gastrin inhibits a novel, pathologi cal colon cancer signaling pathway involving EGR1, AE2, and P-E RK. *J Mol Med*. 2012;90(6):707-718.

132. Li JM, Lee S, Zafar R, Shin E, Choi I. Sodium bicarbonate transpo rter NBCe1 regulates proliferation and viability of human prostate c ancer cells LNCaP and PC3. *Oncol Rep*. 2021;46(1):1-11.

133. Swietach P, Patiar S, Supuran CT, Harris AL, Vaughan-Jones RD. The role of carbonic anhydrase 9 in regulating extracellular and intr acellular ph in three-dimensional tumor cell growths. *J Biol Chem*. 2009;284(30):20299-20310.

134. Morgan PE, Pastoreková S, Stuart-Tilley AK, Alper SL, Casey JR. I nteractions of transmembrane carbonic anhydrase, CAIX, with bicar bonate transporters. *Am J Physiol Physiol*. 2007;293(2):C738-C748.

135. Chiche J, Ilc K, Laferriere J, et al. Hypoxia-inducible carbonic anhy drase IX and XII promote tumor cell growth by counteracting acido sis through the regulation of the intracellular pH. *Cancer Res*. 2009; 69(1):358-368.

136. Swietach P, Wigfield S, Cobden P, Supuran CT, Harris AL, Vaugh an-Jones RD. Tumor-associated carbonic anhydrase 9 spatially coor dinates intracellular pH in three-dimensional multicellular growths. *J Biol Chem*. 2008;283(29):20473-20483.

137. Rode M, Šmid L, Budihna M, Gašpeřsič D, Rode M, Šoba E. The influence of pilocarpine and biperiden on pH value and calcium, ph osphate, and bicarbonate concentrations in saliva during and after r adiotherapy for head and neck cancer. *Oral Surgery, Oral Med Ora l Pathol Oral Radiol Endodontology*. 2001;92(5):509-514.

138. Valkenier H, Davis AP. Making a match for valinomycin: steroidal s caffolds in the design of electroneutral, electrogenic anion carriers. *Acc Chem Res*. 2013;46(12):2898-2909.

139. Muraglia KA, Chorghade RS, Kim BR, et al. Small-molecule ion ch annels increase host defences in cystic fibrosis airway epithelia. *Na ture*. 2019;567(7748):405-408.

140. Liu P-Y, Li S-T, Shen F-F, Ko W-H, Yao X-Q, Yang D. A small sy nthetic molecule functions as a chloride–bicarbonate dual-transporter and induces chloride secretion in cells. *Chem Commun*. 2016;52(4 6):7380-7383.

141. Jowett LA, Howe ENW, Wu X, Busschaert N, Gale PA. New Insigh

ts into the Anion Transport Selectivity and Mechanism of Tren-base d Tris-(thio) ureas. *Chem Eur J*. 2018;24(41):10475-10487.

142. Martínez-Crespo L, Hewitt SH, Simone NA De, et al. Transmembra ne Transport of Bicarbonate Unravelled. *Chem – A Eur J*. 2021;27 (26):7367-7375.

143. Wei E. Huang, Robert I. Griffiths, Ian P. Thompson, Mark J. B ailey and, Whiteley AS. Raman Microscopic Analysis of Single Micr obial Cells. *Anal Chem*. 2004;76(15):4452-4458.

144. K A, T L, HK Y, et al. Raman Microspectroscopic Evidence for the Metabolism of a Tyrosine Kinase Inhibitor, Neratinib, in Cancer Ce lls. *Angew Chem Int Ed Engl*. 2018;57(24):7250-7254.

145. Zois CE, Hendriks AM, Haider S, et al. Liver glycogen phosphoryla se is upregulated in glioblastoma and provides a metabolic vulnera bility to high dose radiation. *Cell Death Dis*. 2022;13(6):573.

146. Sitterley G. Poly-l-lysine cell attachment protocol. *BioFiles*. 2008;3 (8):12.

147. Leyton-Puig D, Kedziora KM, Isogai T, van den Broek B, Jalink K, Innocenti M. PFA fixation enables artifact-free super-resolution imagi ng of the actin cytoskeleton and associated proteins. *Biol Open*. 20 16;5(7):1001-1009.

148. Li Y, Almassalha LM, Chandler JE, et al. The effects of chemical fi xation on the cellular nanostructure. *Exp Cell Res*. 2017;358(2):253-259.

149. Robinson RW, Snyder JA. An innovative fixative for cytoskeletal co mponents allows high resolution in colocalization studies using imm unofluorescence techniques. *Histochem Cell Biol*. 2004;122(1):1-5.

150. De Veij M, Vandenabeele P, De Beer T, Remon JP, Moens L. Ref erence database of Raman spectra of pharmaceutical excipients. *J Raman Spectrosc*. 2009;40(3):297-307.

151. Sedlakova O, Svastova E, Takacova M, Kopacek J, Pastorek J, Pa storekova S. Carbonic anhydrase IX, a hypoxia-induced catalytic co mponent of the pH regulating machinery in tumors. *Front Physiol*. 2 014;4 JAN(January):1-14.

152. Pastorek J, Pastorekova S. Hypoxia-induced carbonic anhydrase IX as a target for cancer therapy: from biology to clinical use. In: *Se minars in Cancer Biology*. Vol 31. Elsevier; 2015:52-64.

153. Allen JWA. Cytochrome c biogenesis in mitochondria – Systems II I and V. *FEBS J*. 2011;278(22):4198-4216.

154. Brazhe NA, Evlyukhin AB, Goodilin EA, et al. Probing cytochrome c in living mitochondria with surface-enhanced Raman spectroscopy. *Sci Rep*. 2015;5(1):1-13.

155. Okada M, Smith NI, Palonpon AF, et al. Label-free Raman observation of cytochrome c dynamics during apoptosis. *Proc Natl Acad Sci*. 2012;109(1):28-32.

156. Arechederra RL, Waheed A, Sly WS, Supuran CT, Minteer SD. Effect of sulfonamides as carbonic anhydrase VA and VB inhibitors on mitochondrial metabolic energy conversion. *Bioorg Med Chem*. 2013;21(6):1544-1548.

157. Owen MR, Doran E, Halestrap AP. Evidence that metformin exerts its anti-diabetic effects through inhibition of complex 1 of the mitochondrial respiratory chain. *Biochem J*. 2000;348(3):607-614.

158. Ben Sahra I, Laurent K, Giuliano S, et al. Targeting cancer cell metabolism: the combination of metformin and 2-deoxyglucose induces p53-dependent apoptosis in prostate cancer cells. *Cancer Res*. 2010;70(6):2465-2475.

159. Shende C, Farquharson S, Farquharson D, Brouillette C. Measurements of Bicarbonate in Water Containing Ocean-Level Sulfate Using a Simple Multi-Pass Optical Raman System. Published online 2021.

160. Pan D, Galli G. A first principles method to determine speciation of carbonates in supercritical water.

161. Nolly MB, Vargas LA, Correa MV, et al. Carbonic anhydrase IX and hypoxia-inducible factor 1 attenuate cardiac dysfunction after myocardial infarction. *Pflugers Arch Eur J Physiol*. 2021;473(8):1273-1285.

162. Benej M, Pastorekova S, Pastorek J. Carbonic Anhydrase IX: Regulation and Role in Cancer. *Subcell Biochem*. 2014;75:199-219.

163. Ledaki I, McIntyre A, Wigfield S, et al. Carbonic anhydrase IX induction defines a heterogeneous cancer cell response to hypoxia and mediates stem cell-like properties and sensitivity to HDAC inhibition. *Oncotarget*. 2015;6(23):19413.

164. Horikawa M, Sabe H, Onodera Y. Dual roles of AMAP1 in the transcriptional regulation and intracellular trafficking of carbonic anhydrase IX. *Transl Oncol*. 2022;15(1):101258.

165. Potter M, Newport E, Morten KJ. The Warburg effect: 80 years on. *Biochem Soc Trans*. 2016;44(5):1499-1505.

166. Yu H, Bian X, Gu D, He X. Metformin synergistically enhances cis

platin-induced cytotoxicity in esophageal squamous cancer cells und er glucose-deprivation conditions. *Biomed Res Int*. 2016;2016.

167. Warburg O. On the origin of cancer cells. *Science (80-)*. 1956;123 (3191):309-314.

168. Schwartz L, T Supuran C, O Alfarouk K. The Warburg effect and t he hallmarks of cancer. *Anti-Cancer Agents Med Chem (Formerly Curr Med Chem Agents)*. 2017;17(2):164-170.

169. Wallace DC. Mitochondria and cancer. *Nat Rev Cancer*. Published online 2012.

170. de la Cruz López KG, Toledo Guzmán ME, Sánchez EO, García C arrancá A. mTORC1 as a regulator of mitochondrial functions and a therapeutic target in cancer. *Front Oncol*. 2019;9:1373.

171. Denko NC. Hypoxia, HIF1 and glucose metabolism in the solid tum our. *Nat Rev Cancer 2008 89*. 2008;8(9):705-713.

172. Pescador N, Villar D, Cifuentes D, et al. Hypoxia promotes glycoge n accumulation through hypoxia inducible factor (HIF)-mediated indu ction of glycogen synthase 1. *PLoS One*. 2010;5(3):e9644.

173. Jamali S, Klier M, Ames S, et al. Hypoxia-induced carbonic anhydr ase IX facilitates lactate flux in human breast cancer cells by non-c atalytic function. *Sci Rep*. 2015;5(1):1-16.

174. Mboge MY, Mahon BP, McKenna R, Frost SC. Carbonic anhydrase s: role in pH control and cancer. *Metabolites*. 2018;8(1):19.

175. Dagogo-Jack I, Shaw AT. Tumour heterogeneity and resistance to cancer therapies. *Nat Publ Gr*. 2017;15.

176. Okada M, Smith NI, Palonpon AF, et al. Label-free Raman observa tion of cytochrome c dynamics during apoptosis. *Proc Natl Acad S ci U S A*. 2012;109(1):28-32. doi:10.1073/pnas.1107524108

177. Vaughn AE, Deshmukh M. Glucose metabolism inhibits apoptosis in neurons and cancer cells by redox inactivation of cytochrome c. P ublished online 2008.

178. Bensaad K, Tsuruta A, Selak MA, et al. TIGAR, a p53-inducible re gulator of glycolysis and apoptosis. *Cell*. 2006;126(1):107-120.

179. McDonald PC, Chafe SC, Brown WS, et al. Regulation of pH by c arbonic anhydrase 9 mediates survival of pancreatic cancer cells wi th activated KRAS in response to hypoxia. *Gastroenterology*. 2019; 157(3):823-837.

180. Boyd NH, Walker K, Fried J, et al. Addition of carbonic anhydrase

9 inhibitor SLC-0111 to temozolomide treatment delays glioblastoma growth in vivo. *JCI insight*. 2017;2(24).

181. Logsdon DP, Shah F, Carta F, et al. Blocking HIF signaling via no vel inhibitors of CA9 and APE1/Ref-1 dramatically affects pancreatic cancer cell survival. *Sci Rep*. 2018;8(1):1-14.

182. Wang Y, Zhou X, Wang W, Wu Y, Qian Z, Peng Q. Sodium bicar bonate, an inorganic salt and a potential active agent for cancer th erapy. *Chinese Chem Lett*. Published online June 23, 2021.

183. Hoang BX, Tran DM, Tran HQ, et al. Dimethyl Sulfoxide and Sodiu m Bicarbonate in the Treatment of Refractory Cancer Pain. *http://d x.doi.org/103109/153602882010536306*. 2011;25(1):19-24.

184. Robey IF, Lopez AM, Roe DJ. Integrative Oncology Safety and Tol erability of Long-Term Sodium Bicarbonate Consumption in Cancer Care. 2015;4(1):1-8.

185. Keevil CW, Marsh PD, Ellwood DC. Regulation of glucose metaboli sm in oral streptococci through independent pathways of glucose 6-phosphate and glucose 1-phosphate formation. *J Bacteriol*. 1984;15 7(2):560-567.

186. Bollen M, Keppens S, Stalmans W. Specific features of glycogen metabolism in the liver. *Biochem J*. 1998;336(1):19-31.

187. Meléndez R, Meléndez-Hevia E, Cascante M. How did glycogen str ucture evolve to satisfy the requirement for rapid mobilization of glu cose? A problem of physical constraints in structure building. *J Mol Evol*. 1997;45:446-455.

188. Taylor C, Cox AJ, Kernohan JC, Cohen P. Debranching enzyme fr om rabbit skeletal muscle: purification, properties and physiological role. *Eur J Biochem*. 1975;51(1):105-115.

189. Stewart D, Yahiaoui N, McDougall GJ, et al. Fourier-transform infra red and Raman spectroscopic evidence for the incorporation of cin namaldehydes into the lignin of transgenic tobacco (Nicotiana tabac um L.) plants with reduced expression of cinnamyl alcohol dehydro genase. *Planta*. 1997;201(3):311-318.

190. Huang WE, Bailey MJ, Thompson IP, Whiteley AS, Spiers AJ. Sing le-cell Raman spectral profiles of Pseudomonas fluorescens SBW25 reflects in vitro and in planta metabolic history. *Microb Ecol*. 2007; 53(3):414-425.

191. Chan JW, Lieu DK, Huser T, Li RA. Label-free separation of huma n embryonic stem cells and their cardiac derivatives using Raman

spectroscopy. *Anal Chem*. 2009;81(4):1324-1331.

192. Kast RE, Auner GW, Rosenblum ML, et al. Raman molecular imaging of brain frozen tissue sections. *J Neurooncol*. 2014;120(1):55-62.

193. Kast R, Auner G, Yurgelevic S, et al. Identification of regions of normal grey matter and white matter from pathologic glioblastoma and necrosis in frozen sections using Raman imaging. *J Neurooncol*. 2015;125(2):287-295.

194. Draux F, Gobinet C, Sulé-Suso J, et al. Raman spectral imaging of single cancer cells: probing the impact of sample fixation methods. *Anal Bioanal Chem*. 2010;397(7):2727-2737.

195. Matthews Q, Isabelle M, Harder SJ, et al. Radiation-induced glycogen accumulation detected by single cell Raman spectroscopy is associated with radioresistance that can be reversed by metformin. *PLoS One*. 2015;10(8):e0135356.

196. Li H, Chen X, Yu Y, et al. Metformin inhibits the growth of nasopharyngeal carcinoma cells and sensitizes the cells to radiation via inhibition of the DNA damage repair pathway. *Oncol Rep*. 2014;32(6):2596-2604.

197. Storozhuk Y, Hopmans SN, Sanli T, et al. Metformin inhibits growth and enhances radiation response of non-small cell lung cancer (NSCLC) through ATM and AMPK. *Br J Cancer*. 2013;108(10):2021-2032.

198. Gajjar K, Heppenstall LD, Pang W, et al. Diagnostic segregation of human brain tumours using Fourier-transform infrared and/or Raman spectroscopy coupled with discriminant analysis. *Anal Methods*. 2013;5(1):89-102.

199. Huang WE, Ferguson A, Singer AC, et al. Resolving genetic functions within microbial populations: in situ analyses using rRNA and mRNA stable isotope probing coupled with single-cell Raman-fluorescence in situ hybridization. *Appl Environ Microbiol*. 2009;75(1):234-241.

200. Zhang H, Li X, Martin DB, Aebersold R. Identification and quantification of N-linked glycoproteins using hydrazide chemistry, stable isotope labeling and mass spectrometry. *Nat Biotechnol*. 2003;21(6):660-666.

201. Carroll N V, Longley RW, Roe JH. The determination of glycogen in liver and muscle by use of anthrone reagent. *J biol Chem*. 1956;220(2):583-593.

202. Gałat A. Study of the Raman scattering and infrared absorption sp ectra of branched polysaccharides. *Acta Biochim Pol*. 1980;27(2):13 5-142.

203. Wiercigroch E, Szafraniec E, Czamara K, et al. Raman and infrare d spectroscopy of carbohydrates: A review. *Spectrochim Acta - Par t A Mol Biomol Spectrosc*. 2017;185:317-335.

204. Dudek M, Zajac G, Szafraniec E, et al. Raman Optical Activity and Raman spectroscopy of carbohydrates in solution. *Spectrochim Act a Part A Mol Biomol Spectrosc*. 2019;206:597-612.

205. Barron LD, Gargaro AR, Wen ZQ, MacNicol DD, Butters C. Vibrati onal Raman optical activity of cyclodextrins. *Tetrahedron: Asymmetr y*. 1990;1(8):513-516.

206. Nikonenko NA, Buslov DK, Sushko NI, Zhbankov RG. Investigation of stretching vibrations of glycosidic linkages in disaccharides and p olysaccarides with use of IR spectra deconvolution. *Biopolym Orig Res Biomol*. 2000;57(4):257-262.

207. Cael JJ, Gardner KH, Koenig JL, Blackwell J. Infrared and Raman spectroscopy of carbohydrates. Paper V. Normal coordinate analysi s of cellulose I. *J Chem Phys*. 1975;62(3):1145-1153.

208. Di Mauro S. Muscle glycogenoses: an overview. *Acta Myol*. 2007;2 6(1):35.

209. Tang K, Zhu L, Chen J, et al. Hypoxia Promotes Breast Cancer C ell Growth by Activating a Glycogen Metabolic Program. *Cancer Re s*. 2021;81(19):4949-4963.

210. Favaro E, Bensaad K, Chong MG, et al. Glucose utilization via gly cogen phosphorylase sustains proliferation and prevents premature senescence in cancer cells. *Cell Metab*. 2012;16(6):751-764.

211. Xu J, Liu X, Liu X, Zhi Y. Long noncoding RNA KCNMB2-AS1 pro motes the development of esophageal cancer by modulating the mi R-3194-3p/PYGL axis. *Bioengineered*. 2021;12(1):6687-6702.

212. Altemus MA, Goo LE, Little AC, et al. Breast cancers utilize hypoxi c glycogen stores via PYGB, the brain isoform of glycogen phosph orylase, to promote metastatic phenotypes. *PLoS One*. 2019;14(9):e 0220973.

213. Favaro E, Harris AL. Targeting glycogen metabolism: a novel strate gy to inhibit cancer cell growth? *Oncotarget*. 2013;4(1):3.

214. Zhu Y, Liu Z, Lv D, et al. Identification of PYGL as a key prognos tic gene of glioma by integrated bioinformatics analysis. *Futur Onco*

l. 2022;18(5):579-596.

215. Drochmans P. Morphology of glycogen. Electron microscopic study of the negative stains of particulate glycogen. *J Ultrastruct Res*. 19 62;6:141-163.

216. Prats C, Graham TE, Shearer J. The dynamic life of the glycogen granule. *J Biol Chem*. 2018;293(19):7089-7098.

217. Thornell L-E. The fine structure of Purkinje fiber glycogen. A comp arative study of negatively stained and cytochemically stained partic les. *J Ultrastruct Res*. 1974;49(2):157-166.

218. Sullivan MA, Aroney STN, Li S, et al. Changes in glycogen structu re over feeding cycle sheds new light on blood-glucose control. *Bio macromolecules*. 2014;15(2):660-665.

219. Marchand I, Chorneyko K, Tarnopolsky M, et al. Quantification of s ubcellular glycogen in resting human muscle: granule size, numbe r, and location. *J Appl Physiol*. 2002;93(5):1598-1607.

220. Marchand I, Tarnopolsky M, Adamo KB, Bourgeois JM, Chorneyko K, Graham TE. Quantitative assessment of human muscle glycogen granules size and number in subcellular locations during recovery from prolonged exercise. *J Physiol*. 2007;580(2):617-628.

221. Graham TE, Yuan Z, Hill AK, Wilson RJ. The regulation of muscle glycogen: the granule and its proteins. *Acta Physiol*. 2010;199(4):48 9-498.

222. Horgan CC, Nagelkerke A, Whittaker TE, et al. Molecular imaging of extracellular vesiclesin vitro viaRaman metabolic labelling. *J Mate r Chem B*. 2020;8(20):4447-4459.

223. Melendez-Hevia E, Waddell TG, Shelton ED. Optimization of molec ular design in the evolution of metabolism: the glycogen molecule. *Biochem J*. 1993;295(2):477-483.

224. Liu Q, Li J, Zhang W, et al. Glycogen accumulation and phase se paration drives liver tumor initiation. *Cell*. 2021;184(22):5559-5576.e 19.

225. Macleod NA, Johannessen C, Hecht L, Barron LD, Simons JP. Fro m the gas phase to aqueous solution: Vibrational spectroscopy, Ra man optical activity and conformational structure of carbohydrates. *I nt J Mass Spectrom*. 2006;253(3):193-200.

226. Nan X, Cheng J-X, Xie XS. Vibrational imaging of lipid droplets in live fibroblast cells with coherent anti-Stokes Raman scattering micr oscopy. *J Lipid Res*. 2003;44(11):2202-2208.

227. Bandekar J. Amide modes and protein conformation. *Biochim Biophys Acta (BBA)-Protein Struct Mol Enzymol*. 1992;1120(2):123-143.

228. Zhang X, Roeffaers MBJ, Basu S, et al. Label-free live-cell imaging of nucleic acids using stimulated Raman scattering microscopy. *ChemPhysChem*. 2012;13(4):1054-1059.

229. Li M, Huang WE, Gibson CM, Fowler PW, Jousset A. Stable isotope probing and Raman spectroscopy for monitoring carbon flow in a food chain and revealing metabolic pathway. *Anal Chem*. 2013;85(3):1642-1649.

230. Wilson KL, Berk JM. The nuclear envelope at a glance. *J Cell Sci*. 2010;123(12):1973-1978.

231. Ragano-Caracciolo M, Berlin WK, Miller MW, Hanover JA. Nuclear glycogen and glycogen synthase kinase 3. *Biochem Biophys Res Commun*. 1998;249(2):422-427.

232. DeFronzo RA. The triumvirate: β-cell, muscle, liver: a collusion responsible for NIDDM. *Diabetes*. 1988;37(6):667-687.

233. Shulman GI, Rothman DL, Jue T, Stein P, DeFronzo RA, Shulman RG. Quantitation of muscle glycogen synthesis in normal subjects and subjects with non-insulin-dependent diabetes by 13C nuclear magnetic resonance spectroscopy. *N Engl J Med*. 1990;322(4):223-228.

234. Son J, Lyssiotis CA, Ying H, et al. Glutamine supports pancreatic cancer growth through a KRAS-regulated metabolic pathway. *Nature*. 2013;496(7443):101-105.

235. Lyssiotis CA, Breitkopf SB, Yuan M, et al. Fluxing Through Cancer: Tracking the Fate of C-Labeled Energy Sources Glucose and Glutamine in Cancer Cells and Mouse Tumors.

236. Christensen CE, Karlsson M, Winther JR, Jensen PR, Lerche MH. Non-invasive in-cell determination of free cytosolic [NAD+]/[NADH] ratios using hyperpolarized glucose show large variations in metabolic phenotypes. *J Biol Chem*. 2014;289(4):2344-2352.

237. Kishimoto S, Brender JR, Crooks DR, et al. Imaging of glucose metabolism by 13C-MRI distinguishes pancreatic cancer subtypes in mice. DeBerardinis R, Akhmanova A, DeBerardinis R, Brindle K, eds. *Elife*. 2019;8:e46312.

238. Hanahan D, Weinberg RA. Hallmarks of cancer: the next generation. *Cell*. 2011;144(5):646-674.

239. Fan S, Kroeger B, Marie PP, et al. Glutamine deprivation alters the origin and function of cancer cell exosomes. *EMBO J*. 2020;39(1

6):e103009.

240. Still ER, Yuneva MO. Hopefully devoted to Q: targeting glutamine addiction in cancer. *Br J Cancer*. 2017;116(11):1375-1381.

241. Newsholme P, Procopio J, Lima MMR, Pithon-Curi TC, Curi R. Glutamine and glutamate—their central role in cell metabolism and function. *Cell Biochem Funct*. 2003;21(1):1-9.

242. Hosios AM, Hecht VC, Danai L V, et al. Amino acids rather than glucose account for the majority of cell mass in proliferating mammalian cells. *Dev Cell*. 2016;36(5):540-549.

243. Bhutia YD, Babu E, Ramachandran S, Ganapathy V. Amino acid transporters in cancer and their relevance to “glutamine addiction”: novel targets for the design of a new class of anticancer drugs. *Cancer Res*. 2015;75(9):1782-1788.

244. Nicklin P, Bergman P, Zhang B, et al. Bidirectional transport of amino acids regulates mTOR and autophagy. *Cell*. 2009;136(3):521-534.

245. Moreadith and RW, Lehninger AL. The pathways of glutamate and glutamine oxidation by tumor cell mitochondria. Role of mitochondrial NAD (P)+-dependent malic enzyme. *J Biol Chem*. 1984;259(10):6215-6221.

246. McKenna MC, Stridh MH, McNair LF, Sonnewald U, Waagepetersen HS, Schousboe A. Glutamate oxidation in astrocytes: roles of glutamate dehydrogenase and aminotransferases. *J Neurosci Res*. 2016;94(12):1561-1571.

247. Ward PS, Patel J, Wise DR, et al. The common feature of leukemia-associated IDH1 and IDH2 mutations is a neomorphic enzyme activity converting α-ketoglutarate to 2-hydroxyglutarate. *Cancer Cell*. 2010;17(3):225-234.

248. Matés JM, Campos-Sandoval JA, de Los Santos-Jiménez J, Segura JA, Alonso FJ, Márquez J. Metabolic reprogramming of cancer by chemicals that target glutaminase isoenzymes. *Curr Med Chem*. 2020;27(32):5317-5339.

249. Bott AJ, Maimouni S, Zong W-X. The pleiotropic effects of glutamine metabolism in cancer. *Cancers (Basel)*. 2019;11(6):770.

250. Pachnis P, Wu Z, Faubert B, et al. In vivo isotope tracing reveals a requirement for the electron transport chain in glucose and glutamine metabolism by tumors. *Sci Adv*. 2022;8(35):eabn9550.

251. Leone RD, Zhao L, Englert JM, et al. Glutamine blockade induces

divergent metabolic programs to overcome tumor immune evasion. *Science (80-)*. 2019;366(6468):1013-1021.

252. Schiliro C, Firestein BL. Mechanisms of metabolic reprogramming in cancer cells supporting enhanced growth and proliferation. Cells 2021, 10, 1056.

253. Pawlukojć A, Hołderna-Natkaniec K, Bator G, Natkaniec I. L-glutamine: Dynamical properties investigation by means of INS, IR, RAMAN, 1H NMR and DFT techniques. *Chem Phys*. 2014;443:17-25.

254. DeBerardinis RJ, Cheng T. Q's next: the diverse functions of glutamine in metabolism, cell biology and cancer. *Oncogene*. 2010;29(3):313-324.

255. Li R, Yu JC, Jiang ZT, Zhou RH, Liu HY. A solid-phase fluorescent quenching method for the determination of trace amounts of nitrite in foods with neutral red. *J Food Drug Anal*. 2003;11(3):251-257.

256. Tsuji A, Ohnishi S. Restriction of the lateral motion of band 3 in the erythrocyte membrane by the cytoskeletal network: dependence on spectrin association state. *Biochemistry*. 1986;25(20):6133-6139.

257. Nag S, Bagchi D, Chattopadhyay D, Bhattacharyya M, Pal SK. Protein assembled nano-vehicle entrapping photosensitizer molecules for efficient lung carcinoma therapy. *Int J Pharm*. 2020;580:119192.

258. Xu L, Wang J, Sun N, et al. Neutral red as a specific light-up fluorescent probe for i-motif DNA. *Chem Commun*. 2016;52(99):14330-14333.

259. Matsuyama S, Llopis J, Deveraux QL, Tsien RY, Reed JC. *Changes in Intramitochondrial and Cytosolic PH: Early Events That Modulate Caspase Activation during Apoptosis*. Vol 2.; 2000.

260. Kovacevic Z, McGivan JD. Mitochondrial metabolism of glutamine and glutamate and its physiological significance. *Physiol Rev*. 1983;63(2):547-605.

261. Zhang J, Ahn WS, Gameiro PA, Keibler MA, Zhang Z, Stephanopoulos G. 13C isotope-assisted methods for quantifying glutamine metabolism in cancer cells. In: *Methods in Enzymology*. Vol 542. Elsevier; 2014:369-389.

262. Shen J, Petersen KF, Behar KL, et al. Determination of the rate of the glutamate/glutamine cycle in the human brain by in vivo 13C NMR. *Proc Natl Acad Sci*. 1999;96(14):8235-8240.

263. Bak LK, Ziemińska E, Waagepetersen HS, Schousboe A, Albrecht J. Metabolism of [U-13C] glutamine and [U-13C] glutamate in isolat

ed rat brain mitochondria suggests functional phosphate-activated gl utaminase activity in matrix. *Neurochem Res*. 2008;33(2):273-278.

264. Huang WE, Ude S, Spiers AJ. Pseudomonas fluorescens SBW25 b iofilm and planktonic cells have differentiable Raman spectral profile s. *Microb Ecol*. 2007;53(3):471-474.

265. Wang X, Liu N-M, Zhao Y-F, Yang F, Zhu Z-J, Song D. Research Progress in the Medical Application of Heavy Water, Especially in t he Field of D(2)O-Raman Spectroscopy. *Int J Med Sci*. 2022;19(8): 1357-1363.

266. Hartmann J, Bader Y, Horvath Z, et al. Effects of Heavy Water on Human Pancreatic Tumor Cells. *Anticancer Res*. 2005;25(5):3407 L P-3411.

267. Jenkins AL, Larsen RA, Williams TB. Characterization of amino aci ds using Raman spectroscopy. *Spectrochim Acta Part A Mol Biomo l Spectrosc*. 2005;61(7):1585-1594.

268. Rygula A, Majzner K, Marzec KM, Kaczor A, Pilarczyk M, Baransk a M. Raman spectroscopy of proteins: a review. *J Raman Spectros c*. 2013;44(8):1061-1076.

269. Ganar K, Das M, Sinha S, Kumar S. Newcastle disease virus: curr ent status and our understanding. *Virus Res*. 2014;184:71-81.

270. Russell SJ. RNA viruses as virotherapy agents. *Cancer Gene Ther*. 2002;9(12):961-966.

271. Sinkovics J. Studies on the biological characteristics of the Newcas tle disease virus (NDV) adapted to the brain of newborne mice. *Ar ch Gesamte Virusforsch*. 1957;7:403-411.

272. Chia S-L, Yusoff K, Shafee N. Viral persistence in colorectal cance r cells infected by Newcastle disease virus. *Virol J*. 2014;11:1-8.

273. Rangaswamy US, Wang W, Cheng X, McTamney P, Carroll D, Jin H. Newcastle disease virus establishes persistent infection in tumor cells in vitro: contribution of the cleavage site of fusion protein and second sialic acid binding site of hemagglutinin-neuraminidase. *J Vi rol*. 2017;91(16):e00770-17.

274. Chan L-C, Kalyanasundram J, Leong S-W, et al. Persistent Newca stle disease virus infection in bladder cancer cells is associated wit h putative pro-survival and anti-viral transcriptomic changes. *BMC C ancer*. 2021;21(1):1-13.

275. Huang WE, Griffiths RI, Thompson IP, Bailey MJ, Whiteley AS. Ra man microscopic analysis of single microbial cells. *Anal Chem*. 200

4;76(15):4452-4458.

276. Xu J, Preciado-Llanes L, Aulicino A, et al. Single-cell and time-reso lved profiling of intracellular Salmonella metabolism in primary hum an cells. *Anal Chem*. 2019;91(12):7729-7737.

277. Kim M, Garant KA z, Zur Nieden NI, et al. Attenuated reovirus dis plays oncolysis with reduced host toxicity. *Br J Cancer*. 2011;104 (2):290-299.

278. Lu F-K, Basu S, Igras V, et al. Label-free DNA imaging in vivo wit h stimulated Raman scattering microscopy. *Proc Natl Acad Sci*. 20 15;112(37):11624-11629.

279. Paudel BB, Harris LA, Hardeman KN, et al. A nonquiescent “idling” population state in drug-treated, BRAF-mutated melanoma. *Biophys J*. 2018;114(6):1499-1511.

280. Hammerlindl H, Schaider H. Tumor cell-intrinsic phenotypic plasticity facilitates adaptive cellular reprogramming driving acquired drug re sistance. *J Cell Commun Signal*. 2018;12:133-141.

281. Echeverria G V, Ge Z, Seth S, et al. Resistance to neoadjuvant ch emotherapy in triple-negative breast cancer mediated by a reversibl e drug-tolerant state. *Sci Transl Med*. 2019;11(488):eaav0936.

282. Ramirez M, Rajaram S, Steininger RJ, et al. Diverse drug-resistanc e mechanisms can emerge from drug-tolerant cancer persister cells. *Nat Commun*. 2016;7(1):10690.

283. Oren Y, Tsabar M, Cuoco MS, et al. Cycling cancer persister cells arise from lineages with distinct programs. *Nature*. 2021;596(7873): 576-582.

284. Talari ACS, Movasaghi Z. I. u. Rehman. 2015. *Raman Spectrosc B iol tissues Appl Spectrosc Rev*. 50(1):46-111.

285. Czamara K, Majzner K, Pacia MZ, Kochan K, Kaczor A, Baranska M. Raman spectroscopy of lipids: a review. *J Raman Spectrosc*. 20 15;46(1):4-20.

286. Larraona-Puy M, Ghita A, Zoladek A, et al. Development of Raman microspectroscopy for automated detection and imaging of basal c ell carcinoma. *J Biomed Opt*. 2009;14(5):54031.

287. Cheng W, Liu M, Liu H, Lin S. Micro-Raman spectroscopy used to identify and grade human skin pilomatrixoma. *Microsc Res Tech*. 2 005;68(2):75-79.

288. Xu J, Webb I, Poole P, Huang WE. Label-free discrimination of Rh

izobial bacteroids and mutants by single-cell Raman microspectrosc opy. *Anal Chem*. 2017;89(12):6336-6340.

289. Dukor RK. Vibrational spectroscopy in the detection of cancer. *Han db Vib Spectrosc*. Published online 2006.

290. Stone N, Stavroulaki P, Kendall C, Birchall M, Barr H. Raman spe ctroscopy for early detection of laryngeal malignancy: preliminary re sults. *Laryngoscope*. 2000;110(10):1756-1763.

291. Schuster KC, Reese I, Urlaub E, Gapes JR, Lendl B. Multidimensio nal information on the chemical composition of single bacterial cells by confocal Raman microspectroscopy. *Anal Chem*. 2000;72(22):55 29-5534.

292. Lakshmi RJ, Kartha VB, Murali Krishna C, R. Solomon JG, Ullas G, Uma Devi P. Tissue Raman spectroscopy for the study of radiatio n damage: brain irradiation of mice. *Radiat Res*. 2002;157(2):175-1 82.

293. Shipp DW, Sinjab F, Notingher I. Raman spectroscopy: techniques and applications in the life sciences. *Adv Opt Photonics*. 2017;9(2): 315-428.

294. Adhikari P, Hasan M, Sridhar V, Roy D, Pradhan P. Studying nano scale structural alterations in cancer cells to evaluate ovarian cance r drug treatment, using transmission electron microscopy imaging. *P hys Biol*. 2020;17(3):36005.

295. Babak M V, Meier SM, Huber KVM, et al. Target profiling of an an timetastatic RAPTA agent by chemical proteomics: relevance to the mode of action. *Chem Sci*. 2015;6(4):2449-2456.

296. Yhee JY, Lee S, Kim K. Advances in targeting strategies for nanop articles in cancer imaging and therapy. *Nanoscale*. 2014;6(22):1338 3-13390.

297. Herrmann AM, Ritz K, Nunan N, et al. Nano-scale secondary ion mass spectrometry — A new analytical tool in biogeochemistry and soil ecology: A review article. *Soil Biol Biochem*. 2007;39(8):1835-1850.

298. Vakoc BJ, Fukumura D, Jain RK, Bouma BE. Cancer imaging by o ptical coherence tomography: preclinical progress and clinical potent ial. *Nat Rev Cancer*. 2012;12(5):363-368.

299. Zhu S, Tian R, Antaris AL, Chen X, Dai H. Near-Infrared-II Molecul ar Dyes for Cancer Imaging and Surgery. *Adv Mater*. 2019;31(24):1 900321.

300. Testoni G, Duran J, García-Rocha M, et al. Lack of Glycogenin Ca uses Glycogen Accumulation and Muscle Function Impairment. *Cell Metab*. 2017;26(1):256-266.e4.

301. Curtino JA, Aon MA. From the seminal discovery of proteoglycogen and glycogenin to emerging knowledge and research on glycogen biology. *Biochem J*. 2019;476(21):3109-3124.

302. Xu J, Yi X, Jin G, et al. High-Speed Diagnosis of Bacterial Pathog ens at the Single Cell Level by Raman Microspectroscopy with Ma chine Learning Filters and Denoising Autoencoders. *ACS Chem Bio l*. 2022;17(2):376-385.

303. Abdolghader P, Ridsdale A, Grammatikopoulos T, et al. Unsupervis ed hyperspectral stimulated Raman microscopy image enhancement: denoising and segmentation via one-shot deep learning. *Opt Expre ss*. 2021;29(21):34205-34219.

304. He H, Xu M, Zong C, et al. Speeding up the line-scan Raman ima ging of living cells by deep convolutional neural network. *Anal Che m*. 2019;91(11):7070-7077.

305. Tian M, Morais CLM, Shen H, et al. Direct identification and visuali sation of real-world contaminating microplastics using Raman spectr al mapping with multivariate curve resolution-alternating least squar es. *J Hazard Mater*. 2022;422:126892.

306. Lin H, Lee HJ, Tague N, et al. Microsecond fingerprint stimulated Raman spectroscopic imaging by ultrafast tuning and spatial-spectra l learning. *Nat Commun*. 2021;12(1):3052.

307. Samoylenko A, Kögler M, Zhyvolozhnyi A, et al. Time-gated Raman spectroscopy and proteomics analyses of hypoxic and normoxic re nal carcinoma extracellular vesicles. *Sci Rep*. 2021;11(1):19594.

308. Xu T, Gong Y, Su X, et al. Phenome–genome profiling of single b acterial cell by Raman-activated gravity-driven encapsulation and se quencing. *Small*. 2020;16(30):2001172.

309. Doherty T, McKeever S, Al-Attar N, et al. Feature fusion of Raman chemical imaging and digital histopathology using machine learning for prostate cancer detection. *Analyst*. 2021;146(13):4195-4211.

310. Li Z, Li Z, Chen Q, et al. Machine-learning-assisted spontaneous R aman spectroscopy classification and feature extraction for the diag nosis of human laryngeal cancer. *Comput Biol Med*. 2022;146:1056 17.

311. Watanabe TM, Sasaki K, Fujita H. Recent Advances in Raman Sp

ectral Imaging in Cell Diagnosis and Gene Expression Prediction. *Genes (Basel)*. 2022;13(11).

312. Ralbovsky NM, Lednev IK. Towards development of a novel univer sal medical diagnostic method: Raman spectroscopy and machine l earning. *Chem Soc Rev*. 2020;49(20):7428-7453.

Appendix

Paper 1. Unveiling Cancer Metabolism through Spontaneous and Coherent Raman Spectroscopy and Stable Isotope Probing.

Paper 2. Metabolic reprogramming in colon cancer cells persistently infected by Newcastle disease virus.

cancers

MDPI

Review

Unveiling Cancer Metabolism through Spontaneous and Coherent Raman Spectroscopy and Stable Isotope Probing

Jiabao Xu [1,*], Tong Yu [1], Christos E. Zois [2,3], Ji-Xin Cheng [4], Yuguo Tang [5], Adrian L. Harris [2,*] and Wei E. Huang [1,*]

1 Department of Engineering Science, University of Oxford, Oxford OX1 3PJ, UK; tong.yu@spc.ox.ac.uk
2 Molecular Oncology Laboratories, Department of Oncology, Weatherall Institute of Molecular Medicine, John Radcliffe Hospital, Oxford University, Oxford OX3 9DS, UK; christos.zois@oncology.ox.ac.uk
3 Department of Radiotherapy and Oncology, School of Health, Democritus University of Thrace, 68100 Alexandroupolis, Greece
4 Department of Biomedical Engineering, Boston University, Boston, MS 02215, USA; jxcheng@bu.edu
5 Suzhou Institute of Biomedical Engineering and Technology, Chinese Academy of Sciences, Suzhou 215163, China; tangyg@sibet.ac.cn
* Correspondence: jiabao.xu@eng.ox.ac.uk (J.X.); adrian.harris@oncology.ox.ac.uk (A.L.H.); wei.huang@eng.ox.ac.uk (W.E.H.)

Simple Summary: Raman spectroscopy and imaging are label-free, non-destructive techniques to study cellular metabolism with subcellular spatial resolution. This review focuses on applications of Raman-based methods in a combination of stable isotope probing on cancer metabolism and cancer imaging.

Abstract: Metabolic reprogramming is a common hallmark in cancer. The high complexity and heterogeneity in cancer render it challenging for scientists to study cancer metabolism. Despite the recent advances in single-cell metabolomics based on mass spectrometry, the analysis of metabolites is still a destructive process, thus limiting in vivo investigations. Being label-free and nonperturbative, Raman spectroscopy offers intrinsic information for elucidating active biochemical processes at subcellular level. This review summarizes recent applications of Raman-based techniques, including spontaneous Raman spectroscopy and imaging, coherent Raman imaging, and Raman-stable isotope probing, in contribution to the molecular understanding of the complex biological processes in the disease. In addition, this review discusses possible future directions of Raman-based technologies in cancer research.

Keywords: cancer metabolism; Raman spectroscopy; stimulated Raman scattering; coherent Raman anti-Stokes scattering; Raman imaging; lipid metabolism; stable isotope probing

check for updates

Citation: Xu, J.; Yu, T.; Zois, C.E.; Cheng, J.-X.; Tang, Y.; Harris, A.L.; Huang, W.E. Unveiling Cancer Metabolism through Spontaneous and Coherent Raman Spectroscopy and Stable Isotope Probing. *Cancers* **2021**, *13*, 1718. https://doi.org/10.3390/cancers13071718

Academic Editor: Mark W Dewhirst

Received: 9 March 2021
Accepted: 28 March 2021
Published: 5 April 2021

Publisher's Note: MDPI stays neutral with regard to jurisdictional claims in published maps and institutional affiliations.

Copyright: © 2021 by the authors. Licensee MDPI, Basel, Switzerland. This article is an open access article distributed under the terms and conditions of the Creative Commons Attribution (CC BY) license (https://creativecommons.org/licenses/by/4.0/).

1. Introduction

Reprogrammed metabolism is considered a hallmark of cancer [1]. Cancer metabolism is a question of great interest in a wide range of fields since the "Warburg Effect" indicated aerobic glycolysis, as a characteristic of cancer cells [2]. Cancer cells rely on the acquisition of nutrients from the environment to meet the demand for energy and biomass production. In the last few decades, features of tumor-associated metabolic alteration were widely observed. Key questions among the tumor metabolic reprogramming rapidly expanded our understanding of carcinogenesis. In particular, how cancer cells reprogram their metabolism and interact with other biological processes, which mechanisms and functions of nutrient acquisition in cancer cells are achieved, and what targeted pathways in metabolism can be engaged to selective development of inhibitors during therapeutic evaluation [3].

Cancer metabolism is highly complex and heterogeneous, subject to environmental cues. The metabolic phenotype is dependent on the tumor microenvironment. It is now

clear that even though cancer cells are from the same tumor with the same genotypes, they can manifest distinct phenotypic states in different positions [4]. Challenges remain in investigating the vastly complex metabolism of cancer with regards to intra-tumoral heterogeneity, different tissues, and tumor types.

Metabolomics based on mass spectrometry is a gold standard for study of cellular metabolites. Although lagging behind other single-cell omics methods, it recently advances to the level where multiplex analysis from single cells could be achieved [5,6]. However, the disadvantages of mass spectrometry metabolomics remain due to its destructive nature, prohibiting live cell analysis. Moreover, it does not offer insights on the spatial information of metabolite distribution, which can be crucial in heterogeneous intra-tumor environments. Fluorescence-based methods offer high sensitivity and selectivity, and they can provide subcellular resolution. However, the fluorophore labels are often much larger than the targeted molecules and thus can hinder the intrinsic metabolism [7]. The prerequisite of knowing the target molecules also hinders multiplex targeting and investigative probing. Considering the high complexity and heterogeneity in cancer, minimally invasive, non-destructive, and label-free tools with imaging ability providing subcellular spatial information, are in need to study cancer metabolism and fulfill the translational clinical need.

Raman spectroscopy technologies present several advantages for the cancer research community. In particular, Raman spectroscopy is a label-free spectroscopic method to provide comprehensive biochemical information, the so-called "biomolecular fingerprint", regarding metabolic processes in cells and tissues. In addition, Raman imaging offers high spatial resolution at the sub-cellular level and is capable of real-time, noninvasive examination of living cells, tissues, and organisms, based on their metabolic profiles.

This review aims to present Raman-based technologies in the area of cancer research, to study the metabolism of single cells as well as physio-pathological tissues. First, we present applications of label-free Raman spectroscopy and imaging in cancer metabolism. Second, we discuss Raman-based technologies combined with stable isotope probing (SIP) for studying metabolic fates of specific metabolites. The primary focus of the methodology is on spontaneous Raman spectroscopy and coherent Raman scattering (CRS) microscopy. Readers interested in surface-enhanced Raman scattering and other Raman-based methodologies are referred to excellent reviews elsewhere [8–11].

2. Background of Raman Spectroscopy and Coherent Raman Scattering

2.1. Spontaneous Raman Spectroscopy and a Cell's Fingerprint

Raman spectroscopy is an essential tool for chemists, physicists, biologists, and materials scientists. It was first experimentally observed by C. V. Raman in 1928, for which he was awarded the Nobel Prize in 1930 [12]. In Raman spectroscopy, a sample is illuminated with a monochromatic laser beam (Figure 1A). The incident laser beam with a frequency of v_0 interacts with a molecule in the sample that has a vibrational frequency of v_m. This interaction originates scattered light. The vast majority of the scattered light is elastic scattering, the so-called Rayleigh scattering. However, due to energy exchange between the incident photons and molecular vibration, there is a small fraction of inelastic scattering, which has a different frequency from that of the incident light, collectively called Raman scattering. Raman scattering consists of both Stokes scattering, which has a lower frequency at $v_0 - v_m$, and anti-Stokes scattering, which has a higher frequency at $v_0 + v_m$ (Figure 1B) The Stokes spectrum is often presented as the Raman spectrum, due to its higher intensity, as compared to the anti-Stokes lines.

Cancers **2021**, *13*, 1718

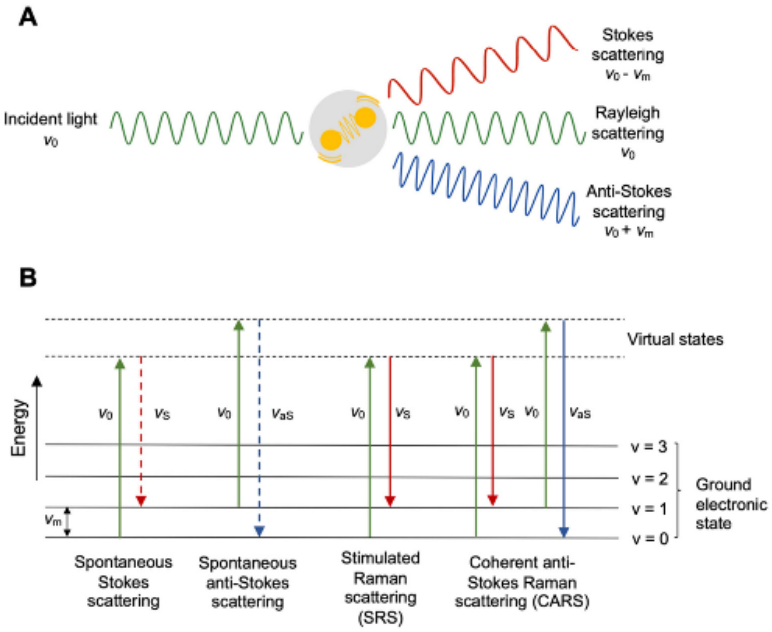


Figure 1. (**A**) Electromagnetic radiation interacting with a vibrating molecule. (**B**) Schematic energy diagrams of spontaneous Raman scattering and coherent Raman scattering (CRS). The solid arrows indicate laser excitation or stimulated emission; the dashed arrows indicate spontaneous scattering process.

Raman spectroscopy is now increasingly popular among biologists. A Raman spectrum can be regarded as a phenotype of a biological system because it provides an overall molecular vibrational profile, containing Raman bands for major cellular building blocks, such as proteins, nucleic acids, lipids, and carbohydrates. Figure 2 illustrates a Raman spectrum of a single glioblastoma cell with Raman bands marked with assignments of major biological macromolecules. A biological Raman spectrum can be divided into three regions—the 'fingerprint' region that contains essential bio-information and can be seen as a fingerprint of a cell (400–1800 cm^{-1}); the 'silent' region that usually does not involve vibrational modes contributed by biomolecules formed of naturally occurring isotopes and can involve bands contributed by stable isotopes or triple bonds (1800–2700 cm^{-1}); the high-wavenumber region that is specifically contributed by the stretching vibrations of CH groups, predominantly from lipids and proteins (2700–3200 cm^{-1}).

The advantages of using Raman micro-spectroscopy in biological studies are high spatial resolution; ability to detect aqueous samples; intrinsic and label-free characterization; non-contacting and non-destructive analysis; and easy preparation and small sample volume.

By combining the power of optical magnification and direct visualization, Raman micro-spectroscopy can probe biological systems at a subcellular resolution. For large biological systems like tissues, it can collectively produce label-free Raman images with subcellular structural and chemical information. The ability to analyze aqueous samples separates Raman spectroscopy from other vibrational spectroscopies like infrared (IR) spectroscopy. A water molecule has low polarizability, thus, it minimally hinders sample signals in Raman spectroscopy and can be easily subtracted during preprocessing procedures. This is particularly advantageous in biological studies because it avoids laborious sample drying preparation, which might also alter the biochemistry of the samples.

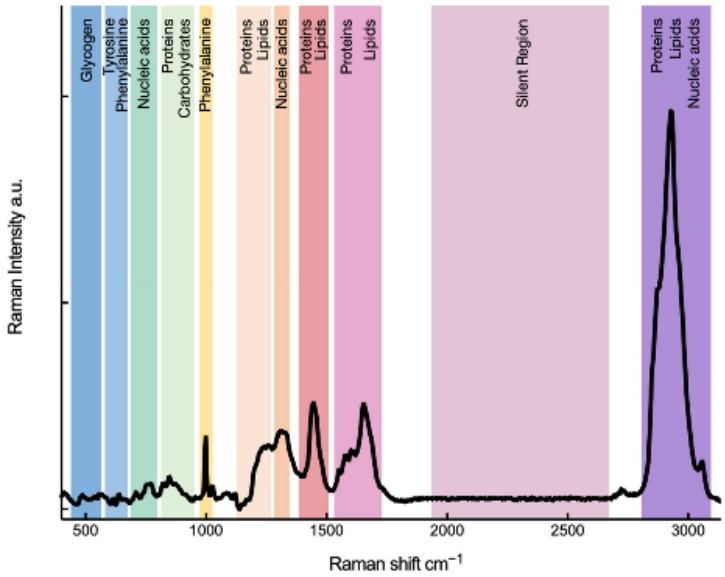


Figure 2. Raman spectrum—a cell's fingerprint. Raman spectrum of a single cell of human primary glioblastoma U87 cell line, demonstrating various bands representative of cellular constituents.

Molecular labeling using genetically encoded reporters (e.g., green fluorescent protein) is used extensively for monitoring cellular events in biological systems [13]. The introduction of unnatural functional groups might risk interfering with the native biological processes. Raman spectroscopy, on the other hand, is label-free and able to probe biological samples in their natural setting. It also does not require any prior knowledge of the particular substrate for selective labeling. It unbiasedly probes all macromolecules and collectively displays their vibrational modes in one spectrum. Raman spectroscopy is also non-contacting and non-destructive, as opposed to other analytical tools such as gas chromatography and mass spectrometry that destroy the sample to achieve results. This non-invasive, label-free, and spatially resolved nature renders Raman spectroscopy suitable for in vitro and in vivo biological investigations, from investigating a single cancer cell, to producing biochemical maps of cancerous tissues.

2.2. *Coherent Raman Scattering for High-Speed Imaging*

Having discussed the advantages of Raman micro-spectroscopy, the challenge is intrinsically weak Raman scattering as approximately only 1 in 10^7 photons experiences inelastic scattering [14]. Another Raman-based approach is emerging in recent decades to obtain much stronger vibrational signals by coherent Raman scattering (CRS), which employs multiple light sources to produce coherent Raman signals.

Coherent anti-Stokes Raman scattering (CARS) and stimulated Raman scattering (SRS) are two CRS processes [15–18]. During spontaneous Raman scattering, the pump beam with a frequency of ν_0 is incident upon the sample generating a Stokes signal ν_S and an anti-Stokes signal ν_{aS}. In SRS, two laser beams at frequencies ν_0 and ν_S are directed onto the sample, such that the frequency difference $\nu_0 - \nu_S$ matches the frequency of a molecular vibrational mode ν_m (Figure 1B). This process causes stimulated excitation of a chemically specific signature and brings the advantage of suppressing non-resonant background. Experimentally, either stimulated-Raman gain (SRG) of the Stokes or stimulated-Raman loss (SRL) of the pump is measured, and optical modulation and demodulation are required to extract the proper SRS signal [19].

CARS involves a complex four-beam mixing process probing, as shown in Figure 1B. As in SRS, the resonance occurs when the difference between the pump and Stokes beam $\nu_0 \mp \nu_S$ matches a molecular vibration in the sample. This resonance is then probed by the third field at ν_0 and generates an anti-Stokes signal at $2\nu_0 \mp \nu_S$. With respect to SRS, no complex demodulation schemes are required in CARS. However, the presence of a strong non-resonant background due to the four-wave mixing that does not carry any chemical information can distort and overwhelm the resonant signal [20].

With the advantages of dramatically enhanced Raman signal and little autofluorescence interference, CARS and SRS microscopy are emerging techniques for real-time analysis and video-rate imaging of cells and tissues in a living system, with high speed and 3D spatial resolution [21]. Nonetheless, both techniques are limited to the complex set-up of two synchronized trains of laser pulses. CARS and SRS are also limited by the small spectral range due to the narrow bandwidths between lasers. Therefore, so far in most cases, these were demonstrated for chemical signatures with high concentrations and strong Raman signals, for example, the CH_2 stretching vibrations that are typically found in lipids in cells [22]. In addition, CARS suffers from the complicated interpretation of Raman bands due to changed band frequencies [20]. SRS, on the other hand, shows a comparable spectrum like spontaneous Raman. Its signal also shows an intensity that is linearly proportional to the concentration of the targeted molecules and is free of non-resonant background. With the intensity of the signal proportional to the concentration of the metabolites of interest, semi-quantitative molecular profiling of single cells and tissues is possible [23–27]. SRS would be a complementary tool to spontaneous Raman scattering and simultaneously using the two can be beneficial (Table 1) [28]. The investigation of a biological system can begin with spontaneous Raman scattering (acquisition time from seconds to minutes) covering the entire spectral window of molecular vibrations and looking for a defined marker of interest. It could then be followed with SRS focusing on a predefined spectral window and offering high-speed benefit (acquisition time microseconds) for imaging and collection of a huge amount of spectral data.

Table 1. Comparison of spontaneous Raman spectroscopy and spectroscopic SRS microscopy, which are complementary to each other and can be used simultaneously.

	Spontaneous Raman	**Spectroscopic SRS**
Advantages	• Relatively cost-effective and easy operation • Whole spectral range with high spectral resolution	• Enhanced signal • Free from fluorescence and non-resonant backgroung • Comparable spectrum with spontaneous Raman
Disadvantages	• Intrinsically weak signal • Fluorescence interference	• Complex and expensive set-up • Narrow spectral range with low spectral resolution
Suitability	Investigative spectral study	Targeted high-speed imaging
Speed per spectra	100 millisecond	20 microsecond
Time required for a 200×200 image	~1 hour	~1 second
Spectral width	Whole spectral range up to 4000 cm^{-1}	200 cm^{-1}
Target	Whole spectrum	Mostly CH stretching [15,16], recently also fingerprint [17]
Spectral resolution	~1 cm^{-1}	10 cm^{-1}

3. Raman Spectroscopy as a Label-Free Tool for Cancer Metabolism Investigation

Metabolic reprogramming is now a widely accepted hallmark of cancer [3]. Monitoring metabolites and understanding the reprogramming pathways are crucial to fully understand cellular metabolism in cancer development and to provide new therapeutic targets. Raman spectroscopy and Raman imaging benefit cancer research and understanding of metabolic regulation in cancers, because it offers single-cell resolution or spatial information about biochemical composition of nucleic acids, proteins, lipids, and other metabolites. The defined subcellular locations cannot be provided by conventional analytical methods that rely on bulk or fractionated analyses of extracted components, e.g., mass spectrometry, nuclear magnetic resonance spectroscopy, and high-performance liquid chromatography. As a label-free technique, Raman spectroscopy also outperforms many fluorescence-based approaches that involve exogenous probes and can interfere with intrinsic biological processes.

3.1. Investigation of Lipid Metabolism in Cancer Cells

Lipid reprogramming is one of the key features of cancer's metabolic adaptation [29]. Alterations in lipid metabolism were observed in many different cancer types [30–33], and have important therapeutic inferences, as they affect the survival, dynamics, and response of cancer cells. Raman microscopy is one of the most powerful techniques for analyzing the properties of lipids in cancer cells, offering lipid compositional information as well as spatial information within cellular compartments. As the lipidic CH stretching vibrations are the strongest among all Raman vibrations generated in the high-frequency region of 2800–3200 cm^{-1}, lipid metabolism is possibly the most investigated subject by Raman spectroscopy.

To satisfy proliferation demand, cancer cells exhibit a higher content of cellular lipid content than normal cells. Lipids are particularly in demand as nutrient sources for energy supply, building blocks for membrane biogenesis, and as lipid-derived signaling molecules [34]. A number of studies found an altered lipid metabolism related to the progression of cancer by Raman spectroscopy [23,35–38]. Abramczyk et al. found an increasing content of lipid droplets in mildly malignant (MCF7) and malignant (MDA-MB-231) breast cancer cells, as compared to the non-malignant (MCF10A) cells [36]. They also demonstrated altered lipid metabolism in adipocytes of the breast tissue from breast epithelial cells. Nieva et al. used Raman micro-spectroscopy to characterize lipid metabolism of breast cancer cells with different degrees of malignancy [39]. By analyzing characteristic Raman bands related to lipid content at 3014, 2935, 2890, and 2845 cm^{-1}, they hypothesized that the lipid content of breast cancer cells might be a useful indirect measure of a variety of functions coupled to breast cancer progression. A study by Tirinato et al. demonstrated the capability of functional characterization of lipid droplets in cancer stem cells (CSCs) by Raman spectroscopy, and confirmed lipid droplets as a distinctive mark of CSCs in colorectal cancer [40]. Similarly, lipid upregulation and reprogramming was observed by Raman spectroscopy in cells of prostate cancer [23], lung cancer [41], and melanoma [42,43].

Subcellular composition and distribution of lipids were the center of the subject by both CARS and SRS microscopy, due to strong contrast in the CH vibrations. The high-speed capacity of CRS realizes rapid biochemical–optical lipid imaging, which is comparable to the traditional optical methods. In 2003, Nan et al. first used CARS microscopy to image neutral lipid droplets (LDs) in live fibroblast cells [44]. In 2008, Freudiger et al. used SRS microscopy to visualize lipid distribution with depth information [45]. They monitored lipids along varying depths of mouse skin, as well as DMSO penetrating into the skin. Since then, CRS microscopy was used extensively in lipid imaging with structural diversity tightly associated with their biological functions [43,46–55].

Hyperspectral CRS microscopy was applied to study changes in lipid composition (e.g., saturated vs. unsaturated) of cancer cells and tissues, which plays an important role in cancer metabolism and development. For example, increased saturation in phospholipids markedly alters signal transduction, protects cancer cells from oxidative damage, and potentially inhibits chemotherapeutic drug uptake [56]. Wang et al. visualized a substantial

amount of saturated lipids accumulated in liver cancer tissues, compared with the adjacent noncancerous tissues [49]. Li et al. reported significantly increased levels of unsaturated lipids in ovarian CSCs, as compared to non-CSCs (Figure 3) [48]. Subsequent experiments showed that inhibition of lipid desaturases effectively eliminated CSCs, suppressed sphere formation, and blocked tumor initiation capacity in vivo. With spontaneous Raman spectroscopy, followed by SRS microscopy and transcriptomics analysis, Du et al. investigated and imaged lipids droplets in patient-derived melanoma cells during differentiation [43]. They identified fatty acid synthesis pathway as a druggable susceptibility and a lipid mono-unsaturation within de-differentiated mesenchymal cells, with innate resistance to BRAF inhibition.

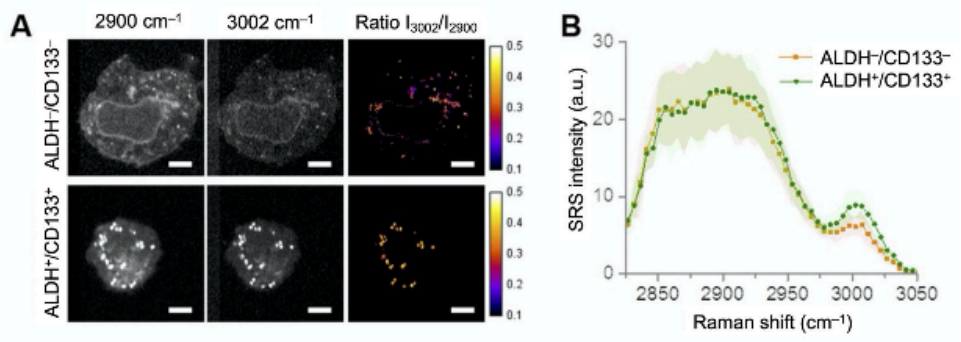


Figure 3. Increased lipid unsaturation level in ovarian cancer cells represented by intensity ratio between 2900 and 3002 cm^{-1}. (**A**) Representative hyperspectral SRS images of flow-sorted $ALDH^-/CD133^-$ and $ALDH^+/CD133^+$ COV362 cells. Images at 2900 and 3002 cm^{-1}, and the intensity ratio image between 3002 and 2900 cm^{-1} are shown. Scale bars: 10 µm. (**B**) Average SRS spectra from the lipid droplets in $ALDH^-/CD133^-$ ($n = 3$) and $ALDH^+/CD133^+$ cells ($n = 8$). Shaded area indicates the standard deviation of SRS spectral measurement from different cells. Reprinted and adapted with permission from reference [48].

3.2. *Investigation of Cellular Metabolism beyond Lipids*

The applicability of Raman-based techniques is not limited to lipid in the high-frequency CH region. The fingerprint region between 300 and 1800 cm^{-1} contains a collection of biological information of a cell. Investigative research focusing on the fingerprint region can either aim for a particular biomarker or use the whole region with chemometric techniques, to deconstruct Raman bands into biological information. Figure 4 shows an example of spontaneous Raman imaging of a HeLa cell, using the fingerprint region as well as the high-wavenumber region of Raman spectra.

The study of proteins can be conducted by investigating Raman bands of Amide vibrational modes, including Amide I that ranges from 1600–1670 cm^{-1}, Amide II that ranges from 1480–1580 cm^{-1}, and Amide III that ranges from 1230–1300 cm^{-1}. A study of two breast cancer and one normal breast cell lines (MDA-MB-436, MCF-7, and MCF-10A) illustrated decreased protein content in cancerous cell line [57]. A linear discriminant analysis (LDA) model on the entire spectral range predicted the three cell lines with 100% sensitivity and 91% specificity. Abramczyk et al. demonstrated a Raman biomarker of protein phosphorylation using the ratio between two Raman peaks at 1586 and 829 cm^{-1}, representing tyrosine phosphorylation [58]. They subsequently found overexpressed phosphorylation in the human breast, small intestine, and brain tissues, and in the glioblastoma U-87 MG cell line using this Raman biomarker. Using a multivariate curve resolution (MCR) to deconstruct the whole Raman spectra, Marro et al. demonstrated different intensities of proteins, lipids, and mitochondria Raman bands in primary breast cancer cell lines and their metastatic variants in bone [59]. Kopec et al. imaged and located glycogen, glycosaminoglycan, chondroitin sulfate, heparan sulfate proteoglycan, and distinguished each chemical species in normal and cancer tissues [60]. As a result, the study concluded that the metabolism

of proteins, lipids, and glycans was markedly deregulated in breast (adenocarcinoma) and brain (medulloblastoma) tumors. Using a principal component–linear discriminant analysis (PC–LDA) to deconstruct the Raman spectra of primary normal breast cells, and immortalized, transformed, non-invasive, and invasive breast cancer cells, Chaturvedi et al. identified distinct clustering of cell types with a high degree of sensitivity [61]. A study by Lemoine included 547 in situ Raman spectra from 65 patients undergoing glioma resection and systematic literature analysis of Raman study of glioma [62]. They subsequently used band fitting for extraction of Raman features and identified oncogenic processes involved with increased nucleic acid content, overexpression of type IV collagen, and a shift in the primary metabolic engine.

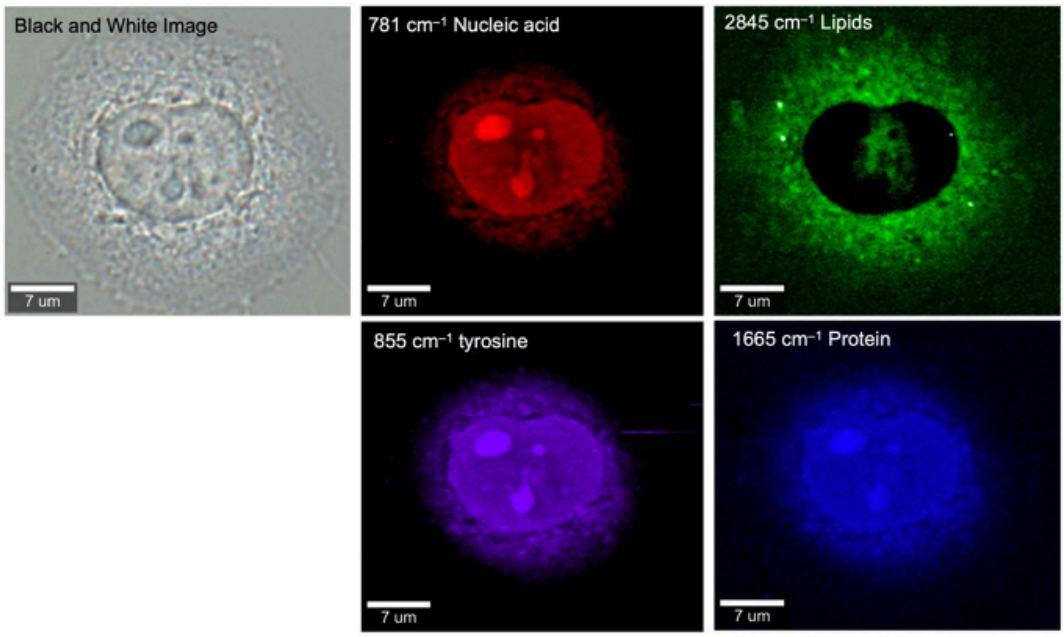


Figure 4. Raman images of a HeLa cell based on fingerprint Raman spectra, reconstructed from intensities at 781 (nucleic acids), 855 (tyrosine), 1665 (protein), and 2845 cm^{-1} (lipids). The Raman images show the distributions of these biomolecules with various intensities at the subcellular level.

Coherent Raman imaging of proteins besides lipids is also a common practice in both SRS and CARS microscopy. Imaging the CH moiety at the high-frequency region provides information of both proteins and lipids, as it is rich in both proteins and lipids. Therefore, protein images can be obtained indirectly by subtracting the lipid moiety contribution from CH-derived images [52,55,63–65]. In addition, protein molecules can be imaged at 1655 cm^{-1} at the Amide I peak [64]. The Xie group demonstrated that DNA distribution could also be retrieved from the strong background of proteins and lipids at the CH region through linear decomposition of the SRS images [65].

Molecular vibrations in the fingerprint region other than the Amide I group show markedly reduced intensities, compared to the high-frequency CH stretching region, which is less studied in CRS microscopy [55]. At the fingerprint region, Sunney Xie's group demonstrated the first SRS imaging of DNA at the fingerprint region in living cells [64], by using Raman bands at 785 and 1090 cm^{-1}. Recently, advancement in instrumentation and data science enabled SRS metabolic imaging of cancer cells in the fingerprint region with enhanced sensitivity. Cheng's group reported SRS imaging of retinoids with significantly boosted molecular sensitivity to 34 micromolar, via visible preresonance SRS (VP–SRS)

microscopy [66]. By shifting the excitation laser wavelength to visible range, approaching the absorption of intrinsic chromophores, the study demonstrated heterogeneous distribution of retinoid storage inside various cancer cells and chemoresistant ovarian cancer cells. Combining advanced instrumentation using a polygon-based ultrafast delay scanner and advanced data science approach of a spatial–spectral residual learning network, the group further demonstrated 100 times improvement of signals in fingerprint SRS imaging. They illustrated distribution of proteins, cholesterols, and lipids, in live pancreatic cancer cells, as well as in a whole mouse brain [17].

3.3. Cellular Responses to Anti-Cancer Drugs and Radiotherapy

The uptake, metabolism, and distribution of a drug candidate in targeted cancer cells or tissues are pivotal during drug discovery and development. Raman spectroscopy and CRS microscopy were used to exploit metabolic transformation in cancer cells as a drug target. Jamieson et al. investigated responses of PC3 prostate cancer cells to a series of lipid-targeting drugs [67]. Compared to the non-cancerous cells, the beta-blocker propranolol selectively chose the cancer cells in their Raman lipid profiles, showing an unexpected anti-cancer potential. The cellular lipid content in response to the drug was also studied by CARS microscopy [68]. By imaging the subcellular lipid distribution in hormone-treated breast and prostate cancer cells, the researchers found an increased number and size of intracellular lipid droplets and a higher degree of saturation in treated T47D and LNCaP cells than untreated cells.

In addition to lipids, comprehensive metabolic adaptations of cancer cells in response to anti-cancer drugs could be investigated by studying the entire Raman spectral region [69–74]. El-Mashtoly et al. applied Raman spectral imaging to study the effect of the epidermal growth factor receptor (EGFR) inhibitor panitumumab on cell lines expressing wild-type Kirsten-Ras (K-Ras) and oncogenic K-Ras mutations [70]. Larion et al. investigated the drug response of FK866, an inhibitor of NAD^+ salvage pathway, with both a fibrosarcoma cell line and mouse models [71]. The anti-cancer drug doxorubicin was studied by Farhane et al. [72] and Zhang et al. [73] to characterize its interaction with cancer cells. Note that Raman-based techniques could be used in combination with other techniques to be capable of conducting rapid drug screening and discovery. Wen et al. combined results from Raman spectroscopy with mass spectrometry, which is the gold standard in metabolomics, and characterized breast cancer responders and nonresponders to small molecule inhibitors [69].

Intracellular drug distribution and metabolism are traditionally visualized by fluorescent-labeled drug molecules. Despite the molecular specificity, fluorescent labels are often much larger than the drug molecules themselves and could largely alter the drug pharmacokinetic activities. Raman imaging offers new possibilities for label-free drug imaging with subcellular spatial resolution. Aljakouch et al. reported the intracellular spatial distribution and metabolism of neratinib, a tyrosine kinase inhibitor with antitumor property, in different cancer cells, using label-free Raman imaging [75]. Using the intrinsic CN bond in neratinib, which generates a Raman band at 2208 cm^{-1} in the silent region, the authors generated label-free images of neratinib distribution in cancer cells (Figure 5). A study by El-Mashtoly et al. used Raman microscopy to show the spatial distribution of the molecular-targeted drug erlotinib within the cell and that erlotinib was metabolized within cells to its demethylated derivative [76]. Recently, the advance of SRS microscopy enabled ultra-rapid images of cells and subcellular distribution of drugs. Fu et al. reported SRS visualization and quantification of two tyrosine kinase inhibitor drugs (imatinib and nilotinib), as well as the process of drug uptake into lysosomes [77]. Visualization of other drugs including ponatinib and retinol was also reported by SRS microscopy [15,78].

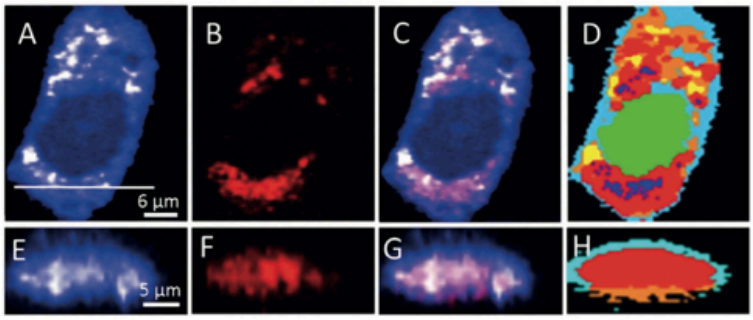


Figure 5. Raman imaging of SK-BR-3 cells treated with 5 µM neratinib for 8 h. Raman images reconstructed from the CH deformation (**A**) and CN stretching (**B**) intensities. (**C**) Overlay of Panels A and B. (**E**–**G**) Cross-section of Raman images of the same cell measured along the x–z axis. Scanning positions are indicated by the white line in Panel A. (**D**,**H**) HCA results based on the Raman data shown in Panels A and E. Reprinted with permission from reference [75].

Besides chemotherapy, radiotherapy is the mainstay of the treatment for a range of types of cancer. Monitoring radiation-induced cellular response of cancer at both cell and tissue levels was studied by Raman spectroscopy [79–83]. Roman et al. reported a change in the lipid composition and concentration in prostate cancer cells after X-ray radiation [80]. Similarly, metabolic alterations of cancer cells after radiation were also seen in nasopharyngeal cancer [79], non-small lung cancer [83], and glioblastoma [82]. A study by Milligan et al. found different biochemical responses between radio-resistant and radio-sensitive cell types in lung (H460), breast (MCF7), and prostate (LNCaP) cells [81]. The main differences were found in glycogen, phosphatidylcholine, glucose, arginine, and asparagine based on restricted non-negative matrix factorization approach.

3.4. Potential Applications in Clinical Cancer Diagnosis

Noninvasive or minimally invasive in vivo tools that can provide rapid tissue assessment have potential application in clinical diagnosis of cancer. With many advantageous features of Raman spectroscopic methods (non-destructive, capable of deep penetration and high resolution, and chemical specificity), here, we discuss their potential in tissue imaging and potential clinical diagnosis. We also direct readers to a few more reviews on applications of Raman spectroscopy in cancer diagnosis [84–86].

A recent work by Contorno et al. compiled data from 41 papers aiming at characterizing breast cancer by using various modalities of Raman spectroscopy [87]. They identified aromatic amino acids as the most prominent biomarker for identifying cancerous breast tissues from their healthy counterparts. Cancer cells and tissues exhibited markedly higher expression of aromatic amino acids, specifically tryptophan, phenylalanine, and tyrosine. A study by Haka et al. acquired Raman spectra from ex vivo samples of human breast tissue (normal, fibrocystic change, fibroadenoma, and infiltrating carcinoma) from 58 patients [88]. The study reported an increase in collagen in all abnormal breast tissues and less fat content in the samples diagnosed as fibroadenoma than those diagnosed as infiltrating carcinoma. By using the different fit coefficients for fat and collagen, the authors demonstrated a Raman diagnostic algorithm illustrating 94% sensitivity, 96% specificity, and 86% overall accuracy for detecting infiltrating carcinoma. A range of other studies also demonstrated the potential of Raman spectroscopy in diagnosing breast cancer in human and mouse breast tissues [89–96]. By exploiting the fingerprint region of the Raman spectrum and various machine learning techniques, Raman spectroscopy showed diagnostic potential for distinguishing cancerous tissues from normal tissues in brain cancer [56,97–100], skin cancer [42,101–105], gastrointestinal cancer [106–109], and lung cancer [110,111].

The ability of CRS for generating rapid chemical images makes it ideal for tissue and whole organ imaging and subsequently localizing the tumor margins. Ji et al. reported the

use of SRS imaging for differentiating healthy human and mouse brain tissues from tumor-infiltrated brain tissues [53]. They demonstrated that these label-free histopathological images provided very similar results to those obtained by conventional hematoxylin & eosin (H&E) staining, providing intrinsic chemical information without the need of routine tissue processing. The authors further applied SRS microscopy to obtain in vivo mouse brain images during tumor resection surgery, to reveal tumor margins that were undetectable under standard operative conditions. Through SRS microscopy, Freudiger et al. generated multi-color images of lipids, proteins, and hemoglobin in fresh-frozen tissue sections from mice models of invasive glioma, breast cancer metastases, stroke, and demyelination. A good correlation between SRS and H&E microscopy was also shown. These findings suggest that SRS microscopy can generate high-quality histological images for clinical diagnosis without the need for tissue fixation, sectioning, or staining. Noteworthy, with the recent advances of CARS and SRS endoscopy [112–114], further improvements to these Raman-based systems would open up exciting possibilities for in vivo, label-free, and non-invasive histopathological imaging and clinical diagnostics in the near future.

4. You Are What You Eat—Stable Isotope Probing (SIP)

The introduction of stable isotope probing to Raman spectroscopy was first demonstrated in bacteria [115], which was later referred as Raman–SIP technology [116]. Huang et al. showed that the incorporation of 'heavy' ^{13}C stable isotope into cells causes significant shifts of some Raman bands in single cell Raman spectra (SCRS) [115]. Later it was found that other stable isotopes D (^{2}H) and ^{15}N also generated Raman shifts in SCRS at different positions [117]. Following those discoveries, Raman–SIP are found applicable to many biological models including cancer cells, revealing the metabolic activity of cancer.

Stable isotope labeling by amino acids in cell culture (SILAC) has become increasingly popular for accurate protein quantitation, by using isotopically labeled amino acids that are later metabolically incorporated into cells [118]. In cancer research, SILAC was also recognized as an important tool for metabolic profiling of cancer cells, with respect to their environments [119,120]. Techniques like SILAC are stable isotope probing (SIP) methods that involve exposing cells to isotopically labeled substrates that are consequently assimilated into cells that are actively involved in specific metabolic processes. Molecular analysis of the labeled biomarkers thereby reveals functional information about the cell responsible for the metabolism of a particular substrate.

SIP to study cell metabolism, in general, shows great advantages over other specific probes that have larger molecular weights, and can disturb the intrinsic metabolic activity of cells. Using isotopes that mimic their naturally abundant counterparts does not alter the natural substrate pool. Among all SIP techniques, Raman spectroscopy has its unique strengths. While modalities like isotope ratio mass spectrometry and NMR spectroscopy require at least 300,000 cells, Raman spectroscopy or secondary ion mass spectrometry (SIMS) coupled with SIP enables an analysis of cell functions at a single-cell level [121]. However, SIMS is limited by its destructive nature and expensive equipment. Raman spectroscopy exceeds other techniques in its non-destructive, sensitive, and relatively cheap nature. While a Raman spectrum already conveys intrinsic and phenotypic information, more insight into cell functions can be obtained by combining Raman micro-spectroscopy with SIP, using D (^{2}H), ^{13}C, and ^{15}N-containing substrates to replace their primordial isotopes (^{12}C, ^{14}N, and ^{1}H) [116]. Among those stable isotopes, D (^{2}H) and ^{13}C are mostly commonly used due to the stronger C–H bond strength. Heteroatomic X–H bonds such as O–H, N–H, and S–H can be exchanged from nonenzymatic reactions, while C–H bond formation depends solely on enzyme-catalyzed chemical reactions that occurred within the metabolic pathways [122]. This provides unique advantages of D (^{2}H) and ^{13}C for probing the biological metabolism. Providing a wide variety of possible isotopic substrates, Raman–SIP probe the metabolism of most biomolecular constituents of a cell, including proteins, lipids, carbohydrates, and nucleic acids, revealing both molecule-specific and general metabolisms, as well as drug–cancer interactions (Figure 6).

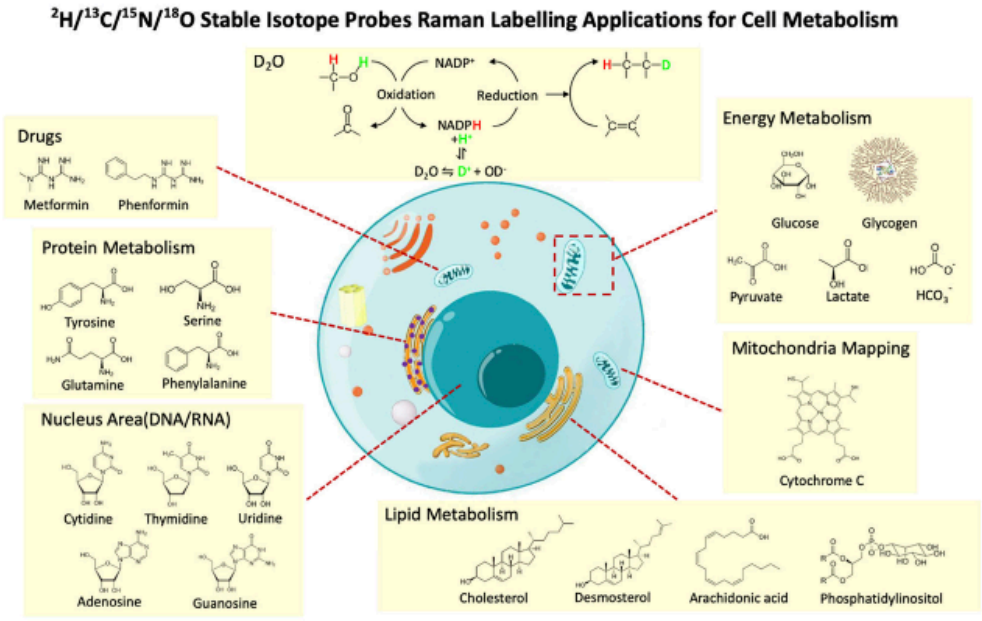


Figure 6. Raman–SIP strategies to study cellular metabolism. Heavy water (D_2O) is involved in NADPH regeneration, which is able to indicate the general anabolism activity in cells. Stable isotope labeled sugars, amino acids, nucleic acids, lipid precursors, and drugs can be used to probe the dynamics of metabolic flux and interactions of drugs and cancer cells.

Although Raman–SIP is now a mature tool to study cell ecology and biology, its application in cancer research is new. Most applications demonstrate the capability of the technique rather than answer specific questions. One of this review's purposes is to introduce Raman–SIP to a broader community and share our perspectives on its potential for studying cancer metabolism.

4.1. Principles of Raman–SIP

As Raman spectroscopy considers changes in vibrational modes of molecules, a mechanical model can be used to consider a molecular vibration as a spring model. A classical 'two-balls-on-a-spring' approach provides an equivalence of a diatomic molecule with two atoms with masses m_1 and m_2 connected by a chemical bond. The vibrational frequency v of such a molecule is described as:

$$v = \frac{1}{2\pi c}\sqrt{\frac{k}{\mu}}$$

where c is the speed of light, k is the force constant of the spring (diatomic bond), and μ is the reduced mass given by:

$$\mu = \frac{m_1 m_2}{m_1 + m_2}$$

. Therefore, the vibrational frequency v is inversely proportional to the square root of the reduced mass μ. When an atom is replaced by its heavier isotope, μ increases, therefore, v decreases. Taking C–D replacement of C–H as an example, if the ^{1}H atom is replaced by the ^{2}D atom, μ almost doubles and the ratio of the new v to the old v is 1.36. Therefore, C–D vibrations usually appear in the silent zone of a Raman spectrum at around 2100–2200 cm^{-1}, red-shifted from the C–H vibrations at 2800–3000 cm^{-1}. Thus, a strategy

to quantify D incorporation is to calculate the percentage of the integrated C–D band area to the sum of the areas of the C–D and C–H bands:

$$D_{incorp} = \frac{Area_{C-D}}{Area_{C-D} + Area_{C-H}}$$

. Redshifts of Raman bands can also be observed when replacing ^{12}C, ^{14}N, ^{18}O, or ^{32}S with their heavier analogs. Compared with the C–D shifts, the extent of the redshift is considerably less dramatic in the ^{13}C and ^{15}N substitutions, due to the comparably low changes in μ. By feeding cells with isotope-labeled substrates, the active cells metabolize these substrates and the isotopic-dependent shifts in Raman spectra can be used as indicators of isotopic incorporation, thereby 'you are what you eat'.

4.2. Raman–SIP Monitors Intracellular Metabolic Activities

Raman spectroscopy combined with isotopically labeled molecules is used to study the specific metabolic features of cell constituents such as lipids, proteins, and nucleic acids (Figure 6). Table 2 summarizes a collection of studies using Raman–SIP approaches to study cell metabolism and behaviors, together with their choices of probes, targeted molecules, and platform of research.

Table 2. Studies using Raman–SIP to probe metabolism in mammalian cells. "Spont." refers to spontaneous Raman.

Case Studies	Spont.	CRS	Isotope	Substrate	Target	Platform
Matthäus, C. et al. (2012) [123]	√		D	d31-palmitic acid d33-oleic acid	Lipids	THP-1 monocytes
Stiebing, C. et al. (2014) [124]	√		D	d8-arachidonic acidd 31-palmitic acidd 6-cholesterol-2,2,3,4,4,6	Lipids	Human macrophages
Stiebing, C. et al. (2017) [125]	√	√	D	d31-palmitic acid	Lipids	Human macrophages
Majzner, K. et al. (2018) [126]	√		D	d8-arachidonic acid	Lipids	Endothelial cell line (HMEC-1)
Li, J. & Cheng, J.-X. (2015) [127]	√	√	D	d7-glucosed 5-glutamined 31-palmitic acid-d31	Lipids	PANC1, A549, MIA PaCa2, MCF7, LNCaP, PC3, HPDE6 and RWPE1 cell lines
García, A. et al. (2015) [128]	√	√	D	d38-cholesterol	Lipids	Y1 cell line
Weeks, T. J. et al. (2011) [129]		√	D	d2-oleic Acid-9,10	Lipids	Human monocytes
Du, J. et al. (2020) [43]	√	√	D	d7-glucose 31-palmitic acidd 35-stearic acid d33-oleic acid>	Lipids	Patient-derived melanoma cell lines
Dodo, K. et al. (2021) [130]	√		D	d-γ-Linolenic acid	γ-Linolenic acid metabolism and cytotoxicity	WI-38 cell line and VA-13 tumor cell line
Matthäus, C. et al. (2008) [131]	√		D	1,2-Distearoyl-d70-sn-glycero3-phosphocholine (DSPC-d70)	Liposomal Drug Carrier Systems	MCF-7 cell line
Van Manen, H.-J. et al. (2008) [132]	√		D	d5-phenylalanine d4-tyrosine d3-methoine	Proteins	HeLa cell line
Wei, L. et al. (2013) [133]	√	√	D	d10-leucine	Newly synthesized proteins	Live HeLa cell line Human embryonic kidney HEK293T cell line Neuron-like neuroblastoma mouse N2A cell line
Wei, L. et al. (2015) [134]	√	√	D	deuterated amino acids	Proteins	HeLa cell line
Shen, Y. et al. (2014) [135]	√	√	^{13}C	^{13}C-phenylalanine	Protein degradation	HeLa, HEK293T and PC12 cell lines

Table 2. *Cont.*

Case Studies	Spont.	CRS	Isotope	Substrate	Target	Platform
Miao, K. & Wei, L. (2020) [136]		√	D	d5-glutamine	Proteins	HeLa cell line
Zhang, L. *et al.* (2019) [137]	√	√	D	d12-glucose	Glucose metabolism	PC3, HeLa, MCF7, RWPE-1 and U87MG cell linesMouse model
Lee, D. et al. (2020) [138]	√	√	D	d7-glucose	Glucose metabolism; glycogen synthesis	U87 and HeLa cell lines
Hu, F. *et al.* (2015) [139]	√	√	D	3-*O* -propargyl-D-glucose	Glucose metabolism	HeLa cell line U-87 MG tumor xenograft tissue
Long, R. *et al.* (2018) [140]	√	√	D/^{13}C	^{13}C-3-O-propargyl-D-glucose	Glucose metabolism	U87 MG, PC-3, COS-7 and RWPE-1 cell lines
Chen, Z. *et al.* (2014) [141]	√	√	^{13}C	^{13}C isotopologues of EdU	DNA	HeLa cell lines
Zhang, L. & Min, W. (2017) [142]	√	√	D	d-amino acidsd31-palmitate acidd7-glucose	Lipids and proteins	MCF-7 cell lines
Shi, L. *et al.* (2018) [143]	√	√	D	D_2O	Lipids, proteins and DNA	HeLa, COS-7, and U-87 MG cell lines Zebrafish embryos Mouse model
Hekmatara, M. *et al.* (2021) [144]	√		D	D_2O	Lipids, proteins and DNA	MCF-7 cell line

There is increasing evidence of upregulated demand for fatty acids in cancer cells, compared to their non-malignant counterparts [30]. Lipid uptake, distribution, and metabolism was extensively studied using Raman–SIP approach with labeled fatty acids in various types of cells [123–129]. D-labeled free fatty acids such as d_{31}-palmitic acid, d_{33}-oleic acid, and d_8-palmitic acid were used to image lipid metabolism in human macrophages [123–125]. Intracellular cholesterol storage can also be observed in cells by using d_{38}-cholesterol [128]. Heterogeneous distributions of neutral lipid species were found, where some lipid droplets accumulated preferentially unesterified cholesterol, whereas others stored cholesteryl esters.

De novo lipogenesis in cells can also be studied using deuterated carbon sources such as deuterated glucose or glutamine. Li and Cheng were the first to visualize the direct de novo lipid synthesis that originated from deuterated glucose through SRS imaging [127] (Figure 7A and 7B). They observed that glucose was largely utilized for lipid synthesis in pancreatic cancer cells, which occurred at a much lower rate in immortalized normal pancreatic epithelial cells. Similarly, de novo synthesis of fatty acids was also studied in undifferentiated and differentiated melanoma cell lines using deuterated glucose with spontaneous Raman spectroscopy and SRS [43]. In combination with transcriptomics analysis, the authors identified the fatty acid synthesis pathway as a druggable susceptibility for differentiated melanocytic cells.

Tumor-selective cytotoxicity of particular fatty acids was also studied. Dodo et al. synthesized several deuterated γ-linolenic acids and evaluated their metabolism and cytotoxicity towards normal human fibroblast WI-38 cells and VA-13 tumor cells [130]. Through Raman imaging of intracellular lipid droplets, they suggested the tumor-selective cytotoxicity of γ-linolenic acids from itself, as opposed to its oxidized metabolites.

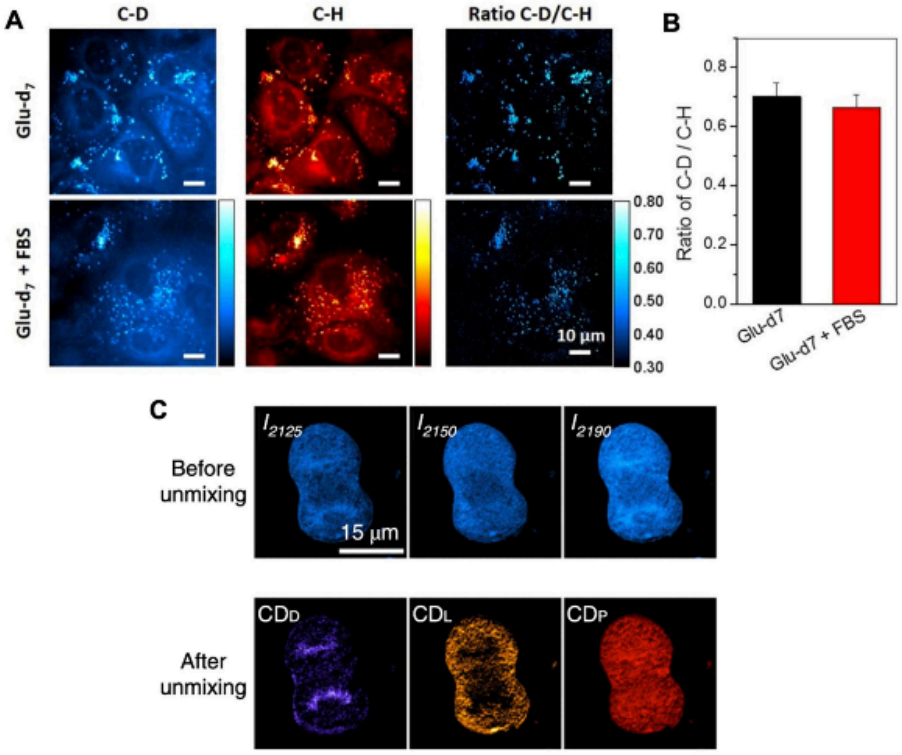


Figure 7. SRS imaging of cancer cells from deuterated glucose (**A**,**B**). Glucose-d_7-incubated pancreatic cancer PANC1 cells were treated without or with 10% FBS for 3 days. SRS imaging at C–D and C–H vibration were taken and the ratio of C–D/C–H was used to analyze the level of de novo lipogenesis and increased lipogenesis. Reprinted and adapted with permission from reference [127]. (**C**) SRS images of a glucose-d7-labelled mitotic HeLa cell before and after unmixing, showing distribution of DNA, lipids, and proteins. Reprinted and adapted with permission from Reference [137].

Cancer cells exhibit significant metabolic alterations with respect to their primary energy sources, including glucose. Deuterated glucose in Raman–SIP are shown to be valuable for the evaluation and exploration of glucose metabolism in cancer cells. Zhang et al. generated a comprehensive study to visualize the metabolic dynamics of macromolecules, such as DNA, protein, lipids, and glycogen, from glucose, in various cancer cell lines, and a mouse model with glioblastoma xenograft [137] (Figure 7C). The pathway from glucose to glycogen, which is important glucose storage in cancer cells, was also investigated by subcellular visualization of deuterated glycogen from deuterated glucose [138]. Hu et al. developed a protocol for synthesizing deuterated glucose with an alkyne tag, 3-O-propargyl-D-glucose [139]. By using this tag that shows a distinctive Raman band at 2129 cm^{-1}, they quantified the glucose uptake and found different metabolic activities in different cancer cell types. Long et al. further developed this approach to add a second ^{13}C labeling to synthesize ^{13}C-3-O-propargyl-D-glucose [140]. Thus, they demonstrated two-color imaging of glucose uptake and incorporation activity in U-87 MG human glioblastoma cells, PC-3 human prostate cancer cells, COS-7 monkey kidney cells, and RWPE-1 human prostate normal cells, as well as in ex vivo mouse brain tissues.

Just as in SILAC, protein synthesis could be observed in Raman–SIP through the incorporation of isotopically labeled amino acids. Back in 2008, van Manen et al. demonstrated the incorporation of deuterated phenylalanine, tyrosine, and methionine into proteins in single HeLa cells, also observed by the C–D vibrations in the 2100–2300 cm^{-1} spectral region [132]. It was shown that Raman images could be generated by illustrating newly

synthesized proteins from deuterated amino acids, in a range of live mammalian cells with high spatial–temporal resolution [133]. Using this approach, subcellular compartments could be identified, revealing fast protein turnover in HeLa and HEK293T cells, and newly grown neurites in differentiating neuron-like N2A cells. Metabolic changes of proteins and lipids were also studied in cancer cells during epithelial–mesenchymal transition [142]. Compared with approaches like SILAC or fluorescence, this approach with Raman–SIP could examine the proteome of a cell in a spatially resolved, non-destructive manner on living single cells with only minor modifications [145]. This approach could also be used to study protein degradation using ^{13}C labelled amino acids [134,135].

Compared with lipid and protein metabolism, there are fewer studies utilizing Raman–SIP approach to study DNA synthesis. Apart from newly synthesized DNA observed from deuterated glucose metabolism, EdU as an analog of thymidine was exclusively used as a DNA metabolic tag, which was incorporated into cellular biomass during cell division [146]. Chen et al. synthesized various designs of ^{13}C isotopologues of EdU and demonstrated three-color chemical imaging of nascent DNA, RNA, and newly synthesized fatty-acid in live HeLa cells.

4.3. Raman–SIP with D_2O Measures General Metabolic Activity

Apart from specifically labeled precursors of cellular constituents, heavy water (D_2O) is suggested to be a unique and universal tool to monitor the synthesis of biomolecules on a global scale. As an isotopologue of water, D_2O can rapidly and freely equilibrate with the total body water inside a cell, and D atoms can exchange with the H atoms to form a variety of X–D bonds. Different from the often non-enzymatic reactions to form heteroatomic X–D bonds, such as O–D, N–D, and S–D, the C–D bond formation depends solely on enzyme-catalyzed chemical reactions, due to the stronger C–H bond strength [122]. In C–H/C–D exchanges, D atoms from D_2O are rapidly incorporated into metabolic precursors of different classes of biomolecules such as deoxyribose, acetyl-CoA/NADPH, amino acids, and phosphoenolpyruvate (PEP) (Figure 8). These precursors with D labeling are then slowly incorporated into their final products, which are nucleic acids, lipids, proteins, and carbohydrates. Therefore, D_2O serves as an ideal agent to probe general metabolic activities through the emergence of a variety of D-labelled macromolecules.

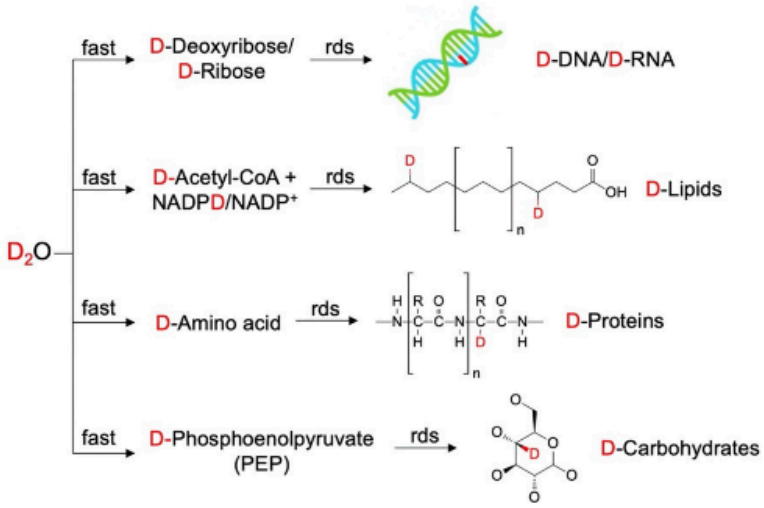


Figure 8. D_2O as a unique and universal tracer for different biomolecules. 'rds' stands for rate-determining step.

Raman–SIP using D_2O was demonstrated to measure the general metabolic activities of single microbial cells, first reported by Berry et al. [117]. By incubating microbes with D_2O, physiologically active cells could be rapidly and sensitively identified with Raman, by measuring the C–D peak at 2170–2300 cm^{-1}. The metabolic activity could then be semi-quantified and compared by measuring the degree of D incorporation. This approach was extensively applied to study microbial activity and ecology [116,121,147–154]. Recently, it also generated an impact in the area of metabolic studies of animal cells.

Shi et al. demonstrated SRS imaging based on D_2O in various animal models, achieving dynamic visualization of proteins, lipids, and DNA [143]. Based on the fact that tumor cells show inherently higher metabolic activities than normal cells, the study was able to visualize the boundaries between tumors and the surrounding normal tissues. The distribution of intratumor heterogeneity was also observed, which is considered a driver of tumor aggressiveness. In this study, the authors also suggested that D_2O is a better probe than deuterium-labeled carbon substrates. For visualizing lipogenic activities, D_2O is better than deuterated fatty acids, as well as deuterated glucose, which at high concentrations, could potentially create hyperglycemia and might be less efficient in labeling newly synthesized lipids. In addition, D_2O is cost-effective, as compared to other Raman–SIP probes and is universal in probing a range of metabolic activities simultaneously. Most recently, Hekmatara et al. applied Raman–SIP with D_2O to study anticancer drug response of MCF-7 cells [144]. They discovered high subcellular activities of cancer cells after high-dosage rapamycin exposure at the single-cell level, which was masked in a population-wise cytotoxicity test.

Although Raman–SIP application in cancer research using heavy water is just coming of age, recent studies exhibit its great potential in metabolic studies, as it is non-invasive, cost-effective, easily accessible, and universally applicable. It can be adapted to a broad range of model systems and cancer research areas to study cancer development, tissue homeostasis, tumor heterogeneity, cancer drug response, and pharmacokinetics. It would be of particular value in diagnosis at surgery, categorizing cancers by their metabolic status, evaluating new drugs, their uptake and metabolism, their antitumor effects, resistance mechanisms, and responses. Characterizing the changes in stroma at the local and distant sites and in premalignant disease, is likely to provide new insights into cancer development.

5. Conclusions and Outlook

Raman spectroscopy technologies, from comprehensive spectroscopy to advanced imaging, offer exciting new possibilities in cancer research. In this review, we summarize a wide range of applications using Raman and Raman–SIP techniques to investigate metabolism in cancer cells and tissues. Offering intrinsic biochemical information and subcellular spatial resolution, the Raman profile of a cancer cell or tissue is an excellent metabolic indicator and an indicator of phenotypic heterogeneity. It can help uncover the molecular basis of the disease and provide comprehensive, objective, and quantifiable molecular information for diagnosis and treatment evaluation.

Looking into the future, the potential of Raman spectroscopy and imaging in cancer research could be further exploited. Critical improvements and advances are still under development. Raman databases of more metabolites, potentially comparable to a mass spectrometry database, can cover identification of more metabolites. Advanced chemometric algorithms and machine-learning methods can improve and accelerate current spectral processing and data interpretation, especially in a large, high-dimensional clinical dataset. Instrumentation engineering of advanced fiber optics, detectors, and handheld spectrometer would render Raman tools accessible for clinical translation.

Author Contributions: W.E.H., A.L.H. and J.-X.C. conceived and designed the study. J.X. and T.Y. performed the systematic review of the literature and wrote the manuscript. C.E.Z. and Y.T. conducted critical review of the study. All authors contributed to interpreting the data, revised the work, and approved the final version of the manuscript.

Funding: W.E.H. acknowledges finance and instrumentation support from EPSRC (EP/M002403/1, EP/M02833X/1) and NERC (NE/M002934/1).

Institutional Review Board Statement: Not applicable.

Acknowledgments: We thank Shanghai D-band Medical Instrument Co, Shanghai China for providing spontaneous Raman images and constructive discussion. J.X. and W.E.H. thank the Suzhou Institute of Biomedical Engineering and Technology, Chinese Academy of Sciences for financial support. A.L.H. and C.Z. thank the Breast Cancer Research Foundation for support.

Conflicts of Interest: The authors declare no conflict of interest.

References

1. Pavlova, N.N.; Thompson, C.B. The Emerging Hallmarks of Cancer Metabolism. *Cell Metab.* **2016**, *23*, 27–47. [CrossRef] [PubMed]
2. Heiden, M.G.V.; Cantley, L.C.; Thompson, C.B. Understanding the Warburg effect: The metabolic requirements of cell proliferation. *Science* **2009**, *324*, 1029–1033. [CrossRef] [PubMed]
3. DeBerardinis, R.J.; Chandel, N.S. Fundamentals of cancer metabolism. *Sci. Adv.* **2016**, *2*, e1600200. [CrossRef]
4. Gerlinger, M.; Rowan, A.J.; Horswell, S.; Larkin, J.; Endesfelder, D.; Gronroos, E.; Martinez, P.; Matthews, N.; Stewart, A.; Tarpey, P.; et al. Intratumor Heterogeneity and Branched Evolution Revealed by Multiregion Sequencing. *N. Engl. J. Med.* **2012**, *366*, 883–892. [CrossRef]
5. Thiele, C.; Wunderling, K.; Leyendecker, P. Multiplexed and single cell tracing of lipid metabolism. *Nat. Methods* **2019**, *16*, 1123–1130. [CrossRef]
6. Duncan, K.D.; Fyrestam, J.; Lanekoff, I. Advances in mass spectrometry based single-cell metabolomics. *Analyst* **2019**, *144*, 782–793. [CrossRef] [PubMed]
7. Zenobi, R. Single-Cell Metabolomics: Analytical and Biological Perspectives. *Science* **2013**, *342*, 1243259. [CrossRef]
8. Chakraborty, A.; Ghosh, A.; Barui, A. Advances in surface-enhanced Raman spectroscopy for cancer diagnosis and staging. *J. Raman Spectrosc.* **2020**, *51*, 7–36. [CrossRef]
9. Cialla-May, D.; Zheng, X.-S.; Weber, K.; Popp, J. Recent progress in surface-enhanced Raman spectroscopy for biological and biomedical applications: From cells to clinics. *Chem. Soc. Rev.* **2017**, *46*, 3945–3961. [CrossRef]
10. Guerrini, L.; Alvarez-Puebla, R.A. Surface-Enhanced Raman Spectroscopy in Cancer Diagnosis, Prognosis and Monitoring. *Cancers* **2019**, *11*, 748. [CrossRef] [PubMed]
11. Krafft, C.; Schie, I.W.; Meyer, T.; Schmitt, M.; Popp, J. Developments in spontaneous and coherent Raman scattering microscopic imaging for biomedical applications. *Chem. Soc. Rev.* **2015**, *45*, 1819–1849. [CrossRef] [PubMed]
12. Raman, C.V.; Krishnan, K.S. A New Type of Secondary Radiation. *Nat. Cell Biol.* **1928**, *121*, 501–502. [CrossRef]
13. Thorn, K. Genetically encoded fluorescent tags. *Mol. Biol. Cell* **2017**, *28*, 848–857. [CrossRef] [PubMed]
14. Zhang, Y.; Hong, H.; Cai, W. Imaging with Raman Spectroscopy. *Curr. Pharm. Biotechnol.* **2010**, *11*, 654–661. [CrossRef]
15. Liao, C.-S.; Slipchenko, M.N.; Wang, P.; Li, J.; Lee, S.-Y.; Oglesbee, R.A.; Cheng, J.-X. Microsecond scale vibrational spectroscopic imaging by multiplex stimulated Raman scattering microscopy. *Light. Sci. Appl.* **2015**, *4*, e265. [CrossRef] [PubMed]
16. Liao, C.-S.; Huang, K.-C.; Hong, W.; Chen, A.J.; Karanja, C.; Wang, P.; Eakins, G.; Cheng, J.-X. Stimulated Raman spectroscopic imaging by microsecond delay-line tuning. *Optica* **2016**, *3*, 1377–1380. [CrossRef]
17. Lin, H.; Lee, H.J.; Tague, N.; Lugagne, J.-B.; Zong, C.; Deng, F.; Shin, J.; Tian, L.; Wong, W.; Dunlop, M.J.; et al. Microsecond Fingerprint Stimulated Raman Spectroscopic Imaging by Ultrafast Tuning and Spatial-Spectral Learning. *arXiv* **2020**, arXiv:2003.02224.
18. Cheng, J.X.; Xie, X.S. (Eds.) *Coherent Raman Scattering Microscopy*; CRC Press, Taylor & Francis Group: Boca Raton, FL, USA, 2013.
19. Liao, C.-S.; Cheng, J.-X. In Situ and In Vivo Molecular Analysis by Coherent Raman Scattering Microscopy. *Annu. Rev. Anal. Chem.* **2016**, *9*, 69–93. [CrossRef]
20. Marangoni, M.; Gambetta, A.; Manzoni, C.; Kumar, V.; Ramponi, R.; Cerullo, G. Fiber-format CARS spectroscopy by spectral compression of femtosecond pulses from a single laser oscillator. *Opt. Lett.* **2009**, *34*, 3262–3264. [CrossRef]
21. Zhang, C.; Zhang, D.; Cheng, J.-X. Coherent Raman Scattering Microscopy in Biology and Medicine. *Annu. Rev. Biomed. Eng.* **2015**, *17*, 415–445. [CrossRef]
22. Palonpon, A.F.; Ando, J.; Yamakoshi, H.; Dodo, K.; Sodeoka, M.; Kawata, S.; Fujita, K. Raman and SERS microscopy for molecular imaging of live cells. *Nat. Protoc.* **2013**, *8*, 677–692. [CrossRef] [PubMed]
23. O'Malley, J.; Kumar, R.; Kuzmin, A.N.; Pliss, A.; Yadav, N.; Balachandar, S.; Wang, J.; Attwood, K.; Prasad, P.N.; Chandra, D. Lipid quantification by Raman microspectroscopy as a potential biomarker in prostate cancer. *Cancer Lett.* **2017**, *397*, 52–60. [CrossRef] [PubMed]
24. Lita, A.; Kuzmin, A.N.; Pliss, A.; Baev, A.; Rzhevskii, A.; Gilbert, M.R.; Larion, M.; Prasad, P.N. Toward Single-Organelle Lipidomics in Live Cells. *Anal. Chem.* **2019**, *91*, 11380–11387. [CrossRef] [PubMed]

25. Kuzmin, A.N.; Levchenko, S.M.; Pliss, A.; Qu, J.; Prasad, P.N. Molecular profiling of single organelles for quantitative analysis of cellular heterogeneity. *Sci. Rep.* **2017**, *7*, 1–9. [CrossRef] [PubMed]
26. Kuzmin, A.N.; Pliss, A.; Rzhevskii, A.; Lita, A.; Larion, M. BCAbox Algorithm Expands Capabilities of Raman Microscope for Single Organelles Assessment. *Biosensors* **2018**, *8*, 106. [CrossRef]
27. Lita, A.; Pliss, A.; Kuzmin, A.; Yamasaki, T.; Zhang, L.; Dowdy, T.; Burks, C.; de Val, N.; Celiku, O.; Ruiz-Rodado, V.; et al. IDH1 mutations induce organelle defects via dysregulated phospholipids. *Nat. Commun.* **2021**, *12*, 1–16. [CrossRef]
28. Zhang, D.; Wang, P.; Slipchenko, M.N.; Cheng, J.-X. Fast Vibrational Imaging of Single Cells and Tissues by Stimulated Raman Scattering Microscopy. *Accounts Chem. Res.* **2014**, *47*, 2282–2290. [CrossRef]
29. Munir, R.; Lisec, J.; Swinnen, J.V.; Zaidi, N. Lipid metabolism in cancer cells under metabolic stress. *Br. J. Cancer* **2019**, *120*, 1090–1098. [CrossRef]
30. Ackerman, D.; Simon, M.C. Hypoxia, lipids, and cancer: Surviving the harsh tumor microenvironment. *Trends Cell Biol.* **2014**, *24*, 472–478. [CrossRef]
31. Zaidi, N.; Lupien, L.; Kuemmerle, N.B.; Kinlaw, W.B.; Swinnen, J.V.; Smans, K. Lipogenesis and lipolysis: The pathways exploited by the cancer cells to acquire fatty acids. *Prog. Lipid Res.* **2013**, *52*, 585–589. [CrossRef]
32. Kuemmerle, N.B.; Rysman, E.; Lombardo, P.S.; Flanagan, A.J.; Lipe, B.C.; Wells, W.A.; Pettus, J.R.; Froehlich, H.M.; Memoli, V.A.; Morganelli, P.M.; et al. Lipoprotein Lipase Links Dietary Fat to Solid Tumor Cell Proliferation. *Mol. Cancer Ther.* **2011**, *10*, 427–436. [CrossRef] [PubMed]
33. Menendez, J.A.; Lupu, R. Fatty acid synthase and the lipogenic phenotype in cancer pathogenesis. *Nat. Rev. Cancer* **2007**, *7*, 763–777. [CrossRef] [PubMed]
34. Cha, J.-Y.; Lee, H.-J. Targeting Lipid Metabolic Reprogramming as Anticancer Therapeutics. *J. Cancer Prev.* **2016**, *21*, 209–215. [CrossRef]
35. Abramczyk, H.; Brozek-Pluska, B. New look inside human breast ducts with Raman imaging. Raman candidates as diagnostic markers for breast cancer prognosis: Mammaglobin, palmitic acid and sphingomyelin. *Anal. Chim. Acta* **2016**, *909*, 91–100. [CrossRef]
36. Abramczyk, H.; Surmacki, J.; Kopeć, M.; Olejnik, A.K.; Lubecka-Pietruszewska, K.; Fabianowska-Majewska, K. The role of lipid droplets and adipocytes in cancer. Raman imaging of cell cultures: MCF10A, MCF7, and MDA-MB-231 compared to adipocytes in cancerous human breast tissue. *Analyst* **2015**, *140*, 2224–2235. [CrossRef] [PubMed]
37. Surmacki, J.; Brozek-Pluska, B.; Kordek, R.; Abramczyk, H. The lipid-reactive oxygen species phenotype of breast cancer. Raman spectroscopy and mapping, PCA and PLSDA for invasive ductal carcinoma and invasive lobular carcinoma. Molecular tumorigenic mechanisms beyond Warburg effect. *Analyst* **2015**, *140*, 2121–2133. [CrossRef] [PubMed]
38. You, S.; Tu, H.; Zhao, Y.; Liu, Y.; Chaney, E.J.; Marjanovic, M.; Boppart, S.A. Raman Spectroscopic Analysis Reveals Abnormal Fatty Acid Composition in Tumor Micro- and Macroenvironments in Human Breast and Rat Mammary Cancer. *Sci. Rep.* **2016**, *6*, 32922. [CrossRef] [PubMed]
39. Nieva, C.; Marro, M.; Santana-Codina, N.; Rao, S.; Petrov, D.; Sierra, A. The Lipid Phenotype of Breast Cancer Cells Characterized by Raman Microspectroscopy: Towards a Stratification of Malignancy. *PLoS ONE* **2012**, *7*, e46456. [CrossRef] [PubMed]
40. Tirinato, L.; Liberale, C.; Di Franco, S.; Candeloro, P.; Benfante, A.; La Rocca, R.; Potze, L.; Marotta, R.; Ruffilli, R.; Rajamanickam, V.P.; et al. Lipid Droplets: A New Player in Colorectal Cancer Stem Cells Unveiled by Spectroscopic Imaging. *Stem Cells* **2015**, *33*, 35–44. [CrossRef] [PubMed]
41. Le, T.T.; Huff, T.B.; Cheng, J.-X. Coherent anti-Stokes Raman scattering imaging of lipids in cancer metastasis. *BMC Cancer* **2009**, *9*, 42. [CrossRef]
42. Gniadecka, M.; Philipsen, P.A.; Wessel, S.; Gniadecki, R.; Wulf, H.C.; Sigurdsson, S.; Nielsen, O.F.; Christensen, D.H.; Hercogova, J.; Rossen, K.; et al. Melanoma Diagnosis by Raman Spectroscopy and Neural Networks: Structure Alterations in Proteins and Lipids in Intact Cancer Tissue. *J. Investig. Dermatol.* **2004**, *122*, 443–449. [CrossRef] [PubMed]
43. Du, J.; Su, Y.; Qian, C.; Yuan, D.; Miao, K.; Lee, D.; Ng, A.H.C.; Wijker, R.S.; Ribas, A.; Levine, R.D.; et al. Raman-guided subcellular pharmaco-metabolomics for metastatic melanoma cells. *Nat. Commun.* **2020**, *11*, 1–16. [CrossRef]
44. Nan, X.; Cheng, J.-X.; Xie, X.S. Vibrational imaging of lipid droplets in live fibroblast cells with coherent anti-Stokes Raman scattering microscopy. *J. Lipid Res.* **2003**, *44*, 2202–2208. [CrossRef] [PubMed]
45. Freudiger, C.W.; Min, W.; Saar, B.G.; Lu, S.; Holtom, G.R.; He, C.; Tsai, J.C.; Kang, J.X.; Xie, X.S. Label-Free Biomedical Imaging with High Sensitivity by Stimulated Raman Scattering Microscopy. *Science* **2008**, *322*, 1857–1861. [CrossRef] [PubMed]
46. Slipchenko, M.N.; Le, T.T.; Chen, H.; Cheng, J.-X. High-Speed Vibrational Imaging and Spectral Analysis of Lipid Bodies by Compound Raman Microscopy. *J. Phys. Chem. B* **2009**, *113*, 7681–7686. [CrossRef]
47. Mitra, R.; Chao, O.; Urasaki, Y.; Goodman, O.B.; Le, T.T. Detection of Lipid-Rich Prostate Circulating Tumour Cells with Coherent Anti-Stokes Raman Scattering Microscopy. *BMC Cancer* **2012**, *12*, 540. [CrossRef]
48. Li, J.; Condello, S.; Thomes-Pepin, J.; Ma, X.; Xia, Y.; Hurley, T.D.; Matei, D.; Cheng, J.-X. Lipid Desaturation Is a Metabolic Marker and Therapeutic Target of Ovarian Cancer Stem Cells. *Cell Stem Cell* **2017**, *20*, 303–314. [CrossRef]
49. Yan, S.; Cui, S.; Ke, K.; Zhao, B.; Liu, X.; Yue, S.; Wang, P. Hyperspectral Stimulated Raman Scattering Microscopy Unravels Aberrant Accumulation of Saturated Fat in Human Liver Cancer. *Anal. Chem.* **2018**, *90*, 6362–6366. [CrossRef] [PubMed]

50. Zhang, C.; Li, J.; Lan, L.; Cheng, J.-X. Quantification of Lipid Metabolism in Living Cells through the Dynamics of Lipid Droplets Measured by Stimulated Raman Scattering Imaging. *Anal. Chem.* **2017**, *89*, 4502–4507. [CrossRef]
51. Huang, K.-C.; Li, J.; Zhang, C.; Tan, Y.; Cheng, J.-X. Multiplex Stimulated Raman Scattering Imaging Cytometry Reveals Lipid-Rich Protrusions in Cancer Cells under Stress Condition. *Science* **2020**, *23*, 100953. [CrossRef]
52. Fu, D.; Holtom, G.; Freudiger, C.; Zhang, X.; Xie, X.S. Hyperspectral Imaging with Stimulated Raman Scattering by Chirped Femtosecond Lasers. *J. Phys. Chem. B* **2013**, *117*, 4634–4640. [CrossRef] [PubMed]
53. Ji, M.; Orringer, D.A.; Freudiger, C.W.; Ramkissoon, S.; Liu, X.; Lau, D.; Golby, A.J.; Norton, I.; Hayashi, M.; Agar, N.Y.R.; et al. Rapid, Label-Free Detection of Brain Tumors with Stimulated Raman Scattering Microscopy. *Sci. Transl. Med.* **2013**, *5*, 201ra119. [CrossRef] [PubMed]
54. Folick, A.; Min, W.; Wang, M.C. Label-free imaging of lipid dynamics using Coherent Anti-stokes Raman Scattering (CARS) and Stimulated Raman Scattering (SRS) microscopy. *Curr. Opin. Genet. Dev.* **2011**, *21*, 585–590. [CrossRef] [PubMed]
55. Yu, Y.; Ramachandran, P.V.; Wang, M.C. Shedding new light on lipid functions with CARS and SRS microscopy. *Biochim. Biophys. Acta BBA Mol. Cell Biol. Lipids* **2014**, *1841*, 1120–1129. [CrossRef]
56. Abramczyk, H.; Imiela, A.; Śliwińska, A. Novel strategies of Raman imaging for exploring cancer lipid reprogramming. *J. Mol. Liq.* **2019**, *274*, 52–59. [CrossRef]
57. Talari, A.C.S.; Evans, C.A.; Holen, I.; Coleman, R.E.; Rehman, I.U. Raman spectroscopic analysis differentiates between breast cancer cell lines. *J. Raman Spectrosc.* **2015**, *46*, 421–427. [CrossRef]
58. Abramczyk, H.; Imiela, A.; Brożek-Płuska, B.; Kopeć, M.; Surmacki, J.; Śliwińska, A. Aberrant Protein Phosphorylation in Cancer by Using Raman Biomarkers. *Cancers* **2019**, *11*, 2017. [CrossRef]
59. Marro, M.; Nieva, C.; De Juan, A.; Sierra, A. Unravelling the Metabolic Progression of Breast Cancer Cells to Bone Metastasis by Coupling Raman Spectroscopy and a Novel Use of Mcr-Als Algorithm. *Anal. Chem.* **2018**, *90*, 5594–5602. [CrossRef]
60. Kopec, M.; Imiela, A.; Abramczyk, H. Monitoring glycosylation metabolism in brain and breast cancer by Raman imaging. *Sci. Rep.* **2019**, *9*, 1–13. [CrossRef]
61. Chaturvedi, D.; Balaji, S.A.; Bn, V.K.; Ariese, F.; Umapathy, S.; Rangarajan, A. Different Phases of Breast Cancer Cells: Raman Study of Immortalized, Transformed, and Invasive Cells. *Biosensors* **2016**, *6*, 57. [CrossRef]
62. Lemoine, É.; Dallaire, F.; Yadav, R.; Agarwal, R.; Kadoury, S.; Trudel, D.; Guiot, M.-C.; Petrecca, K.; Leblond, F. Feature engineering applied to intraoperativein vivoRaman spectroscopy sheds light on molecular processes in brain cancer: A retrospective study of 65 patients. *Analyst* **2019**, *144*, 6517–6532. [CrossRef]
63. Lu, F.-K.; Ji, M.; Fu, D.; Ni, X.; Freudiger, C.W.; Holtom, G.; Xie, X.S. Multicolor stimulated Raman scattering microscopy. *Mol. Phys.* **2012**, *110*, 1927–1932. [CrossRef]
64. Zhang, X.; Roeffaers, M.B.J.; Basu, S.; Daniele, J.R.; Fu, D.; Freudiger, C.W.; Holtom, G.R.; Xie, X.S. Label-Free Live-Cell Imaging of Nucleic Acids Using Stimulated Raman Scattering Microscopy. *ChemPhysChem* **2012**, *13*, 1054–1059. [CrossRef]
65. Lu, F.-K.; Basu, S.; Igras, V.; Hoang, M.P.; Ji, M.; Fu, D.; Holtom, G.R.; Neel, V.A.; Freudiger, C.W.; Fisher, D.E.; et al. Label-free DNA imaging in vivo with stimulated Raman scattering microscopy. *Proc. Natl. Acad. Sci. USA* **2015**, *112*, 11624–11629. [CrossRef]
66. Zhuge, M.; Huang, K.; Lee, H.J.; Jiang, Y.; Tan, Y.; Lin, H.; Dong, P.; Zhao, G.; Matei, D.; Yang, Q.; et al. Ultrasensitive Vibrational Imaging of Retinoids by Visible Preresonance Stimulated Raman Scattering Microscopy. *Adv. Sci.* **2021**, 2003136. [CrossRef]
67. Jamieson, L.E.; Wetherill, C.; Faulds, K.; Graham, D. Ratiometric Raman imaging reveals the new anti-cancer potential of lipid targeting drugs. *Chem. Sci.* **2018**, *9*, 6935–6943. [CrossRef]
68. Potcoava, M.C.; Futia, G.L.; Aughenbaugh, J.; Schlaepfer, I.R.; Gibson, E.A. Raman and coherent anti-Stokes Raman scattering microscopy studies of changes in lipid content and composition in hormone-treated breast and prostate cancer cells. *J. Biomed. Opt.* **2014**, *19*, 111605. [CrossRef]
69. Wen, X.; Ou, Y.-C.; Bogatcheva, G.; Thomas, G.; Mahadevan-Jansen, A.; Singh, B.; Lin, E.C.; Bardhan, R. Probing metabolic alterations in breast cancer in response to molecular inhibitors with Raman spectroscopy and validated with mass spectrometry. *Chem. Sci.* **2020**, *11*, 9863–9874. [CrossRef]
70. El-Mashtoly, S.F.; Yosef, H.K.; Petersen, D.; Mavarani, L.; Maghnouj, A.; Hahn, S.; Kötting, C.; Gerwert, K. Label-Free Raman Spectroscopic Imaging Monitors the Integral Physiologically Relevant Drug Responses in Cancer Cells. *Anal. Chem.* **2015**, *87*, 7297–7304. [CrossRef] [PubMed]
71. Larion, M.; Dowdy, T.; Ruiz-Rodado, V.; Meyer, M.W.; Song, H.; Zhang, W.; Davis, D.; Gilbert, M.R.; Lita, A. Detection of Metabolic Changes Induced via Drug Treatments in Live Cancer Cells and Tissue Using Raman Imaging Microscopy. *Biosensors* **2018**, *9*, 5. [CrossRef] [PubMed]
72. Farhane, Z.; Bonnier, F.; Casey, A.; Byrne, H.J. Raman micro spectroscopy for in vitro drug screening: Subcellular localisation and interactions of doxorubicin. *Analyst* **2015**, *140*, 4212–4223. [CrossRef]
73. Zhang, H.; Xiao, L.; Li, Q.; Qi, X.; Zhou, A. Microfluidic chip for non-invasive analysis of tumor cells interaction with anti-cancer drug doxorubicin by AFM and Raman spectroscopy. *Biomicrofluidics* **2018**, *12*, 024119. [CrossRef] [PubMed]
74. Zhang, Y.; Xu, J.; Yu, Y.; Shang, W.; Ye, A. Anti-Cancer Drug Sensitivity Assay with Quantitative Heterogeneity Testing Using Single-Cell Raman Spectroscopy. *Molecules* **2018**, *23*, 2903. [CrossRef]
75. Aljakouch, K.; Lechtonen, T.; Yosef, H.K.; Hammoud, M.K.; Alsaidi, W.; Kötting, C.; Mügge, C.; Kourist, R.; El-Mashtoly, S.F.; Gerwert, K. Raman Microspectroscopic Evidence for the Metabolism of a Tyrosine Kinase Inhibitor, Neratinib, in Cancer Cells. *Angew. Chem. Int. Ed.* **2018**, *57*, 7250–7254. [CrossRef] [PubMed]

76. El-Mashtoly, S.F.; Petersen, D.; Yosef, H.K.; Mosig, A.; Reinacher-Schick, A.; Kötting, C.; Gerwert, K. Label-free imaging of drug distribution and metabolism in colon cancer cells by Raman microscopy. *Analyst* **2014**, *139*, 1155–1161. [CrossRef] [PubMed]
77. Fu, D.; Zhou, J.; Zhu, W.S.; Manley, P.W.; Wang, Y.K.; Hood, T.; Wylie, A.; Xie, X.S. Imaging the intracellular distribution of tyrosine kinase inhibitors in living cells with quantitative hyperspectral stimulated Raman scattering. *Nat. Chem.* **2014**, *6*, 614–622. [CrossRef] [PubMed]
78. Sepp, K.; Lee, M.; Bluntzer, M.T.J.; Helgason, G.V.; Hulme, A.N.; Brunton, V.G. Utilizing Stimulated Raman Scattering Microscopy To Study Intracellular Distribution of Label-Free Ponatinib in Live Cells. *J. Med. Chem.* **2019**, *63*, 2028–2034. [CrossRef] [PubMed]
79. Qiu, S.; Weng, Y.; Li, Y.; Chen, Y.; Pan, Y.; Liu, J.; Lin, W.; Chen, X.; Li, M.; Lin, T.; et al. Raman profile alterations of irradiated human nasopharyngeal cancer cells detected with laser tweezer Raman spectroscopy. *RSC Adv.* **2020**, *10*, 14368–14373. [CrossRef]
80. Roman, M.; Wrobel, T.P.; Panek, A.; Paluszkiewicz, C.; Kwiatek, W.M. Lipid droplets in prostate cancer cells and effect of irradiation studied by Raman microspectroscopy. *Biochim. Biophys. Acta BBA Mol. Cell Biol. Lipids* **2020**, *1865*, 158753. [CrossRef]
81. Milligan, K.; Deng, X.; Shreeves, P.; Ali-Adeeb, R.; Matthews, Q.; Brolo, A.; Lum, J.J.; Andrews, J.L.; Jirasek, A. Raman spectroscopy and group and basis-restricted non negative matrix factorisation identifies radiation induced metabolic changes in human cancer cells. *Sci. Rep.* **2021**, *11*, 1–11. [CrossRef] [PubMed]
82. Kumar, S.; Visvanathan, A.; Arivazhagan, A.; Santhosh, V.; Somasundaram, K.; Umapathy, S. Assessment of Radiation Resistance and Therapeutic Targeting of Cancer Stem Cells: A Raman Spectroscopic Study of Glioblastoma. *Anal. Chem.* **2018**, *90*, 12067–12074. [CrossRef] [PubMed]
83. Van Nest, S.J.; Nicholson, L.M.; Pavey, N.; Hindi, M.N.; Brolo, A.G.; Jirasek, A.; Lum, J.J. Raman spectroscopy detects metabolic signatures of radiation response and hypoxic fluctuations in non-small cell lung cancer. *BMC Cancer* **2019**, *19*, 474. [CrossRef] [PubMed]
84. Auner, G.W.; Koya, S.K.; Huang, C.; Broadbent, B.; Trexler, M.; Auner, Z.; Elias, A.; Mehne, K.C.; Brusatori, M.A. Applications of Raman spectroscopy in cancer diagnosis. *Cancer Metastasis Rev.* **2018**, *37*, 691–717. [CrossRef] [PubMed]
85. Cui, S.; Zhang, S.; Yue, S. Raman Spectroscopy and Imaging for Cancer Diagnosis. *J. Health Eng.* **2018**, *2018*, 1–11. [CrossRef] [PubMed]
86. Austin, L.A.; Osseiran, S.; Evans, C.L. Raman technologies in cancer diagnostics. *Analyst* **2015**, *141*, 476–503. [CrossRef] [PubMed]
87. Contorno, S.; Darienzo, R.E.; Tannenbaum, R. Evaluation of aromatic amino acids as potential biomarkers in breast cancer by Raman spectroscopy analysis. *Sci. Rep.* **2021**, *11*, 1–9. [CrossRef]
88. Haka, A.S.; Shafer-Peltier, K.E.; Fitzmaurice, M.; Crowe, J.; Dasari, R.R.; Feld, M.S. Diagnosing breast cancer by using Raman spectroscopy. *Proc. Natl. Acad. Sci. USA* **2005**, *102*, 12371–12376. [CrossRef] [PubMed]
89. Hu, C.; Wang, J.; Zheng, C.; Xu, S.; Zhang, H.; Liang, Y.; Bi, L.; Fan, Z.; Han, B.; Xu, W. Raman spectra exploring breast tissues: Comparison of principal component analysis and support vector machine-recursive feature elimination. *Med. Phys.* **2013**, *40*, 063501. [CrossRef]
90. Abramczyk, H.; Brozek-Pluska, B.; Surmacki, J.; Jablonska-Gajewicz, J.; Kordek, R. Raman 'optical biopsy' of human breast cancer. *Prog. Biophys. Mol. Biol.* **2012**, *108*, 74–81. [CrossRef]
91. Brozek-Pluska, B.; Musial, J.; Kordek, R.; Bailo, E.; Dieing, T.; Abramczyk, H. Raman spectroscopy and imaging: Applications in human breast cancer diagnosis. *Analyst* **2012**, *137*, 3773–3780. [CrossRef]
92. Abramczyk, H.; Brozek-Pluska, B.; Surmacki, J.; Jabłońska, J.; Kordek, R. The label-free Raman imaging of human breast cancer. *J. Mol. Liq.* **2011**, *164*, 123–131. [CrossRef]
93. Bendau, E.; Smith, J.; Zhang, L.; Ackerstaff, E.; Kruchevsky, N.; Wu, B.; Koutcher, J.A.; Alfano, R.; Shi, L. Distinguishing metastatic triple-negative breast cancer from nonmetastatic breast cancer using second harmonic generation imaging and resonance Raman spectroscopy. *J. Biophotonics* **2020**, *13*, e202000005. [CrossRef] [PubMed]
94. Kopeć, M.; Abramczyk, H. Angiogenesis—A crucial step in breast cancer growth, progression and dissemination by Raman imaging. *Spectrochim. Acta Part A Mol. Biomol. Spectrosc.* **2018**, *198*, 338–345. [CrossRef] [PubMed]
95. Brozek-Pluska, B.; Kopeć, M.; Abramczyk, H. Development of a new diagnostic Raman method for monitoring epigenetic modifications in the cancer cells of human breast tissue. *Anal. Methods* **2016**, *8*, 8542–8553. [CrossRef]
96. Chrabaszcz, K.; Kochan, K.; Fedorowicz, A.; Jasztal, A.; Buczek, E.; Leslie, L.S.; Bhargava, R.; Malek, K.; Chlopicki, S.; Marzec, K.M. FT-IR- and Raman-based biochemical profiling of the early stage of pulmonary metastasis of breast cancer in mice. *Analyst* **2018**, *143*, 2042–2050. [CrossRef] [PubMed]
97. Koljenović, S.; Choo-Smith, L.-P.; Schut, T.C.B.; Kros, J.M.; Berge, H.J.V.D.; Puppels, G.J. Discriminating Vital Tumor from Necrotic Tissue in Human Glioblastoma Tissue Samples by Raman Spectroscopy. *Lab. Investig.* **2002**, *82*, 1265–1277. [CrossRef]
98. Koljenovic, S.; Schut, T.C.B.; Wolthuis, R.; Vincent, A.J.P.E.; Hendriks-Hagevi, G.; Santos, L.; Kros, J.M.; Puppels, G.J. Raman Spectroscopic Characterization of Porcine Brain Tissue Using a Single Fiber-Optic Probe. *Anal. Chem.* **2007**, *79*, 557–564. [CrossRef]
99. Krafft, C.; Belay, B.; Bergner, N.; Romeike, B.F.M.; Reichart, R.; Kalff, R.; Popp, J. Advances in optical biopsy—Correlation of malignancy and cell density of primary brain tumors using Raman microspectroscopic imaging. *Analyst* **2012**, *137*, 5533–5537. [CrossRef]
100. Jermyn, M.; Mok, K.; Mercier, J.; Desroches, J.; Pichette, J.; Saint-Arnaud, K.; Bernstein, L.; Guiot, M.-C.; Petrecca, K.; Leblond, F. Intraoperative brain cancer detection with Raman spectroscopy in humans. *Sci. Transl. Med.* **2015**, *7*, 274ra19. [CrossRef]

101. Bratchenko, I.A.; Artemyev, D.N.; Myakinin, O.O.; Khristoforova, Y.A.; Moryatov, A.A.; Kozlov, S.V.; Zakharov, V.P. Combined Raman and autofluorescence ex vivo diagnostics of skin cancer in near-infrared and visible regions. *J. Biomed. Opt.* **2017**, *22*, 027005. [CrossRef] [PubMed]
102. Schut, T.C.B.; Caspers, P.J.; Puppels, G.J.; Nijssen, A.; Heule, F.; Neumann, M.H.; Hayes, D.P. Discriminating Basal Cell Carcinoma from its Surrounding Tissue by Raman Spectroscopy. *J. Investig. Dermatol.* **2002**, *119*, 64–69. [CrossRef] [PubMed]
103. Bodanese, B.; Silveira, L.; Albertini, R.; Zângaro, R.A.; Pacheco, M.T.T. Differentiating Normal and Basal Cell Carcinoma Human Skin Tissues In Vitro Using Dispersive Raman Spectroscopy: A Comparison Between Principal Components Analysis and Simplified Biochemical Models. *Photomed. Laser Surg.* **2010**, *28*, S119–S127. [CrossRef] [PubMed]
104. Bodanese, B.; Silveira, F.L.; Zângaro, R.A.; Pacheco, M.T.T.; Pasqualucci, C.A.; Silveira, L. Discrimination of Basal Cell Carcinoma and Melanoma from Normal Skin Biopsies in Vitro Through Raman Spectroscopy and Principal Component Analysis. *Photomed. Laser Surg.* **2012**, *30*, 381–387. [CrossRef]
105. Nijssen, A.; Maquelin, K.; Santos, L.F.; Caspers, P.J.; Schut, T.C.B.; Hollander, J.C.D.; Neumann, M.H.A.; Puppels, G.J. Discriminating basal cell carcinoma from perilesional skin using high wave-number Raman spectroscopy. *J. Biomed. Opt.* **2007**, *12*, 034004. [CrossRef] [PubMed]
106. Ishigaki, M.; Maeda, Y.; Taketani, A.; Andriana, B.B.; Ishihara, R.; Wongravee, K.; Ozaki, Y.; Sato, H. Diagnosis of early-stage esophageal cancer by Raman spectroscopy and chemometric techniques. *Analyst* **2016**, *141*, 1027–1033. [CrossRef]
107. Almond, L.M.; Hutchings, J.; Lloyd, G.; Barr, H.; Shepherd, N.; Day, J.; Stevens, O.; Sanders, S.; Wadley, M.; Stone, N.; et al. Endoscopic Raman spectroscopy enables objective diagnosis of dysplasia in Barrett's esophagus. *Gastrointest. Endosc.* **2014**, *79*, 37–45. [CrossRef]
108. Hsu, C.-W.; Huang, C.-C.; Sheu, J.-H.; Lin, C.-W.; Lin, L.-F.; Jin, J.-S.; Chen, W. Differentiating gastrointestinal stromal tumors from gastric adenocarcinomas and normal mucosae using confocal Raman microspectroscopy. *J. Biomed. Opt.* **2016**, *21*, 75006. [CrossRef]
109. Petersen, D.; Naveed, P.; Ragheb, A.; Niedieker, D.; El-Mashtoly, S.; Brechmann, T.; Kötting, C.; Schmiegel, W.; Freier, E.; Pox, C.; et al. Raman fiber-optical method for colon cancer detection: Cross-validation and outlier identification approach. *Spectrochim. Acta Part A Mol. Biomol. Spectrosc.* **2017**, *181*, 270–275. [CrossRef]
110. Huang, Z.; McWilliams, A.; Lui, H.; McLean, D.I.; Lam, S.; Zeng, H. Near-infrared Raman spectroscopy for optical diagnosis of lung cancer. *Int. J. Cancer* **2003**, *107*, 1047–1052. [CrossRef]
111. Magee, N.D.; Villaumie, J.S.; Marple, E.T.; Ennis, M.; Elborn, J.S.; McGarvey, J.J. ExVivo Diagnosis of Lung Cancer Using a Raman Miniprobe. *J. Phys. Chem. B* **2009**, *113*, 8137–8141. [CrossRef]
112. Légaré, F.; Evans, C.L.; Ganikhanov, F.; Xie, X.S. Towards CARS Endoscopy. *Opt. Express* **2006**, *14*, 4427–4432. [CrossRef] [PubMed]
113. Saar, B.G.; Johnston, R.S.; Freudiger, C.W.; Xie, X.S.; Seibel, E.J. Coherent Raman scanning fiber endoscopy. *Opt. Lett.* **2011**, *36*, 2396–2398. [CrossRef] [PubMed]
114. Orringer, D.A.; Pandian, B.; Niknafs, Y.S.; Hollon, T.C.; Boyle, J.; Lewis, S.; Garrard, M.; Hervey-Jumper, S.L.; Garton, H.J.L.; Maher, C.O.; et al. Rapid intraoperative histology of unprocessed surgical specimens via fibre-laser-based stimulated Raman scattering microscopy. *Nat. Biomed. Eng.* **2017**, *1*, 1–13. [CrossRef] [PubMed]
115. Huang, W.E.; Griffiths, R.I.; Thompson, I.P.; Bailey, M.J.; Whiteley, A.S. Raman Microscopic Analysis of Single Microbial Cells. *Anal. Chem.* **2004**, *76*, 4452–4458. [CrossRef] [PubMed]
116. Wang, Y.; E Huang, W.; Cui, L.; Wagner, M. Single cell stable isotope probing in microbiology using Raman microspectroscopy. *Curr. Opin. Biotechnol.* **2016**, *41*, 34–42. [CrossRef]
117. Berry, D.; Mader, E.; Lee, T.K.; Woebken, D.; Wang, Y.; Zhu, D.; Palatinszky, M.; Schintlmeister, A.; Schmid, M.C.; Hanson, B.T.; et al. Tracking heavy water (D2O) incorporation for identifying and sorting active microbial cells. *Proc. Natl. Acad. Sci. USA* **2015**, *112*, E194–E203. [CrossRef]
118. Hoedt, E.; Zhang, G.; Neubert, T.A. Stable Isotope Labeling by Amino Acids in Cell Culture (SILAC) for Quantitative Proteomics. *Adv. Exp. Med. Biol.* **2014**, *806*, 93–106. [CrossRef]
119. Everley, P.A.; Krijgsveld, J.; Zetter, B.R.; Gygi, S.P. Quantitative Cancer Proteomics: Stable Isotope Labeling with Amino Acids in Cell Culture (SILAC) as a Tool for Prostate Cancer Research. *Mol. Cell. Proteom.* **2004**, *3*, 729–735. [CrossRef]
120. Wang, X.; He, Y.; Ye, Y.; Zhao, X.; Deng, S.; He, G.; Zhu, H.; Xu, N.; Liang, S. SILAC–based quantitative MS approach for real-time recording protein-mediated cell-cell interactions. *Sci. Rep.* **2018**, *8*, 1–9. [CrossRef]
121. Abraham, W.-R. Applications and impacts of stable isotope probing for analysis of microbial interactions. *Appl. Microbiol. Biotechnol.* **2014**, *98*, 4817–4828. [CrossRef]
122. Miyagi, M.; Kasumov, T. Monitoring the synthesis of biomolecules using mass spectrometry. *Philos. Trans. R. Soc. A Math. Phys. Eng. Sci.* **2016**, *374*, 20150378. [CrossRef] [PubMed]
123. Matthäus, C.; Krafft, C.; Dietzek, B.; Brehm, B.R.; Lorkowski, S.; Popp, J. Noninvasive Imaging of Intracellular Lipid Metabolism in Macrophages by Raman Microscopy in Combination with Stable Isotopic Labeling. *Anal. Chem.* **2012**, *84*, 8549–8556. [CrossRef]
124. Stiebing, C.; Matthäus, C.; Krafft, C.; Keller, A.-A.; Weber, K.; Lorkowski, S.; Popp, J. Complexity of fatty acid distribution inside human macrophages on single cell level using Raman micro-spectroscopy. *Anal. Bioanal. Chem.* **2014**, *406*, 7037–7046. [CrossRef]

125. Stiebing, C.; Meyer, T.; Rimke, I.; Matthäus, C.; Schmitt, M.; Lorkowski, S.; Popp, J. Real-time Raman and SRS imaging of living human macrophages reveals cell-to-cell heterogeneity and dynamics of lipid uptake. *J. Biophotonics* **2017**, *10*, 1217–1226. [CrossRef]
126. Majzner, K.; Tott, S.; Roussille, L.; Deckert, V.; Chlopicki, S.; Baranska, M. Uptake of fatty acids by a single endothelial cell investigated by Raman spectroscopy supported by AFM. *Analyst* **2018**, *143*, 970–980. [CrossRef] [PubMed]
127. Li, J.; Cheng, J.-X. Direct Visualization of De novo Lipogenesis in Single Living Cells. *Sci. Rep.* **2014**, *4*, 6807. [CrossRef] [PubMed]
128. Alfonso-Garcia, A.; Pfisterer, S.G.; Riezman, H.; Ikonen, E.; Potma, E.O. D38-cholesterol as a Raman active probe for imaging intracellular cholesterol storage. *J. Biomed. Opt.* **2015**, *21*, 061003. [CrossRef]
129. Weeks, T.; Schie, I.; Hartigh, L.J.D.; Rutledge, J.C.; Huser, T. Lipid-cell interactions in human monocytes investigated by doubly-resonant coherent anti-Stokes Raman scattering microscopy. *J. Biomed. Opt.* **2011**, *16*, 021117. [CrossRef] [PubMed]
130. Dodo, K.; Sato, A.; Tamura, Y.; Egoshi, S.; Fujiwara, K.; Oonuma, K.; Nakao, S.; Terayama, N.; Sodeoka, M. Synthesis of deuterated γ-linolenic acid and application for biological studies: Metabolic tuning and Raman imaging. *Chem. Commun.* **2021**, *57*, 2180–2183. [CrossRef]
131. Matthäus, C.; Kale, A.; Chernenko, T.; Torchilin, V.; Diem, M. New Ways of Imaging Uptake and Intracellular Fate of Liposomal Drug Carrier Systems inside Individual Cells, Based on Raman Microscopy. *Mol. Pharm.* **2008**, *5*, 287–293. [CrossRef]
132. Van Manen, H.-J.; Lenferink, A.T.; Otto, C. Noninvasive Imaging of Protein Metabolic Labeling in Single Human Cells Using Stable Isotopes and Raman Microscopy. *Anal. Chem.* **2008**, *80*, 9576–9582. [CrossRef]
133. Wei, L.; Yu, Y.; Shen, Y.; Wang, M.C.; Min, W. Vibrational imaging of newly synthesized proteins in live cells by stimulated Raman scattering microscopy. *Proc. Natl. Acad. Sci. USA* **2013**, *110*, 11226–11231. [CrossRef] [PubMed]
134. Wei, L.; Shen, Y.; Xu, F.; Hu, F.; Harrington, J.K.; Targoff, K.L.; Min, W. Imaging Complex Protein Metabolism in Live Organisms by Stimulated Raman Scattering Microscopy with Isotope Labeling. *ACS Chem. Biol.* **2015**, *10*, 901–908. [CrossRef] [PubMed]
135. Shen, Y.; Xu, F.; Wei, L.; Hu, F.; Min, W. Live-cell quantitative imaging of proteome degradation by stimulated Raman scattering. *Angew. Chem. Int. Ed.* **2014**, *53*, 5596–5599. [CrossRef]
136. Miao, K.; Wei, L. Live-Cell Imaging and Quantification of PolyQ Aggregates by Stimulated Raman Scattering of Selective Deuterium Labeling. *ACS Central Sci.* **2020**, *6*, 478–486. [CrossRef]
137. Zhang, L.; Shi, L.; Shen, Y.; Miao, Y.; Wei, M.; Qian, N.; Liu, Y.; Min, W. Spectral tracing of deuterium for imaging glucose metabolism. *Nat. Biomed. Eng.* **2019**, *3*, 402–413. [CrossRef] [PubMed]
138. Lee, D.; Du, J.; Yu, R.; Su, Y.; Heath, J.R.; Wei, L. Visualizing Subcellular Enrichment of Glycogen in Live Cancer Cells by Stimulated Raman Scattering. *Anal. Chem.* **2020**, *92*, 13182–13191. [CrossRef]
139. Hu, F.; Chen, Z.; Zhang, L.; Shen, Y.; Wei, L.; Min, W. Vibrational Imaging of Glucose Uptake Activity in Live Cells and Tissues by Stimulated Raman Scattering. *Angew. Chem. Int. Ed.* **2015**, *54*, 9821–9825. [CrossRef] [PubMed]
140. Long, R.; Zhang, L.; Shi, L.; Shen, Y.; Hu, F.; Zeng, C.; Min, W. Two-color vibrational imaging of glucose metabolism using stimulated Raman scattering. *Chem. Commun.* **2018**, *54*, 152–155. [CrossRef]
141. Chen, Z.; Paley, D.W.; Wei, L.; Weisman, A.L.; Friesner, R.A.; Nuckolls, C.; Min, W. Multicolor Live-Cell Chemical Imaging by Isotopically Edited Alkyne Vibrational Palette. *J. Am. Chem. Soc.* **2014**, *136*, 8027–8033. [CrossRef]
142. Zhang, L.; Min, W. Bioorthogonal chemical imaging of metabolic changes during epithelial–mesenchymal transition of cancer cells by stimulated Raman scattering microscopy. *J. Biomed. Opt.* **2017**, *22*, 1–7. [CrossRef] [PubMed]
143. Shi, L.; Zheng, C.; Shen, Y.; Chen, Z.; Silveira, E.S.; Zhang, L.; Wei, M.; Liu, C.; De Sena-Tomas, C.; Targoff, K.; et al. Optical imaging of metabolic dynamics in animals. *Nat. Commun.* **2018**, *9*, 1–17. [CrossRef] [PubMed]
144. Hekmatara, M.; Baladehi, M.H.; Ji, Y.; Xu, J. D2O-Probed Raman Microspectroscopy Distinguishes the Metabolic Dynamics of Macromolecules in Organellar Anticancer Drug Response. *Anal. Chem.* **2021**, *93*, 2125–2134. [CrossRef] [PubMed]
145. Matanfack, G.A.; Rüger, J.; Stiebing, C.; Schmitt, M.; Popp, J. Imaging the invisible—Bioorthogonal Raman probes for imaging of cells and tissues. *J. Biophotonics* **2020**, *13*, e202000129. [CrossRef]
146. Yamakoshi, H.; Dodo, K.; Okada, M.; Ando, J.; Palonpon, A.; Fujita, K.; Kawata, S.; Sodeoka, M. Imaging of EdU, an Alkyne-Tagged Cell Proliferation Probe, by Raman Microscopy. *J. Am. Chem. Soc.* **2011**, *133*, 6102–6105. [CrossRef]
147. Huang, W.E.; Stoecker, K.; Griffiths, R.; Newbold, L.; Daims, H.; Whiteley, A.S.; Wagner, M. Raman-FISH: Combining stable-isotope Raman spectroscopy and fluorescence in situ hybridization for the single cell analysis of identity and function. *Environ. Microbiol.* **2007**, *9*, 1878–1889. [CrossRef] [PubMed]
148. Song, Y.; Cui, L.; López, J.; Ángel, S.; Xu, J.; Zhu, Y.-G.; Thompson, I.P.; Huang, W.E. Raman-Deuterium Isotope Probing for in-situ identification of antimicrobial resistant bacteria in Thames River. *Sci. Rep.* **2017**, *7*, 1–10. [CrossRef]
149. Hong, W.; Karanja, C.W.; Abutaleb, N.S.; Younis, W.; Zhang, X.; Seleem, M.N.; Cheng, J.-X. Antibiotic Susceptibility Determination within One Cell Cycle at Single-Bacterium Level by Stimulated Raman Metabolic Imaging. *Anal. Chem.* **2018**, *90*, 3737–3743. [CrossRef]
150. Xu, J.; Zhu, D.; Ibrahim, A.D.; Allen, C.C.R.; Gibson, C.M.; Fowler, P.W.; Song, Y.; Huang, W.E. Raman Deuterium Isotope Probing Reveals Microbial Metabolism at the Single-Cell Level. *Anal. Chem.* **2017**, *89*, 13305–13312. [CrossRef]
151. Wang, Y.; Xu, J.; Kong, L.; Liu, T.; Yi, L.; Wang, H.; Huang, W.E.; Zheng, C. Raman-Deuterium isotope probing to study metabolic activities of single bacterial cells in human intestinal microbiota. *Microb. Biotechnol.* **2019**, *13*, 572–583. [CrossRef]

152. Xu, J.; Preciado-Llanes, L.; Aulicino, A.; Decker, C.M.; Depke, M.; Salazar, M.G.; Schmidt, F.; Simmons, A.; Huang, W.E. Single-Cell and Time-Resolved Profiling of Intracellular Salmonella Metabolism in Primary Human Cells. *Anal. Chem.* **2019**, *91*, 7729–7737. [CrossRef] [PubMed]
153. Li, H.-Z.; Zhang, D.; Yang, K.; An, X.-L.; Pu, Q.; Lin, S.-M.; Su, J.-Q.; Cui, L. Phenotypic Tracking of Antibiotic Resistance Spread via Transformation from Environment to Clinic by Reverse D2O Single-Cell Raman Probing. *Anal. Chem.* **2020**, *92*, 15472–15479. [CrossRef] [PubMed]
154. Wang, Y.; Xu, J.; Kong, L.; Li, B.; Li, H.; Huang, W.E.; Zheng, C. Raman-activated sorting of antibiotic-resistant bacteria in human gut microbiota. *Environ. Microbiol.* **2020**, *22*, 2613–2624. [CrossRef] [PubMed]

cancers

MDPI

Article

Metabolic Reprogramming in Colon Cancer Cells Persistently Infected with Newcastle Disease Virus

Tong Yu [1,†], Archana Chandrabhan Jadhav [2,3,†], Jiabao Xu [1,*], Adrian L. Harris [4], Venugopal Nair [3,5] and Wei E. Huang [1,*]

1 Department of Engineering Science, University of Oxford, Parks Road, Oxford OX1 3PJ, UK
2 Beamline B24, Diamond Light Source, Harwell Science and Innovation Campus, Oxfordshire OX11 0DE, UK
3 Viral Oncogenesis Group, The Pirbright Institute, Surrey GU24 0NF, UK
4 Molecular Oncology Laboratories, Department of Oncology, Weatherall Institute of Molecular Medicine, John Radcliffe Hospital, Oxford University, Oxford OX3 9DS, UK
5 Department of Biology, University of Oxford, 11a Mansfield Road, Oxford OX1 3SZ, UK
* Correspondence: jiabao.xu@eng.ox.ac.uk (J.X.); wei.huang@eng.ox.ac.uk (W.E.H.)
† The authors contributed equally to this work.

Simple Summary: It is vitally important to understand the development of cancer resistance to therapies. Newcastle disease virus (NDV) is a promising oncolytic agent for cancer therapy. A small subpopulation of Caco-2 colon cancer cells persistently infected with NDV was found, which demonstrated resistance to NDV reinfection. By applying Raman spectroscopic and stable isotopic techniques, we found possible mechanisms of the resistant cells to escape from the viral attack, by slowing down their replication and diverting the energy to protein and lipid synthesis. Understanding metabolic reprogramming would be extremely helpful in creating novel cancer treatments to identify and target resistant cells at the single-cell level with great precision.

Abstract: Newcastle disease virus (NDV) is an oncolytic agent against various types of mammalian cancers. As with all cancer therapies, the development of cancer resistance, both innate and acquired, is becoming a challenge. In this study, we investigated persistently NDV-infected Caco-2 colon cancer cells, designated as virus-resistant (VR) Caco-2 cells, which were then able to resist NDV-mediated oncolysis. We applied single-cell Raman spectroscopy, combined with deuterium isotope probing (Raman-DIP) techniques, to investigate the metabolic adaptations and dynamics in VR Caco-2 cells. A linear discriminant analysis (LDA) model demonstrated excellent performance in differentiating VR Caco-2 from Caco-2 cells at single-cell level. By comparing the metabolic profiles in a time-resolved manner, the de novo synthesis of proteins and lipids was found upregulated, along with decreased DNA synthesis in VR Caco-2. The results suggest that VR Caco-2 cells might reprogram their metabolism and divert energy from proliferation to protein synthesis and lipidic modulation. The ability to identify and characterise single resistant cells among a population of cancer cells would help develop a deeper understanding of the resistance mechanisms and better tactics for developing effective cancer treatment.

Keywords: Newcastle disease virus; Raman spectroscopy; cancer resistance; drug resistance; single cells

check for updates

Citation: Yu, T.; Jadhav, A.C.; Xu, J.; Harris, A.L.; Nair, V.; Huang, W.E. Metabolic Reprogramming in Colon Cancer Cells Persistently Infected with Newcastle Disease Virus. *Cancers* **2023**, *15*, 811. https://doi.org/10.3390/cancers15030811

Academic Editor: Antonio V. Sterpetti

Received: 25 November 2022
Revised: 19 January 2023
Accepted: 25 January 2023
Published: 28 January 2023

Copyright: © 2023 by the authors. Licensee MDPI, Basel, Switzerland. This article is an open access article distributed under the terms and conditions of the Creative Commons Attribution (CC BY) license (https://creativecommons.org/licenses/by/4.0/).

1. Introduction

Newcastle disease virus (NDV) is a single-stranded RNA avulavirus causing Newcastle disease. Over the last five decades, NDV has been known to have oncolytic properties and is a potential candidate for oncovirotherapy due to its tumour-selective replication sparing healthy cells [1]. Tumours provide a favourable environment for NDV replication, spreading due to compromised antiviral defences related to the weaker sensitivity and expressions of type 1 interferon (IFN) as well as developing resistance to cell death pathways [2]. Since 1957, when NDV's anti-tumour potential was first demonstrated in

NDV-coated ascitic cancer cells [3], both preclinical and clinical research have made substantial use of NDV as an oncolytic drug, with its non-pathogenic strains (e.g. Hitchner B1, LaSota, Ulster and V4UPM), mildly-pathogenic strains (e.g. PV701 and 73T) and highly-pathogenic strains (e.g. AF2240) all proven to be potent anti-cancer agents.

Despite promising responses observed in clinical studies, persistent NDV infections have been reported in a range of in vitro cancer cell infections [4,5,6]. In colorectal cancer, the persistently infected cells were discovered to harbour viral offspring that formed smaller plaques, in contrast to the uninfected cancer cells [4]. Hyperfusogenic NDV activity and the emergence of persistence infection were linked by two alterations in the glycoproteins of NDV, F and HN proteins in persistently infected ovarian cancer [5]. Upregulation of genes associated with cell growth, pro-survival, and anti-apoptosis have also been reported during the development of persistently infected bladder cancer cells [6]. Persistent NDV infections in cancer cells result in reduced NDV-induced oncolysis and therefore hinders the development and translation of NDV as an oncolytic virotherapy. As the mechanism of NDV persistent infection in cancer cells remains poorly understood, further investigation and identification of the persistency in cancer cells is critical.

Here, we apply label-free single-cell Raman spectroscopy for investigating cellular resistance at a single-cell level. This spectroscopic technique can provide a comprehensive 'biomolecular fingerprint' of a biological system [7]. In combination with advanced confocal microscopy, the biomolecular fingerprint of a single cell can be obtained as a single-cell Raman spectrum (SCRS) [8]. In addition, Raman techniques can be integrated with deuterium isotope probing (DIP) to map the general metabolic activity of a cell [9]. By incubating cells with heavy water (D_2O), the D atoms in D_2O can exchange with H atoms and form a variety of C–D bonds mediated by NADPH. By quantifying the C–D band at 2170–2300 cm^{-1} in the Raman spectrum, the degree of D incorporation can be used to estimate the anabolic activity. This method has been widely used to research the ecological and microbiological activity of microbes [9, 10, 11, 12]. Recently, Raman-DIP using D_2O has also been reported to study the metabolism of cancer cells [13, 14]. Raman-DIP has many advantages over other targeted probes, for example, fluorophores, that are invasive and may interfere with a cell's inherent metabolic activity.

In this study, we unintentionally observed the emergence of infection-persistent Caco-2 cells, initially the most sensitive to the NDV strain, after infection in a succession of cancer cell lines with a non-pathogenic strain of NDV, B1-GFP. The persistently infected cells were isolated and named virus-resistant (VR) Caco-2. We employed single-cell Raman spectroscopy and Raman-DIP to explore the metabolic differences within the VR Caco-2 cells and compared them to the parental uninfected Caco-2 cells. Raman spectral profiles of the VR Caco-2 cells were found to be distinctly different from those of the uninfected Caco-2 cells, suggesting significant metabolic reprogramming in those persistently infected cells.

2. Materials & Methods

2.1. Virus Strain and Cell Lines Used in This Study

The virus strain used in this study was a non-pathogenic strain of NDV Hitchner B1-GFP, obtained from the Department of Microbiology, Mount Sinai School of Medicine, New York.

Human cancer lines used include lung adenocarcinoma A549, hepatocellular Hep G2, prostate adenocarcinoma PC3, cervical adenocarcinoma HeLa, colorectal adenocarcinoma Caco-2 and virus-resistant Caco-2 (VR Caco-2). A non-cancer human lung fibroblast cell line MRC5 was also used. A549, Hep G2, HeLa, Caco-2, PC3 and MRC cell lines were obtained from the cell line inventory run by the Pirbright Institute's cell services unit. A549, MRC5, PC3, Caco-2 and VR Caco-2 cells were authenticated using short tandem repeat (STR) profiling from ECACC.

For VR Caco-2 cells, Caco-2 cells were first infected with undiluted stock of B1-GFP virus, resulting in an estimated multiplicity of infection (MOI) of 50. About >98% cells were infected within 24 h and >95% of infected cells were dead within 48 h post-infection. A few cells survived 12 days post-infection and were identified by cultivation and further isolated as VR Caco-2 cells.

2.2. Cell Culture and Virus Infection

The complete media used for culturing each cell line are as follows. For culturing Caco-2 and VR Caco-2 cells, minimum essential medium eagle (MEM) with Earle's salts and sodium bicarbonate without L-Glutamine (Sigma-Aldrich, Gillingham, Dorset, UK) was supplemented with 1.0 mg/mL D-glucose, 1% penicillin-streptomycin (10,000 U/mL), 1 x NEAA, 4 mM L-glutamine, 1 μg/mL amphotericin B and 20% foetal bovine serum (FBS). For culturing Hep G2 and MRC cells, MEM was used, supplemented with 1.0 mg/mL of D-glucose, 1% penicillin-streptomycin, 4 mM L-glutamine, 1 μg/mL amphotericin B and 10% FBS. Roswell Park Memorial Institute (RPMI) (2.2 mg/mL of D-glucose) medium (Sigma-Aldrich, UK) and Ham's F-12K (Kaighn's) (1.26 mg/mL of D-glucose) medium (Gibco, Thermo Fisher Scientific, Loughborough, UK) were used for culturing HeLa cells and PC3 cells, respectively, both supplemented with 1% penicillin-streptomycin, 1 μg/mL amphotericin B and 10% FBS. For culturing A549 cells, Dulbecco's modified eagle's medium (DMEM) with high glucose of 4.5 μg/mL, L-glutamine and sodium bicarbonate without sodium pyruvate (Sigma-Aldrich) was supplemented with 1% penicillin-streptomycin, 1 mM sodium pyruvate, 1 μg/mL amphotericin B and 10% FBS. The cell culture media was changed every 48 h during the prolonged cell-culturing process.

2.3. Cell Viability and Toxicity Assay

CellTiter-Blue® Cell Viability Assay (Promega, Southampton, UK) was used to compare the viability of NDV-infected cells to mock-infected control cells. The manufacturer's instructions were followed. The reduction reaction of the resorufin to the fluorescent product was done by incubating the metabolically active cells at 37 °C and 5% CO_2 for up to 4–6 h. A Promega GloMax® Explorer Multimode Microplate Reader was used to measure the fluorescence generated at an excitation of 560 nm and emission at 590 nm. The measured viability fraction was computed by dividing the normalised fluorescence reading of the infected cells by that of the uninfected cells.

CellToxTM Green Cytotoxicity Assay (Promega) was used to evaluate cell toxicity brought on by NDV infection. The DNA-binding cyanine dye was only taken up by dead cells due to a breakdown of cell membrane integrity and the fluorescent signal was detected at 520–530 nm. The manufacturer's instructions were followed when performing the end-point cytotoxicity assay at day 4 of infection by B1-GFP (MOI~0.1) to Caco-2 and VR Caco-2 cells. The fold change in

cytotoxicity was calculated by cytotoxicity of NDV-infected cells divided by cytotoxicity of mock-infected cells.

2.4. Cell Proliferation Assay

CellTrace™ CFSE Cell Proliferation Kit (Invitrogen™, Thermo Fisher Scientific, Loughborough, UK) and flow cytometry analysis of CFSE-labelled cells at 488 nm were used to measure cell proliferation in Caco-2 and VR Caco-2 cells. Cells were cultured in complete growth media at 37 °C inside a 5% CO_2 incubator until 80–90% confluence was reached. Cells were then trypsinised with 0.25% trypsin-EDTA solution, centrifuged at 325 g, and washed and resuspended with serum-free MEM media. CFSE buffer was added to the resuspended cells to reach 1×10^6 cells/mL in 2.5 μM CFSE buffer. The mixture was then incubated in a water bath at 37 °C for 15 min to label DNA. Following a serum-free MEM medium wash, CFSE-labelled cells were resuspended in complete growth media at 37 °C for 1 hour. After washing and resuspending, 5×10^5 cells per well were seeded into 24-well plates, which were then cultured at 37 °C with 5% CO_2. Using a MACSQuant Analyzer (Miltenyi Biotec, Bisley, Woking, UK), the fluorescence of the CFSE-labelled cells was monitored at five different time intervals (0, 12, 24, 48 and 72 h) after labelling. The Incucyte Live-Cell Analysis system (Sartorius, Epsom,UK) was used to monitor the proliferation of Caco-2 and VR Caco-2 cells seeded at different densities (5 k/well, 10 k/well and 15 k/well) in real time.

2.5. Caco-2 and VR Caco-2 Cells for Raman and Raman-DIP Measurements

Non-infected parental Caco-2 and VR Caco-2 cells were grown for up to 5–6 days until 80–90% confluence was attained. In Raman-DIP experiments, Caco-2 complete media with 30% D_2O (Sigma-Aldrich) were used for culturing Caco-2 and VR Caco-2 cells, with cells obtained at different time points at 0, 12, 24, 48 and 72 h. The 30% D_2O Caco-2 media was formulated by using 10 mL of 10 x MEM (10 mg/mL of D-glucose) without L-glutamine and sodium bicarbonate (Sigma-Aldrich), 30 mL of 99% D_2O (Sigma-Aldrich), 1 mL of 100 x NEAA (Gibco), 1 mL of 200 mM L-glutamine (Gibco), 3 mL of 7.5% sodium bicarbonate solution (Sigma-Aldrich), 1 mL of penicillin-streptomycin (10,000 U/mL) (Gibco), 0.04 mL of Amphotericin B (Gibco), 20 mL of heat-inactivated FBS and 33.6 mL of sterile deionised water.

The cells were washed with PBSa and trypsinised. Trypsin was neutralised using serum-containing media and cells were washed with PBSa at 325 g for 5 min. Following that, cells were resuspended with cold solution of 4% paraformaldehyde (PFA) in PBSa and fixed for 1 hour at room temperature. The PFA-fixed cells were then washed once with PBSa and twice with Milli-Q water, following which the cell suspensions were dropped onto an aluminium-coated Raman slide and air dried before the measurements.

2.6. Single-Cell Raman Spectroscopic Measurements and Analysis

A LabRAM HR Evolution Raman microscope (Horiba Scientific, UK) was used for spectroscopic measurements, equipped with a 532-nm neodymium-yttrium aluminium garnet laser. Raman spectra were acquired via a 50× objective lens and 300 grooves/mm diffraction grating using 90-mW input laser power through a 25% neutral density (ND) filter and 3-s acquisition time. Raman scattering was detected by a charge-coupled device (CCD) cooled at –68 °C. The spectra were acquired in the range of 300 to 3400 cm^{-1}. For VR Caco-2 and Caco-2 cells, 218 and 92 single cells were measured, respectively. In Raman-DIP experiments, >30 cells were measured for each time point. For each cell, around 30 spectra were measured. As the dried cells lost the original spatial distribution, spectra were averaged into one spectrum per single cell, which was used in the following analysis.

All spectra were pre-processed by cosmic ray correction and polyline baseline fitting using LabSpec 6 (Horiba Scientific, Montpellier, France). The entire spectrum

region was vector normalised. Data analysis, statistics and visualisation were carried out in an R environment. Intracellular biomolecules were semi-quantified by quantifying corresponding band areas. The C–D (2070–2300 cm^{-1}) and C–H (2800–3030 cm^{-1}) band areas were quantified to determine deuterium content originating from incubation with D_2O, while the metabolic rate was calculated by the ratio of C–D / C–D + C–H. Performance of the statistics was done between single cells of VR Caco-2 and Caco-2 at each Raman wavenumber by comparing their intensities with Student's *t*-test (ns: $p > 0.05$; *: $p < 0.05$; **: $p < 0.01$; ***: $p < 0.001$; ****: $p < 0.0001$).

3. Results & Discussion

3.1. Cell Line Screening for Establishing an NDV-Susceptible Cancer Cell System

A non-pathogenic reporter strain of NDV, Hitchner B1-GFP, was introduced to infect various cancer/non-cancer cell lines for screening and establishing an NDV-susceptible system. Six different human cell lines were used, including five cancer cell lines derived from various tissues, the colon (Caco-2), prostate adenocarcinoma cells derived from a metastatic site in bone (PC3), the lung (A549), the liver (Hep G2), the cervix (HeLa) and a non-cancerous fibroblast cell line developed from lung tissue (MRC5). All cell lines were infected with B1-GFP neat virus (MOI of 50) and its ten-fold dilutions. Time- and NDV dose-dependent cell viability was monitored during a nine-day period (Figure 1).

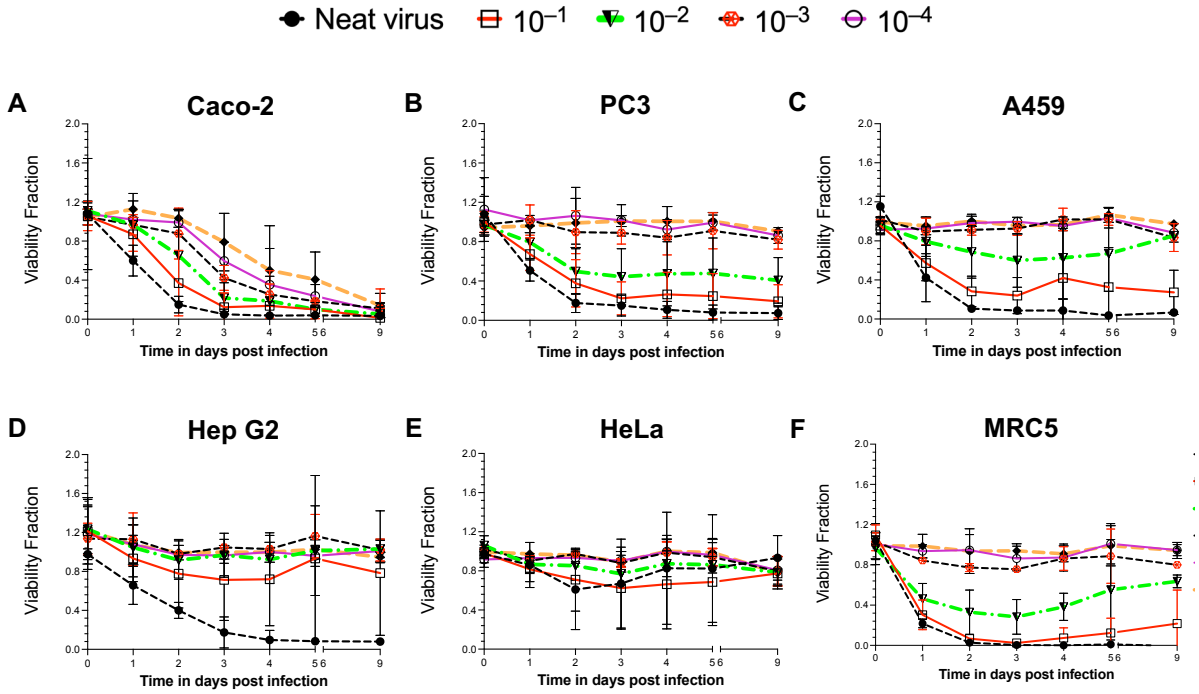


Figure 1. Time- and NDV dose-dependent cell viability assay in different human cancer cells. Cell lines were infected with a neat virus (MOI of 50) of a non-pathogenic reporter strain of NDV B1-GFP and its 10-fold dilutions. Cell lines derived from different cancerous tissues such as (**A**) the colon (Caco-2), (**B**) prostate adenocarcinoma cells derived from the metastatic site in bone (PC3), (**C**) lung (A549), (**D**) liver (Hep G2), (**E**) cervix (HeLa) and (**F**) non-cancerous human lung fibroblast cells (MRC5) were used for the study. Cell viability was measured throughout nine days of infection study. Data (mean ± SD) represented here is the combination of three repeats for each cell line. Viability Fraction = Normalised fluorescence reading of infected cells at (560 Ex/590 Em)/Normalised fluorescence reading of uninfected cells at (560 Ex/590 Em).

A consistent decrease in cell viability was only observed in the infected Caco-2 cells with all concentrations of virus (Figure 1A). The B1-GFP virus infection reduced cell viability by more than 90% within 48 h of neat virus infection. A gradual decrease in cell viability with more diluted virus was observed in successive 10-fold dilutions of the virus after 48 h post-infection in Caco-2 cells. PC3 (Figure 1B) and A549 (Figure 1C) cells were found to be moderately susceptible to the B1-GFP infection only at higher viral doses (neat virus, 10^{-1} and 10^{-2} dilutions for PC3 cells; neat virus and 10^{-1} dilution for A549 cells). Liver cancer Hep G2 cells were susceptible only to the B1-GFP neat virus infection within 72 h (Figure 1D), whereas HeLa cells remained unaffected by the viral infection regardless of viral dose or duration of the infection (Figure 1E). Within 48 h post-infection (neat virus and 1:10 dilution), the non-cancerous MRC5 cells showed a reduction in cell viability. However, with a 1:10 dilution of B1-GFP, an increase in the cell viability of MRC5 cells was observed after 5 days (Figure 1F).

Oncolytic viruses acquire oncotropism by favourably infecting and replicating in cancer cells, as cancer cells have deficient cell death pathways and weaker antiviral responses. On the contrary, non-cancer cells' antiviral responses and cell death pathways are intact, hence non-cancer cells like MRC5 when infected with NDV at higher viral load are susceptible to death. However, with decreasing viral doses, MRC5 cells recovered from the infection and regained cell viability. The oncolytic efficacy of the virus is dependent on multiple factors, such as the efficiency of infection in cancer cells, type of virus, and natural and induced viral tropisms leading to the types of cell deaths, hence cancer cells like HeLa, Hep G2, PC3 and A549 cells showed varying degrees of response to NDV doses in a time-dependent manner.

3.2. Identification of Persistently Infected VR Caco-2 Cells

After examining the susceptibility of Caco-2 cells to B1-GFP virus, further study focused on the Caco-2 cells. With the neat virus, which resulted in an estimated MOI of 50, most cells were infected and consequently died after 48 h post-infection. A small number of surviving cells (<1%) were unintentionally found after 12 days under microscopic examination, despite a high level of oncolysis, named as virus-resistant Caco-2 (VR Caco-2) cells. The VR Caco-2 cells that initially survived required 4–6 weeks to form colonies and ~4 months to reach 80–90% confluence. Infected and mock-infected Caco-2 cells were observed routinely under a conventional inverted bright-field microscope to assess the cell morphology and cytopathic effects of NDV infection. Under the microscope, the VR Caco-2 cells proliferated much more slowly than the uninfected Caco-2 cells.

NDV reinfection experiments with B1-GFP demonstrated a significant difference in the cell viability of the infected Caco-2 and VR Caco-2 cells (Figure 2A, B). While Caco-2 cells responded to B1-GFP infection in a dose-dependent manner (Figure 2A), no viral doses had an effect on VR Caco-2 cells at any time point, resulting in constant cell viability (Figure 2B). The cell cytotoxicity was measured in the infected Caco-2 and VR Caco-2 cells at low MOI of 0.1; Caco-2 cells showed significantly higher cytotoxicity than the VR Caco-2 cells upon infection, as illustrated in Figure 2C. Both tests confirmed the resistance of VR Caco-2 cells to NDV reinfection and NDV-induced oncolysis.

The resistance to NDV superinfection and NDV-mediated cell death was acquired only in persistently infected (VR Caco-2) cells. VR Caco-2 cells produced a significantly low titre of replicating virus continuously. There are many possible reasons why only a small population of the cells sustained persistent infection. For instance, one possible explanation could be that Caco-2 is a heterogenous cell line known to differentiate spontaneously into different intestinal epithelial cells. Therefore, it is possible that some cells are more likely to inhabit persistent infection than others. The difference in the metabolic remodelling of parental wild-type

Caco-2 cells relative to persistently NDV-infected VR Caco-2 cells is not substantial, as VR Caco-2 cells harbour a significantly low level of virus and do not become reinfected by NDV in the continuous cell culture. Although more research is required, it is possible that either receptor alteration of VR Caco-2 cells or the induction of an antiviral state in VR Caco-2 cells accounted for the resistance to reinfection.

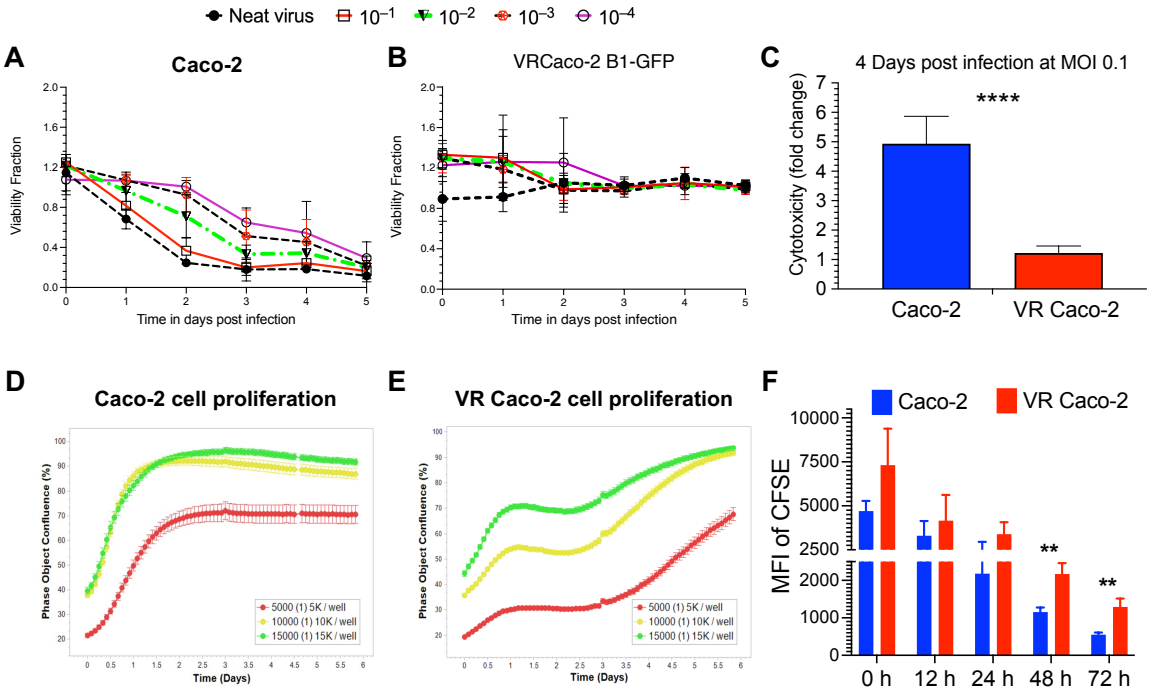


Figure 2. Characterisation of VR Caco-2 and Caco-2 cells. Cell viability measured in NDV B1-GFP neat virus and 10-fold virus dilutions infected (**A**) Caco-2 and (**B**) VR Caco-2 cells in a 5-day virus killing curve assay. NDV reinfection experiments demonstrated resistance in VR Caco-2 cells. (**C**) Cell cytotoxicity assay of 0.1-MOI NDV B1-GFP-infected Caco-2 and VR Caco-2 cells 4 days post-infection demonstrated reduced cytotoxicity of VR Caco-2 cells. Cell proliferation assays showing (**D**) Caco-2 and (**E**) VR Caco-2 cell confluence monitored in real time using the Incucyte imaging system at different seeding densities. Phase object confluence (%) represents the surface area covered by cell monolayer in the culture plate. (**F**) Mean fluorescence intensity (MFI) of CFSE-stained Caco-2 and VR Caco-2 cells at different proliferation time points. CFSE dilution is significant at 48 h and 72 h in Caco-2 cells, indicating greater numbers of cell divisions than VR Caco-2 cells. Data (mean ± SD) shown here are from three independent experiments and analysed using multiple non-parametric t-tests (****: $p < 0.0001$; **: $p < 0.01$).

Similar to the microscopic observation of slower VR Caco-2 cell growth compared to the uninfected Caco-2 cells, cell proliferation assays by real-time monitoring of the cell confluence confirmed the slower proliferation of VR Caco-2 cells (Figure 2D,E). Caco-2 cells entered the log phase after less than 12 h in the lag phase and reached more than 90% confluence in 1.5 days after being seeded at 10,000 and 15,000 cells/well, at which point they entered the stationary phase. A similar pattern was seen in 5000 cells/well that had reached 70% confluence and had begun stationary development (Figure 2D). Contrarily, VR Caco-2 cells entered the exponential phase after around three days in the lag phase across all three densities, regardless of confluence. At all cell densities, VR Caco-2 cells displayed a distinct growth phase curve from Caco-2 cells. It took VR Caco-2 cells 5.5 days to reach >90% cell confluence at seeding densities of 10,000 and 15,000 cells/well (Figure 2E). The CFSE cell proliferation experiment confirmed that the growth of VR Caco-2 cells was twice as slow as that of Caco-2 cells at 48 and 72 h after CFSE

labelling (Figure 2F). Notably, VR Caco-2 cells displayed similar morphology in the cell culture monolayers as the Caco-2 cells.

3.3. Persistent VR Caco-2 Can Be Identified by Metabolic Profiles at Single-Cell Level

Despite initially being the most susceptible cell line for NDV-induced oncolysis, Caco-2 cells developed infection persistence in a small population of VR Caco-2 cells. To understand whether the metabolic profiles can be discriminated in the two groups of cells responsible for distinct infection manifestations, we employed single-cell Raman spectroscopy to investigate Caco-2 and VR Caco-2 cells. The averaged Raman spectra for VR Caco-2 and Caco-2 cells are shown in Figure 3A, averaged from 218 and 92 single cells, respectively. The fingerprint region (300–1800 cm^{-1}) illustrates biomolecular vibrational modes within a single cell, and the high wavenumber region (2800–3100 cm^{-1}) shows the intensive C–H stretching vibrations from lipids, proteins and nucleic acids.

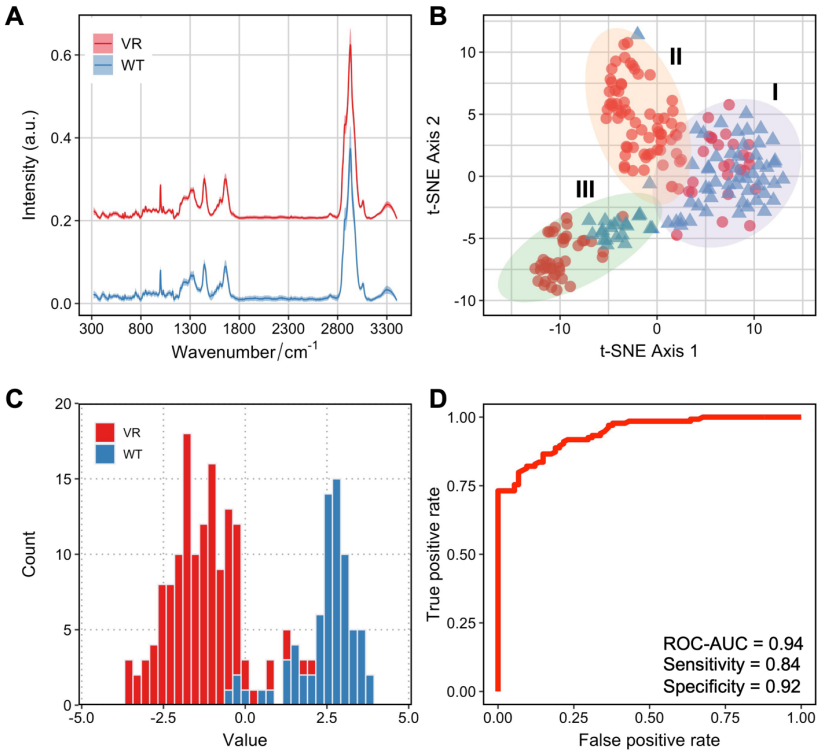


Figure 3. Distinct Raman profiles of Caco-2 and VR Caco-2 cells. Raman spectra of VR Caco-2 and Caco-2 cells averaged from 218 and 92 single cells, respectively. The shaded area represents standard deviation at each wavenumber from single-cell measurements. Raman spectra from each group was shifted and scaled in intensity to aid visualisation and the intensity is expressed in arbitrary unit (a.u.). (**B**) Unsupervised tSNE visualisation observes three distinct clusters I, II and III comprised of heterogeneous Caco-2 and VR Caco-2 single cells. (**C**) Histogram of values of a linear discriminant analysis (LDA) model to differentiate Caco-2 and VR Caco-2 based on their Raman spectra. (**D**) A receiver operating characteristic (ROC) curve was used to evaluate the LDA model performance. The area under the ROC curve (ROC-AUC) was 0.94 where 1 indicates perfect classification.

First, an unsupervised t-distributed stochastic neighbour embedding (tSNE) analysis was used to visualise the high-dimensional Raman dataset in a two-dimensional space (Figure 3C). Interestingly, a degree of heterogeneity within populations was observed, especially in the VR Caco-2 cells. Three clusters were identified via k-means clustering. Cluster I was comprised mostly of the wild-type

Caco-2 cells (73%); some of the VR Caco-2 cells in this cluster might still have had phenotypic resemblance to the wild-type cells. Cluster II was mostly made up of VR Caco-2 cells (97%) while cluster III, the most distant from the other two clusters, was the most heterogeneous (34% Caco-2 wild type and 66% VR Caco-2).

We then visualised the Raman profiles of the two groups in a supervised manner via linear discriminant analysis (LDA). The histogram of the LD values from the LDA clearly separates the VR Caco-2 and Caco-2 cells (Figure 3C). In a binary classification task using LDA for differentiating VR Caco-2 and Caco-2 cells based on their SCRS, a receiver operating characteristic (ROC) curve was used to evaluate the model performance (Figure 3D). The area under the ROC curve (ROC-AUC) achieved 0.94 at single-cell level, where 1 indicates perfect classification. The supervised machine learning model demonstrates that the Raman profiles of the VR Caco-2 cells are distinctly different from those of the uninfected parental Caco-2 cells, suggesting significant metabolic reprogramming in those persistently infected cells. The development of persistent infections for oncolytic viruses may result in reduced oncolytic potential and compromised therapeutic outcomes [15]. Importantly, the persistent cancer cells are able to proliferate and produce populations that are resistant to the viruses. The ability to identify the subpopulations of resistant cells from the wild-type cancer cells is imperative in clinical settings.

3.4. Raman Profiles Differentiate VR Caco-2 and Caco-2 Cells

Based on the most important variables selected by the LDA model (Figure S1), differential biomolecules were semi-quantified by integrating corresponding Raman bands and compared between VR Caco-2 and Caco-2 cells (Figure 4 and Table 1). Assignment of a Raman band is most accurate for the corresponding vibrational modes; nevertheless, assignments to biomolecules with specific vibrations are possible. A number of changes related to DNA/RNA, lipids and proteins are colour-coded in green, orange and blue, respectively, in Figure 4. Raman bands related to DNA/RNA at 680 cm^{-1}, which can be assigned to ring breathing modes in the DNA bases, were significantly lower in the resistant cells compared to the uninfected parental cells. This is consistent with the observation in the cell proliferation experiments that VR Caco-2 cells had a much slower replication rate than Caco-2 cells. A number of Raman biomarkers related to protein synthesis were significantly lower in the VR Caco-2 cells, including Amide III at 1200–1300 cm^{-1}, Amide I at 1600–1690 cm^{-1} and C–C vibrations of tryptophan and phenylalanine at 1210 cm^{-1} (Figure 4). An increase in protein synthesis and a decrease in nucleic acids in the VR Caco-2 cells suggest that energy could be redirected from proliferation to anabolism in those resistant cells for synthesising more proteins and metabolic reprogramming.

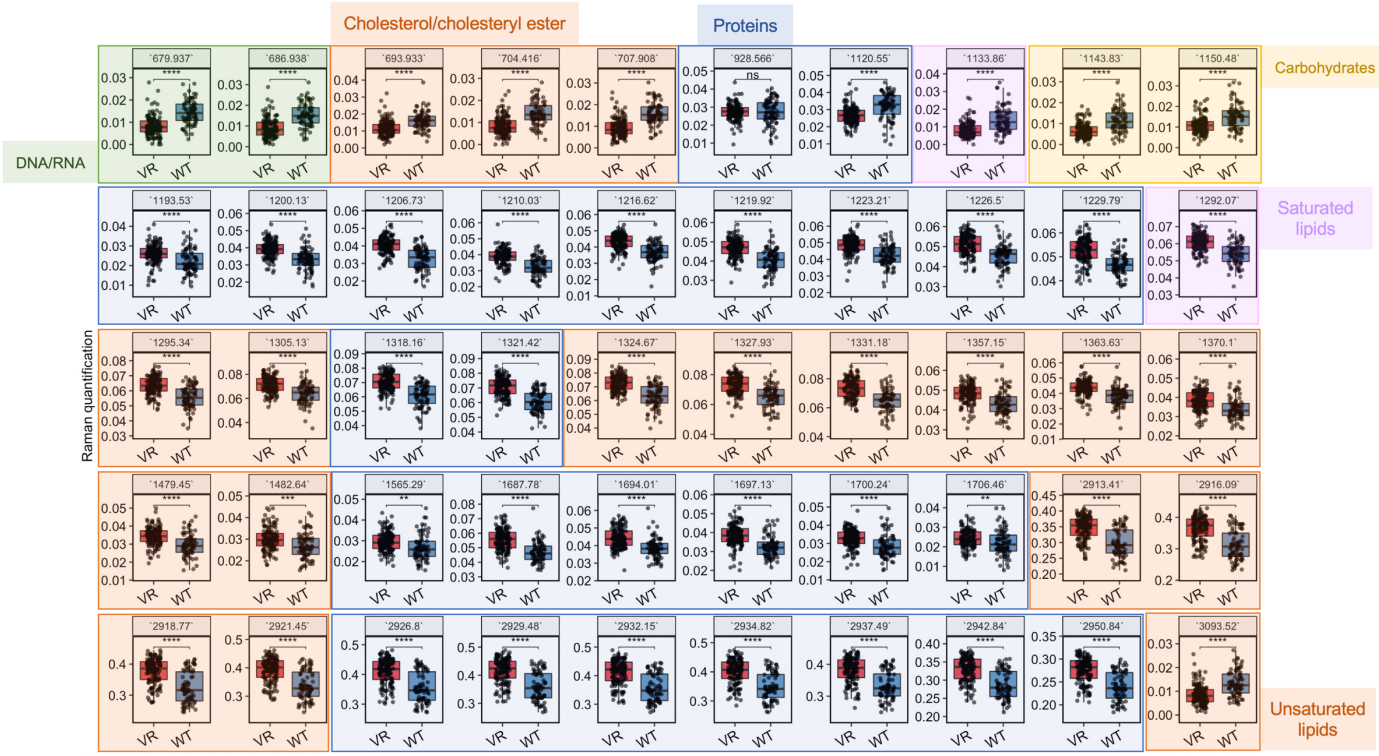


Figure 4. Quantification of biomolecules in Caco-2 and VR Caco-2 based on their SCRS. Differential Raman bands selected based on the LDA model were quantified and compared between Caco-2 and VR Caco-2 cells. All Raman bands are colour-coded as green (DNA/RNA), orange (lipids) or blue (proteins). Statistics was done with Student's *t*-test (ns: $p > 0.05$; **: $p < 0.01$; ***: $p < 0.001$; ****: $p < 0.0001$). VR: VR Caco-2; WT: Caco-2.

The lipidic profiles were also significantly modified in the VR Caco-2 cells. Several bands of saturated lipids exhibited an increase in the VR Caco-2 cells; for example, 1295 cm^{-1} for CH_2 deformation, 1370 cm^{-1} for CH_3 stretching, 1480 cm^{-1} for CH_2 bending and 2913 cm^{-1} for CH_2 stretching. On the other hand, =CH stretching for unsaturated lipids and vibrations in cholesterols and cholesteryl esters demonstrated significant decreases in the VR Caco-2 cells compared to the parental Caco-2. Production of phospholipids in combination with deceased proliferation rates suggests the development of a more saturated and robust plasma membrane. A plasma membrane is made up of lipids, particularly phospholipids and cholesterol, which function as integral pump proteins for multidrug efflux transporters from the ATP-binding cassette (ABC) superfamily. It has been shown that efflux pump activity could be modulated via the development of a more robust plasma membrane for favourable drug binding and release, thus conferring resistance to anti-cancer agents [1]. A decrease in the C–C and C–O ring breathing in the carbohydrates at 1150 cm^{-1} was also observed, suggesting that utilisation of carbohydrates might not be advantageous and the resistant Caco-2 cells might use alternative nutrients, such as lipids.

3.5. Raman-DIP Reveals Metabolic Reprogramming via Newly Synthesised Biomolecules

We next sought to use Raman-DIP to probe the general and specific metabolic activities of VR Caco-2 and Caco-2 cells. SCRS of cells incubated with D_2O showed a distinguishable C–D band centred at 2170 cm^{-1}, with its intensity gradually increased from 0 h to 72 h in both VR Caco-2 and Caco-2 cells (Figure 5A). This band was shifted from the C–H stretching from 2800–3100 cm^{-1} due to the incorporation of D via C/D exchange during active metabolism. Hence, the D

incorporation in cells can be used as a universal indicator of metabolic activity and was calculated as the ratio of (C–D) / (C–D) + (C–H).

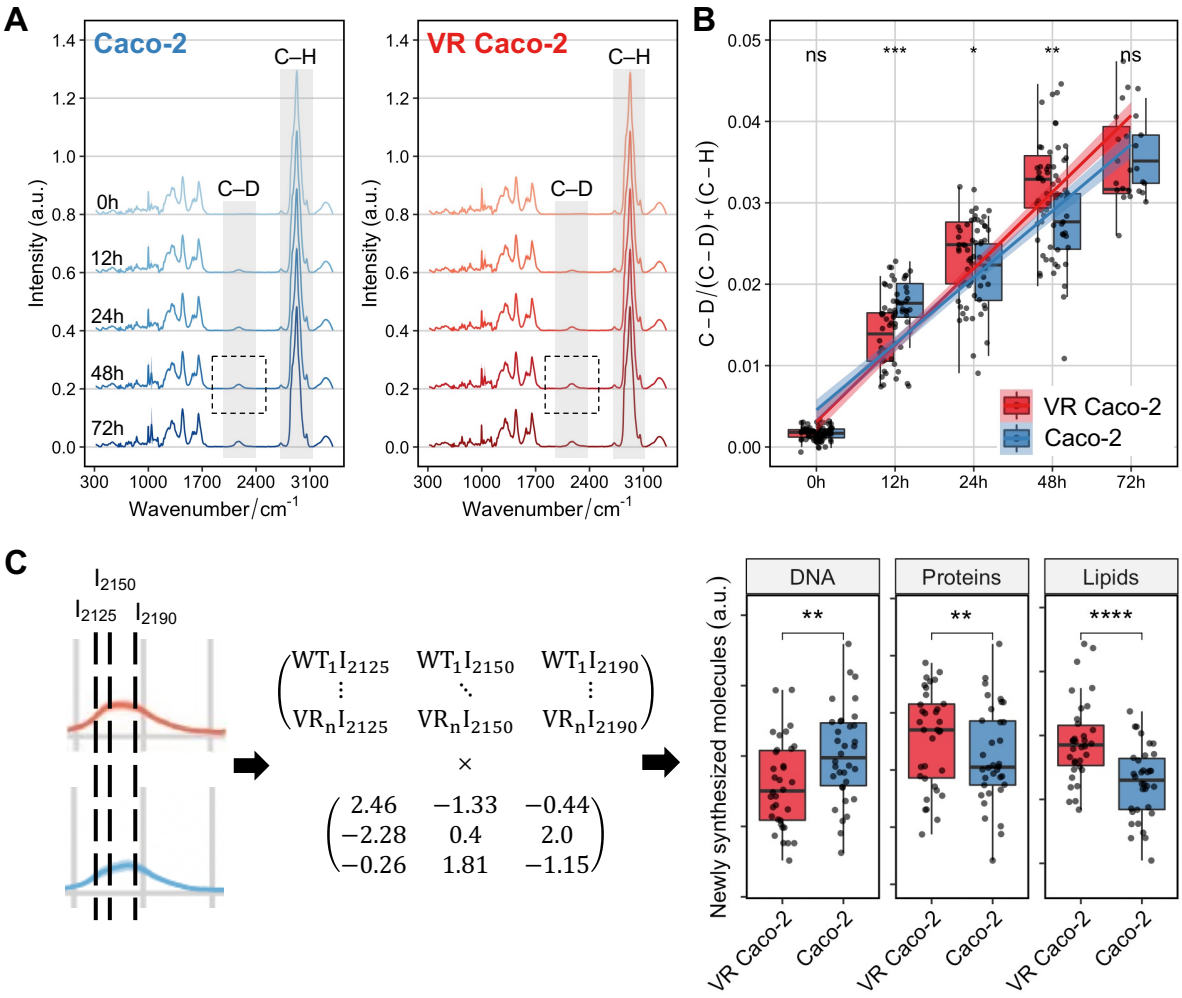


Figure 5. Raman-DIP of newly synthesised DNA, proteins and lipids. (**A**) Raman spectra of VR Caco-2 and Caco-2 cells cultured with 30% D_2O at different incubation time points. The Raman band of C–H vibrations was shifted to a C–D band at 2070–2300 cm^{-1}, highlighted in the grey box. (**B**) Metabolic activities of VR Caco-2 and Caco-2 cells were quantified and compared at each time point by calculating the ratio of C–D/(C–D) + (C–H). (**C**) Linear unmixing algorithm for calculating newly synthesised DNA at 2125 cm^{-1}, proteins at 2150 cm^{-1} and lipids at 2190 cm^{-1}. WT: Caco-2; VR: VR Caco-2. Statistics was done with Student's *t*-test (ns: $p > 0.05$; *: $p < 0.05$; **: $p < 0.01$; ***: $p < 0.001$; ****: $p < 0.0001$).

Figure 5B shows the comparison of D incorporation, hence the metabolic activities, between the two groups of cells at 0, 12, 48 and 72 h. At 12 h, Caco-2 cells exhibited a higher metabolic rate compared to the VR Caco-2 cells, in agreement with the cell proliferation assay showing that the Caco-2 cells replicated much faster than the VR Caco-2 cells and had a much shorter lag phase (Figure 2D,E). Intriguingly, metabolism at 24 and 48 h suggested opposite results to the proliferation assay. Despite being two times slower in proliferation at 48 h and 72 h (Figure 2F), VR Caco-2 showed a significantly higher metabolic activity at 24 and 48 h (Figure 5B). At 72 h, the Caco-2 cells caught up and the 2 groups of cells had similar metabolic activities.

Due to the statistical significance at 48 h in both the proliferation assay and DIP experiment, the C–D band at 48 h was selected for further analysis. Previous studies have shown the C–H signal is a linear overlap of C–H stretching from lipids, proteins and DNA; therefore, the C–D signal is a combination of de novo lipid

synthesis (I_{2190}), de novo protein synthesis (I_{2150}) and DNA replication (I_{2125}) [16, 17]. The C–D band can therefore be resolved into individual components of newly synthesised biomolecules via a linear unmixing algorithm (Figure 5C). At 48 h, both the de novo protein and de novo lipid synthesis in the VR Caco-2 cells increased, while the newly synthesised DNA was significantly lower than the control Caco-2 cells. Together with the decreased DNA/RNA content and increased protein synthesis (Figure 4), the DIP experiments suggest that the escape strategy of the resistant VR Caco-2 cells from the viral infection might be slowing down their replication and redirecting the energy to protein synthesis and metabolic reprogramming, such as forming a more robust plasma membrane. Notably, this finding should be tested in other cell lines to determine if it is one of the universal mechanisms to generate resistance. In future studies, it should also be confirmed using other technologies, such as measurements of cellular respiration or lipidomic mass spectroscopy.

Resistance to chemotherapy and targeted small molecule inhibitors has been found in multiple cancer types [18-21]. It has been proposed that a sizeable proportion of "idling" cells contribute to the persistent disease in BRAF-mutated melanoma patients after targeted inhibitor therapy [18]. Persisters' observed nonquiescent and antiproliferative properties matched well with our persisters' slower proliferation but more active metabolism. It has also been found that upregulation of antioxidant genes and metabolic engineering towards fatty acid oxidation are associated with persisters across multiple cancer types [22], which may correlate with the observation of increased fatty acid synthesis in VR Caco-2 cells. Our study provides phenotypic and metabolic evidence of cancer cells' resistance to viral infection, while little is known about the mechanisms of resistance to viral therapy. Moreover, the emerging reservoir of heterogeneous drug-resistance cells and mechanisms [20] highlights the importance of single-cell techniques in investigating drug-tolerant cancer persister cells. By combining the power of optical magnification and confocality, Raman micro-spectroscopy even has the potential to explore biological processes at subcellular level. It may collectively provide label-free Raman images with subcellular structural and chemical information. In future studies, spatially resolved Raman images could be generated to locate biomolecules within a specific cellular compartment and therefore further pin down the underlying mechanistic pathways.

Table 1. Molecular vibrations and biological assignment of Raman wavenumbers of importance via LDA model.

Raman Wavenumber (cm^{-1})	Molecular Vibrations and Biological Assignment	Reference
680	Guanine; ring breathing modes in the DNA bases/C-2′-endo-anti	[23]
700	Cholesterol, cholesterol ester	[24]
929	Proline, hydroxyproline, ν(C–C) skeletal of collagen backbone	[25]
1121	C–N stretching of proteins	[26]
1134	ν(C–C) skeletal of acyl backbone in lipid (trans conformation)	[27]
1150	C–C, C–O ring breath, glycogen	[28]
1200	Amide III and CH_2 wagging vibrations	[29]
1210	Tryptophan and phenylalanine ν(C–C6H5) mode	[30]
1230–1300	Amide III (arising from coupling of C–N stretching and N–H bonding)	[31]
1295	CH_2 deformation in lipids	[32]
1320	Amide III, C–H deformation	[31]
1370	CH_3 stretching in phospholipids	[32]
1479	CH_2 bending mode of proteins and lipids	[33]
1483	CH_2 bending mode of proteins and lipids	[33]

Appendix

1480–1580	Amide II of proteins	[26]
1600–1690	Amide I of proteins	[26]
2913	CH_3 stretching of lipids	[24]
2950	CH_3 stretching of proteins	[23]
3010	Unsaturated =CH stretching	[24]

4. Conclusions

Resistance of cancer cells to NDV is a major obstacle to the development of the oncolytic virus as a promising cancer treatment. Upon infection of a non-pathogenic strain of NDV to a range of cancer cell lines, Caco-2 cells were found to be most susceptible to NDV killing. However, a subpopulation of Caco-2 cells with persistent infection was identified as VR Caco-2. Compared to their non-infected counterpart, VR Caco-2 cells grew much more slowly and demonstrated resistance towards NDV reinfection and NDV-induced cell death. To understand the metabolic adaptations of the resistant VR Caco-2 cells, single-cell Raman spectroscopy and Raman-DIP techniques were employed to identify the persistent NDV infection in cancer cells. The LDA model has achieved high performance in distinguishing VR Caco-2 and Caco-2 cells at single-cell level with an ROC-AUC of 0.94. Furthermore, the metabolism of those resistant cells was investigated. The Raman profiling and Raman-DIP experiments unveiled an increased de novo synthesis of proteins and lipids, accompanied by a decreased DNA/RNA synthesis. Despite having a much slower replication rate, the VR Caco-2 cells exhibited more active metabolism at 24 and 48 h after infection. The results suggest that the resistant VR Caco-2 cells might employ an escape mechanism from the viral infection to slow down their replication and redirect the energy to protein synthesis and metabolic reprogramming.

As with other cancer therapies, treatments based on oncolytic viruses like NDV face the challenge of resistance. The existence of a subpopulation of drug-resistant cancer cells poses difficulty and complexity in identifying them due to their small number, <1% in the case of Caco-2. Being able to recognise them at single-cell level with high accuracy would be hugely beneficial in the process of developing new cancer treatment. Applying the methods in combinational and personalised medicine, Raman and Raman-D_2O techniques can quickly identify and characterise resistant cells that are still metabolically active based solely on their metabolic phenotypes, thus helping equip better strategies and improve efficacy for fighting treatment resistance in cancer.

Supplementary Materials: The following supporting information can be downloaded at: www.mdpi.com/xxx/s1, Figure S1: Variable importance of Raman wavenumber contributing to the LDA classification.

Author Contributions: Conceptualisation and design: V.N. and W.E.H.; data curation: T.Y. and A.C.J.; data analysis and visualisation: A.C.J. and J.X.; supervision: A.L.H., V.N. and W.E.H.; original manuscript writing: J.X. and W.E.H. All authors have read and agreed to the published version of the manuscript.

Funding: The authors thank EPSRC (EP/M002403/1 and EP/M02833X/1) and NERC (NE/M002934/1) for finance and instrumentation support. This research was also supported by the Biotechnology and Biological Sciences Research Council (BBSRC) grants BBS/E/I/00007032, BBS/E/I/00007039 and BB/R007896/1, the BBSRC Newton Fund which supported Joint Centre Awards on "UK-China Centre of Excellence for Research on Avian Diseases" (BBS/OS/NW/000007) and UK-India Joint Centre on Animal Technology. We also thank the international collaboration project between the University of Oxford and Suzhou Institute of Biomedical Engineering and Technology, Chinese Academy of Sciences.

Institutional Review Board Statement: Not applicable.

Informed Consent Statement: Not applicable.

Data Availability Statement: Data is available from Figshare at 10.6084/m9.figshare.21960743.

Conflicts of Interest: The authors declare no conflict of interest.

References

1. Ganar, K.; Das, M.; Sinha, S.; Kumar, S. Newcastle Disease Virus: Current Status and Our Understanding. Virus Res. 2014, 184, 71–81. https://doi.org/10.1016/j.virusres.2014.02.016.
2. Russell, S.J. RNA Viruses as Virotherapy Agents. Cancer Gene Ther. 2002, 9, 961–966. https://doi.org/10.1038/sj.cgt.7700535.
3. Sinkovics, J. Studies on the Biological Characteristics of the Newcastle Disease Virus (NDV) Adapted to the Brain of Newborne Mice. Arch. Gesamte Virusforsch. 1957, 7, 403–411. https://doi.org/10.1007/BF01240748.
4. Chia, S.-L.; Yusoff, K.; Shafee, N. Viral Persistence in Colorectal Cancer Cells Infected by Newcastle Disease Virus. Virol. J. 2014, 11, 91. https://doi.org/10.1186/1743-422X-11-91.
5. Rangaswamy, U.S.; Wang, W.; Cheng, X.; McTamney, P.; Carroll, D.; Jin, H. Newcastle Disease Virus Establishes Persistent Infection in Tumor Cells In Vitro: Contribution of the Cleavage Site of Fusion Protein and Second Sialic Acid Binding Site of Hemagglutinin-Neuraminidase. J. Virol. 2017, 91, e00770-17. https://doi.org/10.1128/JVI.00770-17.
6. Chan, L.-C.; Kalyanasundram, J.; Leong, S.-W.; Masarudin, M.J.; Veerakumarasivam, A.; Yusoff, K.; Chan, S.-C.; Chia, S.-L. Persistent Newcastle Disease Virus Infection in Bladder Cancer Cells Is Associated with Putative Pro-Survival and Anti-Viral Transcriptomic Changes. BMC Cancer 2021, 21, 625. https://doi.org/10.1186/s12885-021-08345-y.
7. Xu, J.; Yu, T.; Zois, C.E.; Cheng, J.-X.; Tang, Y.; Harris, A.L.; Huang, W.E. Unveiling Cancer Metabolism through Spontaneous and Coherent Raman Spectroscopy and Stable Isotope Probing. Cancers 2021, 13, 1718. https://doi.org/10.3390/cancers13071718.
8. Huang, W.E.; Griffiths, R.I.; Thompson, I.P.; Bailey, M.J.; Whiteley, A.S. Raman Microscopic Analysis of Single Microbial Cells. Anal. Chem. 2004, 76, 4452–4458. https://doi.org/10.1021/ac049753k.
9. Berry, D.; Mader, E.; Lee, T.K.; Woebken, D.; Wang, Y.; Zhu, D.; Palatinszky, M.; Schintlmeister, A.; Schmid, M.C.; Hanson, B.T.; et al. Tracking Heavy Water (D2O) Incorporation for Identifying and Sorting Active Microbial Cells. Proc. Natl. Acad. Sci. USA 2015, 112, E194–E203. https://doi.org/10.1073/pnas.1420406112.
10. Wang, Y.; Huang, W.E.; Cui, L.; Wagner, M. Single Cell Stable Isotope Probing in Microbiology Using Raman Microspectroscopy. Curr. Opin. Biotechnol. 2016, 41, 34–42. https://doi.org/10.1016/j.copbio.2016.04.018.
11. Wang, Y.; Xu, J.; Kong, L.; Li, B.; Li, H.; Huang, W.E.; Zheng, C. Raman-activated Sorting of Antibiotic-resistant Bacteria in Human Gut Microbiota. Environ. Microbiol. 2020, 22, 2613–2624. https://doi.org/10.1111/1462-2920.14962.
12. Xu, J.; Preciado-Llanes, L.; Aulicino, A.; Decker, C.M.; Depke, M.; Gesell Salazar, M.; Schmidt, F.; Simmons, A.; Huang, W.E. Single-Cell and Time-Resolved Profiling of Intracellular Salmonella Metabolism in Primary Human Cells. Anal. Chem. 2019, 91, 7729–7737. https://doi.org/10.1021/acs.analchem.9b01010.
13. Shi, L.; Zheng, C.; Shen, Y.; Chen, Z.; Silveira, E.S.; Zhang, L.; Wei, M.; Liu, C.; de Sena-Tomas, C.; Targoff, K.; et al. Optical Imaging of Metabolic Dynamics in Animals. Nat. Commun. 2018, 9, 2995. https://doi.org/10.1038/s41467-018-05401-3.
14. Hekmatara, M.; Heidari Baladehi, M.; Ji, Y.; Xu, J. D 2 O-Probed Raman Microspectroscopy Distinguishes the Metabolic Dynamics of Macromolecules in Organellar Anticancer Drug Response. Anal. Chem. 2021, 93, 2125–2134. https://doi.org/10.1021/acs.analchem.0c03925.

15. Kim, M.; Garant, K.A.; zur Nieden, N.I.; Alain, T.; Loken, S.D.; Urbanski, S.J.; Forsyth, P.A.; Rancourt, D.E.; Lee, P.W.K.; Johnston, R.N. Attenuated Reovirus Displays Oncolysis with Reduced Host Toxicity. Br. J. Cancer 2011, 104, 290–299. https://doi.org/10.1038/sj.bjc.6606053.
16. Lu, F.-K.; Basu, S.; Igras, V.; Hoang, M.P.; Ji, M.; Fu, D.; Holtom, G.R.; Neel, V.A.; Freudiger, C.W.; Fisher, D.E.; et al. Label-Free DNA Imaging in Vivo with Stimulated Raman Scattering Microscopy. Proc. Natl. Acad. Sci. USA 2015, 112, 11624–11629. https://doi.org/10.1073/pnas.1515121112.
17. Zhang, L.; Shi, L.; Shen, Y.; Miao, Y.; Wei, M.; Qian, N.; Liu, Y.; Min, W. Spectral Tracing of Deuterium for Imaging Glucose Metabolism. Nat. Biomed. Eng. 2019, 3, 402. https://doi.org/10.1038/s41551-019-0393-4.
18. Paudel, B.B.; Harris, L.A.; Hardeman, K.N.; Abugable, A.A.; Hayford, C.E.; Tyson, D.R.; Quaranta, V. A Nonquiescent "Idling" Population State in Drug-Treated, BRAF-Mutated Melanoma. Biophys. J. 2018, 114, 1499–1511. https://doi.org/10.1016/j.bpj.2018.01.016.
19. Hammerlindl, H.; Schaider, H. Tumor Cell-Intrinsic Phenotypic Plasticity Facilitates Adaptive Cellular Reprogramming Driving Acquired Drug Resistance. J. Cell Commun. Signal. 2018, 12, 133–141. https://doi.org/10.1007/s12079-017-0435-1.
20. Ramirez, M.; Rajaram, S.; Steininger, R.J.; Osipchuk, D.; Roth, M.A.; Morinishi, L.S.; Evans, L.; Ji, W.; Hsu, C.-H.; Thurley, K.; et al. Diverse Drug-Resistance Mechanisms Can Emerge from Drug-Tolerant Cancer Persister Cells. Nat. Commun. 2016, 7, 10690. https://doi.org/10.1038/ncomms10690.
21. Echeverria, G.V.; Ge, Z.; Seth, S.; Zhang, X.; Jeter-Jones, S.; Zhou, X.; Cai, S.; Tu, Y.; McCoy, A.; Peoples, M.; et al. Resistance to Neoadjuvant Chemotherapy in Triple-Negative Breast Cancer Mediated by a Reversible Drug-Tolerant State. Sci. Transl. Med. 2019, 11, eaav0936. https://doi.org/10.1126/scitranslmed.aav0936.
22. Oren, Y.; Tsabar, M.; Cuoco, M.S.; Amir-Zilberstein, L.; Cabanos, H.F.; Hütter, J.-C.; Hu, B.; Thakore, P.I.; Tabaka, M.; Fulco, C.P.; et al. Cycling Cancer Persister Cells Arise from Lineages with Distinct Programs. Nature 2021, 596, 576–582. https://doi.org/10.1038/s41586-021-03796-6.
23. Talari, A.C.S.; Movasaghi, Z.; Rehman, S.; Rehman, I. ur Raman Spectroscopy of Biological Tissues. Appl. Spectrosc. Rev. 2015, 50, 46–111. https://doi.org/10.1080/05704928.2014.923902.
24. Czamara, K.; Majzner, K.; Pacia, M.Z.; Kochan, K.; Kaczor, A.; Baranska, M. Raman Spectroscopy of Lipids: A Review. J. Raman Spectrosc. 2015, 46, 4–20. https://doi.org/10.1002/jrs.4607.
25. Larraona-Puy, M.; Ghita, A.; Zoladek, A.; Perkins, W.; Varma, S.; Leach, I.H.; Koloydenko, A.A.; Williams, H.; Notingher, I. Development of Raman Microspectroscopy for Automated Detection and Imaging of Basal Cell Carcinoma. J. Biomed. Opt. 2009, 14, 054031. https://doi.org/10.1117/1.3251053.
26. Rygula, A.; Majzner, K.; Marzec, K.M.; Kaczor, A.; Pilarczyk, M.; Baranska, M. Raman Spectroscopy of Proteins: A Review. J. Raman Spectrosc. 2013, 44, 1061–1076. https://doi.org/10.1002/jrs.4335.
27. Cheng, W.-T.; Liu, M.-T.; Liu, H.-N.; Lin, S.-Y. Micro-Raman Spectroscopy Used to Identify and Grade Human Skin Pilomatrixoma. Microsc. Res. Technol. 2005, 68, 75–79. https://doi.org/10.1002/jemt.20229.
28. Xu, J.; Webb, I.; Poole, P.; Huang, W.E. Label-Free Discrimination of Rhizobial Bacteroids and Mutants by Single-Cell Raman Microspectroscopy. Anal. Chem. 2017, 89, 6336–6340. https://doi.org/10.1021/acs.analchem.7b01160.
29. Dukor, R.K. Vibrational Spectroscopy in the Detection of Cancer. In Handbook of Vibrational Spectroscopy; John Wiley & Sons, Ltd.: Hoboken, NJ, USA, 2006; ISBN 978-0-470-02732-5.
30. Stone, N.; Stavroulaki, P.; Kendall, C.; Birchall, M.; Barr, H. Raman Spectroscopy for Early Detection of Laryngeal Malignancy: Preliminary Results. Laryngoscope 2000, 110, 1756–1763. https://doi.org/10.1097/00005537-200010000-00037.
31. Schuster, K.C.; Reese, I.; Urlaub, E.; Gapes, J.R.; Lendl, B. Multidimensional Information on the Chemical Composition of Single Bacterial Cells by Confocal Raman Microspectroscopy. Anal. Chem. 2000, 72, 5529–5534. https://doi.org/10.1021/ac000718x.

32. Jyothi Lakshmi, R.; Kartha, V.B.; Murali Krishna, C.; Solomon, J.G.R.; Ullas, G.; Uma Devi, P. Tissue Raman Spectroscopy for the Study of Radiation Damage: Brain Irradiation of Mice. Radiat. Res. 2002, 157, 175–182. https://doi.org/10.1667/0033-7587(2002)157[0175:trsfts]2.0.co;2.
33. Shipp, D.W.; Sinjab, F.; Notingher, I. Raman Spectroscopy: Techniques and Applications in the Life Sciences. Adv. Opt. Photonics 2017, 9, 315–428.

Disclaimer/Publisher's Note: The statements, opinions and data contained in all publications are solely those of the individual author(s) and contributor(s) and not of MDPI and/or the editor(s). MDPI and/or the editor(s) disclaim responsibility for any injury to people or property resulting from any ideas, methods, instructions or products referred to in the content.